THERMAL EFFECTS ON CONCRETE BRIDGES IN A CHANGING CLIMATE

SAAD SAAD

A DISSERTATION SUBMITTED TO THE FACULTY OF GRADUATE STUDIES IN PARTIAL FULFILLMENT OF THE REQUIREMENTS FOR THE DEGREE OF DOCTOR OF PHILOSOPHY

GRADUATE PROGRAM IN CIVIL

ENGINEERING YORK UNIVERSITY

TORONTO, ONTARIO

January 2024

Abstract

The research presented herein aims to: 1) Investigate the suitability of AASHTO Bridge Design Specifications in quantifying the design thermal gradients that account for cold wave events, 2) Study the effect of different climate parameters on thermal gradients to help improve current guidelines and ensure that thermal gradients are derived based on the actual bridge location, 3) Quantify the effect of freezing temperature on the coefficient of thermal expansion (CTE) of concrete, 4) Analyze the structural response of a bridge structure to cold wave events, while considering the effect of temperature on the magnitude and sign of the CTE of concrete, and 5) Investigate the effect of climate change on thermal load.

The objectives of this work were achieved mainly using numerical finite element 3D models. Furthermore, the relationship between sub-freezing temperature and thermal strain was studied through experimental testing of concrete cylinders. A weather generator was used to simulate future climate conditions to study the impact of climate change on thermal loads.

The findings indicated that current guidelines fail to capture the true thermal load distribution within a bridge superstructure, which leads to an underestimation of the resulting structural implications, particularly the tensile stresses at the bottom of the cross section. It was also determined that a correlation exists between the direct normal irradiance at a specific location and the resulting thermal differential in a bridge. In addition, the effects of subfreezing temperature on the CTE of concrete were found to be significant and to strongly impact the structural behavior of bridges under cold wave events. For instance, a significant increase in tensile stress in both transverse and vertical direction was predicted during a high intensity cold wave event, an issue which can cause concrete cracking. Furthermore, a methodology to model future hourly climate data was developed, through which it was determined that climate change will have

considerable effects on thermal loads on bridges in the future. For example, it was determined that climate change can cause an increase of about 5℃ and 6℃ in the absolute maximum positive thermal differential in bridges located in Toronto and Whitehorse respectively.

Acknowledgments

I feel greatly indebted to my supervisors, Dr. Rashid Bashir and Dr. Stavroula Pantazopoulou, who were always supportive and helpful during this thesis. I am very thankful to Dr. Bashir for his support both on a professional and personal level. Your hard work, attention to detail, and scholarship are exemplary. I am grateful to Dr. Pantazopoulou for sharing with me your vast knowledge in the field of structural engineering, the breadth of which still astounds me to this day. Thank you both for giving me the opportunity to work on this project. I am forever grateful to you for making me a better engineer and researcher and I look forward to working with you in the future.

I would also like to thank my committee members, Dr. John Gales and Dr. Neil Tandon, for their constructive criticism and time throughout the duration of my research. Thanks to Sindy Mahal and Gillian Moore of the Civil Engineering Department, for their assistance and support with many administrative affairs during my studies.

I would also like to thank Riad Rajab and Kunjan Rupakheti who were always available for any support I needed during the experimental component of my research. Thank you to Dr. Aleksander Czekanski of the mechanical engineering department for allowing me to work in the IDEA lab and to the researchers who welcomed me into that lab. A special thanks goes to Usman Ali, who trained me on the equipment and always offered his support.

Thanks to all the graduate and undergraduate students that I have worked with in the High Bay lab for making it an enjoyable work experience. It was a pleasure working alongside all of you. A special thank you goes to my good friend Mario Antoun for your help in all my concrete casts as well as your insights on my work. A huge thank you goes to Abdul Nasir. You were a major contributor to this research, and it would not have been possible without you. I am very glad to have worked with you over the past few years.

I want to thank my friends in Canada and Lebanon for your support throughout these four years. I am forever grateful to my cousins Carmen Matta and Tassos Tsiris for welcoming me into their home during the pandemic. I am also grateful to my sisters and to my cousins, George and Youssef, whom I consider brothers, for their continuous and unconditional love. Finally, I am forever indebted to my parents for their understanding, endless patience, and encouragement when it was most required.

Table of Contents

List of Tables

List of Figures

Chapter I

Introduction

This chapter serves as an introductory overview of the dissertation, which follows a paper-based thesis format. In this unique structure, each chapter functions as the foundation for an independent paper, collectively contributing to the comprehensive exploration and analysis presented throughout the entire dissertation. The papers have either been published or have been submitted for publication and are therefore presented as published or submitted. This chapter starts with a brief literature review and provides the motivation for the research. An expanded literature review is included within each chapter. Following the literature review, the present chapter includes a succinct summary of each subsequent chapter. The chapter ends by highlighting the contributions made by the author as part of this research effort.

1.1 Literature review and motivation for research

Bridge structures interact with their environment in two different ways. The atmospheric conditions in the bridge vicinity can cause external loads, that increase the overall demand on the structure. These loads include thermal, wind, and snow loads. In addition, the atmospheric conditions strongly influence the mechanical degradation of building materials, which leads to a reduction in structural capacity. For example, typical climate induced degradation mechanisms include corrosion and freeze-thaw cycles.

Bridge codes define environmental loads based on climate data obtained from historical records. Statistical analyses are then performed to determine the design values for different environmental parameters. However, during its service life, a bridge e may be subjected to extreme events which impose structural demands in excess of those prescribed by design codes (Meehl et al. 2000). This concern becomes increasingly significant when considering the ongoing global climate changes, intensifying the risk of subjecting bridges to increased environmental loads and compatibility constraints. Likewise, it can be inferred that the various measures employed to safeguard structural components from mechanical deterioration may prove inadequate in the face of evolving climate change scenarios.

Figure 1.1 illustrates the impact of climate change on the structural demand and capacity of any structure exposed to climate. The figure shows that the size of the failure region (area bounded by demand and capacity curves) can increase due to climate change as the resistance distribution shifts towards the left while the loads distribution shifts towards the right. Considering this change in frequency and intensity of extreme exposures, it is important to re-evaluate the design magnitudes of environmental loads in bridge Codes from the safety and serviceability perspectives.

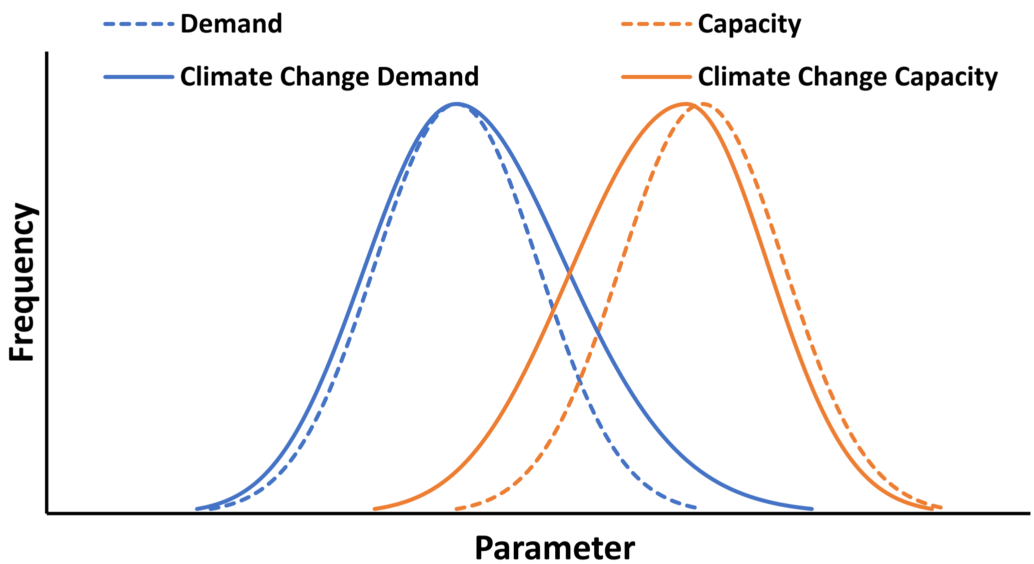

Figure 1.1: Effect of climate change on structural demand and capacity.

The thermal load is one of the main climate induced loads on bridges. The change in atmospheric conditions in the bridge vicinity will lead to a change in the temperature distribution within the bridge. This will lead to the expansion and contraction of the bridge members which can cause internal stresses in the cases where the bridge members are restrained. These stresses, known as compatibility stresses, pose a threat to the bridge's performance, especially when they involve tensile stresses, which can lead to concrete cracking and delamination.

The thermal load can be broken into two components: a thermal gradient and a uniform temperature load. The uniform temperature component mainly arises due to long-term variations in surrounding climatic conditions. Gradients arise over short-term periods due to rapid changes in air temperature and uneven amounts of incident solar radiation received by the surfaces of the bridge (Larsson 2012). The primary focus of this thesis revolves around the thermal gradient, with research efforts dedicated to examining the interplay between climate and the thermal gradient, assessing the influence of thermal gradients on structural performance, and investigating the ramifications of climate change on future thermal gradients. To maintain consistency in result analysis, the term "thermal differentials" will be utilized instead of "thermal gradient."

To comprehensively explore thermal gradients and their impact on structural performance, one must also investigate the coefficient of thermal expansion of concrete. The coefficient of thermal expansion (CTE) is a fundamental material property that quantifies the unit length change (expansion or contraction) that a material will experience in response to a change in temperature (Novikova 1984). Bridge design Codes typically prescribe a constant value for the CTE of concrete when applied in bridge design applications. The specified value is positive, signifying that concrete will expand with rising temperatures and contract with decreasing temperatures. However, it has been shown that saturated or partially saturated concrete specimens can expand rather than contract when subjected to sub-freezing temperatures. This behavior is attributed to the freezing of pore water in the concrete (note that when the water freezes, its volume expands by about 9%.). Therefore, in such instances, the coefficient of thermal expansion may cease to be constant and could even undergo a change in sign, implying that the concrete expands as the temperature decreases. This effect, often overlooked in conventional bridge design, is addressed in this thesis through an experimental investigation. This research explores the connection between sub-freezing temperatures and the coefficient of thermal expansion (CTE) of concrete. The resulting relationship is then incorporated into a numerical analysis, simulating the structural response of bridges to thermal loads.

1.1.1 Thermal Gradients

The spatial temperature distribution within a structure can be deconstructed into various components, including a uniform temperature distribution across the section, linear vertical and horizontal temperature gradients, and a non-linear temperature gradient (Larsson 2012). As mentioned above, the uniform temperature is mainly influenced by long-term variations in surrounding climatic conditions while gradients arise over short-term periods

(Larsson 2012). Gradients are positive when the exterior bridge surfaces have a higher temperature than the bridge interior.

Provisions for thermal loads are included in most bridge Codes. For example, AASHTO LRFD Bridge Design Specifications account for uniform temperature changes using a temperature range which is selected based on the bridge deck material and the climate type (AASHTO 2012). For example, the design temperature range of a concrete bridge deck located in a moderate climate extends from $-18℃$ to $38℃$. AASHTO guidelines also specify a thermal gradient to address short term fluctuations.

The Canadian Highway Bridge Design Code (CHBDC) (CSA 2014) defines the design uniform temperature range as the difference between the minimum and maximum temperatures. These are in turn dependent on the minimum and maximum mean daily temperatures at the location of the bridge. Furthermore, the CHBDC (CSA 2014) defines a linear thermal gradient within the cross section. The magnitude of the gradient is dependent on the depth of the cross section.

The adequacy of bridge Codes in considering the effects of thermal gradients has been investigated in several studies (Lee 2012a; Gu et al 2014; Barr et al 2014; Hagedorn et al 2019). It has been reported that positive thermal gradients arising in both concrete box girders and I girders differ significantly from AASHTO provisions (Lee 2012a; Hagedorn et al 2019). Experimental observations have indicated a substantial underestimation of negative thermal gradients in bridge design Codes. This oversight can carry significant implications for the structural behaviour, as highlighted in studies by Gu et al. (2014) and Barr et al. (2014). Moreover, three-dimensional thermal gradients in arch bridge girders were explored in a study by Zhou et al. (2015), which integrated data from a long-term field monitoring system. In a separate investigation, Hedegaard et al. (2013) measured thermal effects in a post-tensioned concrete box girder bridge in Minneapolis, Minnesota. The stresses and deformations derived from the measured results were notably higher than those obtained using the AASHTO LRFD bilinear design gradients.

The impact of thermal load on the structural behaviour of bridges has also been investigated. In a study conducted by Hossian et al. (2020), it was discovered that the cumulative effect of primary thermal stresses, coupled with additional positive restraint moments induced by thermal gradients, could surpass the tensile strength of concrete. Another investigation by Tan et al. (2023) employed finite element modeling to analyze the structural response of the main beam in a single-tower hybrid beam cable-stayed subjected bridge to thermal loads. The study revealed that vertical temperature gradients exert a significant influence on the longitudinal stress in the lower flange of the steel I-beam, resulting in tensile and compressive stresses in the girder reaching approximately $14\ MPa$ and $12\ MPa$, respectively. Similarly, research by Abi Shdid and El-Masri (2019) established that thermally induced tensile stresses in composite steel-concrete bridges are notably significant, surpassing service load stresses and constituting a substantial portion of the concrete's tensile strength. In a separate study, Xia et al. (2018) measured temperature-induced strains in a suspension bridge over the Yangtze River in Jiangsu, China. The findings revealed that temperature-induced strains, in some instances, exceeded those resulting from traffic and static loads. Additionally, other studies, including Pisani (2004), Lee and Kalkan (2012), Lee (2012b), Ghimire (2014), and Song et al. (2016), further explored the implications of thermal gradients on structural behavior.

The studies highlighted above have illustrated the significance of thermal gradients on the structural behaviour of bridges and identify some inadequacies in the current bridge design Codes. Therefore, one of the main objectives of this thesis is to further investigate relevant Code provisions with particular emphasis on the negative thermal gradients which have not been studied sufficiently yet, in comparison with the positive thermal gradients. The findings of this study explore whether these Code limitations constitute serious shortfalls. Furthermore, the structural implications of the thermal load will also be investigated in this thesis.

1.1.2 Climate Change

Anthropogenic climate change is defined as a change in climatic conditions which may be attributed directly or indirectly to human activity that alters the composition of the global atmosphere (IPCC 2014). Climate change may occur naturally, but recent warming trends have been mainly driven by anthropogenic activity and not by natural forcing (IPCC 2014). Climate change exerts its influence on various climate parameters, encompassing temperature, wind, precipitation, and snowfall. Importantly, these changes are not confined to specific regions or countries; rather, their impacts reverberate globally. The projected climate changes are expected to influence the thermal load acting on bridge decks. This is attributed to alterations in climate conditions at the bridge location, encompassing changes in the frequency and intensity of extreme events, as well as fluctuations in minimum and maximum ambient temperature values. Nevertheless, there is a scarcity of research that quantifies the impact of climate change on thermal loads. This dissertation is primarily motivated by this knowledge gap, aiming to address the lack of comprehensive studies in existing literature. Before delving into predictions regarding the effect of climate change on thermal loads, it is imperative to approach the issue from a climate perspective—comprehending climate modeling techniques and their associated limitations is a crucial initial step.

Climate projections are performed using models known as Global Climate Models (GCMs). These models simulate the physical processes that determine the global climate. They attempt to represent the atmospheric and oceanic processes in mathematical form in order to project probable conditions in the future while building on the measured and empirical evidence from the past and present. Some of the physical processes that are modelled in GCMs include convection, solar radiation, infrared radiation, cloud formation, as well as transpirations (Hartmann 2015).

While Global Climate Models (GCMs) are powerful tools for predicting future climate, they also have some limitations in terms of their spatial resolution, parameterization, complexity, boundary conditions, confidence in assessing future emissions, and natural variability (Bader et al. 2008; Lupo et al. 2013; Hartmann et al. 2015). Given the inherent limitations and uncertainties associated with GCMs, a necessity for guidance and standardized climate simulations has emerged. To address this, the Coupled Model Intercomparison Project (CMIP) was established. This is a collaborative effort within the global climate modeling community to improve understanding of the Earth's climate system and to provide a basis for assessing the potential impacts of climate change (Wayne 2014). The most recent phase of the Coupled Model Intercomparison Project is CMIP6, and it comprises an expanded range of modelling groups that produce simulations for different climate change scenarios, including historical, current, and future conditions, with a focus on the period from 2006 to 2100. CMIP6 simulations are more comprehensive than past iterations as they include higher spatial and temporal resolutions and an improved representation of the physical processes (O'Neill et al. 2016).

To perform the simulations discussed above (CMIP6), emission scenarios had to be developed to predict the amounts of expected future emissions. These scenarios are referred to as Shared Socioeconomic Pathways (SSPs) as outlined by Eyring et al. (2016). SSPs consider a broad set of social, economic, and technological factors that can influence greenhouse gas emissions and the global climate. SSPs are useful for exploring possible future scenarios and assessing the potential impacts of climate change and are used by climate modelers in their GCMs to project trends for different climate parameters.

One issue facing engineers working with climate change projections is the availability of climate change projections in an accessible format and in a temporal and spatial scale that aligns with the specific requirements of the intended application. Therefore, another one of the main objectives in this research is to provide engineers with a methodology that can be used to model future hourly climate data at the required spatial scale. This methodology will then be applied to determine the effect of climate change on the thermal load in bridges.

1.1.3 Effect of temperature on the CTE of concrete

AASHTO LRFD Bridge Design Specifications provide guidance on the structural and thermal properties for a concrete bridge deck. The code recommends using a constant thermal expansion coefficient (CTE) equal to $10.8 \times 10^{-6}/°\mathrm{C}$ for normal weight concrete (AASHTO 2012); the CTE of reinforcing steel practically has the same value. The main issue with the constant CTE assumption is that it does not take into consideration the effect of temperature on the CTE of concrete. In cold regions, concrete experiences freezing when exposed to sub-freezing temperatures. During this process, water within the concrete freezes and undergoes approximately a 9% increase in volume (Powell-Palm et al., 2020). Such expansion can lead to a noteworthy reduction or even a change in the sign (from positive to negative) of the effective thermal expansion coefficient of concrete (ECTE), as noted in studies by Planas et al. (1984) and Xia et al. (2017). This tendency for expansion can give rise to unaccounted internal forces, potentially altering the stress state within a bridge deck. Moreover, it is crucial to consider this effect because various depths along the cross-section exhibit different temperatures, resulting in distinct expansion coefficients. Consequently, two points along the depth will undergo different expansion and contraction behaviors, not only owing to temperature disparities but also due to variations in thermal coefficients. Another problem posed by this phenomenon is that it might lead to an incompatibility between the ECTE of concrete and the CTE of steel reinforcement which are identical in traditional concrete design so that the two materials are treated as thermally compatible (Aydin 2018).

Considerable research and effort have been dedicated to exploring the impact of temperature on various structural properties of concrete beyond its effective coefficient of thermal expansion (ECTE). For instance, studies such as Cran (1963) and Dahmani et al. (2017) delved into the influence of temperature and water-to-cement (w/c) ratio on the elastic modulus of concrete. Several models describing the change in elastic modulus with temperature have been proposed, as documented in works by FIB (1982), Van de Veen (1987), and Downie (2005). Likewise, an extensive body of research has investigated the effect of temperature on concrete compressive strength, as demonstrated in studies by Downie (2005), Xie et al. (2014), Xie et al. (2018), and Yamina (2018). Additionally, the impact of temperature on concrete tensile strength has been explored in numerous studies, including those conducted by Yamane et al. (1978), Browne and Bamforth (1981), and Miura (1989).

Conversely, while there has been exploration of the relationship between temperature and the effective coefficient of thermal expansion of concrete, the literature still lacks a comprehensive quantification of this relationship and the influencing factors, particularly for normal strength concrete within temperature ranges not extending below -50℃. Most of the research in this domain has been centered around concrete employed in liquefied natural gas tank applications (Planas et al. 1984; Xia et al. 2017), where temperatures can plummet to around -160℃. Other studies have primarily focused on determining the critical degree of saturation, below which no expansion occurs due to the freezing of ice in concrete (Fagerlund, 1973; Fagerlund, 1977a; Fagerlund, 1977b; Li et al., 2012; Obla et al., 2016). Studies addressing the impact of temperature on the effective coefficient of thermal expansion within the desired temperature range are limited but encompass works such as those conducted by Litvan (1976), Scherer and Valenza (2005), Esmaeeli et al. (2017), and Liu et al. (2020). These studies collectively demonstrate that the relationship between temperature and the ECTE of concrete is influenced by various variables, including pore size distribution, volume of entrained air, internal water pressure, and the presence of chemical charges.

1.1.4 Thesis Objectives

The main objectives of this thesis are summarized as follows:

1. Establish a relationship between various climate parameters and the formation of thermal gradients in bridge decks by comprehending the diverse processes that contribute to the emergence of these gradients.
2. Integrate the above relationship into a thermal finite element model, utilizing climate data to simulate the thermal gradients occurring in bridges throughout any given time period.
3. Investigate whether thermal gradient provisions in current bridge design Codes adequately capture the thermal gradients predicted using the thermal model.
4. Extend the thermal model into a thermal-structural finite element model capable of representing the interaction between the structural behavior of the bridge and the considered climate parameters. Apply the updated model to investigate the effect of limitations in Code prescribed gradients, if any, on the resulting structural performance of the bridge.
5. Design and conduct an experimental investigation on the effect of sub-freezing temperatures on the effective coefficient of thermal expansion of concrete to provide valuable insights into the material behavior under extreme cold conditions, aiding in the improvement of construction practices and structural design in cold climates.
6. Incorporate the effect of sub-freezing temperature on the effective coefficient of thermal expansion into the structural model and determine the implications of neglecting this effect in bridge engineering applications.
7. Develop a methodology for the selection of the most relevant global climate model for analysis and by which future hourly climate data can be projected for a specific location. The methodology is used to determine the effect of climate change on the thermal load in bridges during heatwaves, cold waves, and days of high daily temperature difference.

1.2 Summary of chapters

This section contains a summary of each Chapter from Chapter II to Chapter VI. These chapters were written as journal papers to be submitted for publication. Two of these papers (presented in Chapter II and Chapter III) have already been published, two (Chapter IVand Chapter VI) have been submitted for publication, and one (Chapter

V) is under final revision. Full citations are provided in Section 1.2.6. Note that Chapter VII provides a summary of the thesis, conclusions, as well as recommendations for future research.

1.2.1 Chapter II

The Effect of Cold Waves on the Structural Performance of Concrete Box Girders

The objective of the work presented in this chapter was to scrutinize the adequacy of AASHTO Bridge Design Specifications in reliably quantifying design thermal gradients that consider cold wave events. This objective was achieved using an advanced finite element platform to model the thermal and structural performance of a prestressed concrete box girder. The analysis focused on evaluating the thermal gradients that are manifested during cold wave events and their consequential impact on structural performance. To commence, climate data, encompassing ambient temperature, dew point temperature, cloud cover, windspeed, and solar radiation, from four distinct cold wave events in Toronto, Ontario, Canada, was compiled. Subsequently, these climate conditions were utilized as boundary inputs in a three-dimensional thermal finite element model, specifically designed for a prestressed concrete box girder bridge (St. Joseph Bridge (R017)) in Ontario. This model predicted the temperature distribution within the bridge deck during each of the cold wave events. Details on the physical processes governing this model are presented in the chapter. Furthermore, the model was validated against field measurements from a concrete box girder bridge located in Jiangsu, China.

The maximum negative thermal differentials predicted by the four models were then analyzed in comparison with the AASHTO and CHBDC prescribed thermal differentials. The results revealed that the negative differentials predicted by thermal simulations at the bottom of the cross-section are notably larger than the corresponding Code-prescribed thermal differentials. Furthermore, the temperature-time history acquired for the bridge was utilized as a thermal load in a structural model of the concrete deck. The structural model, incorporating prestressing and reinforcement details, represented the bridge deck as simply supported. The maximum and minimum stresses calculated at the top and bottom fiber of the cross section along the length of the span for the four cold wave simulations were then compared against maximum and minimum stresses obtained from simulating the AASHTO prescribed thermal load. The results for all the cold waves indicated an increase in tensile stresses near the bottom of the cross section. Furthermore, the results for some of the cold wave events indicated an increase in compressive stress at the top of the cross section.

1.2.2 Chapter III

Numerical Study on the Effect of Climate Parameters on the Extreme Thermal Gradients in Concrete Box Girders

The aim of the study presented in this chapter was to help enhance current guidelines to ensure that thermal gradients are derived based on the bridge location. This objective was achieved through the investigation of the relationship between climate parameters and the resulting thermal differentials.

A total of 20 locations from across Canada were chosen to represent the different climate zones and subdivisions defined according to the Köppen classification system. Meteorological data for these locations was subsequently compiled and organized into datasets for each location, encompassing every climate parameter relevant to the atmosphere-bridge boundary thermal exchange. This dataset consisted of 140 entries where each entry represents average climatic conditions for one climate parameter for one city (20 cities with 7 climate parameters each). The dataset entries were then input as boundary conditions into a thermal model of a concrete box girder. The maximum positive temperature differentials at the top of the bridge were then obtained from each simulation. The study also featured a demonstration of the methodology, showcasing the entire process for the city of Swift Current, Canada.

Upon scrutinizing the results from all simulations, a correlation was established between the direct normal irradiance (DNI) at a specific location and the ensuing thermal differential between the top and the interior of the cross-section. This correlation led to the definition of four categories, each representing a distinct range of DNI values and the resulting thermal differentials between the top and the interior. It was noted that Canadian Highway Bridge Design Code limits are likely to be exceeded when the direct normal irradiance value exceeds $1200\ KJ/m^2$. To showcase the applicability of the established relationship, a case study was conducted. This study delved into the investigation of the maximum limit stipulated by the Canadian Highway Bridge Code across various provinces in Canada.The findings show that limits are exceeded significantly in Central and Western provinces as well as in some of the Northern territories.

1.2.3 Chapter IV

The Effect of Temperature on the Thermal Expansion Coefficient of Concrete

This Chapter presents a comprehensive experimental research study that aimed to investigate and quantify the impact of freezing temperatures on the thermal expansion of concrete in cold regions. Freezing/thawing cycles, with temperatures reaching $-40℃$, were implemented on test specimens derived from four diverse concrete mixes to gather data on the ensuing thermal strain. The study explored three specific water-to-cement (w/c) ratio values, each with a maximum coarse aggregate size of 19 mm. Furthermore, a mix featuring a maximum aggregate size of 10 mm was also examined. The samples underwent testing across various degrees of saturation.

Each sample was subjected to two freeze/thaw cycles that ranged from temperatures of $-40℃$ to $20℃$ using a specialized heating-cooling apparatus. The resulting thermal strain in the instrumented specimens was recorded at 15 minute intervals using a strain gauge. The findings indicated the existence of a critical degree of saturation (about 80%) below which the effect of temperature on the thermal expansion coefficient of concrete is minimal. At degree of saturation values above the critical value, a correlation was observed between the w/c ratio and the effect of subfreezing temperature on the thermal strain. Freezing temperatures caused significant expansion on specimens with a high w/c and negligible effects on specimens with a low w/c ratio. Similar results were observed when investigating residual strains, with the high w/c ratio samples displaying the largest amount of residual strain. Furthermore, the effect of the number of consecutive freezing-thawing cycles on the accumulation of the resulting residual strain was also investigated. It was observed that the residual strain increments decrease with the increase in number of freezing and thawing cycles, converging to a permanent expansion value that quantifies frost-induced damage in the structural component.

The final phase of the chapter presents a numerical investigation on the structural implications of the effect of freezing on thermal strain. The investigation involved a structural finite element 3D model, in which a reinforced concrete beam is subjected to one freeze/thaw cycle. The results of incorporating the effect of freezing temperature are then presented and analyzed.

1.2.4 Chapter V

Bridge Decks Under Cold Waves: The Effect of Concrete's Temperature Dependent CTE

The objective of this study was to assess the structural response of a bridge structure under the influence of cold wave events, with a specific focus on understanding how temperature affects both the magnitude and sign of the effective coefficient of thermal expansion (ECTE) of concrete. An empirical hysteretic model was formulated to account for the temperature dependence of the ECTE. The proposed model is a function of the minimum temperature that the concrete reaches during the cooling cycle. Three historic cold wave events of different intensity (low, medium, and high) were then selected to be used in the investigation. Cold waves of different intensity were chosen to demonstrate the effect of more extreme freezing temperatures. Meteorological data from these events was then input into thermal models to simulate the temperature distribution in the bridge deck. The resulting temperature field was subsequently utilized to determine the resulting stresses using a structural finite element model that incorporates the temperature-dependence of the effective coefficient of thermal expansion, specifically, the proposed hysteretic model. The results indicated that the change in ECTE has a significant effect on the structural response, highlighting the need for appropriate modifications to relevant sections of the bridge design Codes.

1.2.5 Chapter VI

The Effect of Climate Change on Thermal Loads in Concrete Box Girders

The focus of this chapter was to provide a methodology by which engineers can investigate the effect of climate change on thermal load in bridges. Initially, an overview of climate modelling techniques and limitations was presented. A criterion for selecting global climate models was established, considering modeling limitations. After choosing the necessary climate models, a weather generator was employed to downscale the projections from these global climate models, obtaining future daily projections for the specific location of interest. The daily data was then transformed into hourly data using empirical and theoretical models. The projected hourly data could then be used as input in thermal finite element models to predict the thermal load acting on a bridge in a future climate.

To illustrate the methodology, future climate conditions were projected for two locations across Canada (Toronto and Whitehorse). Subsequently, the resulting thermal loads acting on the bridge were determined during heat waves, cold waves, and periods of high daily temperature variation. The results showed that climate change could lead to a significant increase in the magnitude of thermal loads on bridges. It was also shown that the effects of climate change on the thermal load vary significantly depending on the global climate model used, the emission scenario, and the location.

1.2.6 Chapter citations

Chapter II: Saad, S., Bashir, R., and Pantazopoulou, S. 2022. "The effect of cold waves on the structural performance of concrete box girders." *Structural Engineering International*, 32(4), 596–604.

Chapter III: Saad, S., Nasir, A., Bashir, R., and Pantazopoulou, S. J. 2023. "Numerical Study on the Effect of Climate Parameters on the Extreme Thermal Gradients in Concrete Box Girders." *Journal of Bridge Engineering*, *28*(10), 04023069.

Chapter IV: Saad, S., Bashir, R., Pantazopoulou, S. J., Nasir, A., and Czekanski, A. 2023. "The Effect of Temperature on the Thermal Expansion Coefficient of Concrete." *Journal of Cold Regions Engineering* (Submitted)

Chapter V: Saad, S., Bashir, R., Pantazopoulou, S. J. 2023. "Bridge Decks Under Cold Waves: The effect of concrete's temperature dependent CTE." *Journal of Structural Engineering* (Under Final Revision)

Chapter VI: Saad, S., Nasir, A., Bashir, R., and Pantazopoulou, S. J. 2023. "The Effect of Climate Change on Thermal Loads in Concrete Box Girders." *Journal of Bridge Engineering*, (Submitted)

1.3 Contributions

The following is a list of the contributions that have been made to science and engineering as part of this research effort.

1. The second chapter of this thesis provides a framework for modelling the heat exchange at the atmosphere bridge boundary and the resulting structural response. The thermal and structural models developed in this part formed the basis of the remaining investigations presented, in which

these models were used as a means to study different aspects of the interaction between climate and thermal loads. In this part, the models were used to investigate whether thermal gradient guidelines in current bridge design Codes can capture the actual thermal gradients that occur in bride decks during cold wave events. The results highlighted deficiencies in these bridge codes in evaluating the negative temperature differentials that arise at the bottom cross section. Past research on this subject had focused on the positive gradients arising in the superstructure at high ambient temperatures and limited work had been conducted to study negative gradients. Moreover, the chapter underscores the structural implications and complications that may arise due to these deficiencies.

2. The third chapter provides a new approach for the estimation of thermal differentials based on available climate data for a specific location. This approach will be useful to bridge engineers for structural assessment of existing structures. In addition, this approach can aid regulatory authorities in replacing general thermal load guidance with location specific guidelines. Furthermore, the approach was used to produce a map which highlights provinces and territories in which code limits may be potentially exceeded.
3. The study presented in Chapter Four enriches the existing knowledge base regarding the relationship between thermal strain and sub-freezing temperatures. It achieves this by experimentally establishing the impact of the water-to-cement (w/c) ratio on this relationship. Furthermore, it verifies the existence of a critical degree of saturation in concrete and quantifies the resulting residual strains. The study also includes an analytical interpretation of the experimental evidence. Furthermore, the chapter highlights the structural implication of this relationship through numerical modelling, a task that had not been attempted previously in the literature.
4. The fifth chapter extends the exploration of the structural implications of the temperature-dependent effective coefficient of thermal expansion of concrete. This is illustrated by simulating the behavior of a prestressed concrete bridge subjected to cold wave events of varying intensity. The findings underscore the substantial tensile strain that could be manifested in both the lateral and vertical directions, potentially resulting in concrete cracking. This is a contribution to the bridge

community as these strains would have been unaccounted for in traditional bridge design. Moreover, the chapter proposes an original hysteretic model for the relationship between thermal strain and temperature.

5. The contributions of the sixth chapter of this dissertation are threefold. 1) First, it furnishes bridge engineers with an understanding of climate change and climate modeling. Additionally, it demonstrates an approach for selecting global climate models from which future climate data can be derived. 2) Furthermore, it presents a methodology which can be used to generate hourly future climate projection at the required spatial scale. This methodology is not only useful to bridge engineers, but it can be extended to any application where hourly future climate data is required. This approach is innovative and is presented in a manner that can be easily adapted by engineers requiring climate data, without the necessity for an in-depth understanding of climate science. 3) Finally, this chapter highlights the potential increase in thermal loads acting on bridges by using the aforementioned methodology to predict future climate data for two locations and assessing the resulting thermal loads in comparison to the historic loads.

Chapter II

The Effect of Cold Waves on the Structural Performance of Concrete Box Girders

Note: The content of the chapter is presented as published in the Structural Engineering International journal. The format (headings, caption numbering, and citations) has been edited to match the thesis format.

2.1 Introduction

Bridge structures interact with the surrounding environment in two different ways. Atmospheric conditions impose external loads, which increase the overall demand on the structure. For instance, typical environmental loads considered in structural design include thermal, wind and snow loads. Furthermore, climatic conditions play an important role in the mechanical degradation of building materials, resulting in the loss of structural capacity. Corrosion and freeze-thaw cycles are some of the examples of climate induced degradation mechanisms.

Bridge codes tend to define environmental loads based on climate data obtained from historical records. Statistical analyses are then performed to determine the design values for different environmental parameters such as wind speeds, minimum and maximum temperatures, annual precipitation, rainfall intensity, as well as snow effects, with probability of occurrence of 1/n, where n is the return period of the design event. However, throughout its service life, a bridge structure may be exposed to extreme events which may cause structural demands that exceed those prescribed by the design code. This issue becomes more prominent when one considers that the climate is rapidly changing globally. In light of this change in frequency and intensity of extreme exposures, it is important to re-evaluate the design magnitudes of environmental loads in the bridge codes from a safety and serviceability perspective.

One of the main climate induced loads on bridges is the thermal load which results from the fluctuation of ambient temperature and from incoming solar radiation on bridge surfaces. As a bridge responds to the atmospheric conditions in its vicinity, the temperature distribution within the bridge deck changes. This temperature change leads to the expansion and contraction of the bridge components. In the instances where a member is restrained, the resulting expansion/contraction strains will create internal stresses. These stresses are detrimental to the performance of the bridge particularly if they are tensile stresses as that may cause cracking of the concrete.

The spatial temperature distribution in a structure can be decomposed into several components as follows: a uniform temperature distribution over the section, linear vertical and horizontal temperature gradients, as well as a non-linear temperature gradient (Larsson 2012). The uniform temperature component mainly arises due to long-term variations in surrounding climatic conditions. Gradients arise over short-term periods due to rapid changes in air temperature and uneven amounts of incident solar radiation received by the surfaces of the bridge (Larsson 2012). Gradients are assumed to be positive when the temperature at the exterior surfaces of the bridge is higher than the interior. On the other hand, a gradient is negative when the exterior surfaces are cooler than the interior.

Previous research into the effect of thermal gradients on the development of restraint moments in continuous prestressed concrete girder bridges indicates that the thermal gradients can increase the likelihood of the occurrence of cracking at the diaphragm and girder ends (Ghimire 2014). It has been shown that thermal gradients coupled with geometry and support imperfections can cause lateral instability in box girders particularly during construction when the girder has no thermal insulation (Lee 2012a). In fact, during cantilever construction, the temperature gradient may cause longitudinal and transverse tensile stresses in a box girder section that reach up to 2 and 5 MPa respectively (Song et al. 2016). Moreover, the resulting vertical deflections are significant and need to be considered in the formwork design (Song et al.2016). An analytical study to estimate deformations induced by vertical and lateral thermal gradients on a 30m long BT-1600 girder located in Atlanta, Georgia, US, indicated that lateral deformations accounted for about 50 percent of the initial sweep tolerance allowed in the PCI Manual (Lee and Kalkan 2012). Nonlinearity in the thermal strains acting on reinforced and prestressed concrete bridge decks and slabs can also cause significant variation in terms of stress and strain distributions (Pisani 2004). Therefore, it is clear that thermal gradients can greatly affect the structural performance of bridges and must be given special attention particularly when considering projected changes in climate.

Provisions for thermal loads are included in most bridge codes. For example, AASHTO LRFD Bridge Design Specifications account for uniform temperature changes using a temperature range which is selected based on the bridge deck material and the climate type (AASHTO 2012). AASHTO guidelines also provide a thermal gradient to address short term fluctuations as shown in Figure 2.1

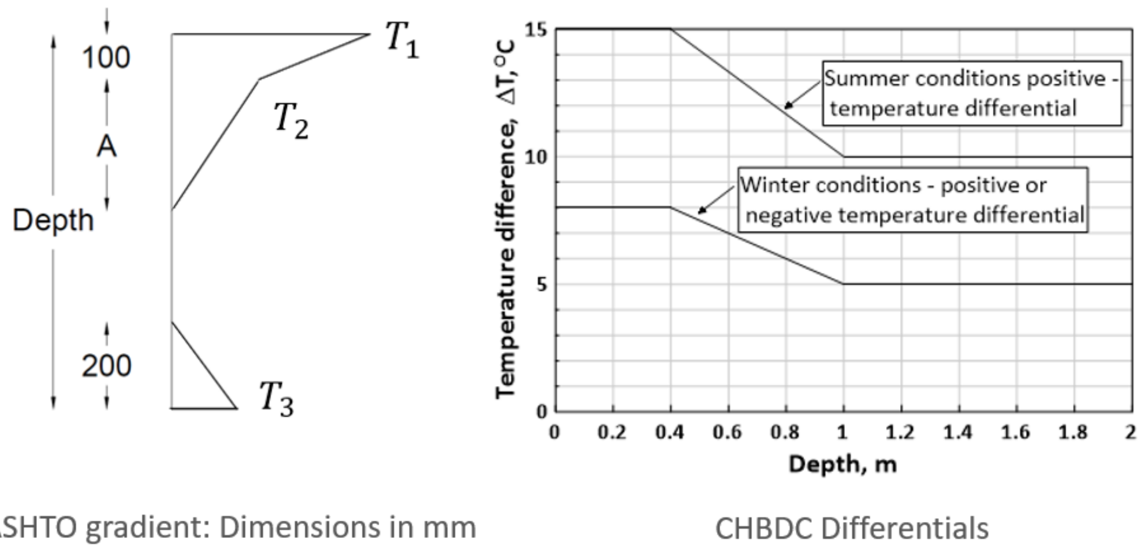

Figure 2.1: AASHTO prescribed gradient (AAHSTO 2012) and CHBDC (CSA 2014) prescribed differentials.

In Figure 2.1, the temperatures T_1, T_2, T_3, and the dimension A are selected based on the location of the bridge and the total depth of the cross section. For instance, the values of T_1 and T_2 for a North-Eastern United States location are 22.7°C and 6.1°C respectively. The value of T_3 is site specific but can reach a maximum of 2.7°C. When considering negative gradients, T_1 and T_2 must be multiplied by a factor of -0.2 or -0.3 depending on whether the deck has an asphalt overlay or not.

The Canadian Highway Bridge Design Code (CHBDC) (CSA 2014) defines the design uniform temperature range as the difference between the minimum and maximum effective temperatures. These are in turn dependent on the minimum and maximum mean daily temperatures at the location of the bridge as well as the type and depth of the superstructure. Furthermore, the CHBDC (CSA 2014) defines a linear thermal gradient within the cross section. The magnitude of the gradient is dependent on the depth of the cross section as shown in Figure 2.1.

The adequacy of bridge codes in considering the effects of thermal gradients has been investigated in several studies (Lee 2012b; Gu et al. 2014; Barr et al. 2014; Hagedorn et al. 2019). During heatwaves, temperature gradients that develop in concrete I-girders differ significantly from AASHTO provisions (Hagedorn et al. 2019). The results of numerical and experimental studies on prestressed I- girders indicate that the horizontal and vertical gradients in AASHTO standards need to be modified (Lee 2012b). It has also been shown that the cold waves can induce unfavourable effects in box girder systems, an aspect that is not considered in the AASHTO recommended thermal gradients (Gu et al. 2014). In addition, measurements on two multi-cell box girders located in the states of Utah and California indicated that AASHTO guidelines significantly underestimate the negative temperature gradients that will develop both at the top and the bottom of the section (Barr et al. 2014). The highlighted studies identify some inadequacies in the AASHTO bridge Code when it comes to quantifying thermal effects on bridge decks both during construction and in service. Therefore, before quantifying the possible effects of climate change on thermal loads, the relevant Code provisions for defining thermal load values during historical extreme events need to be explored further.

The aim of this study is to investigate the suitability of AASHTO Bridge Design Specifications in quantifying the design thermal gradients that account for cold wave events and assessing the structural implications that result from these gradients. This objective is achieved by investigating the thermal behavior of a concrete box girder bridge subjected to four different historic cold wave events through a calibrated numerical three-dimensional finite element model with climate interaction boundary that establishes a rigorous energy balance at all the bridge surfaces. The obtained thermal gradients are then assessed in light of those recommended in AASHTO Codes. The temperature distributions obtained from the thermal analysis are then input as boundary conditions in a structural finite element model to determine the impact of the cold wave events on structural performance. The obtained results are corroborated through a second study of a concrete I girder. The results of this research will help put into perspective the kind of challenges and limitations faced by today's bridge codes and help improve their robustness in dealing with the current and future climate.

2.2 Methodology

The first step in identifying the effect of cold waves on the structural performance is to understand the characteristics of cold wave events and select a sample of such events that can be used in the study. However, a variety of cold wave definitions can be found in the literature, where different site-dependent criteria are used to define cold wave events. For example, the U.S. National Weather Service defines a cold wave event as a rapid fall in temperature within a 24-hour period and categorizes events based on the rate of the temperature drop as well as the minimum recorded temperature (NOAA 2023). Alternative definitions specify cold wave events as either five-day (or longer) periods during which the daily minimum temperature falls below the 5th percentile of temperature recorded at a location (Xie et al.2012) or a 7-day period during which the daily average temperature falls below the 3rd percentile (Ma et al. 2013).

For this study, four cold wave events in Toronto, Canada were selected from the database of notable North American cold waves as classified in (NOAA 2023). These cold waves occurred in January 2004, February 2007, January 2010, and January 2014. Figure 2.2 shows the air temperature and wind speed data during the months in which the cold wave events occurred as obtained from the Canadian Weather Energy and Environmental Datasets (CWEEDS 2020). Solar radiation data is shown in Appendix A. The results of the thermal analysis of the bridge are subsequently introduced as excitation in the structural model of the bridge in order to determine the effects on mechanical behavior of the structural system, such as the increase in tensile and compressive stresses in critical locations throughout the superstructure.

The selected cold wave events were applied to a box girder bridge in Ontario known as the St. Joseph Bridge (R017) bridge. The bridge is a $11.35\ m$ single span prestressed multicell concrete box girder and was modelled using the preliminary design plans that were available in the Ontario tenders listing (Bids and Tenders 2022). Full bridge drawings can be found under tender drawings in (Bids and Tenders 2022). To reduce the computational demand, only a single cell from the box girder was considered in this study and it is assumed that both webs of the cell are outer webs i.e., both webs are exposed to the outside environment. Figure 2.3 shows the modified section used in the analysis. Note that the reinforcement shown in the first two drawings is the prestressed reinforcement. In addition, the girder is overlaid with a $150\ mm$ concrete distribution slab and a $90\ mm$ asphalt layer.

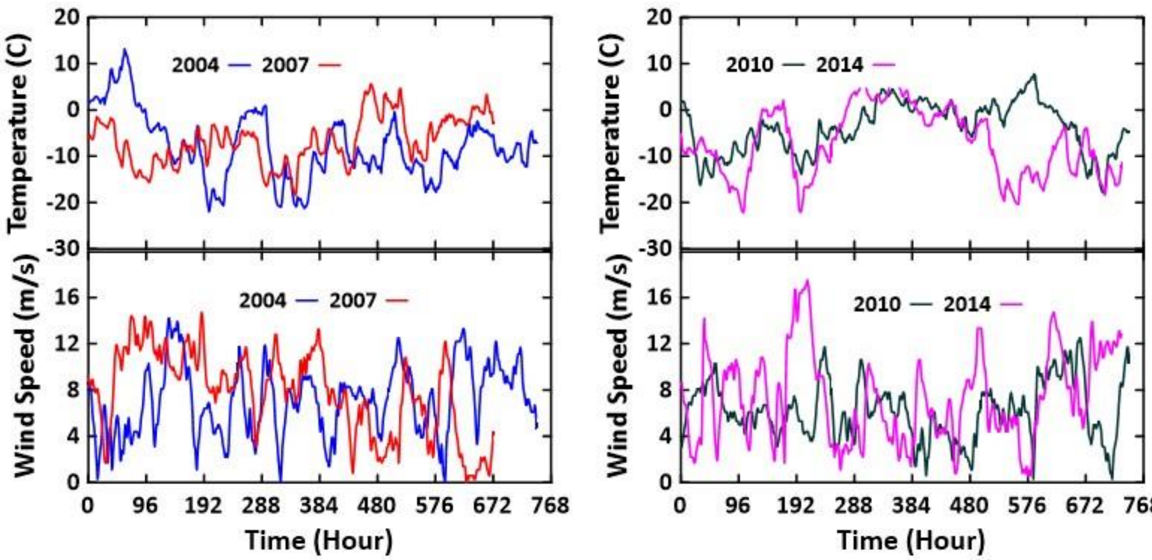

Figure 2.2: The ambient temperature and wind speed recorded during the months in which the cold wave events occurred.

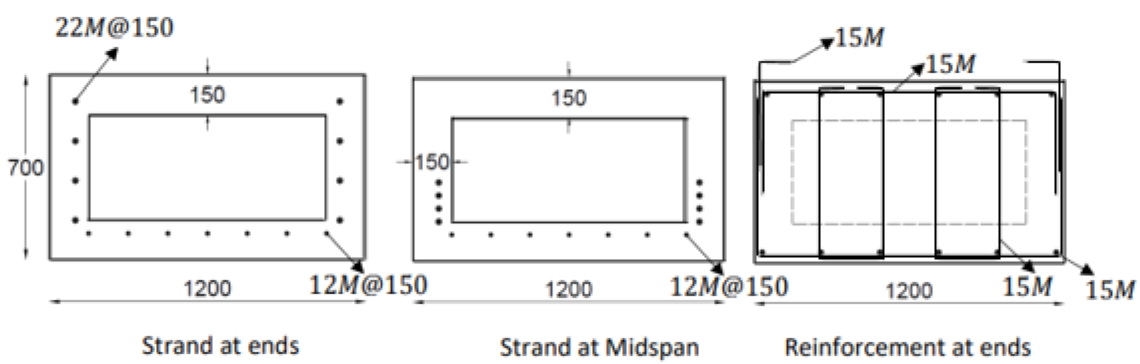

Figure 2.3: Bridge cross section used in the analysis. All dimensions are in mm.

The thermal and structural assessments were carried out by three-dimensional finite element modelling using ANSYS (ANSYS 2019). Transient analysis was performed in both cases. Details on the heat exchange process and the simulations are presented in the sections below.

2.3 Thermal model

The thermal model simulates the interaction between the bridge surface and the surrounding environment to predict the temperature distribution within. The interaction is governed by three physical processes which are the shortwave radiation, longwave radiation, and the convective heat transfer. These processes are influenced by the incident solar radiation, ambient temperature, and wind speed as shown in Figure 2.4. Note that the cloud cover and the reflected radiation can have a significant effect on the amount of incoming solar radiation as shown in the figure.

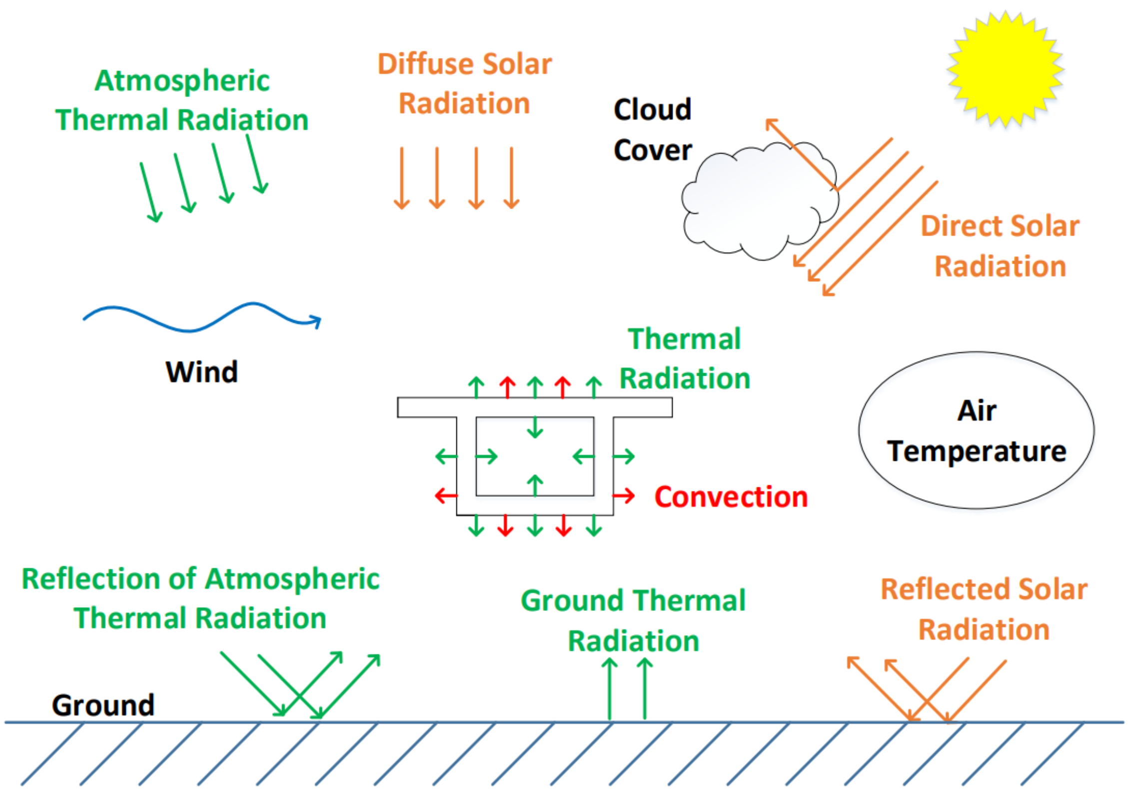

Figure 2.4: Climate interaction boundary conditions for the bridge.

Incident solar radiation comprises three components: Direct (beam) radiation (q_b), diffuse radiation (q_d), and reflected radiation (q_g). Direct radiation strikes the Earth's surface without being scattered in the atmosphere. Diffuse radiation is the solar radiation energy reaching the Earth's surface after being scattered in the atmosphere. Reflected radiation is part of incoming radiation that is reflected from various surfaces. To determine the total incoming solar radiation, the spatial position of the box girder surfaces relative to the sun as well as the shadow length on them need also be considered.

All bridge surfaces will receive longwave radiation from their surroundings and emit a certain amount back. The net flux of longwave radiation (q_r) heat transfer at a bridge surface may be estimated from Eq. (2.1).

$$q_r = E_c - E_{sur} = \sigma \cdot \varepsilon \cdot \left(T_c^4 - {T_{sur}}^4\right) \tag{2.1}$$

where, σ is the Stefan Boltzmann constant, ε is the emissivity of the concrete surface, T_c is the temperature of the concrete, and T_{sur} is the temperature of the surrounding environment. The value of T_{sur} varies depending on the concrete surface in question. For example, the bottom surface of the box girder receives longwave emission from the ground surface which is typically assumed to have the same temperature as the surrounding air. On the other hand, the top surface receives radiation from the sky which may have a lower temperature than the surface air, depending on the prevalent cloud conditions.

The final aspect of the heat exchange is the convective heat transfer between the box girder and the surrounding air. The convective heat flux (q_c) can be modelled using Newton's law of cooling (Incropera et al. 2007):

$$q_c = h_c(T_a - T_c) \tag{2.2}$$

where, h_c is the convective heat transfer coefficient of the concrete surface, T_a is the air temperature, and T_c is the concrete surface temperature. The heat convection coefficient is dependent on the conditions in the vicinity of the surface i.e., the roughness of the surface as well as the wind speed. Several empirical models have been proposed to estimate the convection coefficient for concrete surfaces (Civil Engineering Board 1985). The one used in this investigation is:

$$h_c = 5.6 + 4w \; for \; w \leq 5 \tag{2.3}$$

$$h_c = 7.15w^{0.78} \; for \; w > 5 \tag{2.4}$$

where, w is the wind speed in m/s (Civil Engineering Board 1985).

The variation of the temperature field in a concrete structure is described by three-dimensional heat flow equation using Fourier’s law (Incropera et al. 2007):

$$\rho c \frac{\partial T}{\partial t} = k \left(\frac{\partial^2 T}{\partial x^2} + \frac{\partial^2 T}{\partial y^2} + \frac{\partial^2 T}{\partial z^2} \right) \tag{2.5}$$

Parameter ρ is the density, c is the specific heat capacity, $\frac{\partial T}{\partial t}$ is the change in temperature over time, k is the thermal conductivity, and $\frac{\partial^2 T}{\partial x^2}, \frac{\partial^2 T}{\partial y^2}, \frac{\partial^2 T}{\partial z^2}$ are the second spatial derivatives of the temperature in the x, y, and z directions respectively.

2.4 Verification and validation of the thermal model

The thermal model was verified against a heat transfer verification test taken from (Wolfram Research 2013). In this test, a 1-by-2-cm ceramic strip is embedded in a high-thermal-conductivity material so that the sides are maintained at a constant temperature of $1173\ K$. The bottom surface of the ceramic is insulated, and the top surface is exposed to a convection and radiation environment at $T_{ambient} = 323\ K$. The temperature distribution in the strip is to be determined and the results from the finite element model were found to match those from (Wolfram Research 2013) as shown in Appendix B.

To validate the model, a thermal analysis was run for the auxiliary shipping channel bridge of the Sutong Bridge in Jiangsu, China. The analysis results were validated against the field measurements obtained in situ as part of an experimental study that had been conducted on the same superstructure (Gu et al. 2014). The bridge is a prestressed concrete box girder comprising three continuous spans with a total length of $548\ m$. The deck has a variable depth which ranges from $4.5\ m$ at midspan to $15\ m$ at the piers and a total width of $16.4\ m$. Moreover, the concrete is overlain with a $110\ mm$ thick layer of asphalt (Gu et al. 2014). Material properties used in the model are taken directly from the reference study (Gu et al. 2014).

The bridge was subjected to a cold wave event that occurred between December 3 and 6, 2008. The climate data for temperature and wind speed was digitized from the figures in (Gu et al. 2014). The relevant solar radiation data used is neither available in the publication nor in any accessible nearby weather station. Therefore, solar radiation data was obtained from the SOLCAST Database (Solcast 2019). The initial temperature distribution within the box girder was assumed to be uniform at 12℃. The measurements along the bridge cross section at the pier-deck connection were used for model validation.

Figure 2.5 shows a comparison between the results from the thermal model and the measured values reported in (Gu et al. 2014). The points of reference where thermal measurements were made in situ are marked on the cross section with a red dot. As seen in Figure 2.5, the estimated temperature at the overhang and the bottom flange match closely the actual temperature measured at the location. Furthermore, the estimated and actual temperature trends at the top and the middle web are very similar with a slight difference in magnitude near the end of the simulation. A close agreement between the simulated and measured values is observed; wherever they exist, slight differences are mainly attributed to the difficulty in replicating the climate data used in the reference study to a high degree of accuracy as well as to uncertainties regarding the initial conditions of the system. Therefore, it can be concluded that the developed model performs well in replicating the interaction between the climate and the bridge deck.

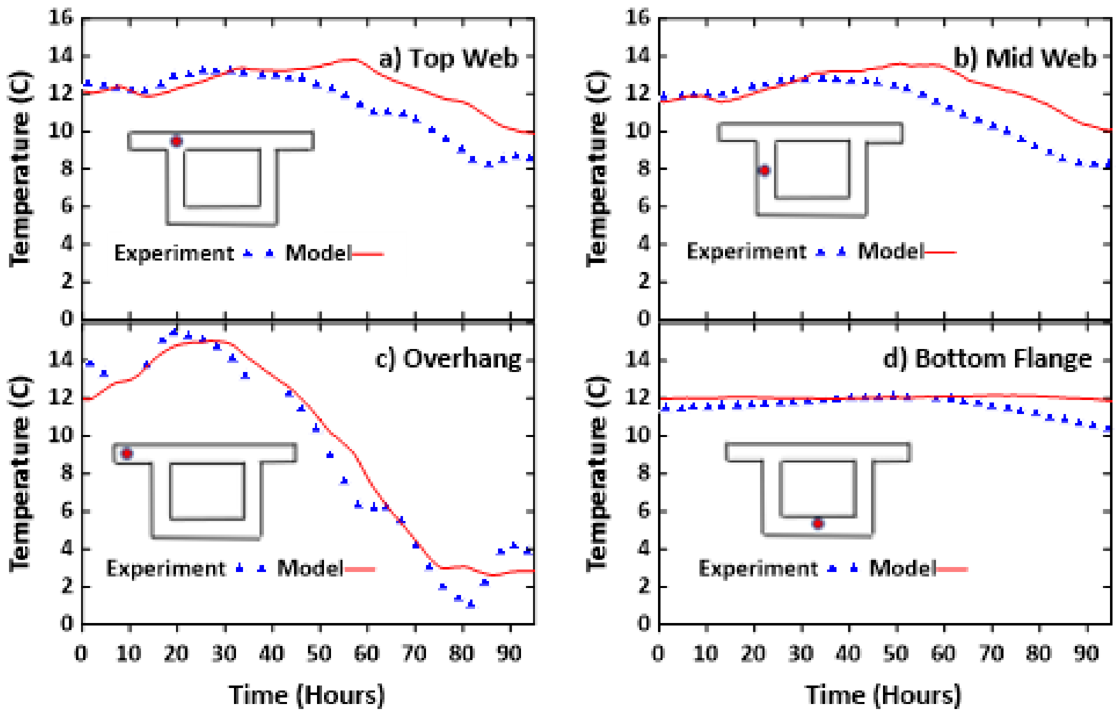

Figure 2.5: Thermal model validation results.

2.5 Application of the thermal model to the St. Joseph Bridge (R017) in Ontario

With the model validated, the four cold wave events were applied to the selected cross section shown in Figure 2.3 for the St. Joseph bridge being considered to study the structural effects resulting from the simulated thermal loads. The concrete distribution-slab and the asphalt layer were also included in the model. The material properties for the concrete and asphalt used are shown in Table 2.1.

Table 2.1: Material properties used in the model (Gu et al. 2014).

Material	Density (kg/m^3)	Heat Capacity ($\frac{J}{kg°C}$)	Conductivity ($\frac{W}{m°C}$)	Emissivity	Absorptivity
Concrete	2500	1010	1.17	0.9	0.65
Asphalt	2100	886	0.98	0.9	0.9

The climate data, in addition to the temperature time history shown in Figure 2.2, were obtained from the Canada Weather Energy and Engineering Datasets (CWEEDS 2020). The initial temperature of the bridge is assumed to be uniform and equal to the initial ambient temperature. The ends of the cross section are assumed to be perfectly insulated and the temperature of the air inside the core of the cross section was taken as 1.5°C higher than the ambient temperature in accordance with (Elbadry and Ghali 1983).

Figure 2.6 depicts the temperature profiles obtained along the sun-facing and the shaded sides of the cross section (girder and concrete slab) for the four different thermal events. The gradients shown were chosen as they represent the largest difference between the bottom exterior surface and the interior of the cross section. The figure also shows the reference negative gradients recommended by the AASHTO and CHBDC. The thermal gradients from the simulation and the one recommended by AASHTO differ in both shape and magnitude near the bottom of the cross section. On the other hand, the CHBDC recommended gradients provide a better approximation of the shape of the gradient but fails to account for the temperature magnitudes. These differences could potentially have significant implications on structural performance due to the development of tensile stresses. Conversely, the simulated and recommended gradients are similar near the top of the cross sections. Therefore, it can be expected that the stresses estimated from simulated and recommended gradients at the top will be similar. The reason that gradients at the bottom are larger in comparison to the top is the absence of the insulating effect of asphalt. The results also show that the interior of the cross section is not very sensitive to short-term changes in atmospheric conditions. In contrast, the temperature distribution near the top and bottom ends of the cross section is more sensitive to changes in atmospheric conditions.

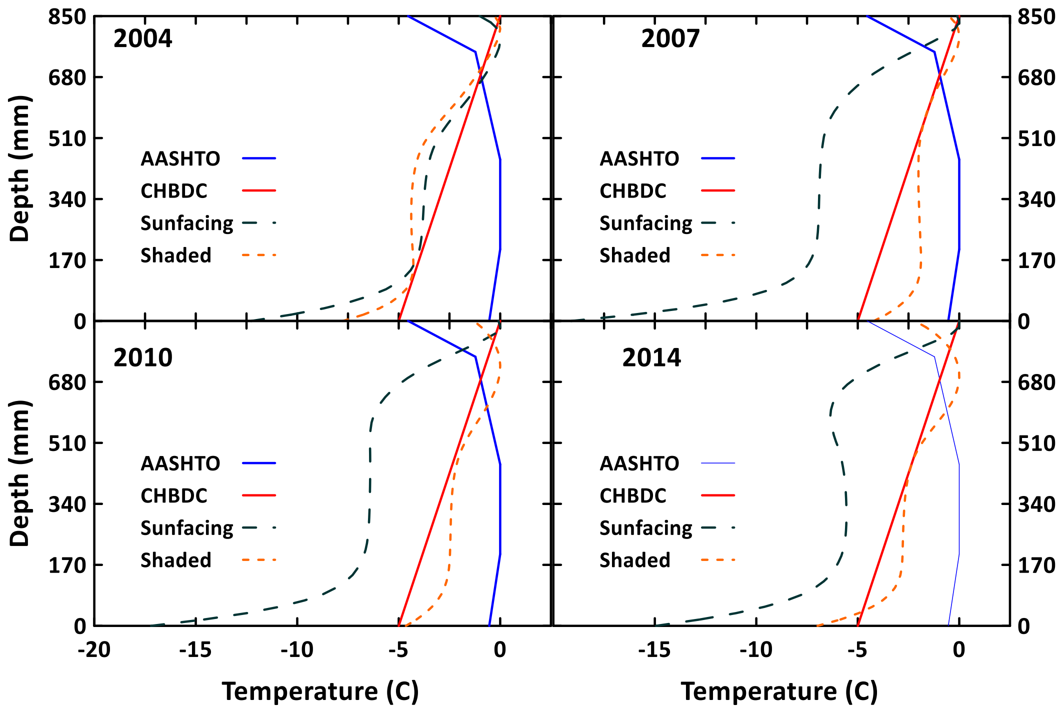

Figure 2.6: Comparison of thermal model results with AASHTO & CHBDC recommended gradients.

2.6 Structural modelling

The structural model was also developed on ANSYS using the Menetrey-Willam (Menetrey 1994) damage plasticity material model for concrete. The tensile strength of the concrete was taken as $3\ MPa$ while the uniaxial and biaxial compressive strengths were taken as 30 and 36 MPa respectively. The elastic modulus was assumed equal to 20 GPa. The prestressed steel tendons were modelled using beam elements with the prestressing force applied as an initial stress. Moreover, the non-prestressed reinforcement bars in the top 150 mm concrete slab were also modelled as beam elements using a linear elastic-perfectly plastic material. The thermal expansion coefficient of concrete was taken as $1.4 \times 10^{-5}/°\text{C}$. All material properties were used at a temperature of 20°C with the effect of temperature on these properties to be incorporated in future research. The temperature distribution within the bridge deck, obtained from the thermal model, was applied as a thermal load. In addition to the applied prestressing and thermal load, the self-weight of the bridge was considered in the model. Furthermore, the bridge deck was modelled as a simply supported member. Figure 2.7 below shows the F.E. discretization used.

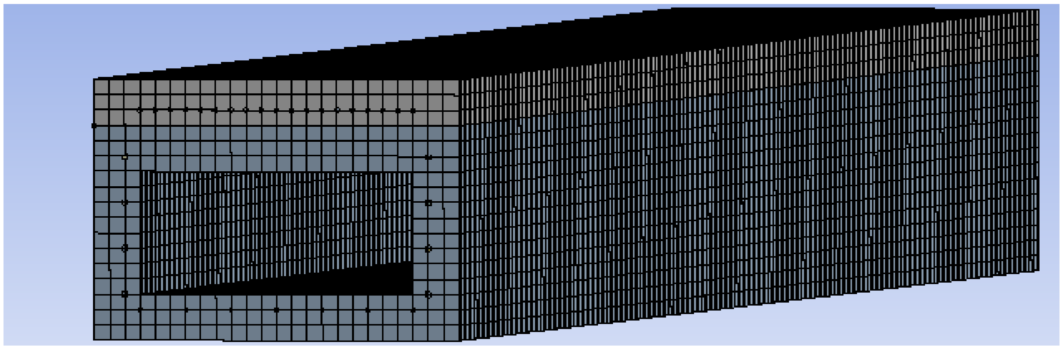

Figure 2.7: Finite element model of the bridge deck.

2.7 Structural simulation results

Figure 2.8 shows the structural results at the top and bottom of the cross section (along the center) from applying the thermal results of the four cold waves. The maximum and minimum stresses shown in the figure refer to the highest and lowest stresses calculated at the top and bottom fiber of the cross section along the length of the span during the respective cold wave event. Plots labelled as AASHTO gradient refer to the stress obtained by applying the AASHTO gradients instead of the temperature distributions from the thermal model. The same color code is used for comparable values: red for minimum, blue for maximum, solid lines for values computed with the proposed methodology, dashed lines for values obtained from the AASHTO gradients. Reported values are tension-positive. Results for the 2004 cold wave indicate that the top of the cross section experienced a maximum compressive stress of about 3 MPa and a maximum tensile stress of about 1.2 MPa. These stresses are within the limits set by the AASHTO prescribed gradients. At the same time, the bottom side of the cross section experienced a maximum stress of about 5 MPa (C for compressive stress) due to the cold wave which is smaller than the 5.5 MPa (C) maximum stress resulting from the AASHTO gradients. This implies that the bridge code fails to account for 0.5 MPa increase in tensile stress near the bottom. The increase is significant considering that the tensile strength of the material is 3 MPa and that live loads will result in additional tensile stresses.

The maximum and minimum stresses resulting from the 2010 cold wave at the top were within code limits. However, the maximum stress at the bottom (3 MPa (C)) was lower than the maximum stress predicted by the AASHTO recommended gradient (6 MPa (C)). This decrease in compressive stress represents a 3 MPa increase in tensile stresses which may lead to exceedance of the serviceability limit state of the bridge if neglected in the design. A similar conclusion was drawn from the structural results of the 2007 and 2014 cold waves where the compressive stresses at the bottom are smaller than AASHTO limits by about $3.5\ MPa$, implying a $3.5\ MPa$ difference in tensile stresses. Moreover, during the 2007 cold wave, the minimum stresses at the top were higher than AASHTO stresses by about $0.5\ MPa$ indicating that the cross section experienced an insignificant increase in compressive stress due to the cold wave. Meanwhile, the top stresses that resulted from the 2014 event are within the AASHTO limits.

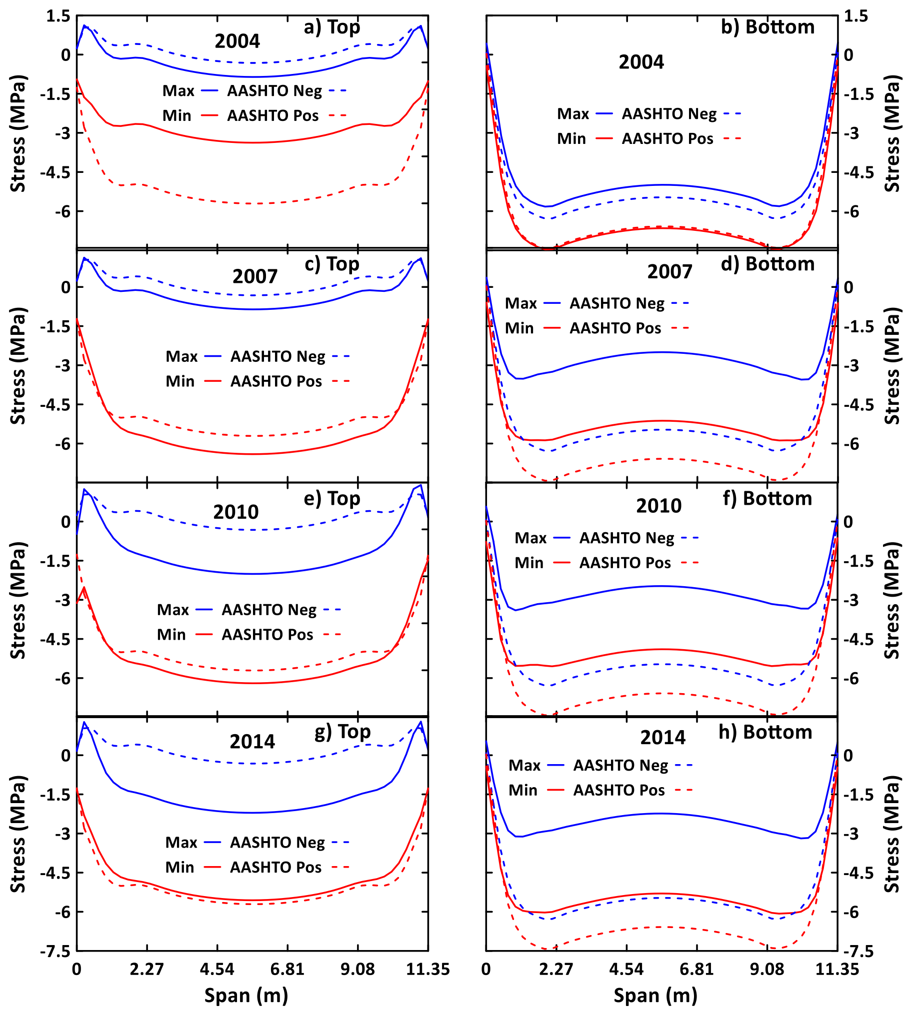

Figure 2.8: Maximum and minimum stresses obtained at the top and bottom of the cross section for the 2004, 2007, 2010 and 2014 cold wave events.

2.8 Corroboration of results for an I-Girder (16 Mile Creek Crossing, Vaughan, Ontario)

As seen above, the structural and thermal results for the box girder subjected to cold wave events show significant variation from the results obtained from the AASHTO prescribed gradients. To check that these trends are a result of limitations in the AASHTO recommended gradient and are not limited to a particular cross section type, a second study was performed on an I-Girder. The girder under consideration is a CPCI 2300 girder and it is an internal girder in the 16 Mile Creek Crossing located in Vaughan, Ontario. Full bridge drawings may be found under tender drawings in (Bids and Tenders 2022). The span of the girder is 43 m; however, the length of the girder in the model was assumed to be 10 m to reduce computational demand. The girder is topped with a 225 mm concrete slab and a 90 mm asphalt topping. The material properties and thermal and structural boundary conditions were identical to those used in case study for the box girder. Figure 2.9a shows the cross-sectional dimensions of the I-Girder.

The plots in Figure 2.9b summarize the thermal results of the I-Girder study. The figure shows that both the AASHTO and CHBDC prescribed gradients fail to capture both the shape and magnitude of the maximum negative gradient that occurs between the top exterior surface and the interior of the cross section along the vertical axis of symmetry.

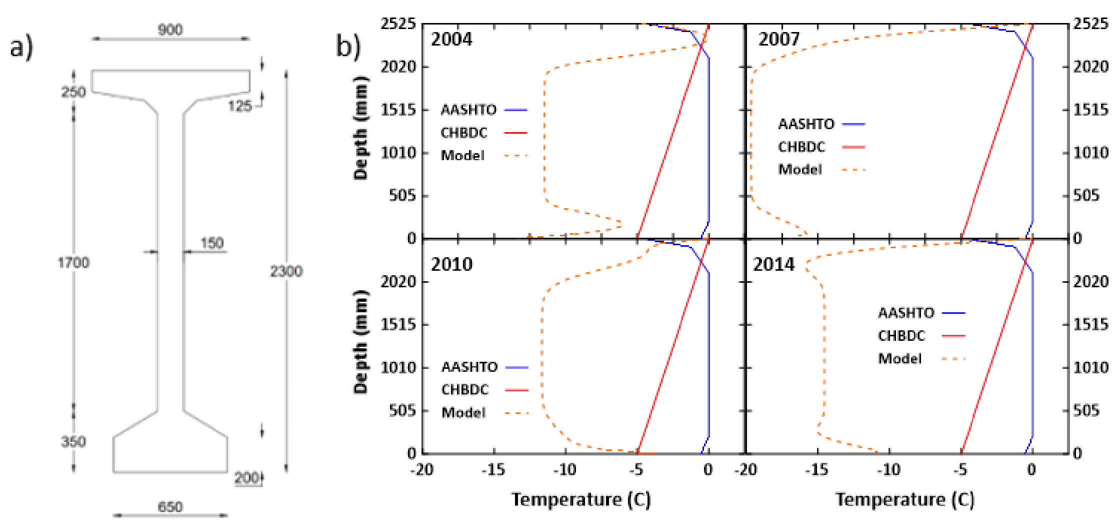

Figure 2.9: a) I-Girder Section (dimensions in mm), b) Comparison of thermal model results with AASHTO & CHBDC gradients.

Figure 2.10 shows the structural results of the I-Girder study. The results show that the maximum stress at the bottom of the cross section during the 2004 cold wave event exceeded AASHTO limits by about 1 MPa. This represents a 1 MPa increase in the tensile stress acting on the girder. Moreover, the minimum stress predicted at the bottom of the girder during the cold wave events of 2007, 2010, and 2014 was smaller than the minimum stress obtained from the AASHTO prescribed gradient by an average of about 2 MPa. This means that the compressive stress experienced during the cold wave events is about 2 MPa larger than that experienced from the AASHTO prescribed gradient. On the other hand, the results at the top of the cross section during all four cold wave events were within AASHTO limits.

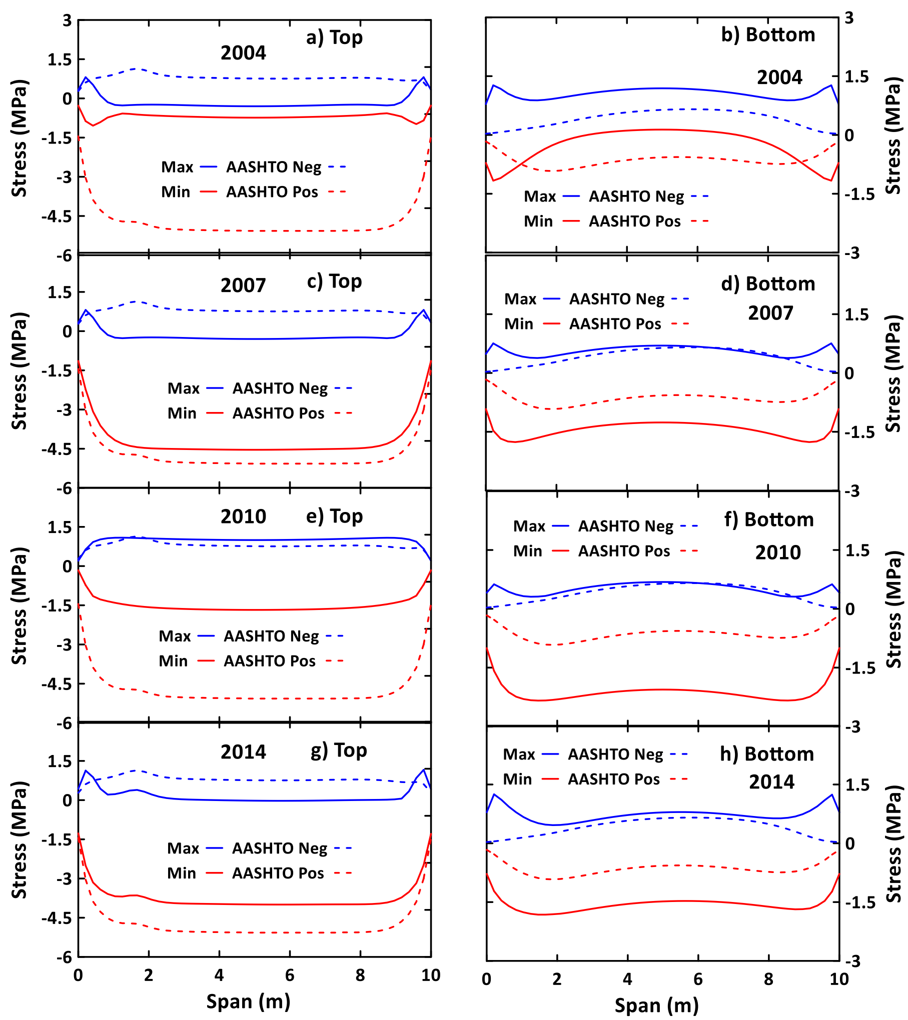

Figure 2.10: Maximum and minimum stresses obtained at the top and bottom of the I-Girder cross section for the 2004, 2007, 2010 and 2014 cold wave events.

2.9 Conclusions

Using three-dimensional finite element thermal and structural models, this study investigated the effect of cold wave events on the development of thermal gradients and the corresponding stresses in prestressed concrete box girders. The thermal model was used to obtain thermal gradients within the box girder cross section due to historical cold wave events. The obtained temperature distributions were then applied as boundary conditions in the structural models to determine the structural response. An additional study on an I-Girder was also performed to corroborate the trends. The conclusions that can be drawn from the investigation are listed below.

- The thermal distributions obtained from the thermal modelling of the cold wave events in the box girder, indicate that the AASHTO recommended gradient does not accurately account for the magnitude and shape of the negative gradients particularly near the bottom of the cross section.
- The structural results for the box girder from all cold waves indicate an increase in tensile stresses near the bottom of the cross sections in comparison to the stresses obtained from code prescribed gradients.
- During the 2014 cold wave, the tensile stress on the box girder was outside the limits prescribed by AASHTO gradients by an excess of 3 MPa. This underestimation is an example of the potential risk to existing and future structures resulting from oversight of the severe thermal stresses that occur during extreme events.
- For some of the cold wave events, the compressive stresses at the top of the box girder cross section could potentially exceed the stresses from AASHTO recommended gradients.
- Similar to the case of the box girder, the thermal results obtained for the I-Girder case show significant differences in shape and magnitude from the AASHTO recommended gradient. The structural results indicate that the gradients proposed by the AASHTO code underestimate the tensile stress in certain cases. Moreover, the AASHTO gradient also underestimates the compressive stress by about $2\ MPa$ at the bottom of the cross section. The findings of this study further reinforce the conclusions made from the box girder case study.
- Another issue to note is that these events occurred almost once every 3 years, which means that the results obtained in this study may underestimate the code deficiencies as it is likely that rarer extreme

events will have more severe consequences on the structural performance. The hysteretic nature of the resulting stress state is another dimension of the problem that may compound the damage implications of tensile stresses exceeding the cracking limits.

- Furthermore, it is expected that the severity and frequency of the extreme events will increase in the future. In anticipation of escalation of climate change, current recommendations in the codes need to further be evaluated and adjusted to respond to the increased temporal stress demands on the structural systems.

2.10 Appendices

2.10.1 Appendix A

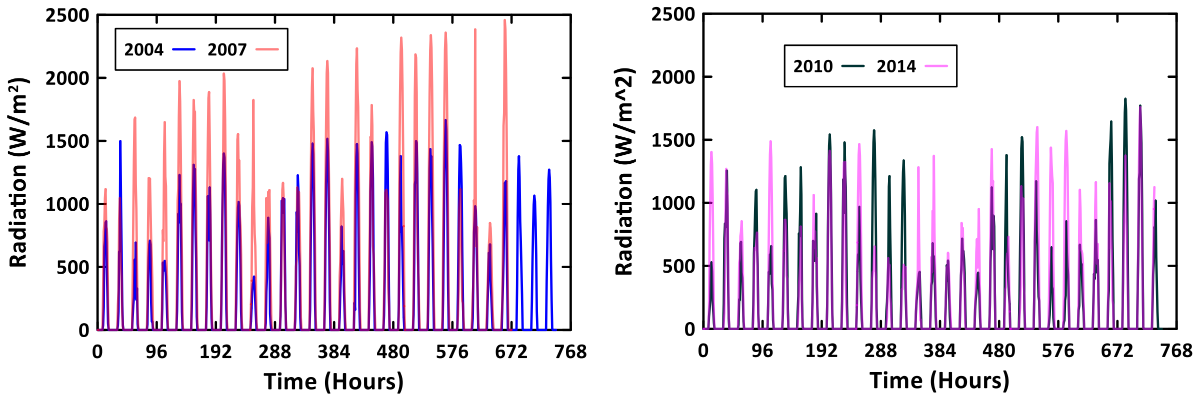

Figure 2.11: Solar radiation data recorded during the months in which the cold wave events occurred.

2.10.2 Appendix B

The results from the Wolfram Mathematica documentation are shown in Figure 2.12 while the results from the finite element model are shown in Figure 2.13.

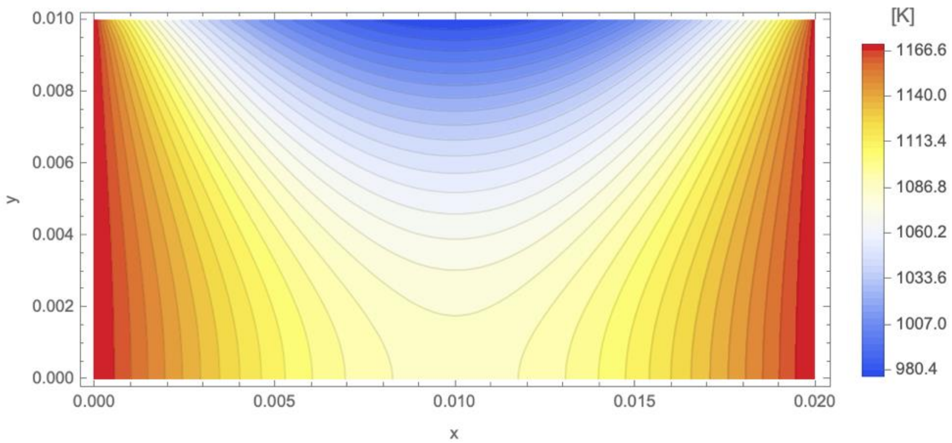

Figure 2.12: Results of the heat transfer test for the ceramic strip as obtained from (Wolfram Research 2013).

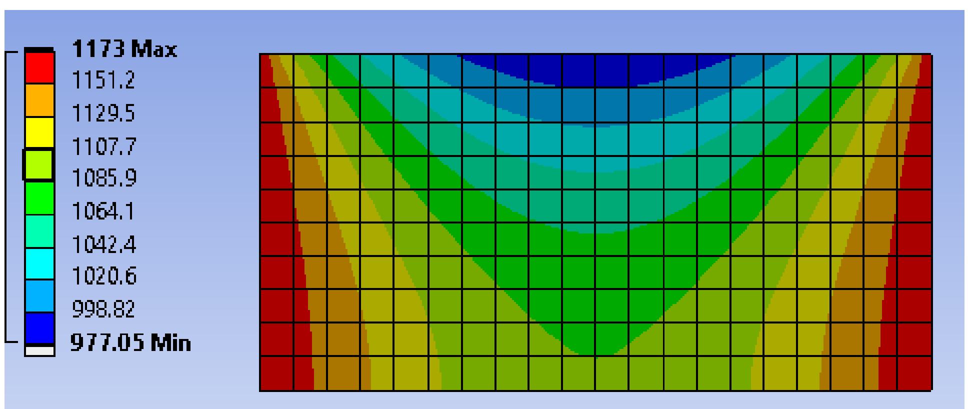

Figure 2.13: Results of the heat transfer test for the ceramic strip as obtained from the ANSYS finite element thermal model.

Chapter **III**

Numerical Study on the Effect of Climate Parameters on the Extreme Thermal Gradients in Concrete Box Girders

Note: The content of the chapter is presented as published in the Journal of Bridge Engineering. The format (headings, caption numbering, and citations) has been edited to match the thesis format.

3.1 Introduction

In addition to the permanent and live loads, a bridge is subjected to environmental loads throughout its service life. Typical environmental loads include thermal, wind, and snow loads. Moreover, bridges may be subjected to extreme accidental loads or environmental events such as earthquakes and flooding. Unlike permanent and live loads, which can be estimated with confidence based on bridge design and function, environmental loads are a function of external factors that relate to the climatic conditions at the various geographical locations. Due to climate's inherent variability as well as the limitations associated with its forecasting, the uncertainty associated with environmental loads is significantly higher than that associated with other types of loads. Bridge codes provide general guidelines that encompass large geographical areas. For this reason, and based on observations from field performance, it is generally known that several bridges subject to extreme climate might be under-designed when it comes to environmental loads.

A thermal gradient refers to the ratio of the temperature difference to the distance between two points within a bridge cross section. Thermal gradients arise over short-term periods due to rapid changes in air temperature and uneven amounts of radiation received by the surfaces of the bridge. Note, that in bridge codes, the gradient effect is provided in terms of a temperature differential between various points along a cross section rather than a gradient value (Canadian Standards Association 2014). For example, the Canadian Highway Bridge

Design Code (CHBDC) (Canadian Standards Association 2014) defines a linear thermal differential in the bridge, with a magnitude that depends only on the depth of the cross section (Figure 3.1). In the results of this study, the thermal load will be expressed in terms of the temperature differential.

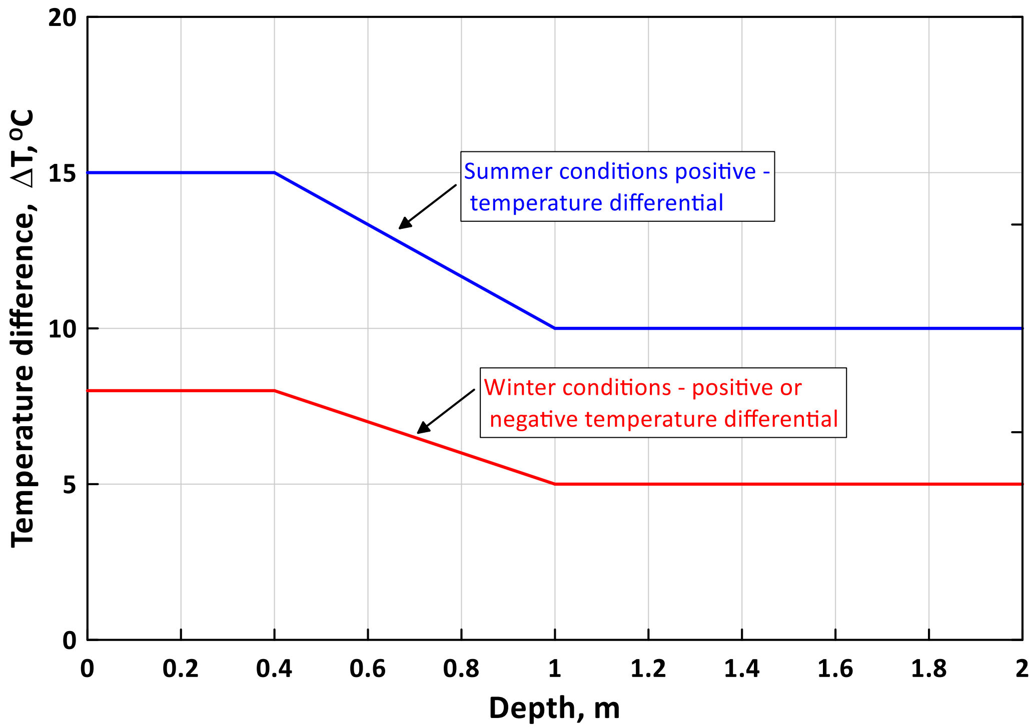

Figure 3.1: CHBDC prescribed differential between the top and bottom of the bridge cross section. Modified from (Canadian Standards Association 2014).

The temperature gradient as defined (i.e., temperature difference between top and bottom fiber divided by the distance of the points of reference) is directly proportional to curvature caused by the thermal loads. If deformation is restrained, then this curvature multiplied by the effective stiffness of the bridge cross section results in a flexural moment generated by the geometric restraint to curvature. If, on the other hand, the bridge deck is unrestrained, thermally induced rotations from the chord of the member may be estimated from the product of the estimated thermal curvature times half the bridge span. This means that the level of comfort of the drivers over the bridge may be affected by the consecutive rise at the ends of successive spans, whereas the residual drift capacity, beyond which permanent damage to bearings and other bridge components occurs, may be affected drastically.

Thermal gradients are an environmental load that is not typically linked to a single climate parameter, and thus, the relationship between the climate parameters and thermal gradients is obscure. This exacerbates uncertainty in the design values of thermal gradients, since these values are not adjusted based on the local climate at the bridge location, or the bridge geometry (dimensions and shape) which has also been found to affect the gradient's intensity. Instead, the design codes resort to more general guidance (e.g., Figure 3.1).

For illustration of the above-mentioned concerns, Canada is considered as a case study owing to its wide variation in latitude and longitude that ranges from $42\ °N$ to $83°N$ and from $53\ °W$ to $141°W$ respectively. Thus, the country encompasses a wide variety of climate types. The northern two-thirds of the country experiences very cold winters and short, cool summers. On the other hand, the Central Southern area of the interior plains (the prairies) has a typical continental climate with very cold winters, hot summers, and relatively sparse precipitation. Furthermore, Southern Ontario and Quebec have a climate with hot, humid summers and cold, snowy winters while the western coast is the only area where the winter season has an average temperature above $0℃$ (Hall et al, 2022). Thus, a bridge located in the city of Vancouver, on the west coast, will be subjected to a different gradient than an identical bridge located in the province of Quebec. Yet, the two bridges are designed based on the same guidelines as far as thermal loads are considered, which implies that one of them is potentially either over-designed or under-designed. A similar issue can be observed with the guidance provided in the AAHSTO bridge code. The code divides the continental US into three separate zones, with the magnitude of thermal differentials varying across the zones. However, due to the sheer size of the US, the issue of having one differential to cover significant areas of land with varying local climates persists. For instance, a bridge in Florida (Southeast) and a bridge in New York (Northeast) are designed to the same thermal load.

Several studies have questioned the accuracy of the existing guidance in bridge codes when it comes to predicting the magnitude of temperature differentials. For example, it was determined that temperature differentials that develop in concrete I-Girders during heat waves differ significantly from the AASHTO provisions, with the difference reaching values of up to $10℃$ between the observed and code recommended differentials (Hagedorn et al. 2019). Furthermore, numerical and experimental studies on prestressed I-Girders indicated that the horizontal and vertical differentials in AASHTO standards need modification (Lee 2012). Additionally, it has been shown that cold wave events can induce unfavorable effects in box girder systems, an aspect that is not considered in the current AASHTO recommendations (Gu et al. 2014). These findings agree with field measurements on two multi-cell box girders located in Utah and California which indicated that AASHTO guidelines severely underestimate the negative temperature differentials that occur between the top surface and the interior and the interior and the bottom surface (Barr and Halling 2014).

The highlighted studies identify some inadequacies in bridge codes when it comes to quantifying the thermal effects on bridge decks both during construction and in service. Moreover, there is no evidence in the peer reviewed literature that any studies to date have attempted or identified a correlation between climate parameters and the resulting thermal differentials on the bridge. Rather, most of the research in this area had focused on linking climate to the uniform (i.e., average) temperature component (which represents long term changes in the bridge temperature) of the thermal load (Black et al. 1976; Roeder 2002).

The objective of the present work is to investigate the link between various climate parameters and thermal differentials in bridges. This relationship will help establish more efficient and accurate guidelines for design thermal loads, based on the local climate at the bridge location. This objective is achieved using a calibrated numerical three-dimensional finite element model with a climate boundary interaction that establishes a rigorous energy balance at all the bridge surfaces. With no loss of generality, and for illustration of the methodology, a concrete box girder was modelled with the application of climate conditions from a vast array of Canadian locations. The temperature differentials predicted by the model are then analyzed to identify the relation between the differentials and the most dominant climate parameters. The resulting relationship is then used to investigate the extent of discrepancy between recommended, globally determined, design Code estimates and local thermal gradient values for an improved, climate-sensitive bridge design.

3.2 Atmosphere bridge boundary

The various paths of thermal energy exchange that influence the interaction at the boundary between the various bridge surfaces and the climate and drive the thermal gradient formation and magnitude are illustrated in Figure 3.2. Three main processes can be identified as follows: 1) Heat transfer through convection between the bridge surfaces and the surrounding air, 2) shortwave (solar) radiation exchange between the bridge and its ambient environment, and 3) longwave radiation exchange between bridge surfaces and any other surface in the bridge vicinity. Furthermore, in the case of a box girder, there are also internal surfaces that are not exposed to the outside environment, except at small openings used for aeration. The heat exchange at an internal surface is governed by convection with the internal air and by longwave radiation exchanged with other internal surfaces. The effect of the aeration openings on the heat exchange is neglected in calculating the differentials. The interaction of the ambient environment with the exterior and interior surfaces of the bridge is described in more detail in the following sections along with the techniques used to model these processes and their implementation in an advanced finite element platform (ANSYS 2019).

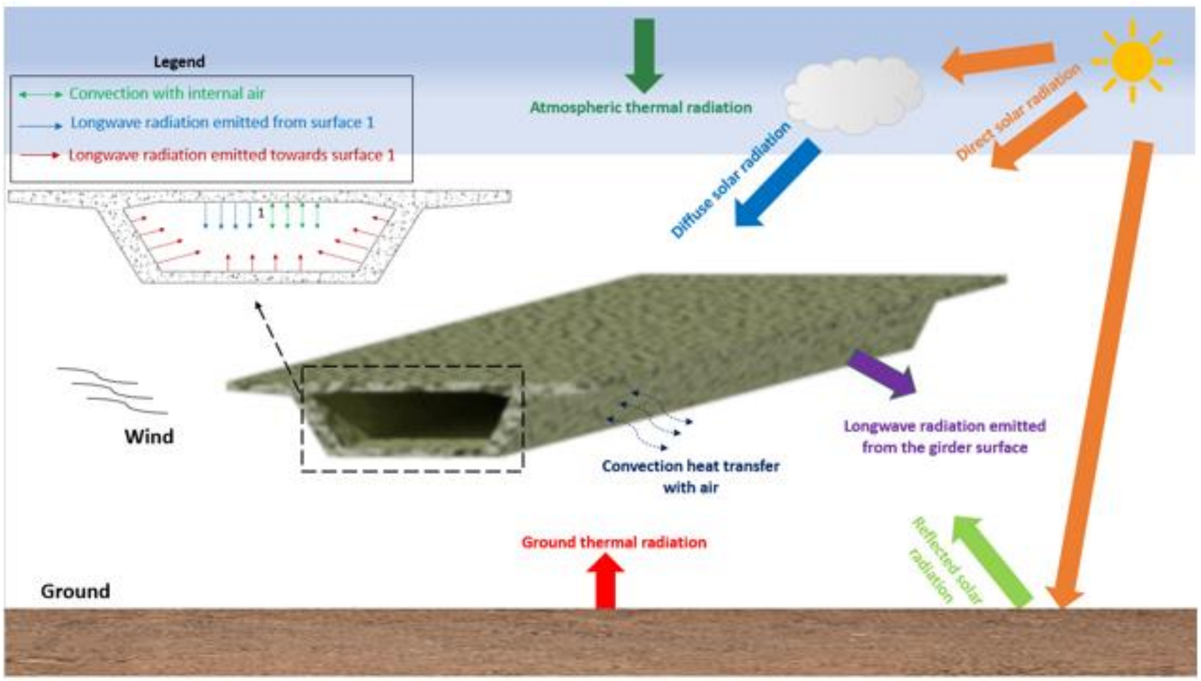

Figure 3.2: Boundary conditions that define climate interaction for a box girder.

3.2.1 Convection

Convection refers to the process of heat transfer between a surface (in the context of this chapter, the bridge surface) and an adjacent moving fluid (here, the air). It also refers to the thermal interaction that occurs between two moving fluids. Convection may be classified as free (natural) convection or as forced convection depending on how fluid movement is initiated (Incropera et al. 2007). The nature of the convection has no effect on the convective heat transfer itself.

The typical approach used to estimate the heat transfer between a surface and a moving fluid is based on Newton's Law of cooling (Incropera et al. 2007). The law postulates that surface flux in convection (q_c) is proportional to the difference in temperature between the surface and the flowing fluid as expressed by Eq. (3.1):

$$q_c \propto (T_s - T_{inf}) \tag{3.1}$$

where, T_s is the surface temperature and T_{inf} is the fluid temperature far away from the surface. A proportionality constant (h_c) is then introduced to express this relation as an equality, as shown in Eq. (3.2). This constant, h_c, is known as the convective heat transfer coefficient and it depends on several factors such as the geometry, the roughness of the solid surface, the fluid properties, and the fluid flow (laminar or turbulent).

$$q_c = h_c \cdot (T_s - T_{inf}) \tag{3.2}$$

Several empirical models have been proposed to estimate the value of $h_c$for concrete surfaces. The model used in the present study was proposed in (Nevander and Elmarsson 2006), in which the convection coefficient is expressed only as a function of the wind speed (w) as defined by Eq. (3.3) and Eq. (3.4).

$$h_c = 5.6 + 4w \; for \; w \leq 5 \; m/s \tag{3.3}$$

$$h_c = 7.15w^{0.78} \; for \; w > 5 \; m/s \tag{3.4}$$

In the model, convection is represented as a surface load applied to a surface. The convection coefficient (h_c) and the fluid temperature at the surface (T_{inf}, in this case T_{inf} is the air temperature) are used as input to calculate the convection heat transfer across that surface. Therefore, the climate parameters required to simulate convection are, the windspeed and the air temperature.

3.2.2 Shortwave radiation

The sun emits radiant energy with wavelengths spanning from infrared to ultraviolet. This energy is known as shortwave radiation. Shortwave radiation is mainly associated with daylight hours. The incoming shortwave radiation flux at the top of the atmosphere does not vary significantly throughout the year and between different years.

However, not all incoming solar radiation reaches the earth's surface. A portion of the incoming radiation is absorbed by the atmosphere, and some is absorbed by clouds. The shortwave radiation that is not reflected or absorbed is available to drive various processes including the bridge thermal exposure, considered in the present work. Incoming shortwave on a surface of a bridge can be decomposed into three main components, i.e.: (i) Direct (beam) radiation I_B, (ii) diffuse radiation I_D, and (iii) reflected radiation I_R. *Direct or beam* radiation (I_B) strikes a surface without being scattered in the atmosphere. *Diffuse* radiation (I_D) is the portion of solar radiation energy that reaches a surface after being scattered in the atmosphere. *Reflected* radiation (I_R) strikes a surface after having been reflected from another surface (i.e., the ground). The total solar radiation arriving on a bridge surface (I_G) is termed the global solar radiation and is equal to the sum of all three components as per Eq. (3.5) (Larsson 2012). The three different components are illustrated schematically in Figure 3.2.

$$I_G = I_B + I_D + I_R \tag{3.5}$$

The direct or beam radiation on the bridge surface (I_B) can be expressed as a function of the direct normal irradiance from the sun ($I_{B,n}$, referred to as DNI) and the angle of incidence θ (the angle between an incident ray and the normal to the bridge surface) as shown in Eq. (3.6). Note that the direct normal irradiation (DNI) can be defined as the amount of solar radiation received by a surface (e.g., a bridge surface) that is perpendicular to the rays that are emitted from the sun.

$$I_B = I_{B,n} \cos\theta \tag{3.6}$$

The distribution of diffuse radiation is anisotropic, more uneven on clear days than on cloudy days. According to (Duffie and Beckman 2006), the diffuse solar radiation can be roughly divided into three parts: circumsolar diffuse radiation (solar irradiance from the circumsolar region (center of the sun)), isotropic diffuse radiation, and horizon brightening (solar irradiance from the sky horizon).

Sky models that describe the diffuse radiation mathematically may be used to estimate the radiation on tilted or vertical surfaces. Typically, models assume that the circumsolar and horizon diffuse components are small, and practically, all diffuse radiation I_D may then be considered isotropic (Larsson 2012). In such a model, the diffuse component on a tilted surface is:

$$I_D = I_{D,h}\left(\frac{1+\cos\beta}{2}\right) \tag{3.7}$$

where, $I_{D,h}$ is the diffuse radiation on a horizontal surface (referred to as horizontal diffuse irradiance in solar datasets) and β is the slope angle which forms between the horizontal and the plane of the surface.

Finally, reflected radiation (I_R) only impacts tilted surfaces and can be calculated as per Eq. (3.8). I_H is the global horizontal irradiance (the total amount of solar radiation received by a horizontal surface) and ρ_R is the reflection factor of the ground surface (typically taken as 0.2) (Thevenard and Haddad 2005).

$$I_R = I_H \rho_R \left(\frac{1-\cos\beta}{2}\right) \tag{3.8}$$

Based on the above and given the geographic location and geometry of the bridge, the only climate parameter needed to model the direct beam radiation is the direct normal irradiance ($I_{B,n}$). To model the incoming diffuse radiation on a bridge surface, the value of the diffuse horizontal irradiance ($I_{D,h}$) is required. Furthermore, the global horizontal irradiance (GHI) data is needed (I_H), to calculate the reflected radiation on a surface. Once all three components are determined, the total incoming shortwave radiation on a bridge surface can be modelled as a heat flux on the surface in a Multiphysics simulation. Figure 3.3 illustrates the angles β and θ as well as additional angles ($\theta_z, \gamma, and\ \gamma_S$) which are used to determine the value of θ.

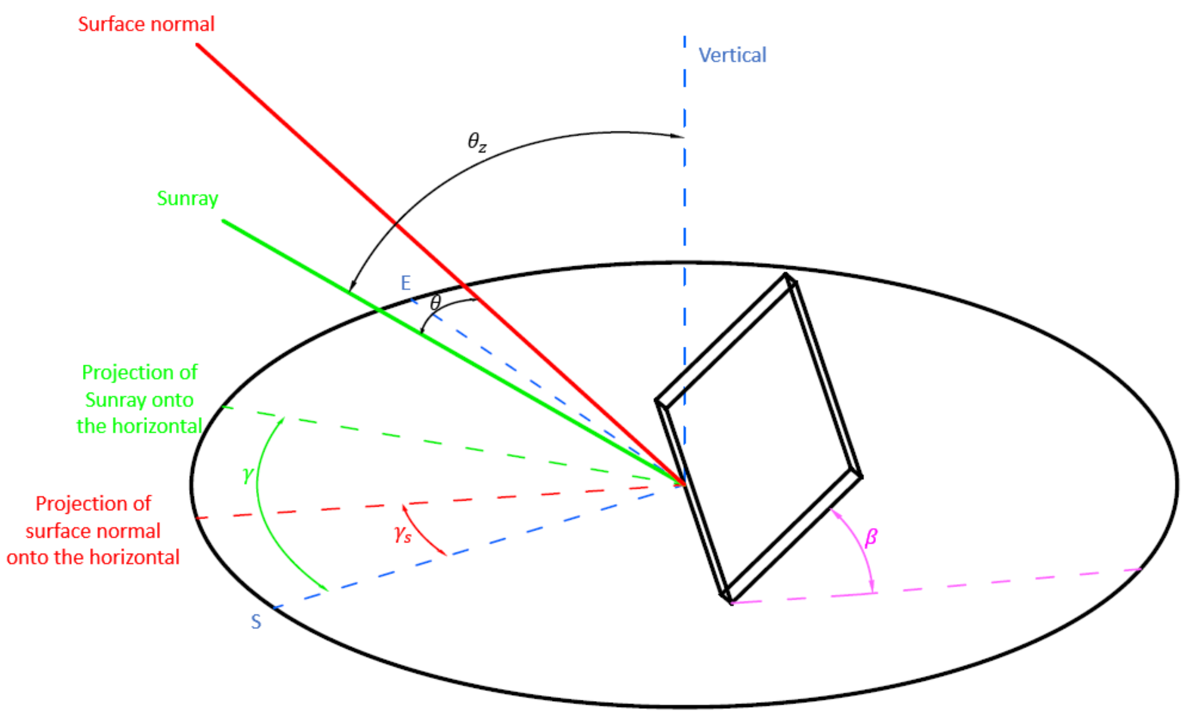

Figure 3.3: Solar geometry angles.

3.2.3 Longwave radiation

Unlike shortwave radiation emitted by the sun, all materials emit a radiation with a longer wavelength known as longwave radiation in the form of infrared rays (Incropera et al. 2007). Therefore, any surface of the bridge deck will receive longwave radiation from its surroundings and emit a certain amount back. The net rate of heat transfer (q_r) at a surface owing to longwave radiation may be estimated from Eq. (3.9) as:

$$q_r = E_c - E_{sur} = \sigma \cdot \varepsilon \cdot \left(T_c^4 - {T_{sur}}^4\right) \tag{3.9}$$

where, E_c is the emitted longwave radiation from the bridge surface, E_{sur} is the emitted longwave radiation from all other surrounding surfaces (note that the term surrounding surfaces refers to any surface in the vicinity of the bridge that emits radiation), σ is the Stefan Boltzmann constant, ε is the emissivity of the bridge surface, T_c is the temperature of the concrete, and T_{sur} is the temperature of the surrounding surfaces.

The method used to estimate T_{sur} varies depending on the bridge surface in question. For example, the bottom surface of the box girder receives longwave emission from the underlying ground, water and/or other parts of the structure. Therefore, T_{sur} is assumed equal to the temperature of the surrounding air. On the other hand, the top surface of the box girder receives radiation from the sky (T_{sky}) which may have a lower temperature than the surface air (T_a), depending on the prevalent cloud conditions. The estimation of T_{sur} for different surfaces of the box girder bridge cross section is explained further in Appendix A.

Once T_{sur} is estimated for all bridge surfaces, the long wave radiation exchange can be modelled in a Multiphysics computational domain (here, (ANSYS 2019)) using the radiosity solver which can simulate the radiation exchange between a surface and the ambient. The solver uses the calculated temperature (T_{sur}) and a surface emissivity as input. As per Appendix A and the above, the climate parameters needed to be able to model this exchange are the dew point temperature, the cloud cover, and the air temperature.

3.2.4 Enclosure Temperature

The inside cavity in a box-girder bridge will also influence the temperature distribution in the cross section. A heat exchange will occur between the internal air and the inside surfaces due to convection heat transfer and between the inside surfaces of the walls and slabs due to long wave radiation heat exchange. The heat exchange at an interior surface is illustrated in the enlarged portion of Figure 3.2 (here the interior surface labelled as 1). To simplify the complex interactions, the internal air temperature is used as input for both the long wave radiation heat exchange and the convection heat transfer as per Eq. (3.10):

$$q_{in} = q_{c,in} + q_{r,in} = h_c \cdot \left(T_{s,in} - T_{a,in}\right) + \sigma \cdot \varepsilon \cdot \left(T_{s,in}^4 - T_{a,in}^4\right) \tag{3.10}$$

where, q_{in} is the heat transfer at an internal bridge surface, $q_{c,in}$ is the internal convective heat transfer, $q_{r,in}$ is the internal radiative heat transfer, $T_{s,in}$ is the internal bridge surface temperature, and $T_{a,in}$ is the internal air temperature (Larsson 2012). If there is no measured data for $T_{a,in}$, it could be assumed as the average daily air temperature plus 1.5℃ (Elbadry and Ghali 1983). Furthermore, the calculation of the heat exchange at an internal surface can be further simplified by using the unified comprehensive heat transfer method which combines the convective and radiative heat transfer into one term ($h_c + h_r$), where h_r is the heat radiation coefficient. Thus, Eq. (3.10) may be replaced by Eq. (3.11).

$$q_{in} = (h_c + h_r)\left(T_{s,in} - T_{a,in}\right) \tag{3.11}$$

In the modelling software (Ansys 2019), the heat exchange at an internal surface can then be modelled in a manner similar to the one used for modeling the convection at an outer surface. The only climate parameter needed is the average daily temperature (used to estimate $T_{a,in}$), whereas the sum $(h_c + h_r)$ may be approximated as $10\,\frac{W}{m^2℃}$ (Incropera et al. 2007; Lu et al. 2021].

3.2.5 Heat Flow Within the Cross Section

The variation of the temperature distribution in a concrete structure can be described by the three-dimensional heat flow equations using Fourier's law of heat conduction Eq. (3.12):

$$\rho \cdot c \cdot \frac{\partial T}{\partial t} = k \cdot \left(\frac{\partial^2 T}{\partial x^2} + \frac{\partial^2 T}{\partial y^2} + \frac{\partial^2 T}{\partial z^2}\right) \tag{3.12}$$

where, ρ is the concrete density, c is the specific heat capacity, $\partial T/\partial t$ is the change in temperature over time, k is the thermal conductivity, and $\partial^2 T/\partial x^2, \partial^2 T/\partial y^2, \partial^2 T/\partial z^2$ are the second spatial derivatives of the temperature in the x, y, and z directions, respectively (Incropera et al. 2007). The relevant boundary condition for the three-dimensional heat transfer problem is described by Eq. (3.13):

$$k \cdot \left(\frac{\partial T}{\partial x} \cdot n_x + \frac{\partial T}{\partial y} \cdot n_y + \frac{\partial T}{\partial z} \cdot n_z\right) - q = 0 \tag{3.13}$$

The partial derivatives $\partial T/\partial x, \partial T/\partial y, \partial T/\partial z$ represent the temperature fluxes in the x, y, and z directions, n_x, n_y, n_z are the direction cosines of the unit outward vector normal to the boundary surface, and q is the rate of heat transferred from the environment to the concrete surface per unit area.

3.3 Thermal model

Using the details provided above for the heat exchange mechanisms that occur on all bridge surfaces, a full transient thermal model was developed (using a physico-mechanical modeling framework) to predict the temperature distribution along the depth of the bridge cross section. Figure 3.4 provides a summary of the climate parameters that were required as input to the thermal model. The bridge cross section used in the model is that of a concrete box girder.

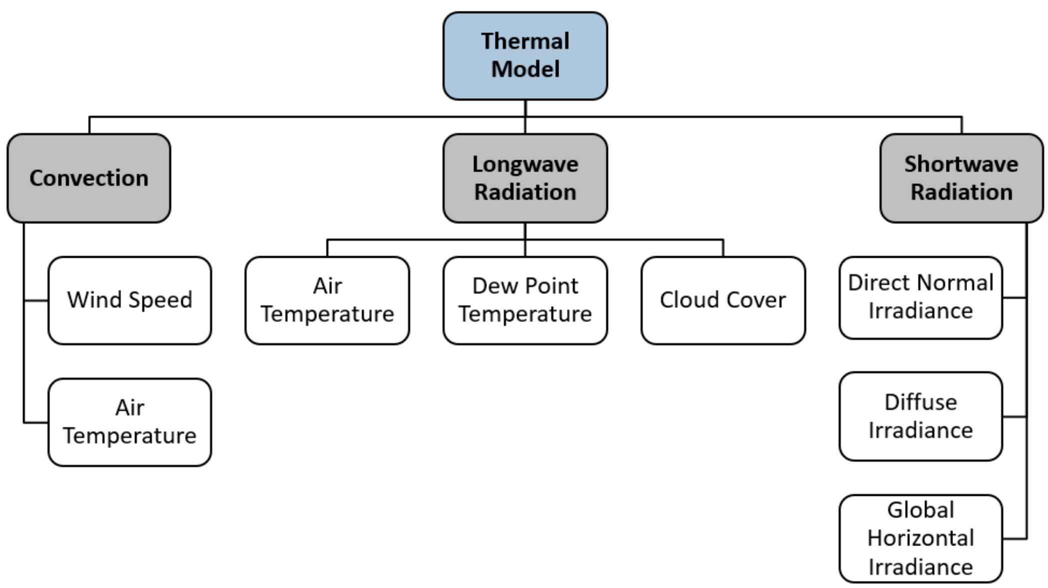

Figure 3.4: The climate parameters required as input in the thermal model.

3.3.1 Bridge description

A 5 m long segment of a box girder bridge was modelled to evaluate the results of the thermal processes described in the preceding sections. Considering that the box is adequately long, thermal conditions and resulting performance along the length are taken to be independent of the position along the longitudinal axis. The bridge cross section is shown in Figure 3.5. The bottom flange has a constant thickness of 250 mm while the top overhangs have a thickness that varies from 400 mm at the web to 250 mm at the outer end. The interior portion of the top flange has a thickness of 250 mm. The thickness of the web is 500 mm. The girder is 2 m in depth. The top surface of the bridge is flat, and the bridge is oriented in the South/North direction. Moreover, the concrete is overlain with a 110 mm thick layer of asphalt.

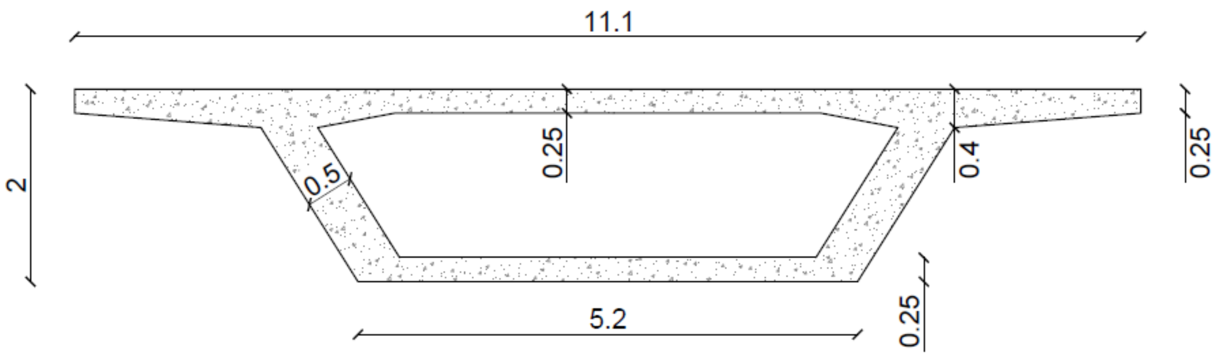

Figure 3.5: Box girder cross section. All dimensions are in m

3.3.2 Modelling details

The developed thermal model was verified against fundamental heat transfer verification tests. Some of the verification examples are shown in (Saad et al. 2022). Moreover, the thermal model was validated against experimental results from literature. The reference experiment used for the validation study had been conducted in China and involved monitoring the temperature development in a box girder during a cold-wave event which occurred between December 3 and 6, 2008 (Gu et al. 2014). The bridge is a prestressed concrete box girder comprising three continuous spans with a total length of $548\ m$. The deck has a variable depth which ranges from $4.5\ m$ at midspan to $15\ m$ at the piers and a total width of $16.4\ m$. Upon running a numerical thermal analysis on the box girder using the developed model, it was found that the numerical results match closely the field measurements for the reference extreme event. A comparison of the measured and numerically determined results is in Figure 3.6 (Saad et al. 2022); note that the color code in the curves is matched to the points in the box girder where thermal records were obtained. Dashed lines represent the model predicted values, whereas the measured points are given by triangular markers of the same color.

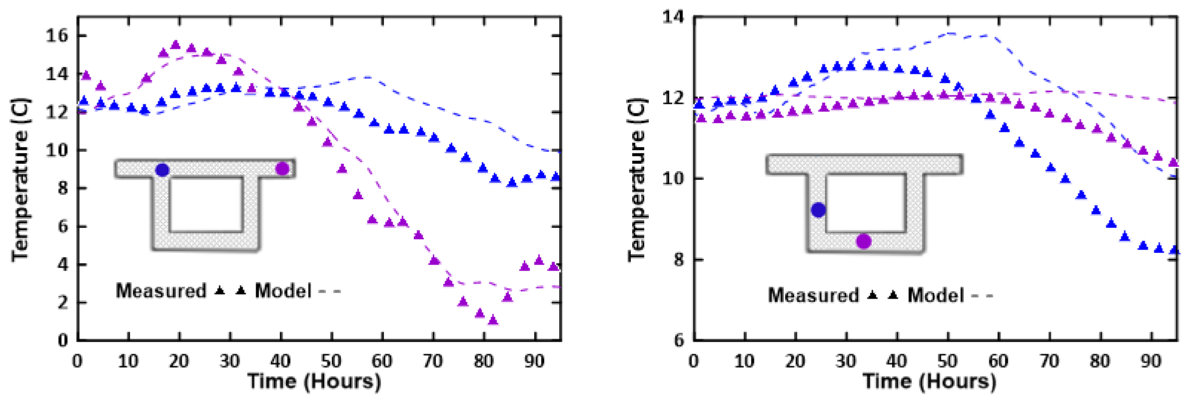

Figure 3.6: Thermal model validation (measured data from (Gu et al. 2014) and model data from (Saad et al. 2022)).

For the needs of the present study, the thermal model will require input in the form of hourly values for each of the climate parameters (Figure 3.3) for a seven-day period. Whereas the development of thermal gradients is typically studied over a three-day event period, this was extended to a longer seven-day period since the additional computing power needed was not significant. A timestep of 30 minutes was used in the analysis.

To represent symmetric conditions along the length of the bridge, the $5\ m$ long segment (cross section of Figure 3.5) was modelled with its ends assumed to be perfectly insulated (so no temperature exchange would occur in the longitudinal direction). The initial temperature distribution within the box girder was assumed to be uniform with a value equal to the value of ambient near surface temperature at the start of the simulation. The top asphalt layer was included in the model as a solid layer with separate thermal properties as shown in Table 3.1. The elements used for modelling both the asphalt and the concrete were 3-D 20 node prism shaped thermal elements (Solid90 (ANSYS 2019)) and the total number of elements used for the bridge cross section and the asphalt was 5600 and 1400 respectively. Input values for the material constants in the thermal model were obtained from (Gu et al. 2014) and are listed in Table 3.1.

Table 3.1: Material properties used in the thermal model (Gu et al. 2014)

Material	Density (kg/m^3)	Heat Capacity (J/kg°C)	Conductivity (W/m°C)	Emissivity	Absorptivity
Concrete	2200	1287	1.97	0.9	0.65
Asphalt	2100	886	0.98	0.9	0.90

3.4 Location selection and data collection

To establish a relationship between ambient climate variables and thermal load, a cluster of locations was selected from across Canada, the climate of which was used as a case study in the thermal simulations. To ensure a representative sample of several different climate types across Canada, a pre-existing climate classification system was used as a starting point.

Climate classification systems are a means of representing the variability in spatial and temporal distribution of climate. Of the available alternatives (such as the Thornthwaite and Berg climate classification systems), the Köppen climate classification system was chosen, since it is the most used system and because its emphasis is on temperature rather than moisture (Oliver 2005) (Temperature differences are likely to affect thermal gradients more than variations in moisture). The following section provides a brief overview of the Köppen climate classification system. The selected locations are then listed, and the climate data collection methodology is also described.

3.4.1 The Köppen system

Köppen studied the world distribution of natural vegetation types, located the boundaries that separated them, and determined what combinations of monthly mean temperature and precipitation were associated with those boundaries. A multi-tiered classification system was thus established, representing primary climates by capital letters from A through E. These five broad categories tend to arrange themselves across Earth's surface in response to the latitude, degree of continentality and location, relative to major topographic features. The main climate groups are briefly described below. Note that climatic zones A, C, D, and E are based on temperature characteristics while climate zone B is the sole type that considers precipitation as well (Oliver 2005).

- A—Tropical. Climates in which the average temperature for all months is greater than 18 °C (64 °F). Almost entirely confined to the region between the equator and the tropics of Cancer and Capricorn.
- B—Dry. Potential evaporation exceeds precipitation.
- C—Mild Mid-latitude. The coldest month of the year has an average temperature higher than –3 °C (27 °F) but below 18 °C (64 °F). Summers can be hot.

- D—Severe Mid-latitude. Winters have at least occasional snow cover, with the coldest month having a mean temperature below –3 °C (27 °F). Summers are typically mild.
- E—Polar. All months have mean temperatures below 10 °C (50 °F)

Each of the A through E climates are further subdivided into sub-categories represented by a second letter, which are then further divided down to a third sub-category represented by a third letter. Thus, each individual climate is represented by a three-letter combination describing its temperature and precipitation characteristics with the meaning of each letter varying among the major groups. Additional details can be found in (Oliver 2005).

3.4.2 Selected locations

Looking at the Köppen climate classification for Canada (Figure 3.7), it is observed that the dominant climate zone is the severe Mid-latitude (Zone D). The upper-most northern region has a polar climate (Zone E). It is also seen that the southern portion of the province of Saskatchewan is characterized by a dry climate (Zone B). Moreover, the south-western section of British Columbia belongs to the Mild Mid Latitude Classification (Zone C). Within the climate zones, the major subdivisions from climate zone D are Dfc (Subarctic), Dfa (Hot summer-humid continental), and Dsc (Dry Summer-Subarctic). On the other hand, the regions that belong to climate zone C can be classified into either Cfb (Oceanic) or Csb (Warm summer-Mediterranean). The areas with climate zones B and E are dominated by subdivisions Bsk (cold semi-arid) and ET (Tundra).

Based on this overview of the Canadian climate, a total of 20 Canadian locations were chosen to represent the different climate zones and subdivisions defined in the Köppen classification system. Furthermore, the locations are also widely spread over the Canadian mainland. Figure 3.7 shows the selected locations within each province and their climates. Note that most of the chosen locations (14 of 20) belong to climate zone D. Three locations are chosen in climate zone E. Furthermore, Zones C and B are represented by two locations and one location respectively. The number of selected locations from each climate zone is representative of the proportion of Canada covered by that climate zone (i.e. Zone D covers the majority of Canada and is therefore most represented). Finally, the Atlantic provinces were not included in this study since the selection process was limited to mainland Canada.

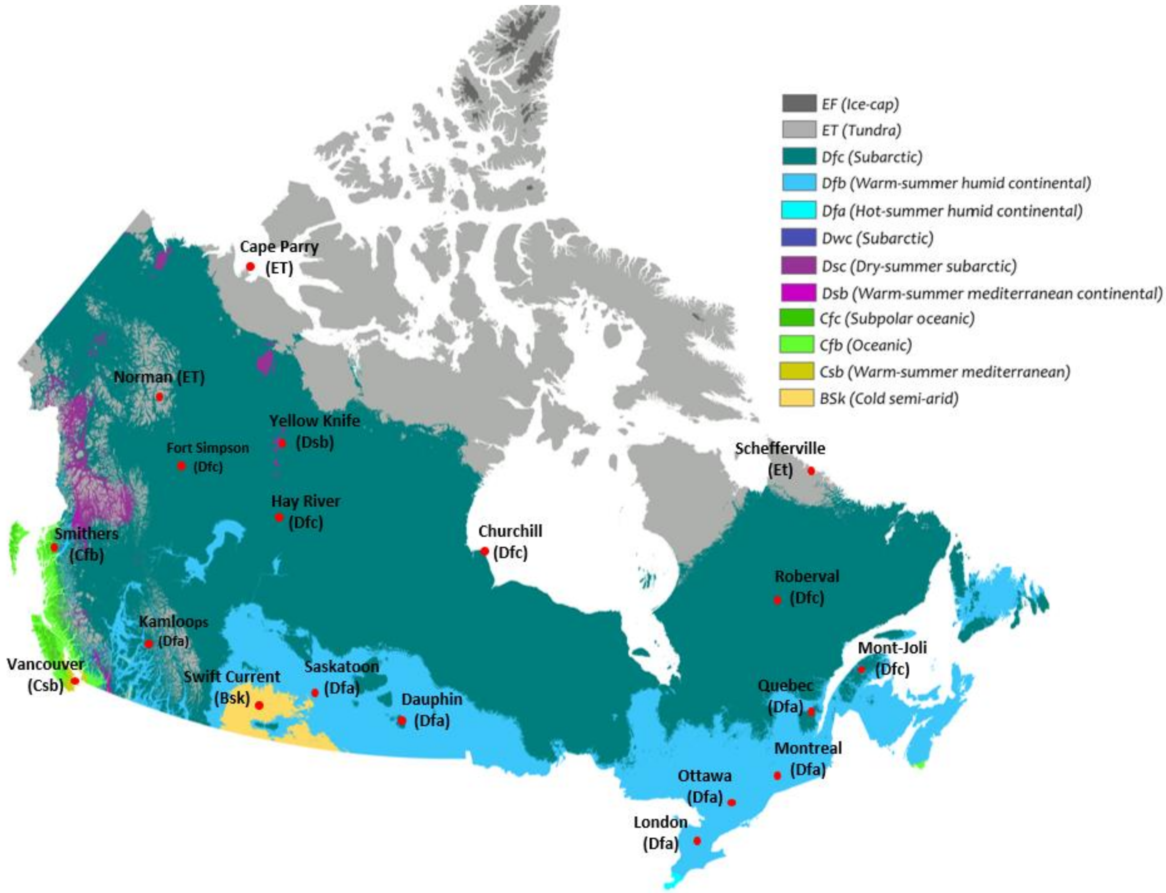

Figure 3.7: Map showing the selected cities within the Köppen classification system (Peterson 2016).

3.4.3 Climate data compilation and organization

Historical Climate data for all the locations were compiled from the Canadian Weather Energy and Engineering Datasets (Environment and Climate Change Canada 2019). The climate parameters extracted were chosen based on their contribution to the atmosphere bridge boundary interaction as shown in Figure 3.3. The obtained data included hourly values of ambient temperature, dew point temperature, windspeed, DNI, GHI, diffuse irradiance, and sky cover.

The hourly baseline climate for each location was then obtained for the 30-year period extending from January 1976 to December 2005. The baseline climate is defined as the historical climate averaged over several years (Belcher et al. 2005). Establishing a baseline climate is essential in determining the general climate characteristics of a particular location since the values experienced in one particular year may represent an anomaly. The hourly baseline climate was determined in accordance with Eq. (3.14) (Belcher et al. 2005):

$$(x_0)_h = \frac{1}{N} \times \sum_N x_0 \tag{3.14}$$

where, N is the number of years in the averaging period (here N is taken equal to 30 years from 1976-2005), x_o is a variable in the present-day period, and $(x_0)_h$ is the variable x_0 averaged hourly over the baseline period.

After the baseline climate for each location was established, the 50th percentile value and standard deviation were calculated in an attempt to represent the average climatic conditions and to eliminate any extreme cases. The daily baseline values at each location and for each parameter were then examined and the day in which the parameter value was closest to the obtained 50th percentile value was selected. The next step was to compile the hourly data for the chosen reference day as well as the three days preceding it, and the three days following it. Thus, a 7-day compiled dataset for each city and each parameter was used in thermal simulations. This dataset represents average climatic conditions and is expected to produce average thermal profiles in the bridge structure.

3.5 Thermal simulation

The compiled climate data for each location was used as input for boundary conditions in the thermal finite element model of the concrete box girder. The maximum temperature differential in each web of the cross section was then determined and the results were analyzed with reference to the input, to determine whether a linkage can be identified between climate parameters and the bridge response. The details of the case study are illustrated in the sections below through an example.

3.5.1 Boundary conditions: Example

The city of Swift Current (52.1° N, 106.6° W) is in the province of Saskatchewan and falls within the dry climate category (Bsk) of the Köppen climate classification system. Once the baseline climate for the city was established, the 50th percentile values for all climate parameters were determined. Figure 3.8 is a box and whisker plot that shows the baseline climate data distribution for each parameter.

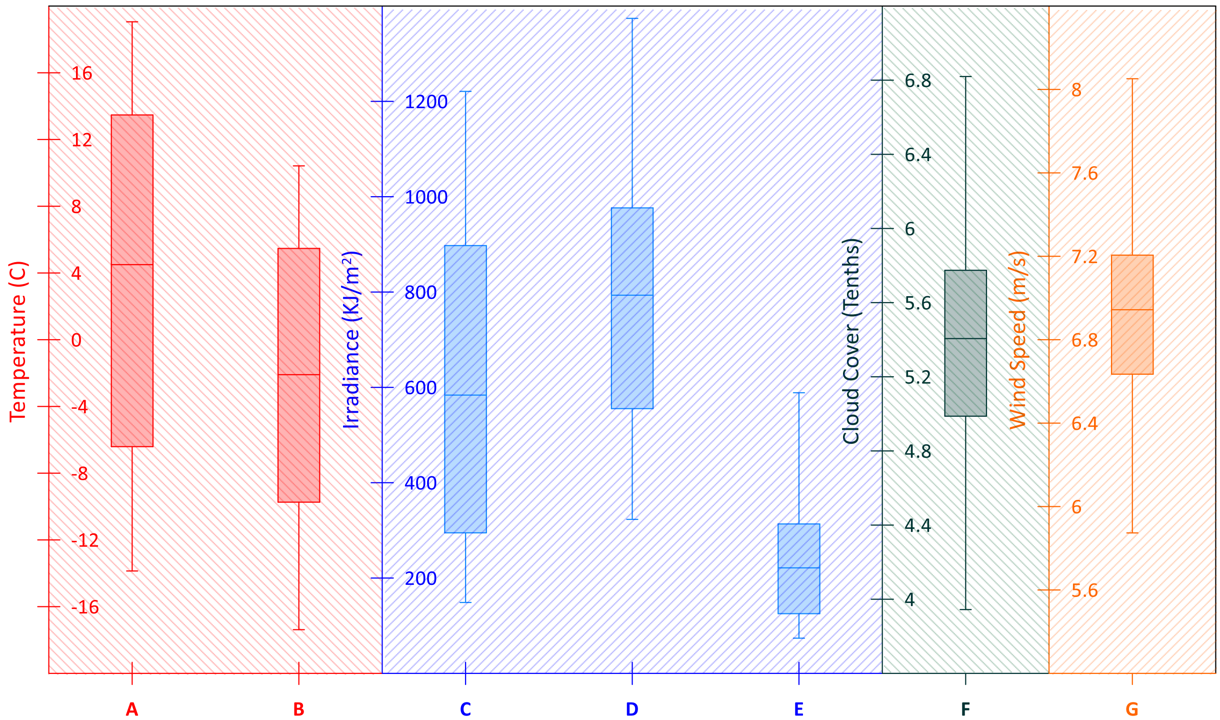

Figure 3.8: Box and whisker plot showing the distribution of: A: Ambient Temperature, B: Dew Point Temperature, C: Global Horizontal Irradiance, D: Direct Normal Irradiance, E: Diffuse Normal Irradiance, F: Cloud Cover, and G: Windspeed.

The next step was to determine the corresponding baseline hourly data for the three-day intervals prior to and after the date on which the 50th percentile value occurs. Table 3.2 shows the 50th percentile values for each parameter along with the date on which it occurs and the corresponding average value over the 7-day period. Furthermore, Figure 3.9 shows the obtained 7-day data for each parameter at its corresponding date.

Table 3.2: Sample Data for Swift Current (Environment and Climate Change Canada 2019).

Parameter	Ambient Temp (℃)	Dew Point Temp (℃)	Diffuse Normal Irradiance (KJ/m^2)	Direct Normal Irradiance (KJ/m^2)	Global Horizontal Irradiance (KJ/m^2)	Sky Cover $(Tenths)$	2m-Wind Speed (m/s)
50th Percentile	4.49	-2.09	221.37	793.36	583.806	6.94	54.06
Day	15-Apr	27-Apr	10-Mar	23-Mar	19-Mar	1-May	1-Oct
Average	3.82	-2.11	232.5	773.7	603.2	6.91	53.8

For each of the time periods shown in Figure 3.9, the values for the remaining parameters over the 7-day period of interest were also obtained. For example, the values of the dew point temperature, windspeed, DNI, GHI, diffuse irradiance, and sky cover between 12-18 April were obtained, since the 50th percentile value of ambient temperature occurred over that period. The time histories of these variables are plotted in Figure 3.10. The data for every parameter for all time periods was then input as boundary condition into the finite element model with each time period constituting one simulation. Thus, for every location, seven climate datasets were compiled, and seven different simulations were run for a total of 140 simulations.

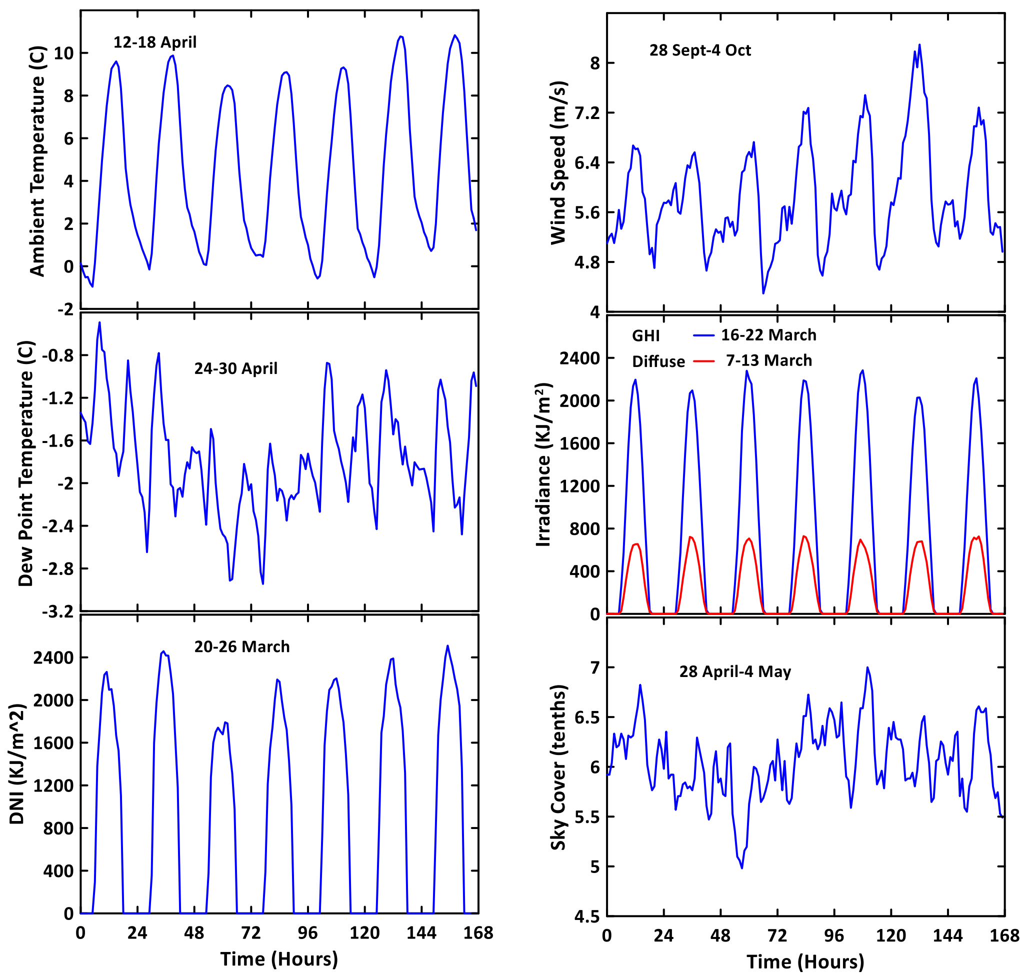

Figure 3.9: 7-day data for the 50th percentile value of each parameter (Time 0 corresponds to the starting day).

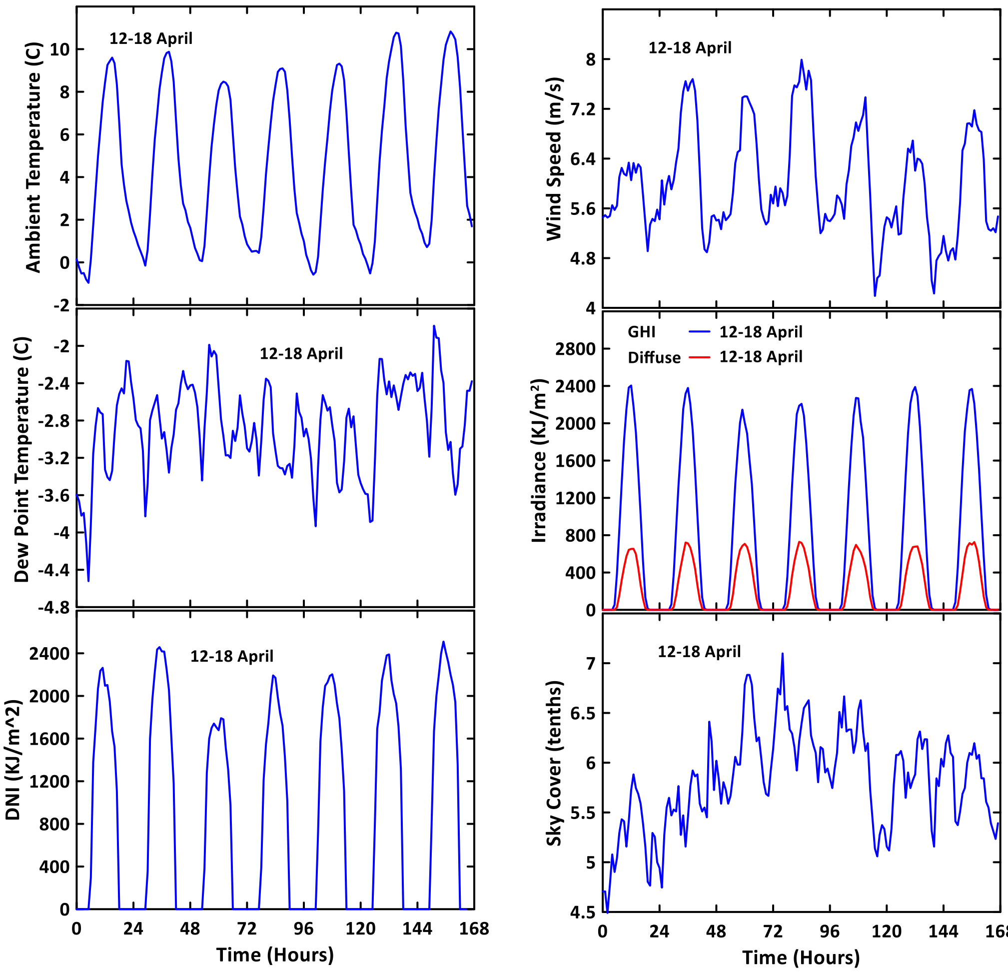

Figure 3.10: Data for the all the parameters during the 7-day period at which the 50th percentile value of dry bulb temperature occurred.

3.6 Results and discussion

3.6.1 Sample of results for one city: Swift Current

The thermal model was used to predict the temperature distribution in the bridge deck over each 7-day period. The temperature distribution along the webs of the bridge cross section was extracted for all instances. The maximum differentials, representing the largest difference between the top exterior surface and the bottom exterior surface were then determined. It should be noted that for the purpose of this study, we have only considered positive temperature differences of concern, associated with warmer temperatures (i.e., positive gradients). While it is possible to model negative gradients of concern in the same way, our design considerations were limited due to the complex structural model that arises in the case of colder temperatures. The reason for this complexity is the strong material property sensitivity to cold temperatures, which falls outside the scope of the present work. The simulations performed and results obtained for the city of Swift Current are shown in Table 3.3, Table 3.4, and Figure 3.11, respectively.

Table 3.3: Input for each simulation for the city of Swift Current.

50th percentile value for the considered parameter in each simulation							
Simulation No.	1	2	3	4	5	6	7
Main Parameter	Ambient Temp (°C)	Dew Point Temp (°C)	Diffuse Normal Irradiance (KJ/m^2)	Direct Normal Irradiance (KJ/m^2)	Global Horizontal Irradiance (KJ/m^2)	Sky Cover $(tenths)$	Wind speed (m/s)
50th percentile Value	4.49	-2.09	221.37	793.36	583.80	6.94	5.46
Time Period	12-18 April	24-30 April	7-13 March	20-26 March	16-22 March	28 April-4 May	28 Sept-4 Oct.

Table 3.3 shows the 50th percentile value of each main parameter. Table 3.4 shows the top and bottom differential (representing the difference between the top exterior surface and the interior and the bottom exterior surface and the interior at the instance at which the maximum differential occurs) from each simulation. Figure 3.11 illustrates the calculated temperature differentials within the web of the girder as well as the 7-day average value for all the parameters. The temperature differentials between the top and the interior of the cross-section and between the bottom and the interior can be seen. It is observed that the temperature differentials between the top and the interior of the cross-section (top differentials) range between 8°C and 12.5°C for different simulations. Meanwhile, the differentials between the bottom and the interior of the cross-section (bottom differentials) range from 4°C to 8°C. The results above are presented to demonstrate the type of simulations performed and results obtained for each location. A similar analysis was performed for all locations and all results were combined and investigated collectively to obtain a meaningful overall picture.

Table 3.4: Results for each simulation for the city of Swift Current.

Results: The top and bottom differentials obtained from each simulation							
Simulation No.	1	2	3	4	5	6	7
Top Differential (°C)	12.32	11.82	8.55	10.97	10.05	11.77	9.16
Bottom Differential (°C)	6.78	6.02	4.16	5.09	4.41	6.07	5.70

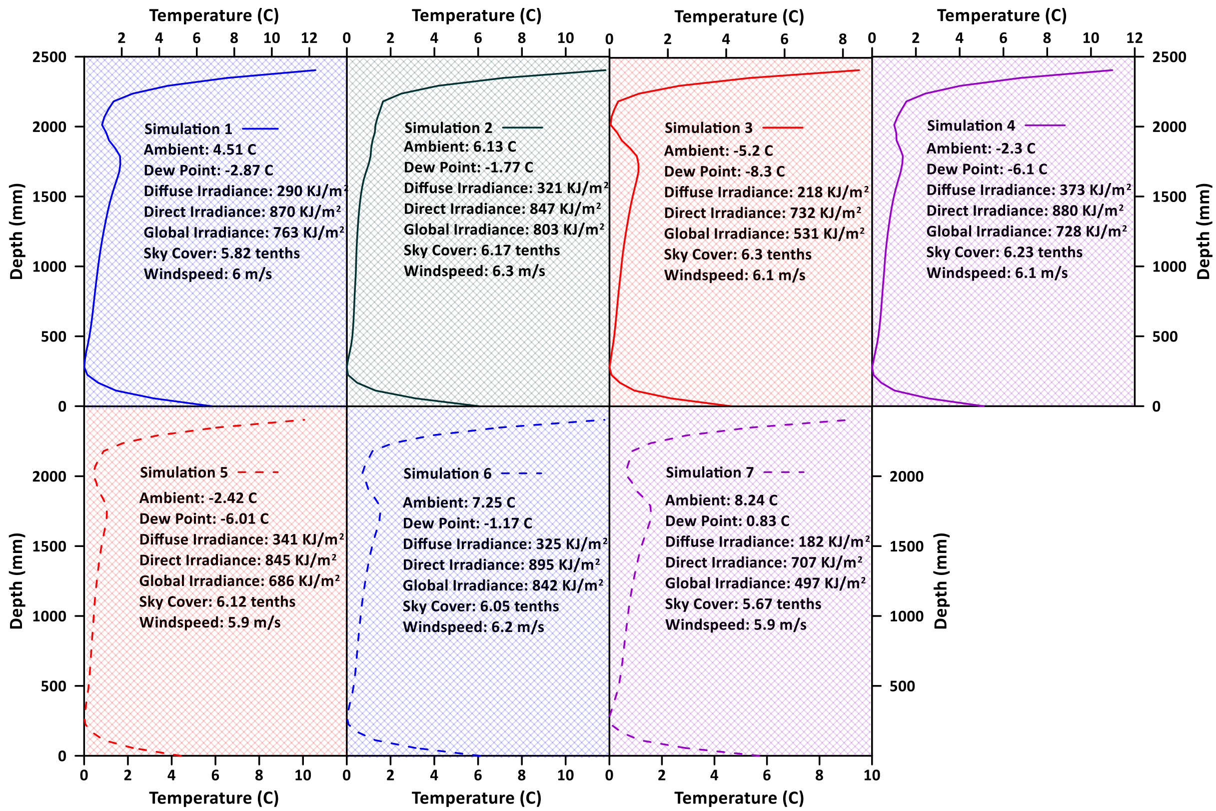

Figure 3.11: Temperature differentials within the webs for all Swift Current simulations along with seven-day averages for all parameters used in each simulation.

3.6.2 Analysis of results

Having established a similar set of results for each location (7 simulations per location), the first observation made was that for most of the considered cases, the top differential was below 15℃ which is the limit provided by the CHBDC (shown by the dashed line in Figure 3.12) (Canadian Standards Association 2014). However, the DNI values considered in the simulations represent average values; therefore, for extreme cases, such as in heat waves or in anomalous conditions where DNI values are high, the limit provided by the CHBDC will likely be exceeded. A detailed analysis of the differentials was carried out to identify which climate parameter has the dominant effect or correlates with the differentials obtained from the simulations. One pattern, that was discovered upon analysis, was the relationship between the direct normal irradiance and the obtained differential at the top. It was found that as the direct normal irradiance at a location increases, the differential at the top of a bridge also increases. This trend is illustrated in Figure 3.12 which plots the DNI values against the corresponding top temperature differentials. The incoming DNI and resulting differential at the top of the cross section can be related by grouping them into the categories described below:

- Category 1: $DNI < 600\frac{KJ}{m^2} \rightarrow Top$ Differential $< 4°C$
- Category 2: $600 < DNI < 800\frac{KJ}{m^2} \rightarrow 4 < Top$ Differential $< 10°C$
- Category 3: $800 < DNI < 1000\frac{KJ}{m^2} \rightarrow 10 < Top$ Differential $< 12.5°C$
- Category 4: $1000 < DNI < 1200\frac{KJ}{m^2} \rightarrow 12.5 < Top$ Differential $< 16°C$

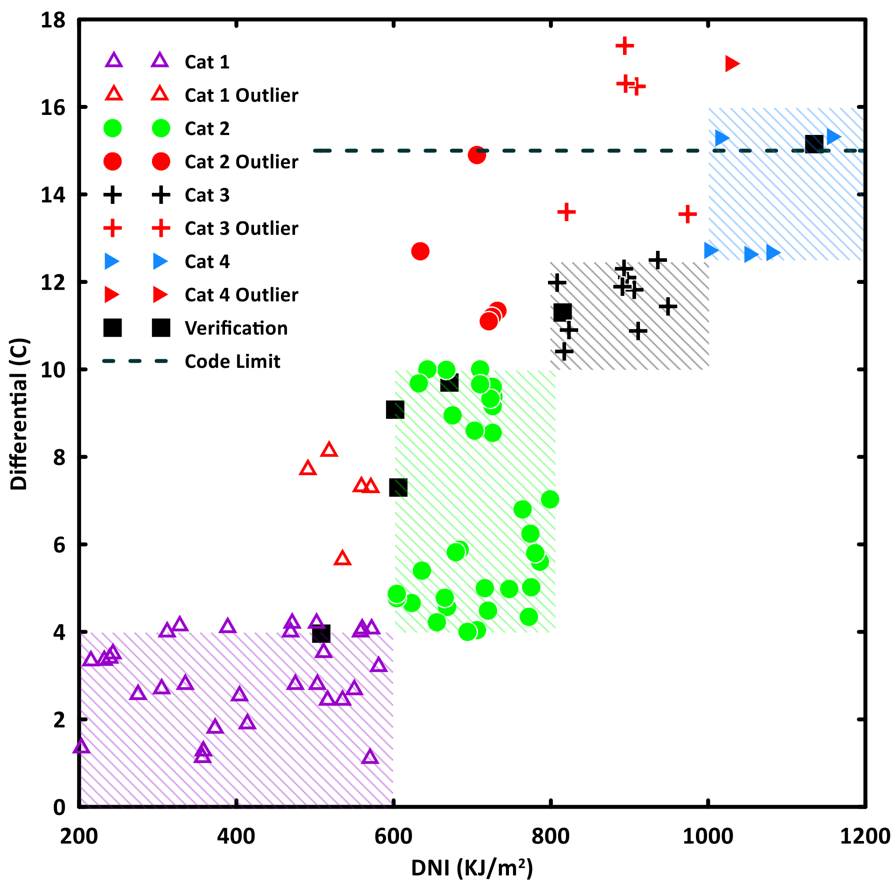

Figure 3.12: Top differential vs Average DNI for all simulations along with the described criteria.

Figure 3.12 highlights the fact that most of the data is within the categories proposed above. However, the results from some simulations are outside the boundaries of these categories and are identified as outliers. It is important to note that most of these outliers are mainly from two locations: Kamloops and Norman Wells.

Therefore, these outliers could likely be attributed to specific geographic features of these locations (Kamloops and Norman Wells being both located in mountainous regions). Figure 3.12 also shows the maximum temperature differential (15℃) recommended in the CHBDC. As noted above, most points fall below this limit. However, since the cases investigated represent 50th percentile values for the climate parameters, it can be inferred that this limit will be exceeded in more extreme cases (in which the seven-day average DNI exceeds $1200\ KJ/m^2$). To investigate this assumption further, four simulations with the seven-day average DNI exceeding $1200\ KJ/m^2$ were conducted. The seven-day average DNI for the simulations were $1341, 1523, 1621$, and $1741\ KJ/m^2$. Figure 3.13a shows the obtained maximum top temperature differential from each simulation and Figure 3.13b shows the predicted temperature distribution within the cross section in comparison with the code prescribed distribution. The results clearly show that code limits will be exceeded when the seven-day average DNI increases beyond $1200\ KJ/m^2$. It should be noted that a similar set of analysis was performed for the bottom temperature differential; However, no direct relationship was established with any of the climate parameters.

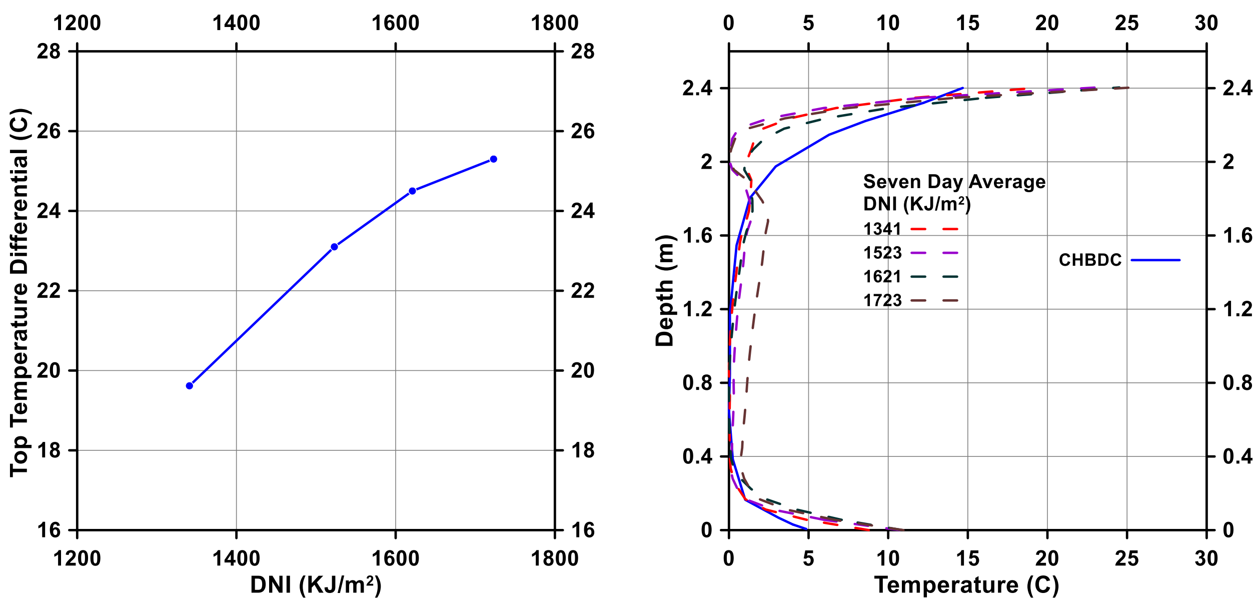

Figure 3.13: Results for the simulations with the seven-day average DNI exceeding $1200\ KJ/m^2$: a) The top temperature differential vs the seven-day average DNI for each simulation, b) Temperature differential with the cross section for each simulation (at the instance of maximum top differential).

3.6.3 Verification

To verify the described categories, 6 cities were selected from different locations across Canada and a random seven-day period was selected for each city. The selected cities were, Whitehorse $(60.7°N, 135.0°W)$, Hamilton

$(43.2°N, 79.8°W)$, Thompson $(55.75°N, 97.8°W)$, Toronto $(43.65°N, 79.3°W)$, La Prairie $(45.41°N, 73.4°W)$, and Regina $(50.4°N, 104.6°W)$. The average DNI for the chosen seven-day periods were $606, 508, 602, 671, 815$ and $1135\ KJ/m^2$ respectively. The results from the simulations agree with the proposed categories and are represented by the black square markers in Figure 3.12.

Furthermore, the study was expanded to determine the applicability of the proposed model to box girders of different sizes. In additional simulations, the box girder cross section was scaled down by a factor of 0.8, and 0.9; it was also scaled up by a factor of 1.1 and 1.2. The different cross sections thus produced were then subjected to the climate conditions that occurred in the city of Regina during a randomly chosen time period (August 28-September 3, 1983). The average seven-day DNI for that period was $1171\ KJ/m^2$; for this value the proposed model (Figure 3.12) estimated a top differential which lies between 12.5℃ and 16℃. The results from the simulations agree with the prediction from the model and show that the top differential for all the scaled sections ranged from $13.2 - 13.8$℃. These results indicate that the difference in the top differential between the scaled sections is negligible. This suggests that the model is applicable to any box girder of realistic size. An additional simulation in which the top slab thickness was increased from 250 to $400\ mm$ demonstrated similar results.

3.6.4 Application of established criteria to all Canadian provinces and territories

Once a relationship between the average seven-day DNI and the resulting differential at the top of the bridge cross section was determined, another case study was performed to investigate the possible discrepancy between CHBDC guidance on thermal differentials and local estimates based on the methodology developed and proposed in this research. The case study involved determining the average DNI for every seven-day period from 1976-2005 for all 154 locations for which the DNI data is provided in the CWEEDS database (Environment and Climate Change Canada 2019). Note that the recorded DNI is a combination of satellite derived measurements and measured observations from ground stations. The 97.5th percentile value of the seven-day DNI average was then determined for each of these locations. The locations were then assembled into their respective provinces and the 97.5th percentile value of the seven-day DNI average for each province is determined as an average of that of the individual locations. The obtained value for each province along with the different locations used is represented in Figure 3.14. Note that the locations were grouped by province and territories due to a lack of a more reasonable grouping criteria, since seven-day average DNI values are mostly available for large urban city centers whereas in suburban and rural locations, these values are not available. Furthermore, no reference seven-day DNI maps are available to be used as a starting point.

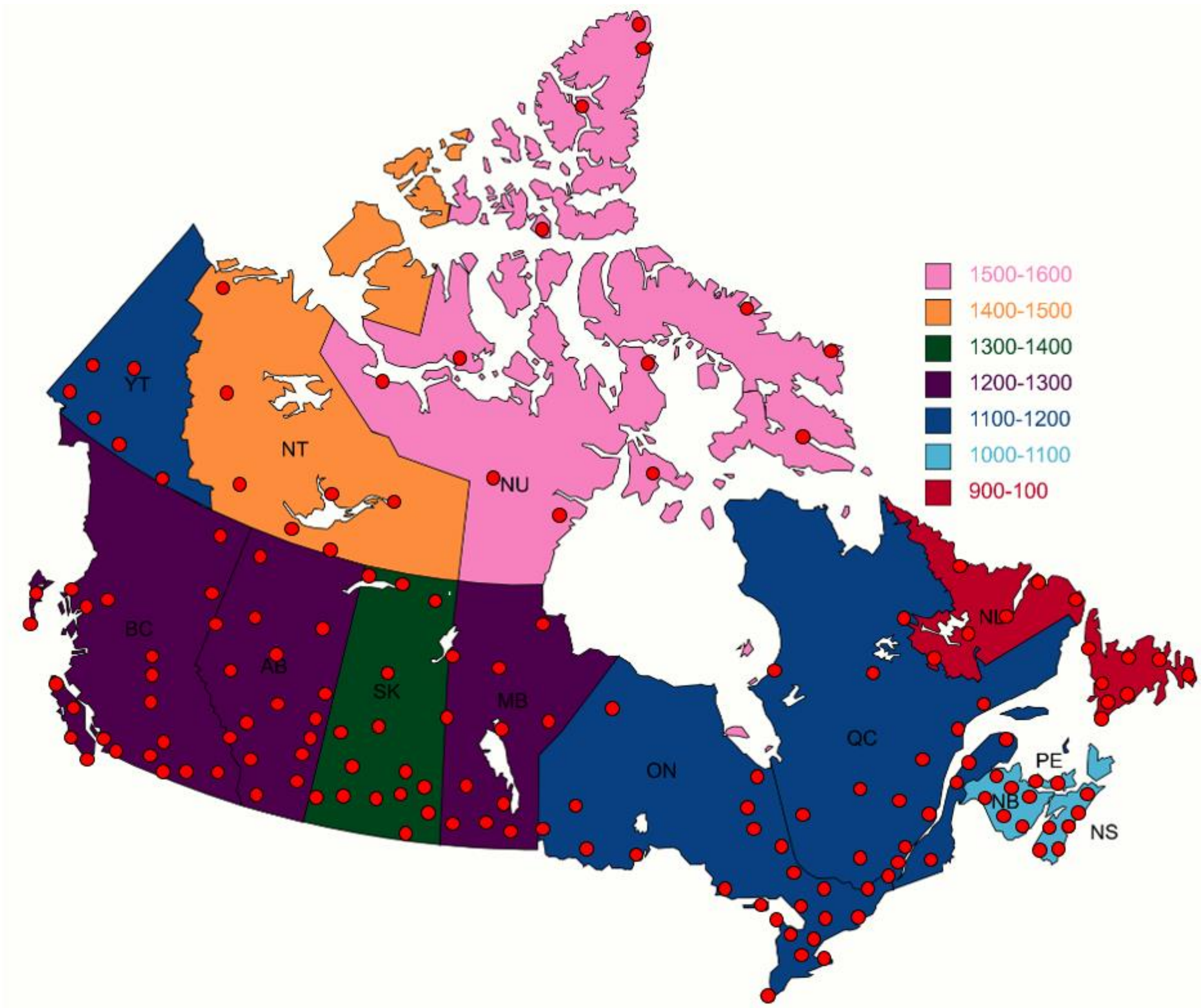

Figure 3.14: 97.5th percentile value of the seven-day DNI average for all Canadian provinces.

From the established criteria (Figure 3.12), it can be estimated that the top differential will likely exceed the code limit of 15 ℃ in locations where the seven-day DNI average exceeds $1200\ KJ/m^2$. Therefore, it is observed that the thermal differential will exceed the established design guidance in a significant number of Canadian provinces. These include the Central and Western provinces of Manitoba, Saskatchewan, Alberta, and British Columbia. Moreover, the limit is greatly exceeded in the northern territories of Nunavut and the Northwestern Territories. This observation seems counter intuitive as these territories are known for extremely cold temperatures and one is therefore likely to assume that solar radiation levels are minimal. However, data from the territories has shown that the average amount of solar radiation in the southern parts of Nunavut and the Northwestern Territories is similar to those observed in the southern parts of Quebec and Ontario. The incoming radiation is concentrated only in the summer months and is negligible in the winter months which explains why the province has a higher 97.5th percentile value of the seven-day DNI average. Furthermore, the figure also shows that the provinces and territories of Ontario, Quebec, New Brunswick, Prince Edward Island, Newfoundland and Labrador, and Yukon are within code limits. Note that in some of the provinces (e.g., British Columbia and Quebec), the locations with available data are not spread out within the province. Instead, the locations are concentrated in certain areas. Therefore, the average value obtained for the province may be an approximate representation of the actual value.

3.7 Concluding Remarks

In summary, 20 locations, representative of various types of Canadian climates as classified by the Köppen climate classification system, were selected and historical climate data for each city was complied over a 30-year period. Thermal finite element simulations were then run in which a concrete box girder bridge cross section was subjected to the climate conditions of each city during the seven-day period over which the 50th percentile value for each considered climate parameter occurs i.e., seven runs were performed for each city since there are seven climate parameters (Ambient temperature, Dew point temperature, Windspeed, DNI, GHI, Diffuse irradiance, and cloud cover). The maximum top and bottom thermal differentials from each run were then obtained.

Upon analysis of the results, it was determined that a relation between the DNI and the top differential can be established, with the top differential increasing with the increase in the DNI. Four categories, relating the DNI to the top differential were proposed; The categories were then verified by running additional thermal simulations using climate conditions from 6 randomly selected cities and 6 randomly selected time periods. The simulations were found to corroborate the proposed relationship. These findings are useful to a bridge engineer as they provide an approach by which the thermal load acting on a bridge can be estimated without the need for complex simulations and is useful as a starting point in providing more efficient thermal load design guidance in bridge codes. For example, it was seen from the examined categories that if the DNI exceeds $1200\ KJ/m^2$then the resulting top differential may likely exceed the 15°C limit provided in the CHBDC guidelines. This observation was then used to determine the provinces and territories in which code limits are exceeded by collecting data from 154 locations and determining the 97.5^{th} percentile value of the seven-day DNI average for each province. The findings show that limits are exceeded significantly in Central and Western provinces as well as some of the northern territories.

The demonstrated methodology may be applied to larger geographic regions beyond the boundaries of Canada to include additional countries and territories where engineered construction may be impacted by thermal effects. Further, refinements may be obtained by investigating additional locations and improving guidance within each province and territory. From such an extension of the application of the methodology, it is possible to derive maps that show seven-day average values of DNI and to link these to resulting bridge gradients. Thus, this model could serve as a catalyst for the development of more location-specific guidelines to enhance the relevance of the differentials available in the code. The model is also essential for structural assessment of existing bridges, since it is possible to estimate the thermal load intensities and number of cycles that have acted on a structure from the incoming DNI at the location of interest and for the duration of the bridge's lifespan. For practical applications, the required procedure to approximate the top thermal differential for a bridge cross section based on DNI climate at a given location is summarized in the following sequence:

Step 1: Obtain the hourly or daily climate data for the location and time period of interest.

Step 2: Identify the average for seven-day intervals within that time period.

Step 3: Select the seven-day period with the maximum DNI (or n^{th} percentile as required)

Step 4: Based on the established relationship (Figure 3.12), estimate the temperature differential at the top of the cross section.

Future research should focus on expanding the study to include additional cross section types (such as I and T girders) to illustrate the range of applicability of the relationship between DNI and the top temperature differential.

3.8 Appendix A

In the section, it is shown that the value of T_{sur} varies depending on the concrete surface in question. For example, the top surface receives radiation from the sky (T_{sky}) which may have a lower temperature than the surface air (T_a), depending on the prevalent cloud conditions. T_{sky} is defined as the temperature that the sky would have it were to be modelled as a flat horizontal surface (Incropera et al. 2007). The value of T_{sky} could be calculated using measurements of the incident long wave heat radiation (q_{sky}) recorded by a pyrgeometer as shown in Eq. (3.15):

$$T_{sky} = \sqrt[4]{\frac{q_{sky}}{\sigma \varepsilon_{sky}}} \tag{3.15}$$

where, ε_{sky} is the emissivity of the sky, typically assumed to be equal to the emissivity of the concrete. In cases where data for incident longwave radiation q_{sky} is unavailable, q_{sky} could be estimated based on the ambient temperature (T_a), dew point temperature (T_{dew}), and the cloud cover (C_{cloud}) as shown in Eq. (3.16).

$$q_{sky} = \varepsilon_{at}\, \sigma T_a^4 \tag{3.16}$$

Parameter ε_{at} is the integrated effective emissivity of the atmosphere and canopy (incorporates T_{dew} and C_{cloud}). ε_{at} can in turn be expressed as:

$$\varepsilon_{at} = (0.53 + 0.2055(e_a)^{0.5})(1 + 0.4C_{cloud}) \tag{3.17}$$

where, e_a is the surface vapor pressure and can be estimated from Eq. (3.18).

$$e_a = 0.6108e^{[\frac{17.27T_{dew}}{T_{dew}+273}]} \tag{3.18}$$

Furthermore, in certain cases where cloud cover data is not available, an alternative option can be used to estimate the cloud cover based on the ratio of measured extra-terrestrial irradiance k_{meas} to theoretical extra-terrestrial irradiance k_{theo} as shown in Eq. (3.19).

$$C_{cloud} = 1 - \frac{1}{0.68}[\frac{k_{meas}}{k_{theo}} - 0.355] \tag{3.19}$$

k_{theo} is in turn expressed as a function of the solar zenith angle θ_s as per Eq. (3.20).

$$k_{theo} = 1367 \cos\, \theta_s \tag{3.20}$$

On the other hand, a vertical surface such as a web wall receives long-wave radiation from both the sky and the ground. Thus, to estimate the net rate of long wave radiation (q_r), the effective sky temperature is replaced by an equivalent temperature (T_{eq}), which is a fictitious temperature combining the sky temperature and the temperature of the ground. The ground can be assumed to have the same temperature T_a as the air. The equivalent temperature for a vertical surface is calculated as the average of T_a and T_{sky} as per Eq. (3.21).

$$T_{eq} = \frac{T_{sky}+T_a}{2} \tag{3.21}$$

Finally, only the air temperature (T_a) is used for calculating the net long radiative heat transfer at a bottom surface, since the long-wave radiative heat transfer to or from the bottom surface is only affected by the underlying ground, water and/or other parts of the structure.

Chapter **IV**

The Effect of Temperature on the Thermal Expansion Coefficient of Concrete

Note: The content of the chapter is presented as submitted for publication in the Journal of Cold Regions Engineering. The format (headings, caption numbering, and citations) has been edited to match the thesis format.

4.1 Introduction

Concrete structures are subjected to various environmental processes (convection, solar radiation, and longwave radiation) that affect their internal temperature distribution. This change in concrete temperature can lead to a significant thermal load on the structure and invariably results in thermally induced length-change of the exposed members, which, if restrained, may cause significant distress. The effective coefficient of thermal expansion plays a pivotal role in elucidating the kinematic characteristics of the resultant strain state. This parameter is indispensable when assessing the compatibility between disparate materials, such as concrete and reinforcing steel, and when considering the implications of kinematic constraints. Additionally, it is needed in member analysis for forecasting the likelihood of cover cracking and delamination.

Bridge Codes specify a constant positive value for the thermal expansion coefficient, where the positive sign implies that contraction occurs upon cooling and expansion occurs upon heating (CSA 2014; AASHTO 2012). However, bridge Codes do not consider cases where bridges are located in cold regions and are subjected to sub-zero temperatures. In such cases, pore water freezing and the macroscopic effect this may have on the effective value of thermal expansion coefficient of concrete are prevalent phenomena that ought to be considered. This is because as water freezes, its volume expands by about 9%. Thus, as concrete capillary water freezes during cold events, a significant reduction or even a change in the sign (from positive to negative) of the effective thermal expansion coefficient of concrete is likely to occur (Planas et al. 1984; Xia et al. 2017). Tensile thermal strains and eventual cracking and delamination may occur in concrete depending on the magnitude of this expansion. Thus, determining a temperature-dependent value for the thermal expansion coefficient of concrete is critical to ensure a durable and serviceable structure, but it also essential in forensic investigations of deck cracking seen in bridges exposed to cold climates.

The coefficient of thermal expansion (CTE) represents the unit length change (expansion or contraction) that a material will experience in response to a change in temperature (Novikova 1984). The linear change in length (ΔL) of a solid material can be expressed as in Eq. (4.1):

$$\Delta L = \alpha_l\left(T_f - T_0\right) \cdot L_0 = \alpha_l(\Delta T)L_0 \tag{4.1}$$

where, α_l is the material linear coefficient of thermal expansion (CTE), T_f is the final temperature, T_0 is the initial temperature, ΔT is the change in temperature, and L_0 is the initial length at temperature T_0. Note that a change in temperature will affect all dimensions of a body if unrestrained. This means that in an unrestrained material volume, V_0, a change in temperature will lead to a change in volume (ΔV) that can be estimated as per Eq. (4.2).

$$\Delta V = \alpha_V(\Delta T)V_0 \tag{4.2}$$

In Eq. (4.2), parameter α_V represents the volumetric expansion coefficient. In the case of an isotropic material, α_V is approximately equal to $3\alpha_l$. If the material in question is anisotropic, then the magnitude of α_l is dependent on the axes of orthotropy (i.e., it will depend on the crystallographic direction along which it is measured (Novikova 1984)).

This chapter investigates through experiment the impact of freezing temperatures on the thermal expansion behavior of concrete in cold environments. The study encompassed tests on various concrete mix compositions and varying degrees of saturation. The test specimens underwent multiple freezing/thawing cycles, reaching temperatures as low as -40°C. This experimental approach was employed to collect data on the ensuing thermal strain, which subsequently served as the basis for constructing a hysteresis model to depict the temperature-dependent behavior of concrete's effective CTE (ECTE). To achieve this objective, four distinct concrete mixes were considered. Key parameters under investigation encompassed the water-cement (w/c) ratio within the concrete paste, aggregate size (for the same aggregate volume ratio), and the degree of saturation within the concrete material. The test specimens were subjected to cyclic thermal histories, spanning from ambient temperature down to $-40℃$.

Experimental investigation was also conducted to examine the effect that the number of freeze-thaw cycles has on residual strain. The enduring consequences of concrete's tendency to expand during cold wave events on the state and functionality of structural elements was evaluated next, using a finite element thermal structural model that incorporates the temperature-dependent behavior of the ECTE. This model was employed to subject a reinforced concrete beam to a cooling/thawing cycle, to examine the impact of variable ECTE on the kinematics of length change and its subsequent influence on structural performance.

4.2 Review of past experimental evidence

The interaction between sub-zero temperatures and the effective thermal expansion coefficient of saturated concrete has been investigated and reported in the literature (Rostasy et al. 1979; Planas et al. 1984; Miura 1989; Xia et al. 2017; Zhengwu et al. 2019). These investigations are mainly experimental studies where the length change (ΔL) normalized by the gauge length (L_0) is expressed as *thermal strain* and is reported as a function of temperature. By definition, the ECTE can then be calculated as the slope of the line connecting two consecutive points on the graph plotting the evolution of thermal strain versus temperature. Note that throughout this paper, the effect of temperature on ECTE will be studied in terms of the relationship of thermal strain versus temperature.

The effect of thermal cycles (cooling down to $-165℃$ followed by reversal to $20℃$) on the thermal deformation of concrete specimens has been investigated experimentally for both saturated and dry concrete (Planas et al. 1984). The results indicated that the cooling process can be divided into three phases. Phase 1 (from 20 to $-15℃$) involves a linear contraction of the concrete specimen with a constant and positive value of ECTE. Phase 2 (from -20 to $-60℃$) is a highly nonlinear expansion phase, where the expansion results from the phase transition of the water into ice in the capillary pores; this freezing process propagates gradually, with decreasing temperature, to the pores of smaller diameter. Finally, in the third phase, the material contracts again, with linear reversible strain, indicating a constant and positive ECTE with a magnitude like that of Phase 1. The findings are summarized in Figure 4.1. A comparable but opposite trajectory is observed during a gradual return to ambient temperature, which will be referred to as 'thawing' for the sake of brevity. Additionally, a residual strain can be recorded, as the concrete returned to normal ambient temperatures (above zero). This residual strain signifies permanent damage in the form of irreversible length increase. Similar findings were also reported in (Rostasy et al. 1979).

These findings also unveil three distinct temperature-related ranges of concrete behavior. The first range exhibits linear contraction within the temperature span of $25℃$ to $-25℃$. The second range, characterized by nonlinear expansion, encompasses temperatures from $-25℃$ to $-70℃$. Lastly, the third range, marked by linear contraction, extends from $-70℃$ to $-160℃$. These three stages were also observed in a third experiment which studied thermal strain development in saturated, cement-based materials under cryogenic temperatures (Zhengwu et al. 2019). The results of this experiment pointed out that as the number of cooling-thawing cycles increases, the incremental growth in residual strain decreases (Zhengwu et al. 2019). Meanwhile, the cumulative residual length change approaches a limit value, serving as a quantitative measure of frost damage in concrete. The experiment described in (Miura 1989) reinforces findings from (Rostasy et al. 1979; Zhengwu et al. 2019). It revealed that concrete experiences contraction as the temperature drops. This contraction eventually transitions to a net expansion phase between $-22℃$ and $-60℃$. Subsequently, there is a phase of linear contraction down to $-70℃$, with a contraction rate resembling that observed at ambient temperatures (similar to the case shown in Fig. 1). During the temperature reversal, the specimen expands linearly until it reaches approximately $-50℃$, but then undergoes a sudden contraction between $-50℃$and $-20℃$, followed by another expansion phase from $-20℃$ upward (Miura 1989).

4.3 Definition of the critical degree of saturation

The results summarized in the preceding section provide sufficient evidence for the qualitative description of the thermal behaviour of saturated concrete exposed to cooling and thawing cycles. The key findings can be summarized as follows: As temperature decreases below $0℃$, the water inside wet concrete begins to turn to ice. As the ice forms, the bulk CTE, or ECTE of the concrete is influenced by the CTE of ice. This process, which continues until all the pore water has frozen, is evidenced by the reversal in strain observed under monotonic temperature changes, as illustrated in Figure 4.1. Once this stage is reached and as the temperature continues to decrease, the concrete transitions back into a phase of linear contraction. During the thawing process, the concrete initially undergoes expansion before subsequently contracting, persisting until all the ice has completely melted. At this juncture, expansion resumes, returning to ambient temperature levels. Notably, a residual strain is observed at the conclusion of the cooling-heating cycle.

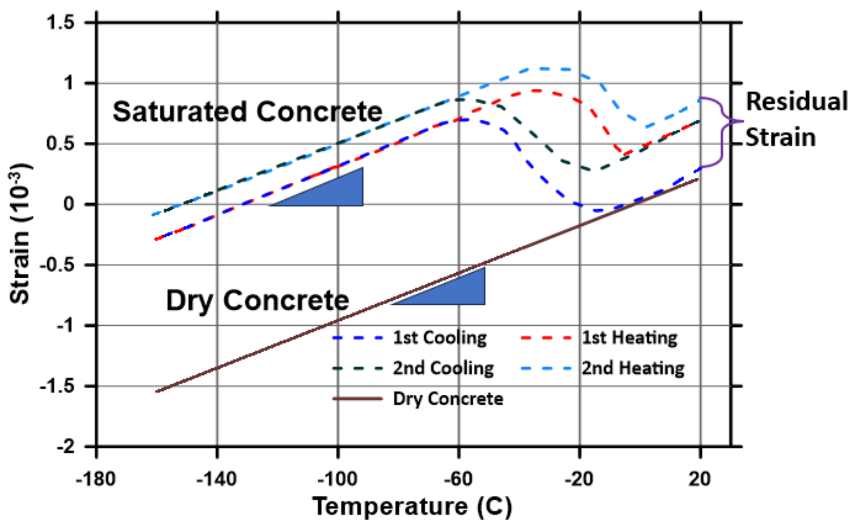

Figure 4.1: Temperature versus thermal strain results. Data obtained from (Planas et al. 1984).

It should be noted that the behavior described above is typical for the saturated concrete. However, the expansive tendency is attenuated or even eliminated if concrete is only partially saturated. The literature defines a critical degree of saturation, below which no expansion takes place during a freeze-thaw cycle (Ghantous et al. 2019). Several studies have attempted to determine the critical degree of saturation (CDS) and the consensus is that the value of CDS is in the range between $79 - 91\%$ (Fagerlund 1973; Fagerlund 1977a; Fagerlund 1977b). As shown in (Fagerlund 1973), the CDS is a function of the specific surface of the air-filled pores, where smaller air-filled pores result in a higher value of CDS. However, others found the CDS to be between $86 - 88\%$ for mortar regardless of the shape and size of the air pores (Li et al. 2012). Furthermore, it has been concluded that air entrainment significantly increased the amount of time required to reach critical saturation, but it did not affect its final value (Li et al. 2012). In a different study, it was determined that the CDS of concrete is about 88% (Obla et al.

2016). The results from this study also suggest that employing a lower water-to-cement (w/c) ratio can enhance performance during freeze-thaw cycles. This improvement arises from a decrease in capillary porosity, which subsequently lowers the amount of water absorbed by the concrete when subjected to saturation conditions. Thus, due to the reduced interconnectivity of the pore network, achieving critical saturation may take longer when using a lower w/c ratio. However, the w/c ratio does not affect the value of the critical degree of saturation itself. This conclusion was reinforced by the findings in (Ghantous and Weiss 2019) which reported that there was not a significant increase in CDS when the w/c ratio increases from 0.35 to 0.55.

Even within concrete exhibiting a degree of saturation surpassing the CDS limit, its performance can exhibit notable variations during cooling-thawing cycles. These variations hinge on multiple factors, including the pore size distribution, the volume of entrained air, internal water pressure and the presence of chemical charges (Powers and Helmuth 1953; Vuorinen 1970; Scherer and Valenza 2005; Siddiqui and Fowler 2014; Esmaeeli et al. 2017). The porosity and pore size distribution are the most important factors influencing the response of concrete to cooling at low temperatures. A concrete with a high capillary porosity will expand more due to its increased water content (Litvan 1976). Furthermore, the capillary pore size distribution will also have a significant effect on the behavior since water in smaller pores requires lower temperatures to freeze (Esmaeeli et al. 2017). The presence of air voids within concrete serves to alleviate hydraulic pressure, thereby potentially reducing macroscopic expansion and associated damage (Powers and Helmuth 1953). It has been reported that the effectiveness of air entrainment depends on the spacing between these air voids (Powers and Helmuth 1953). Furthermore, it was determined that as the degree of saturation of concrete increased, the resulting expansion under cooling also increased (Liu et al. 2020). The curing period has also been found to have a significant effect, with a decrease in thermal expansion under freezing observed as curing times increased. Additionally, thermal expansion under cooling also increased with increasing w/c ratio (Liu et al. 2020) whereas it has also been reported that the rate of cooling may also affect the behavior of concrete at subfreezing temperatures (Litvan 1976), where an increase in cooling rate can cause a significant increase in expansion.

When subjected to cooling, a variably saturated concrete specimen can exhibit three distinct response patterns, contingent on its microstructure and degree of saturation, as detailed below:

- **Type 1**: This response entails an initial contraction followed by significant expansion, which is subsequently succeeded by another contraction phase.
- **Type 2**: Similar to Type 1, but characterized by a relatively minor expansion phase, the extent of which depends on factors such as moisture content and pore size distribution.
- **Type 3**: In this response, the concrete consistently contracts in a linear fashion as the temperature decreases. This occurs when the degree of saturation falls below the corresponding CDS for the specific concrete material under consideration (Xia et al. 2017).

It is noted that expansion is manifested as permanent damage in the form of residual strain accumulation under temperature reversals and macroscopically, by cover delamination.

4.4 Materials and methods

The objectives of this research were achieved by subjecting four different mixes of concrete with varying degrees of saturation to consecutive cooling and thawing cycles. The mixes were differentiated based on their w/c ratio and the maximum aggregate diameter used as shown in Table 4.1. This table also provides the mix design details for each of these concrete mixes. In the study, three distinct water-to-cement (w/c) ratio values were investigated, specifically 0.34, 0.47, and 0.61 (A lower water to cement ratio translates into higher strength but leads to increased costs and lower workability). Additionally, the aggregate volume ratios were set at 60%, 65%, and 68% respectively, with a maximum coarse aggregate size of 19 mm. To establish the impact of aggerate size, mix $SA_{0.47}$ with w/c ratio of 0.47 and a maximum aggregate diameter of $10\ mm$ was also examined.

Table 4.1: Properties of concrete mixes tested.

Mix.	**Cement** $(\boldsymbol{kg/m^3})$	**Fine aggregate** $(\boldsymbol{kg/m^3})$	**Coarse aggregate** $(\boldsymbol{kg/m^3})$	**Water** $(\boldsymbol{kg/m^3})$	$\boldsymbol{W/C}$	**Max C.A. diameter¶**$(\boldsymbol{mm})$	**Slump** $(\boldsymbol{mm})$	**Aggregate Ratio** $(\%)$
$\boldsymbol{S_{0.61}}$	336	822	992	205	0.61	19	150	68
$\boldsymbol{C_{0.47}}$	437	740	992	205	0.47	19	170	65
$\boldsymbol{A_{0.34}}$	603	602	992	205	0.34	19	120	60
$\boldsymbol{SA_{0.47}}$	485	885	736	228	0.47	10	120	61

Each mix was cast in a single batch, with a total of thirty $100\ mm \times 200\ mm$ cylinders cast for each mix. To quantify the effect of the degree of saturation, six different target saturation values were examined: $100, 90, 85, 80, 70,$ and 0% as shown in Table 4.2. These cylinders were then subjected to two cooling/thawing cycles. Furthermore, two saturated cylinders from each mix were subjected to ten cooling-thawing cycles.

The specimen identification code comprises several elements. It begins with the first letter, denoting the concrete mix used, such as $A_{0.34}$, $C_{0.47}$, $S_{0.61}$, and $SA_{0.47}$. It also includes the degree of saturation in percentage and the specific specimen number within each group. It's important to note that three identical specimens were tested for each parameter combination. For instance, consider the case of $S_{0.61}80(2)$, which represents the second specimen (out of the triplicates) from mix $S_{0.61}$ (with a w/c ratio of 0.61) tested at a saturation level of $X = 80\%$. The cylinders used in test number eight have the same identification code but with the addition of the number of cycles. For example, a cylinder from mix $S_{0.61}$ subjected to ten cycles was denoted as $S_{0.61}100(1) - 10$. During the concrete's fresh state, three cylinders from each mix were equipped with thermometers along their centerline, serving as temperature controls (as depicted in Figure 4.2a). All specimens were demolded 24 hours after casting.

The samples from the different mixes were conditioned to reach the required degree of saturation and were then instrumented in preparation for testing. The testing involved subjecting the samples to cycles of cooling and thawing and recording the resulting thermal strain. The full procedure is described in the sections that follow.

Table 4.2: Degree of saturation and number of cycles investigated in each test.

Test No.	1	2	3	4	5	6	7	8
Degree of saturation X (%)	100	100	90	85	80	70	0	100
No. of Cycles	2	2	2	2	2	2	2	10

4.4.1 Conditioning of the specimen's degree of saturation

After demoulding, all cylinders were placed in a water bath for curing and were weighed daily. The cylinders were considered to be saturated once the weight difference between two consecutive measurements was less than 0.5%. At that stage, three saturated cylinders from each mix were placed in an oven at a temperature of $50°C$ and weighed on daily basis until fully dry (i.e., until no further change in their weight could be recorded). The temperature of $50°C$ was used as it has been shown that heating at higher temperatures may cause irreversible damage or cracking in the hardened cement matrix (Safiuddin and Hearn 2005). Subsequently, the capillary porosity of each mix was assessed, enabling the estimation of the water mass needed in cylinders of each mix at various saturation levels.

Detailed information on both porosity and compressive strength for each mix are given in Appendix A. Saturated cylinders were then heated in an oven at $50°C$ for different time periods and weighed on an hourly basis until the required degree of partial saturation was achieved. Once at the required degrees of saturation, the cylinders were wrapped in aluminum foil and placed in a tight plastic container before being returned to the oven set at a temperature of $50°C$. This step was done to ensure homogenization of the moisture content in the cylinders by eliminating any moisture gradients that develop during the drying process (Parrott 1994; Andrade et al. 1997). According to (Parrott 1994), the duration of this moisture redistribution step should be at least equal to the duration of the drying step. In this study, the duration of the redistribution step was taken to be equal to 1.3 times the drying time required. Furthermore, preheating the samples also helps improve the consistency of the ECTE test results (Siddiqui and Fowler 2017). Note that the cylinders were weighed before and after redistribution to ensure that no moisture was lost during this step. The average drying curves for the different mixes at $50°C$ for 360 hours are shown in Appendix B.

4.4.2 Instrumentation of the specimens

Once the step of moisture redistribution was considered complete, the cylinders were instrumented with four DEMEC points (pre-drilled stainless-steel discs (Figure 4.2b) on diametrically opposing sides at a $100\ mm$ distance between points as shown in Figure 4.2c. A strong glue (temp range $-50°C$ to $100°C$) was used to attach the DEMEC points to the cylinders. A DEMEC strain gauge (Figure 4.2d) was used to measure the distance between each pair of points; (initially, the gauge was set to zero for a $100\ mm$ distance). The DEMEC gauge consists of a digital dial gauge attached to an Invar bar. A fixed conical point is mounted at one end of the bar, and a moving conical point is mounted on a knife edge pivot at the opposite end. The pivoting movement of this second conical point was measured by the dial gauge. Each time a reading was to be taken, the conical points of the gauge were inserted into the holes in the discs (DEMEC points) and the reading on the dial gauge was noted. In this way, strain changes in the structure were converted into a change in the reading on the dial gauge. The cylinders were sealed with wrap to ensure minimal water loss during the testing process.

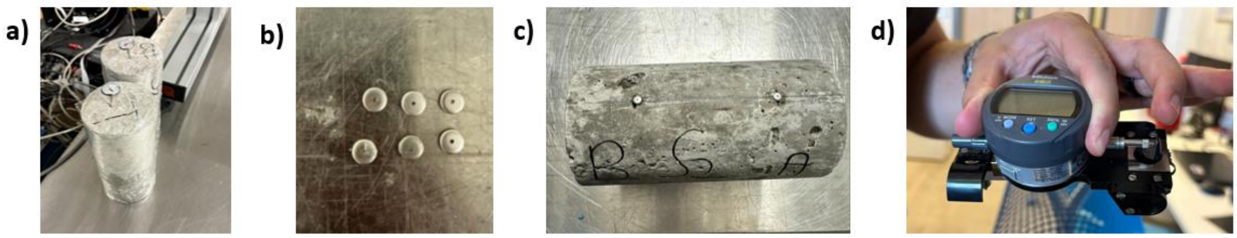

Figure 4.2: a) Cylinder instrumented with thermometers, b) Demec Points, c) Cylinder instrumented with Demec Points, and d) Demec Strain Gauge.

4.4.3 Testing setup

After instrumentation, all cylinders were subjected to a regime comprising of cooling-heating cycles that ranged from temperatures of $-40℃$ to $20℃$. To attain low temperatures, a specialized heating-cooling apparatus was constructed. This apparatus consisted of an insulated chamber equipped with a temperature control system that could introduce either cold or hot air for each cycle. A freezer served as the insulated chamber with the open top of the freezer covered with two layers of polyisocyanurate insulated sheathing. A Thermostream system (serving as the temperature forcing system) was connected to the chamber through an opening in the sheathing which served as the inlet. Thermostream systems are portable systems that deliver clean dry air for precision temperature testing. These fast, precise temperature forcing systems are used to provide effective testing and conditioning of electronic components, materials, and modules. Figure 4.3 shows the Thermostream system as well as the setup of the cooling chamber.

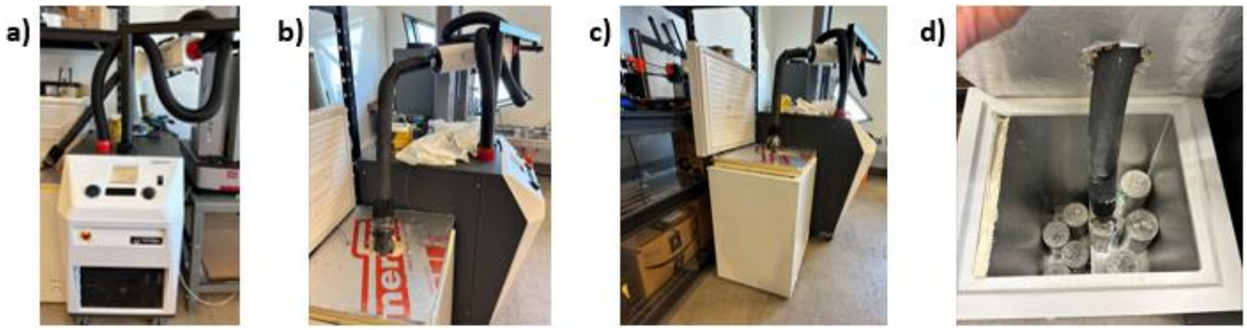

Figure 4.3: a) Thermostream system, b) Connection between Thermostream system and freezer, c) Freezer with polyisocyanurate insulated sheathing, d) Interior of freezer.

4.4.4 Testing protocol

The testing of cylinders was conducted in batches, with each batch comprising three distinct cylinders from each mix, alongside a reference cylinder equipped with a thermometer from each mix. The difference between the various tests of samples from one mix design was in the degree of saturation of the cylinders and the number of thermal cycles applied, as per Table 4.2. Note that the 100% saturation degree test was performed twice. While the tests were being conducted, the Thermostream provided a constant flow of air at $-90^{\circ}\mathrm{C}$ for cooling and $120^{\circ}\mathrm{C}$ for heating at a constant rate of 18 Standard Cubic Feet per Minute. The strain in the cylinders was measured at 15-minute intervals and the temperature in the temperature control specimens was also recorded. Once either the temperature in the cylinders reached $-40^{\circ}\mathrm{C}$ or a cooling time of 180 minutes was achieved (the time limit is introduced to ensure that temperatures did not go below $-40^{\circ}\mathrm{C}$ since the thermometers malfunction at temperatures below that limit), heating commenced until the temperature in the cylinders would rise to $20^{\circ}\mathrm{C}$. This process was then repeated for a total of either two cycles (Tests 1-7) or ten cycles (Test 8). Figure 4.4 shows the development of temperature in the cylinders versus time for two of the tests (number 5 and 7, see Table 4.2). Note that the temperature shown is the average of the three temperature-control cylinders. The average cooling rate for all experiments was about $0.3^{\circ}\mathrm{C}/min$ while the heating rate was about $0.6^{\circ}\mathrm{C}/min$.

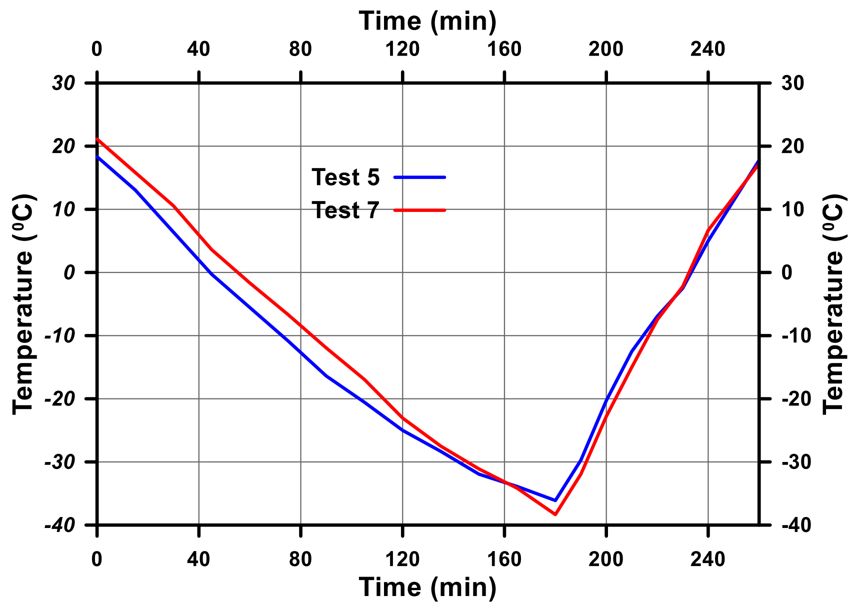

Figure 4.4: Cylinder temperature development with time for tests 5 and 7.

4.5 Results and discussion

As mentioned in the preceding section, the thermal strain was measured during the cooling-thawing process at 15-minute intervals. The thermal strain versus temperature relationship is a function of several factors which include w/c ratio (which affects the capillary porosity of the paste), paste volume in the mix, degree of saturation, and water distribution in pores. Hence, it is anticipated that there will be distinct variations in behavior among the different concrete mixes. Furthermore, the results from cylinders of the same mix (i.e., the triplicates) were found to be mostly reproducible with minor difference attributed mainly to variations in pore structure and water distribution. Figures 4.5 and 4.6 present the behavior of samples from each concrete mix, with the plotted samples serving as representatives for each mix at various saturation levels denoted as X.

The different mixes exhibited a similar behavior when their degrees of saturation fell below 70% or remained within the range of 70% to 80% (Figure 4.5). This behavior was characterized by a linear correlation between temperature and thermal strain, with minimal residual strain. Therefore, it can be concluded that, for less than 80% saturation, the effective thermal expansion coefficient of concrete was not affected by the freezing of water in the capillary pores and the material exhibited a behavior similar to that of the dry concrete. These findings align with prior experiments documented in the literature, which have consistently suggested that the critical saturation degree typically exceeds 80% (Fagerlund 1973; Fagerlund 1977a; Fagerlund 1977b; Li et al. 2012; Obla et al. 2016; Ghantous et al. 2019; Ghantous and Weiss 2019).

For degrees of saturation higher than the CDS, mix design had a strong influence on the thermal response of concrete. Samples of mix $A_{0.34}$ (low water to cement ratio) with a degree of saturation ranging from 80 to 100% exhibited a linear relationship between strain and temperature. On the other hand, a non-linear relationship is observed for the remaining mixes ($C_{0.47}$, $S_{0.61}$, and $SA_{0.47}$) highlighting the effect of water freezing on the resulting thermal strain. In the case of these mixes, it was noted that expansion commenced at temperatures ranging from -8°C to -25°C and persisted down to the lowest temperature reached in this study, which was -40°C. When the temperature reversed, the cylinders began expanding again within the temperature range of -20°C to -15°C. Subsequently, they underwent contraction until reaching a temperature of -5°C, which was followed by a linear expansion as the temperature gradually rose back to ambient levels.

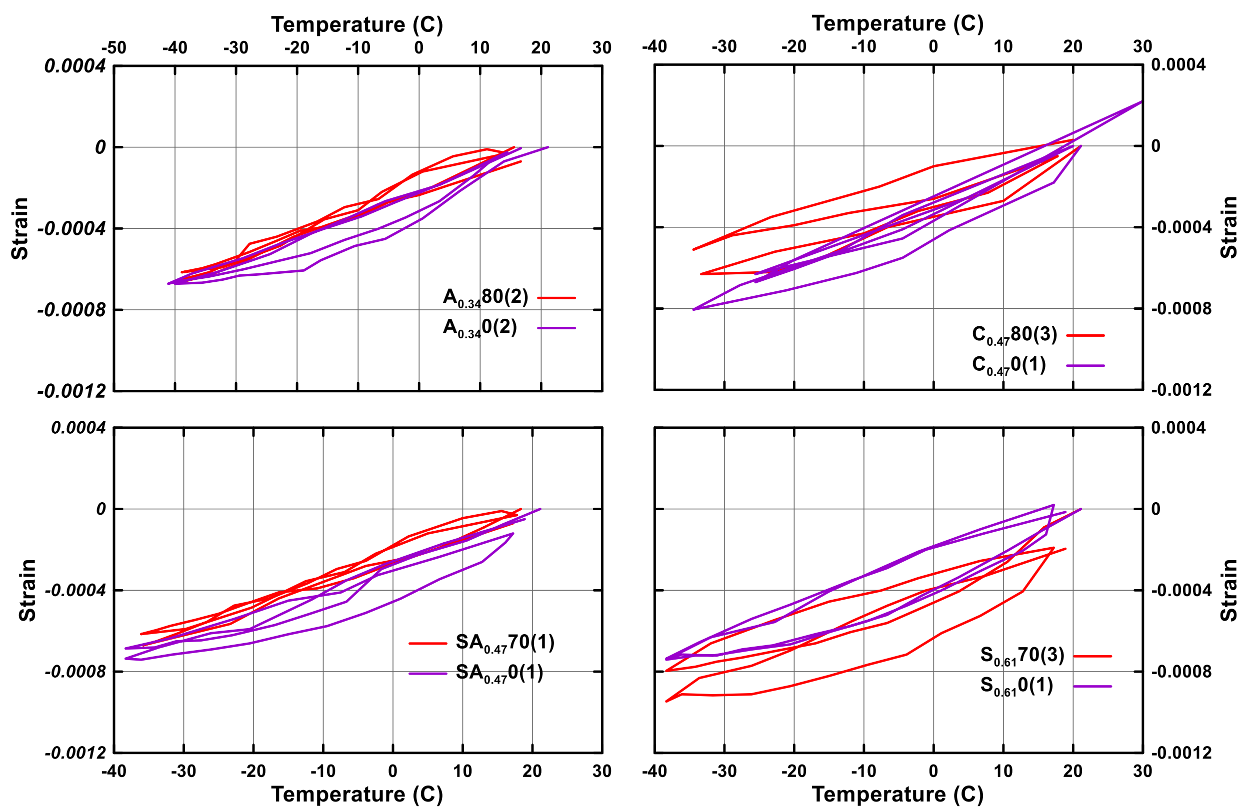

Figure 4.5: Thermal strain versus temperature for samples with degrees of saturation less than or equal to 80% from different concrete mixes. Red represents saturation between 70% and 80%, and purple line represents saturation degrees less than 70%.

It is noteworthy that the extent of expansion during the cooling stages exhibited a marked discrepancy among the three mixes ($C_{0.47}$, $S_{0.61}$, and $SA_{0.47}$) for the same degree of saturation. For instance, when observing Sample $S_{0.61}100(1)$ it became evident that it underwent strains of $0.001\ mm/mm$ and $0.0021\ mm/mm$ at the conclusion of the initial and subsequent cooling phases, respectively. In contrast, the strain experienced by Sample $C_{0.47}100(1)$ was notably lower, measuring at $0.00015\ mm/mm$ and $0.0008\ mm/mm$ following the first and second cooling stages. This stark contrast underscores the substantial impact of the water-to-cement (w/c) ratio on the degree of expansion, as evidenced by the significantly greater expansion observed in mix $S_{0.61}$, which boasted a higher w/c ratio. Furthermore, it was observed that the expansion that occurred in the saturated samples was larger than the expansion that occurred in the samples with a degree of saturation ranging from $80-90\%$.

Moreover, it was also evident that the strains recorded at the conclusion of the cooling stages in Sample $SA_{0.47}100(3)$ were notably less when compared to the corresponding strains in Sample $C_{0.47}100(1)$, despite both mixes sharing the same w/c ratio. Specifically, the strains for Sample $SA_{0.47}100(3)$ were $-0.0001\ mm/mm$ and $0.0002\ mm/mm$ after the first and second cooling stages, respectively (as opposed to $0.00015\ mm/mm$ and $0.0008\ mm/mm$ for sample $C_{0.47}100(1)$ respectively). Note that the primary distinction between these two mixes lies in the size of the aggregates employed: Mix $SA_{0.47}$utilized a maximum aggregate size of $10\ mm$, whereas Mix $C_{0.47}$ employed a larger $19\ mm$ maximum aggregate size. This choice of smaller aggregates in Mix $SA_{0.47}$ resulted in superior compaction, subsequently leading to reduced porosity and a smaller pore size, consistent with results from past research (Fu et al. 2014).

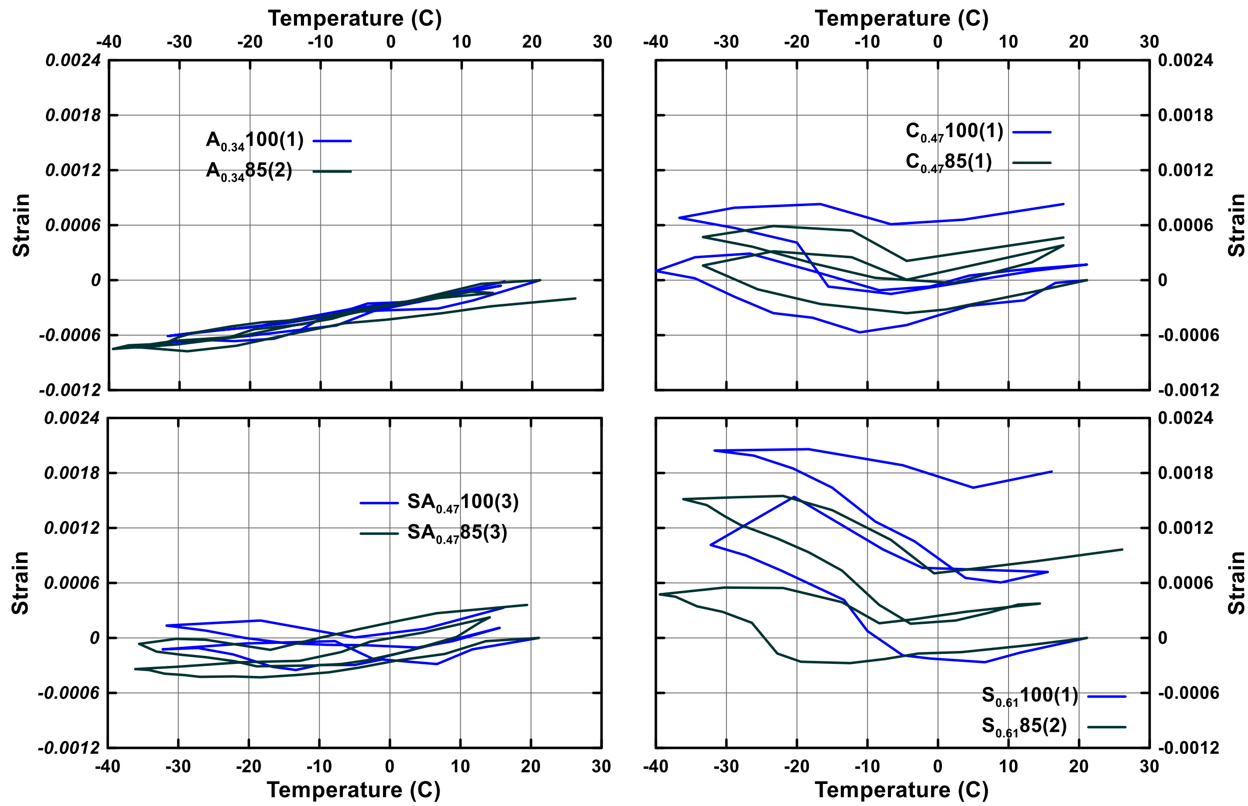

Figure 4.6: Thermal strain versus temperature for samples with degrees of saturation larger than 80% from different concrete mixes. Blue represents 100% saturation; green represents saturation between 80 and 90%.

4.6 Analytical interpretation of the experimental evidence

The different behaviors exhibited by samples of different mixes can be further examined through the calculation of the overall thermal expansion coefficient of the saturated cylinders during the first cooling stage. The overall expansion coefficient ($\alpha_{cooling}$) is calculated as per Eq. (4.3).

$$\alpha_{cooling} = \frac{\varepsilon_2 - \varepsilon_1}{T_2 - T_1} \tag{4.3}$$

where, ε_1 and ε_2 are the thermal strains, and T_1 and T_2 are the temperatures at the start and end of the cooling stages respectively. The average value, $\alpha_{cooling}$ for the saturated cylinders of mixes $C_{0.47}$ and $S_{0.61}$ was found to be $-2.5 \times 10^{-6} \frac{mm}{mm°C}$ and $-1.2 \times 10^{-5} \frac{mm}{mm°C}$ (the negative values imply that the concrete expanded during cooling). It is noted that the Mix $S_{0.61}$ had a higher expansion coefficient than mix $C_{0.47}$ as it expanded more, as shown in Figure 4.5. Furthermore, the average value of $\alpha_{cooling}$ for the saturated cylinders of mix $SA_{0.47}$ was found to be $4.24 \times 10^{-6} \frac{mm}{mm°C}$ which implies that the cylinders contracted under cooling as opposed to cylinders of mix $C_{0.47}$

and $S_{0.61}$. Despite the fact that the $SA_{0.47}$ cylinders developed a positive value for $\alpha_{cooling}$, the value was still lower than the value of $\alpha_{cooling}$ of the dry cylinder (found to be $12 \times 10^{-6} \frac{mm}{mm°C}$) which implies that expansion resulting from ice formation did occur but was not large enough to cause a reversal of sign. On the other hand, $\alpha_{cooling}$ for the saturated cylinders of mix $A_{0.34}$ was found to be $11.8 \times 10^{-6} \frac{mm}{mm°C}$ which is approximately equal to $\alpha_{cooling}$ of a dry cylinder. This indicates that no expansion had taken place during the cooling cycle and the freezing of ice had no effect on the behavior of this particular concrete mix. It can therefore be concluded that no expansion could take place, most likely owing to the small size of pores that prevented the freezing of water. This theory is further supported when considering the relationship between pore size and the freezing temperature of water, shown in Figure 4.7. This relationship is based on the desorption isotherm and is a combination of the Kelvin-Young-Laplace and the Gibbs-Thomson equation as per (Esmaeeli et al. 2017).

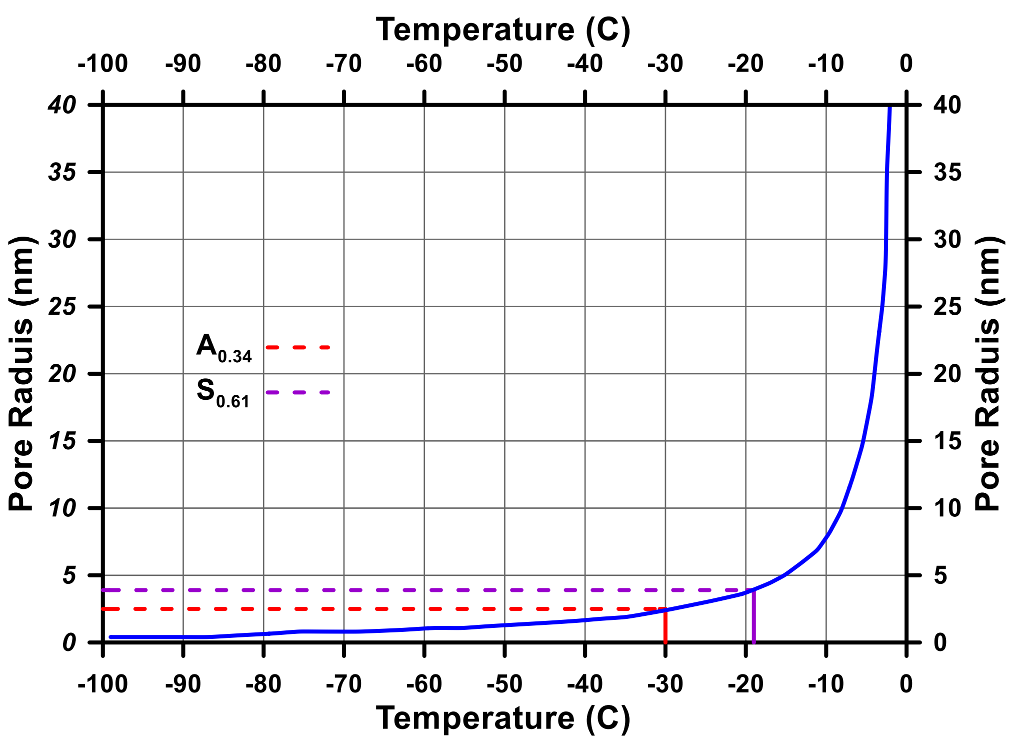

Figure 4.7: The effect of average pore size on the freezing temperature of water (Esmaeeli et al. 2017).

Based on Figure 4.7, the water freezing temperature decreases significantly with decreasing pore size. This might explain why saturated cylinders with different water-to-cement ratios behaved differently since the pore size increases with an increase in the water cement ratio. As per (Pantazopoulou and Mills 1995), the value of hydraulic mean radius r_0, which represents the mean radius of capillary pores of cylindrical shape in the paste, can be expressed as a function of the water cement ratio (w/c) as $r_o = 4.11 \times 10^{-9}\, w/c$ (in m). Therefore, the estimated value of the hydraulic mean radius for mix $A_{0.34}$ is $r_{0,A} = 1.233\, nm$ while the equivalent value for mix $S_{0.61}$ is twice as much, i.e., $r_{o,S} = 2.5\, nm$. Figure 4.8 shows the distribution of pores in mix $A_{0.34}$ and mix $S_{0.61}$ assuming a normal distribution (Xia et al. 2017). It is assumed, for the purpose of this demonstration, that the expansion will become noticeable when more than 10% of the water freezes. Referring to the distribution presented in Figure 4.8, it is observed that in mix $A_{0.34}$, approximately 10% of the pores exhibit a radius less than $2.5\, nm$, whereas in mix $S_{0.61}$, approximately 10% of the pores have a radius smaller than $3.9\, nm$. The freezing temperatures for water in $2.5\, nm$ and $3.9\, nm$ pores can be determined from Figure 4.7 to be about -30°C and -18°C respectively. These values agree with the observed experimental values as expansion started in cylinders of mix $S_{0.61}$ at an average value of about -12°C while expansion was not observed in cylinders of mix $A_{0.34}$ even at an average minimum temperature of -38°C. Therefore, it can be concluded that water did not freeze in the cylinders of mix $A_{0.34}$ due to increased pressure that results from a smaller pore size. It should be noted that there is some discrepancy between the calculated and observed temperatures which can be attributed to the fact that the calculated mean radius as well as the relationship between pore radius and temperature presented in Figure 4.7 are based on empirical relationships while the pore size distribution has been assumed to be normal. Furthermore, Mix $C_{0.47}$ had a water-cement ratio of 0.47 which implies that the minimum temperature required for expansion was only slightly higher than that of mix $S_{0.61}$ (around -21°C). Experimental evidence indicated that expansion was recorded for mix $C_{0.47}$ at a temperature of -16°C . Similarly, expansion started in cylinders of mix $SA_{0.47}$ (same water cement ratio as $C_{0.47}$) at a temperature of -18°C. Nevertheless, it was noted that the extent of expansion observed was considerably smaller than the values documented for mixes $C_{0.47}$ and $S_{0.61}$. As previously mentioned, this difference can likely be attributed to the improved compaction, resulting in lower porosity, and development of smaller pore radii as result of smaller aggerate size.

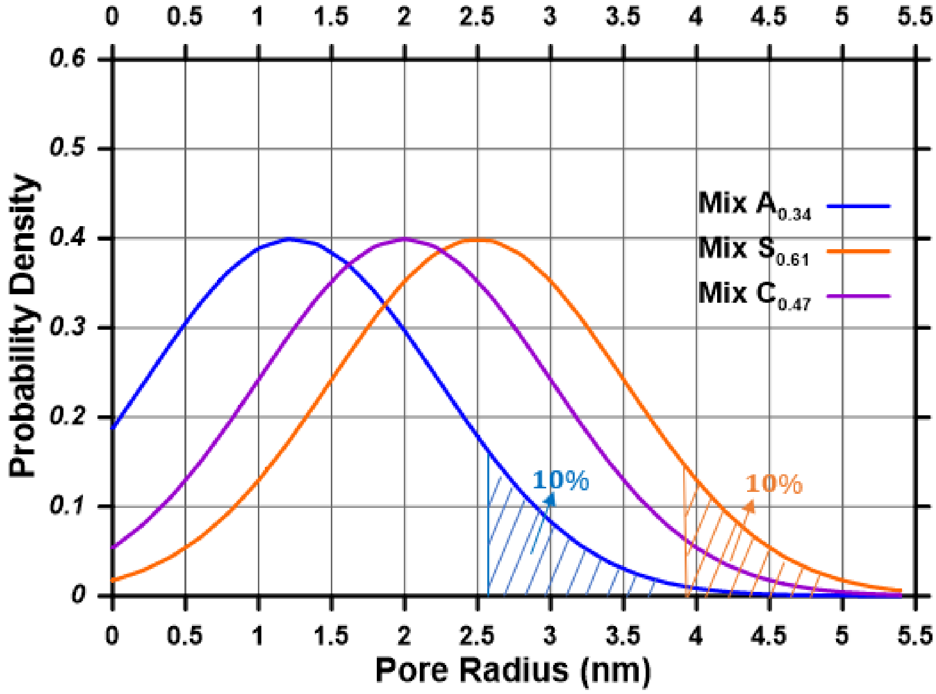

Figure 4.8: The distribution of pores in mixes $A_{0.34}$, $C_{0.47}$, and $S_{0.61}$.

4.7 Residual strain development

Figure 4.9 shows the average residual strain for all samples after one and two cycles for the different mixes at different degrees of saturation. Samples of mix $A_{0.34}$ showed a negligible amount of residual strain after two cycles for all degrees of saturation. In contrast, samples of mix $S_{0.61}$ displayed a notable amount of residual strain, measuring $0.00047\ mm/mm$ after one cycle and increasing to $0.001\ mm/mm$ after two cycles under conditions of 100% degree of saturation. For degrees of saturation between 80% and 90%, the $S_{0.61}$ samples continued to display a notable amount of residual strain, measuring $0.0003\ mm/mm$ and $0.0007\ mm/mm$, although these values were lower compared to the strains observed at 100% saturation.

Minimal residual strains were observed for samples of $S_{0.61}$ with a degree of saturation less than 80%. Samples $C_{0.47}$ behaved in a similar manner to samples $S_{0.61}$ at a 100% saturation and at saturation degree less than 80%. The primary distinction between samples $C_{0.47}$ and $S_{0.61}$ became apparent at degrees of saturation between 80% and 90%. In this range, samples $C_{0.47}$ displayed comparatively lower levels of residual strain, measuring $0.00015\ mm/mm$ and $0.00025\ mm/mm$ after one and two cycles, respectively, for saturation levels between 80% and 90%. Finally, samples $SA_{0.47}$ exhibited an intermediate behavior between those of samples $A_{0.34}$ and $S_{0.61}$ where no residual strain was observed at saturation degrees less than 80% and a strain of about $0.00015\ mm/mm$ was recorded after two cycles for saturation levels above 80%. These results indicate that the amount of residual strain is linked to the amount of expansion observed during the cooling stage, i.e., samples that expanded significantly showed high amounts of residual strains while samples with little or no expansion showed limited residual strain.

4.8 Effect of number of cycles on residual strain

Subsequently, the impact of more than two cycles on the residual strain for each mix was examined to ascertain whether the magnitude of residual strain reached a converging maximum value (Test 8). Therefore, additional experiments were conducted, where two samples from each of the mixes $A_{0.34}$, $S_{0.61}$, and $SA_{0.47}$ were subjected to ten heating cooling cycles from 20 to -40℃ with the strain measured at the end of each cycle. The samples under investigation were saturated at the start of the experiment and were weighed after 6 cycles and after ten cycles to ensure that moisture loss between the cycles was not significant. The results of the experiment are illustrated in Figure 4.10.

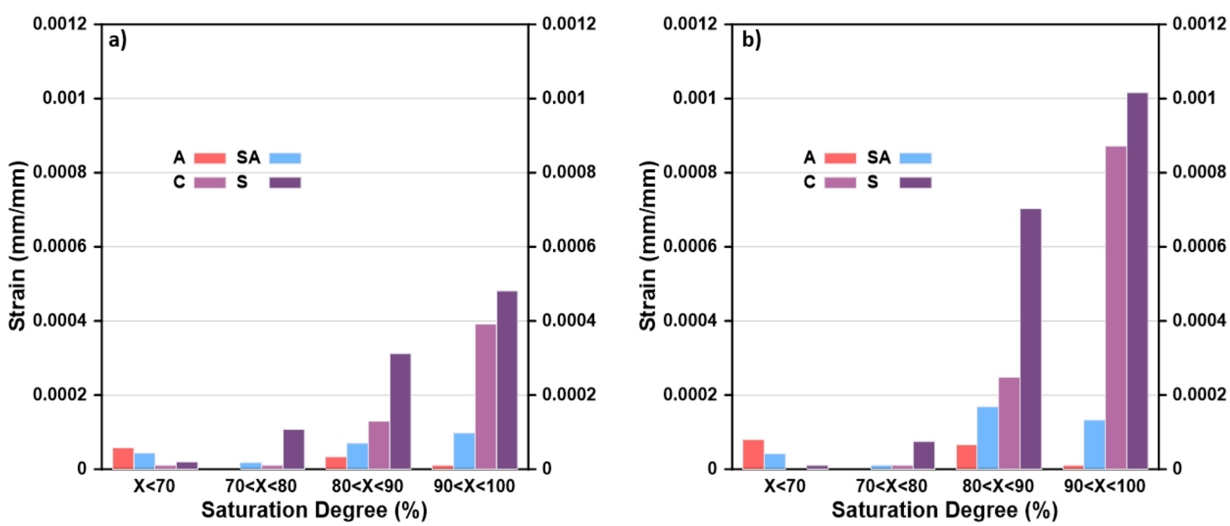

Figure 4.9: Average residual strain at a) the end of one cycle and b) at the end of two cycles for all mixes and degree of saturations.

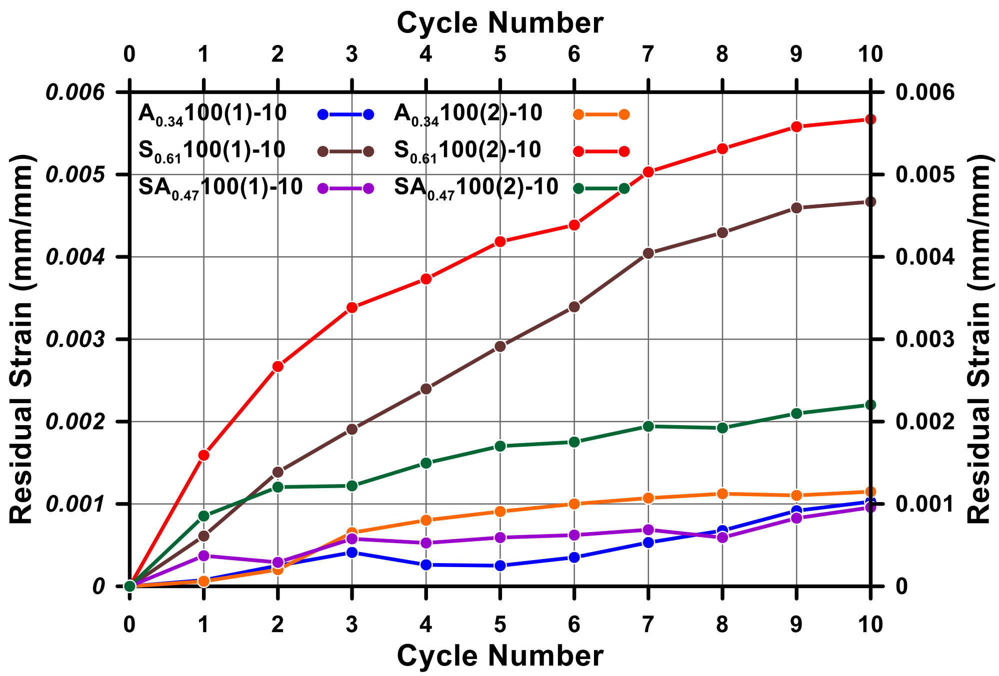

Figure 4.10: Residual strain after ten cycles for mixes A, S, and SA at 100% saturation.

The findings suggest that residual strain consistently shows an increasing trend as the number of cycles increased across all mixtures. Nevertheless, the rate of residual strain accumulation decreased with each additional cycle, gradually approaching an asymptotic limit value. For mix $A_{0.34}$, the increments in residual strain remained relatively constant, hovering around $0.0001\, mm/mm$ between cycles. Note that this level of tensile strain is comparable in magnitude to the tensile cracking strain of concrete. This behavior aligns with the results observed in mix $A_{0.34}$ during tests involving two thermal cycles. In the case of mix $SA_{0.47}$, the increments in residual strain decreased notably after seven cycles. However, the residual strain observed after ten cycles was higher than that recorded in mix $A_{0.34}$, measuring $0.0022\, mm/mm$ for sample $SA_{0.47}100(1) - 8$. Conversely, samples from mix $S_{0.61}$ exhibited the most pronounced and gradual increase in residual strain, with the total strain reaching an average value of $0.005\, mm/mm$ after ten cycles. This is a significant amount of strain and corresponds to a state of delamination. Furthermore, the residual strain increment started to decrease after about seven cycles. The results highlight a robust correlation between the water-cement ratio and the resultant residual strain, with an elevated water-cement ratio resulting in higher strain increments per cycle. This phenomenon can be attributed to the fact that an increase in the water-to-cement ratio led to a greater expansion response under freezing temperatures.

4.9 Implications of the effect of freezing on thermal strain

To assess the potential structural repercussions of this expansive tendency in saturated concrete under freezing conditions, a case study was undertaken. In this study, a reinforced concrete beam was exposed to freeze/thaw conditions using a thermal structural 3D finite element model developed within the ANSYS finite element platform (ANSYS 2019). The model has been validated and verified as documented in (Saad et al. 2022) and (Saad et al. 2023). The beam under investigation has a rectangular cross section, $1\ m$ in height and $0.4\ m$ wide, spanning a length of $10\ m$. It was represented in the model as a simply supported beam and included two layers of longitudinal reinforcement comprising $32\ mm$ bars spaced at $100\ mm$ intervals, and $10\ mm$ diameter stirrups spaced at $300\ mm$. The thermal model was employed to expose the top surface of the beam to a cooling-thawing cycle, ranging from $20℃$ to $-40℃$. Initially, the beam's temperature was assumed to be uniform at $20℃$, after which the top surface temperature was lowered to $-40℃$ and subsequently raised back to $20℃$.

The temperature time history within the beam was obtained from the output of the thermal model and then used as a boundary condition in the structural model to determine the impact on the structural performance. Three different cases were considered in the structural simulations. The first case was that of a concrete with a constant thermal expansion coefficient of $12 \times 10^{-6}\ mm/mm℃$, which corresponds to a "dry" material (i.e., a concrete with less than 70% saturation). The second and third cases were concretes that have the thermal behaviors of samples $S_{0.61}100(1)$ and $S_{0.61}85(2)$ i.e., a water cement ratio of 0.61 and saturation degree of $X = 100\%$ and $80\% < X < 90\%$ respectively. Figures 4.11 and 4.12 show the maximum and minimum longitudinal strain observed in the cross section for the three cases respectively. Furthermore, positive values represent tension while negative values represent compression i.e., Figure 411 and Figure 4.12 illustrate the development of the maximum tensile and compressive strains within the cross section respectively.

Figure 4.11 indicates that a significant difference in behavior occurs between the three cases. It can be observed that for a constant ECTE (Figure 4.11a), the maximum tensile strain (on average $0.0001\ mm/mm$) occured at the bottom of the cross section while the top of the cross section is under compression and does not experience any tension. Meanwhile, the interior of the cross-section experienced tensile strains of about $6 \times 10^{-5}\ mm/mm$. On the other hand, for the case of the concrete representative of sample $S_{0.61}85(2)$, limited tension (2×10^{-5} mm/mm) occured at the bottom of the cross section while the top and interior of the cross section experiences an increased tension of about 6×10^{-5} mm/mm. The results for the concrete based on sample S9 also indicated limited tensile strain (about 2×10^{-5} mm/mm) at the bottom of the cross section and a significant tensile strain of 0.0001 mm/mm at the top of the cross section.

When considering the minimum strains, it can be observed that for a constant ECTE (Figure 4.12a), the bottom of the cross section experienced no compressive strain while the top experienced a compressive strain of about 2×10^{-5} mm/mm. Figure 4.12b (Sample $S_{0.61}85(2)$) indicates an increase in compressive strains throughout the cross section with top and bottom strains reaching 3×10^{-5} and 9×10^{-5} mm/mm respectively. The results from the simulation for concrete based on sample $S_{0.61}100(1)$ showed an overall similar trend but with larger magnitude. The compressive strain in this cross-section ranged from 5×10^{-5} mm/mm at the top to 0.0002 mm/mm at the bottom.

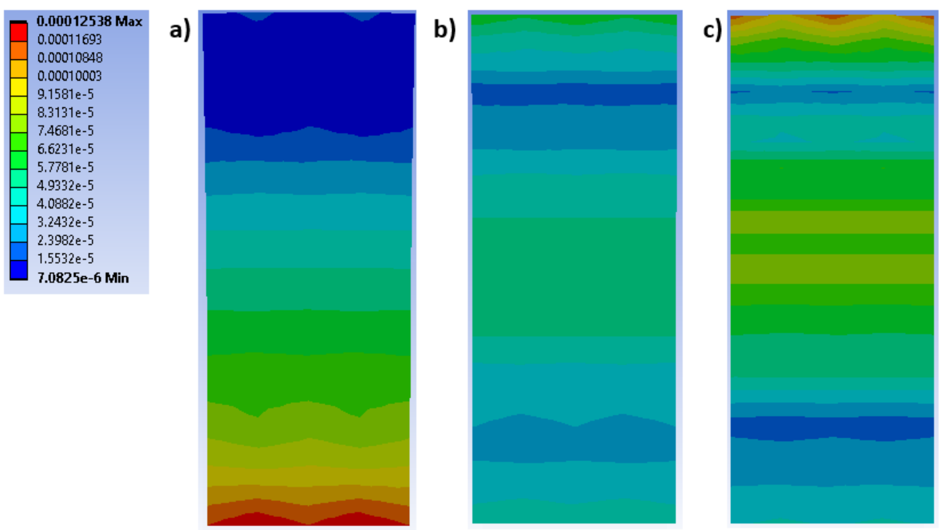

Figure 4.11: Maximum longitudinal strain in the cross section at the middle of the span. a) Concrete with constant ECTE, b) Concrete based on sample $S_{0.61}85(2)$, and c) Concrete based on sample $S_{0.61}100(1)$.

Similar variations in behavior are observed when considering lateral and vertical strains (shown in Appendix C). In summary, it was concluded that both the magnitude and distribution of strains may vary depending on the relationship between thermal strain and temperature. Locations that are subjected to tension in one case may experience compression in another. Furthermore, compressive strains were found to be significantly larger in simulations which incorporate the effect of temperature on the ECTE. The maximum tensile strains observed in the three simulations are similar in magnitude but vary highly in their location within the cross section. This can have significant implications on structural design, particularly on the layout of structural reinforcement but also in interpretation of cracking and delaminations reported in forensic investigations. Therefore, it is essential that the dependence of the thermal expansion coefficient on the temperature be considered both in design and assessment of structures. It was also noted that the largest variation occurs between the simulations based on saturated and dry samples while the simulation based on the partially saturated specimen shows an intermediate behavior.

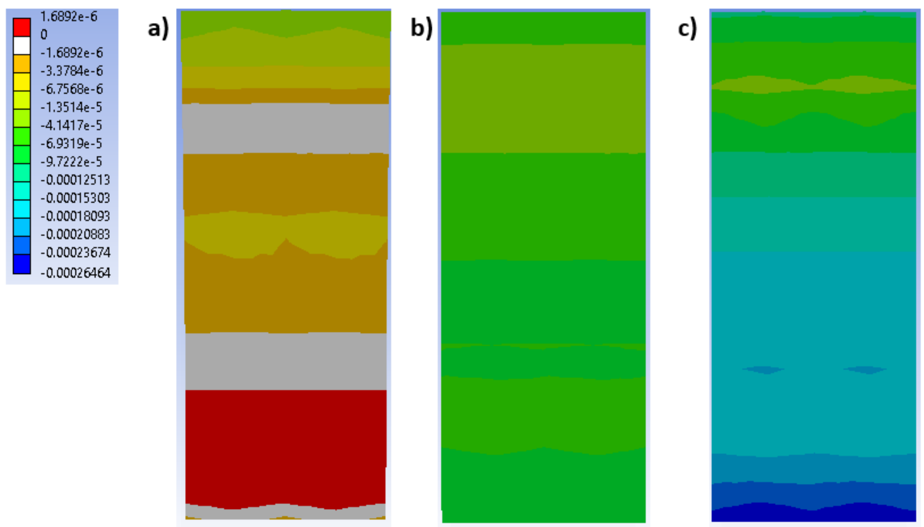

Figure 4.12: Minimum longitudinal strain in the cross section at the middle of the span. a) Concrete with constant ECTE, b) Concrete based on sample $S_{0.61}85(2)$, and c) Concrete based on sample $S_{0.61}100(1)$.

4.10 Conclusions

In summary, the purpose of this experimental and numerical study was to investigate the effect of freezing temperatures on the development of thermal strains in concrete at different degrees of saturation. Four distinct concrete mixes, featuring various water-to-cement ratios and aggregate sizes, underwent two cooling-heating cycles within a temperature range spanning from 20°C to -40°C. Different saturation levels were applied to each of the mixes, including $90\% \leq X < 100\%, 80\% \leq X < 90\%, 70\% \leq X < 80\%,$ and $X < 70\%$. Additionally, a series of saturated cylinders were subjected to ten consecutive cycles to investigate the accumulation of resulting strains. The following conclusions were drawn from this research effort.

- A critical degree of saturation exists below which no expansion under freezing conditions occurs for any of the concrete mixes. That value was found to be in the range $X < 80$, which is consistent with the previous experimental studies reported in the literature.
- For degrees of saturation in excess of 80%, three different types of behavior were observed and can be expected for similar concrete mixes under field conditions.
  - Sample of mixes $C_{0.47}$ and $S_{0.61}$ (water to cement ratios of 0.47 and 0.61 respectively) showed a significant expansion during cooling and therefore a large reduction in the effective coefficient of thermal expansion as well as significant residual strain after two cooling-heating cycles (Behavior 1). It was also noted that the increase in the water to cement ratio leads to an increase in the observed expansion.
  - Samples of mix $A_{0.34}$ had an effective thermal expansion coefficient equal to that of dry samples and negligible residual strain (behavior 2). This behavior can be attributed to the low pore radii (resulting from a low water to cement ratio) which leads to an increase in pressure of the water and thus limited freezing.
  - Samples of mix $SA_{0.47}$ showed an intermediate behavior with a moderate reduction in the effective thermal expansion coefficient upon cooling and a limited amount of residual strain upon thawing (Behavior 3). This behavior is possibly caused by a reduction in both pore size and porosity resulting from the use of a smaller coarse aggregate.
- The relationship between temperature and strain is hysteretic and the degree of hysteresis appears to be a function of w/c ratio, the degree of saturation, and the aggregate size.
- The different behaviors observed can have several implications on structural performance of concrete. Using a thermal structural model, it was determined that concretes with different strain-temperature relationships exhibit significantly different behavior under the effects of a cold wave event. These differences included significant variation in the magnitude of compressive strains in addition to variation in the location of tensile strains within the cross section.

- Saturated cylinders sourced from mixes $SA_{0.47}$, $S_{0.61}$, and $A_{0.34}$ were exposed to ten consecutive cooling-heating cycles. Among these, cylinders from mix $S_{0.61}$ exhibited notable residual strain, reaching values of up to $0.005\, mm/mm$. In contrast, cylinders from Mix $A_{0.34}$ displayed minimal residual strain, whereas cylinders from mix $SA_{0.47}$ demonstrated a moderate level of residual strain, measuring $0.0022\, mm/mm$. It was concluded that the increment in strain decreases as the number of cycles increases and the residual strain increments per cycle decreases with a decrease in the water-cement ratio.
- This study underscores and quantifies the influence of mix design factors, such as water-cement ratio, aggregate volume ratio, and maximum aggregate size, on the thermal behavior of concrete elements that are either saturated or near saturated. Furthermore, it elucidates the potential ramifications for structural performance. It is expected that this research will equip structural engineers with the knowledge needed to comprehend and account for the impact of cold wave events on such concrete elements. This may involve designing appropriate concrete mixes or incorporating reinforcement strategies to mitigate any adverse effects.

4.11 Appendices

4.11.1 Appendix A: Drying Curves

The average drying curves for the different mixes are shown in Figure 4.13.

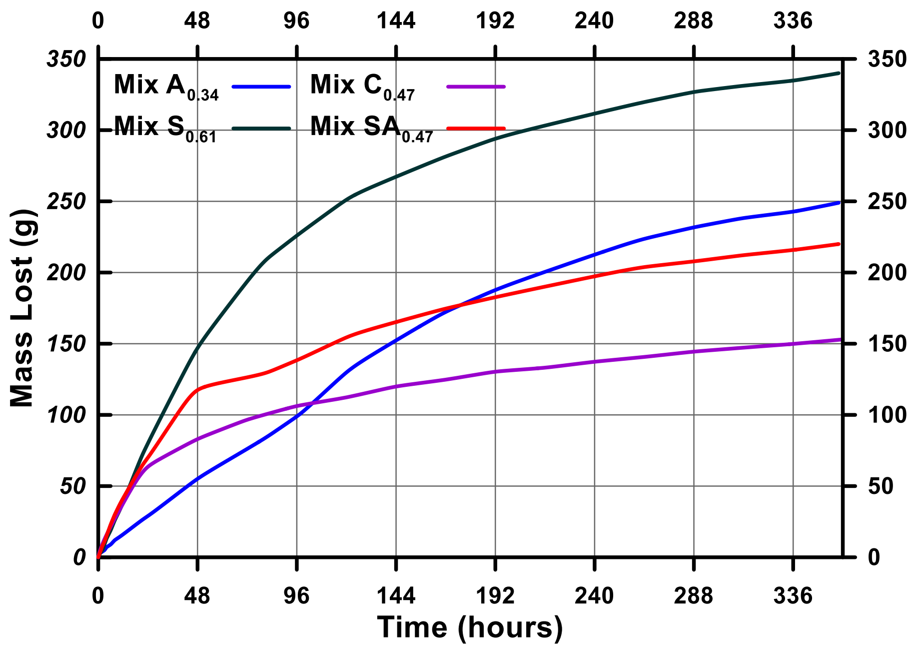

Figure 4.13: Average drying curves for the different mixes at 50°C for the first 15 days.

4.11.2 Appendix B: Compressive strength and Porosity

Table 4.3 shows the average porosity and compressive strength of the different mixes used in the study.

Table 4.3: Measured compressive strength (Wet) and porosity of the four mixes.

Mix	A	C	SA	S
Compressive strength (MPa)	54.31	40.5	41.84	26.8
Standard Deviation (MPa**)**	4.2	2.7	4.1	2.7
$\boldsymbol{Porosity}$ %	0.19	0.19	0.16	0.23

4.11.1 Appendix C: Maximum and Minimum Vertical and Lateral Strains

This Appendix contains figures (Fig 4.14-4.17) which show the maximum and minimum vertical and lateral strains observed in concrete with a constant ECTE, Concrete based on sample $S_{0.61}85(2)$, and Concrete based on sample $S_{0.61}100(1)$.

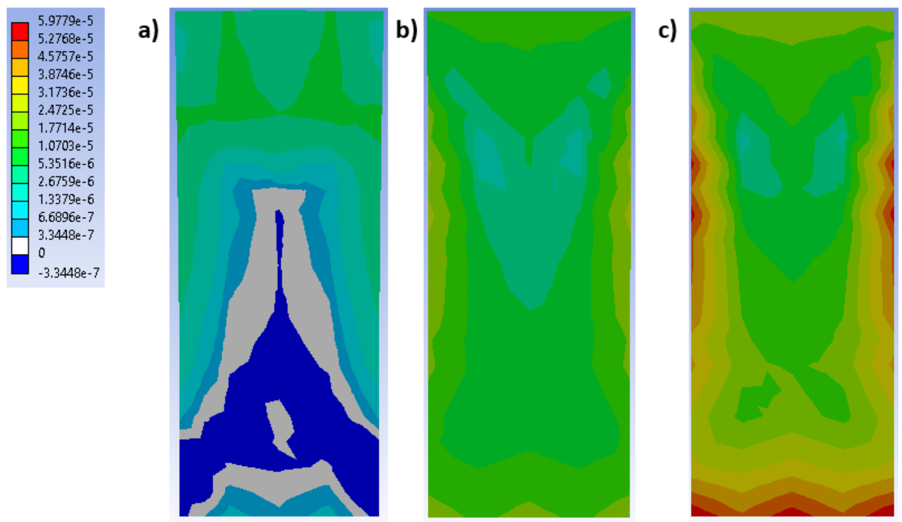

Figure 4.14: Maximum vertical strain in the cross section at the middle of the span. a) Concrete with constant CTE, b) Concrete based on sample$S_{0.61}85(2)$, and c) Concrete based on sample $S_{0.61}100(1)$

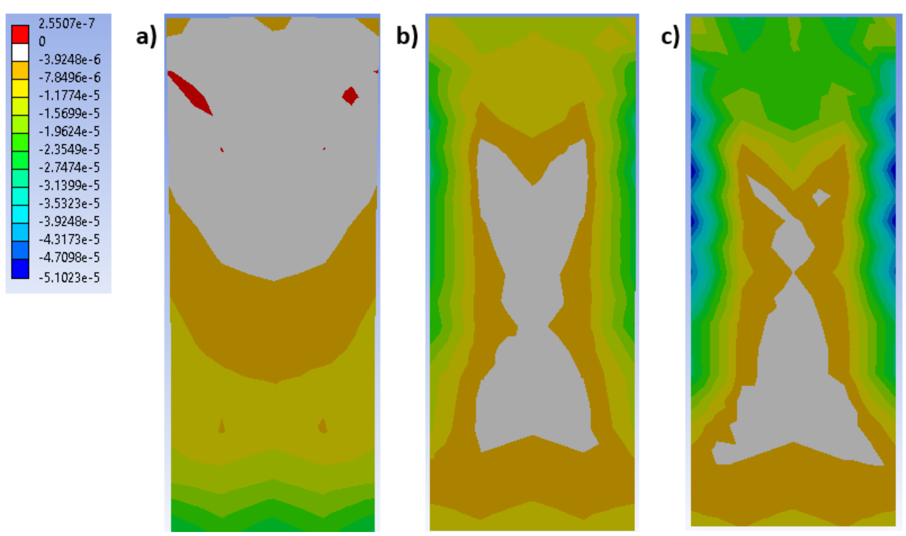

Figure 4.15: Minimum vertical strain in the cross section at the middle of the span. a) Concrete with constant CTE, b) Concrete based on sample $S_{0.61}85(2)$, and c) Concrete based on sample $S_{0.61}100(1)$.

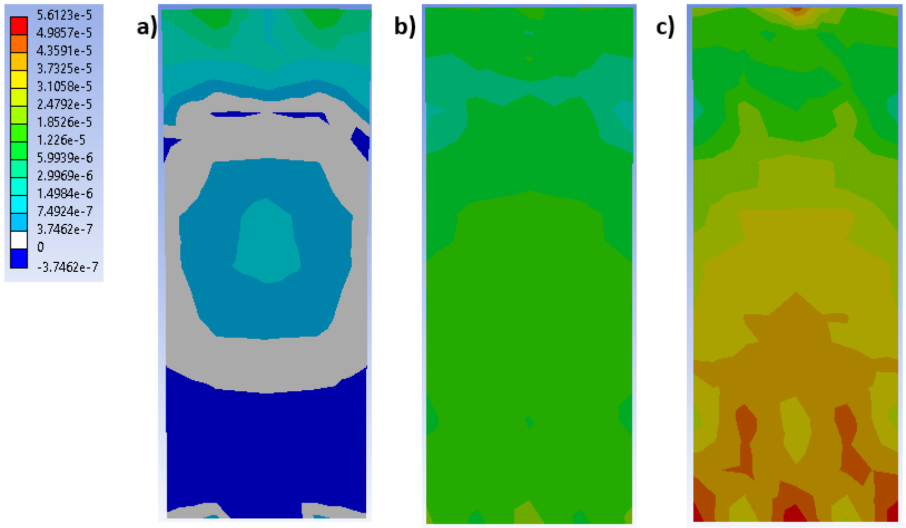

Figure 4.16: Maximum lateral strain in the cross section at the middle of the span. a) Concrete with constant CTE, b) Concrete based on sample$S_{0.61}85(2)$, and c) Concrete based on sample $S_{0.61}100(1)$.

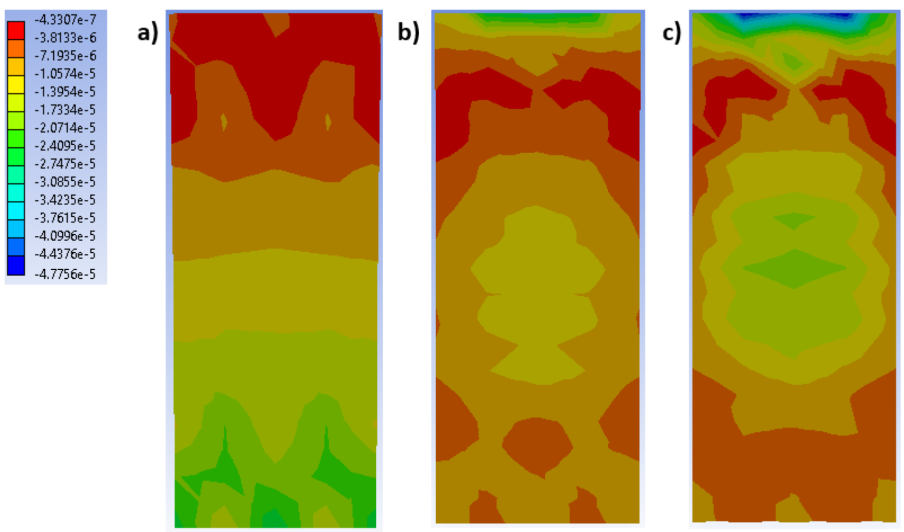

Figure 4.17: Minimum Lateral strain in the cross section at the middle of the span. a) Concrete with constant CTE, b) Concrete based on sample $S_{0.61}85(2)$, and c) Concrete based on sample $S_{0.61}100(1)$.

Chapter V

Bridge Decks Under Cold Waves: The Effect of Concrete's Temperature Dependent ECTE

<u>Note:</u> The content of this study is under final revision for submission to the Journal of Structural Engineering. The format (headings, caption numbering, and citations) has been edited to match the thesis format.

5.1 Introduction

As earth's climate changes rapidly, extreme events are projected to become more severe and frequent in the future (Wayne 2013). This means that as the return period of extreme events decreases, bridge infrastructure can be subjected to loading which is in excess of the demand for which it was designed. Furthermore, climate change does not only affect the demand on a structure but may also accelerate the degradation rate of the physical and mechanical properties of building materials which may lead to a significant reduction in a bridge's capacity.

One of the main concerns in terms of bridge engineering is the effect that the changing temperature might have on the thermal loading that acts on a bridge. One would assume that the increase in heatwave intensity and frequency is the first area to be addressed in this field. However, before focusing on future scenarios, authorities should first address an important concrete material behaviour characteristic, that is typically neglected in bridge design and may be impacting the structural performance of a bridge. This relates to the sensitivity of the effective coefficient of thermal expansion (ECTE) of concrete to freezing temperatures. The ECTE represents the experimentally measured rate at which a material expands or contracts with a change in temperature. It is noted here that whereas the CTE is a fundamental material property, the ECTE is an observed variable. CTE is generally taken constant in structural calculations – an assumption that is valid for ambient temperatures > -5 °C. Being a physical parameter, the theoretical value of CTE is greater than zero (positive number) – e.g., for concrete and steel it is taken as $10 \times 10^{-6}\ mm/mm/°C$, and therefore the length change due to temperature is assumed to be of the same sign (i.e., a temperature increase will lead to expansion and a temperature decrease will lead to contraction), and proportional to the temperature change. However, in reality, the ECTE of concrete can change significantly with subfreezing temperatures (Rostasy et al. 1979; Planas et al. 1984; Lee et al. 2003; Kanagaraj and Pattanayak 2003; Xia et al. 2017; Zhengwu et al. 2019). The range of temperatures where the ECTE of concrete becomes variable is not uncommon in colder climates such as in Northern US and Canada (Hall et al. 2018). In these conditions, the ECTE has been found to be highly nonlinear and the corresponding length change to be expansive under cold temperatures, and therefore reverse to the commonly held expectation that length change is contractive in colder temperatures.

As mentioned above, the temperature-dependence of the effective coefficient of thermal expansion of concrete is generally overlooked. Bridge Codes provide a constant value of ECTE to be used in structural calculations. For example, AASHTO recommends using a constant ECTE of $1.08 \times 10^{-5}/°C$ for normal weight concrete (AASHTO 2012). Similarly, the CHBDC recommends using a ECTE value of $10 \times 10^{-6}/°C$ (CSA 2014). While it is true that the ECTE doesn't change in ambient temperatures above the ice freezing limit, a quick review of the literature reveals that sub-freezing temperatures have a significant effect on length change with temperature, especially for concretes with high degree of saturation (Planas et al. 1984). The phenomenon is most likely related to the expansive behaviour of the pore water which turns to ice as it freezes; the residual deformations and the internal forces resulting from restraint of these deformations can be significant and may affect the state of stress in the exposed part of the structure.

The objective of the present work was to investigate the interaction between temperature and the thermal expansion coefficient and the subsequent impact on the structural performance of bridges while also highlighting deficiencies in Code prescribed thermal loads. The first step was to perform a comprehensive review of the literature to quantify the effect of temperature on the ECTE. After formulating a mathematical relationship between ECTE and temperature that is consistent with the experimental evidence, a thermal finite element analysis of a concrete box girder subjected to the thermal time history of three cold events was conducted. The cold events were selected to represent different levels of intensity in terms of the minimum temperature experienced by the bridge. The results of the thermal simulations were then applied as boundary conditions in a structural finite element model that incorporated the established relationship between temperature and the ECTE. The results were then analyzed to quantify the effect of temperature dependence of ECTE on structural performance for the cold events of different intensity. Finally, the assumption of constant ECTE in different codes was also addressed.

5.2 Thermal expansion coefficient

5.2.1 Background

The interaction between subzero temperatures and the thermal expansion coefficient has been investigated and reported in the literature (Rostasy et al. 1979; Planas et al. 1984; Miura 1989; Xia et al. 2017; Zhengwu et al. 2019). These investigations were mainly experimental studies where the length change normalized over the gauge length was expressed as thermal strain and was reported as a function of temperature. The CTE could then be calculated as the slope between two consecutive points on the plot of thermal strain versus temperature. Throughout this work, the effect of temperature on CTE was studied in terms of the relationship between thermal strain versus temperature, and it therefore refers to the observed, or effective value of this variable (ECTE).

The effect of thermal cycles (cooling down to $-165℃$ followed by reversal to $20℃$) on the thermal deformation of concrete specimens was investigated experimentally for both saturated and dry concrete (Planas et al. 1984). The results indicated that the cooling process could be divided into three phases. Phase 1 (from 20 to $-15℃$) involves contraction of the concrete specimen. Phase 2 (from -20 to $60℃$) is an expansion phase with the expansion resulting from phase transition of water into ice in pores of small diameter. Finally, the third phase is a contraction phase with linear reversible strain. The findings are summarized in Figure 5.1. A similar but reversed track path was observed upon reversal to ambient temperature (for easy reference, this reversal will be referred to hereon as heating). Furthermore, a residual strain was recorded when the concrete returned to room temperature.

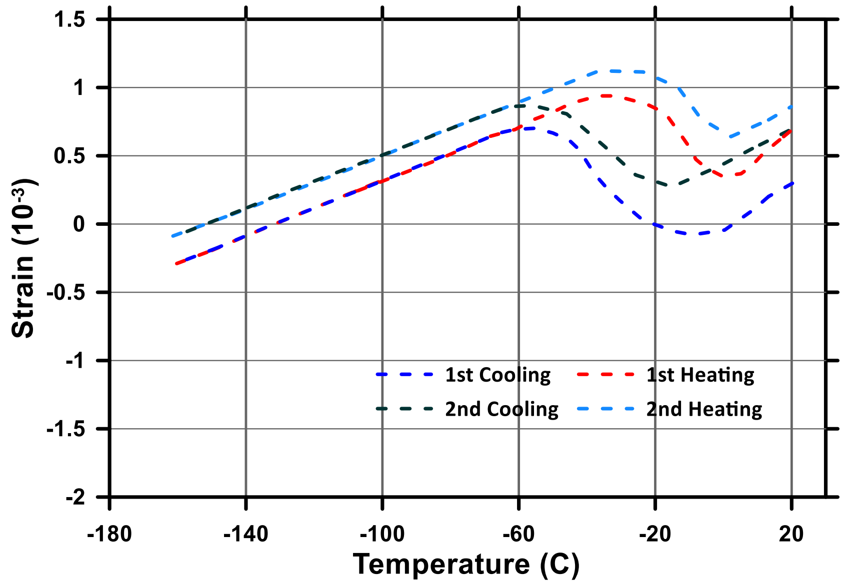

Figure 5.1: Temperature versus thermal strain results. Data from (Planas et al. 1984).

Similarly, thermal strains in concrete specimens at extremely low temperatures had also been reported in (Rostasy et al. 1979). Figure 5.2 shows the obtained temperature-strain curve. These results also indicate three different temperature regions of behavior. Contraction was observed between 25℃ and -25 ℃. The second region (expansion) extended from $-25\ to - 70$ ℃ whereas the third region (linear contraction) extended from -70℃ $to - 160$℃.

Figure 5.3 plots experimental results of thermal strain development in cement-based materials under cryogenic temperatures (Zhengwu et al. 2019). The three stages of behavior discussed previously were again observed in the experimental results. Specimens were also subjected to multiple freeze thaw cycles (fourth cycle shown in Figure 5.3), and it was found that significant residual strain remained in the matrix after the cycles. The residual strain initially increased with the increasing number of freeze-thaw cycles until it eventually stabilizes and converged to a constant upper limit even with increasing number of cycles (Zhengwu et al. 2019).

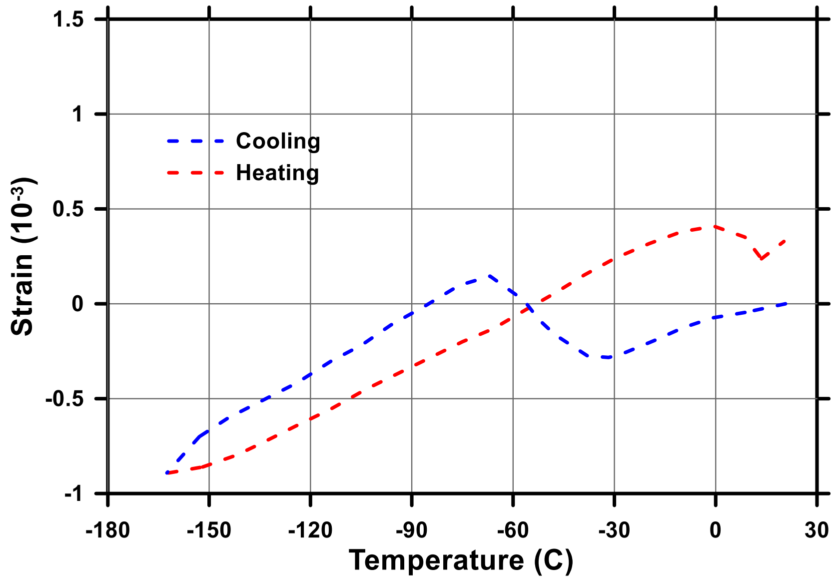

Figure 5.2: Temperature-strain curves of hydrated cement paste specimen. Data from (Rostasy et al. 1979).

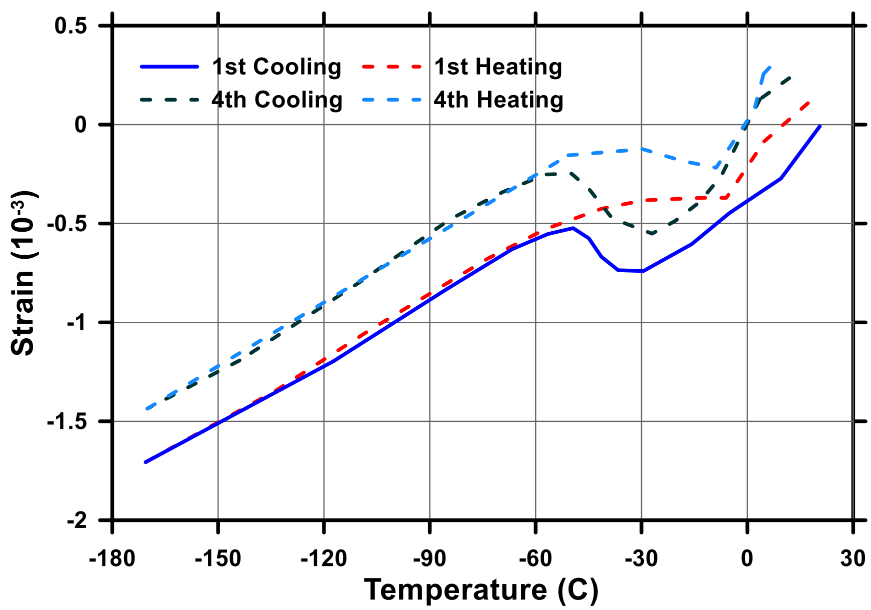

Figure 5.3: Development of thermal strains in cement-based materials under cryogenic temperatures. Data from (Zhengwu et al. 2019).

The findings of another experiment, illustrated in Figure 5.4, indicated that concrete contracted as the temperature fell, expanded between −22 ℃ and −60 ℃, and then contracted again linearly, down to −70 ℃. Upon reversal of temperature, the specimen expanded linearly until about −50 ℃, but contracted suddenly in the range between -50 ℃ and -20 ℃, to expand again from -20 ℃ onwards. Residual strain values were also reported (Miura 1989).

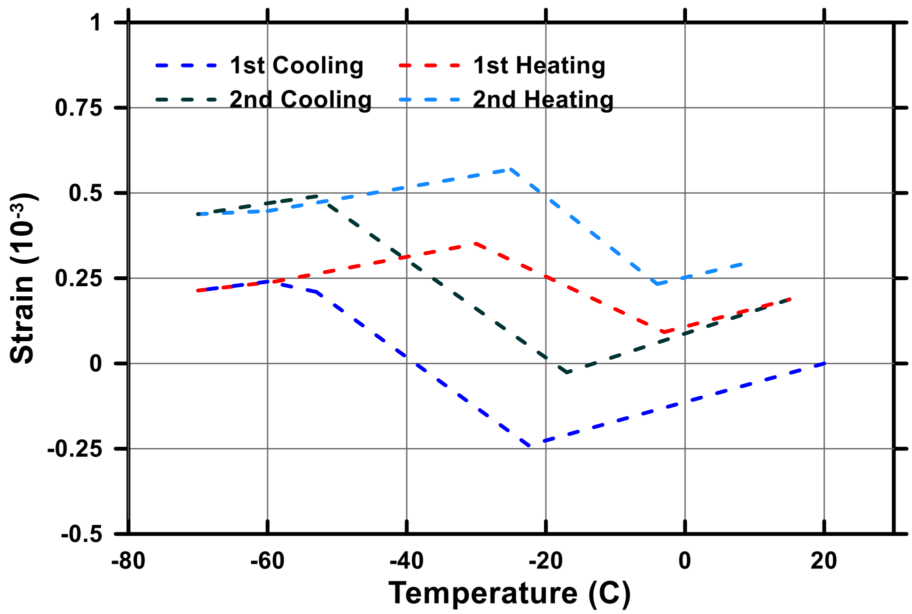

Figure 5.4: Development of thermal strains in a concrete specimen at subzero temperatures. Data from (Miura 1989).

From the results summarized in the preceding, the thermal behaviour of concrete exposed to cooling and heating cycles may be described qualitatively. As temperature decreases below 0°C, the water inside wet concrete begins to turn to ice. As the ice forms, the bulk or effective CTE of the concrete is influenced by the CTE of ice. Water in larger, capillary pores undergoes first the phase change (becoming ice); water in finer pores undergoes phase change at lower temperatures – a process that continues gradually with the pore size distribution of the specific material in hand. This process, until all the pore water would freeze, is manifested by the reversal in strain under monotonic temperature changes as depicted in Figures 5.1-5.4. Beyond that point and for further reduction in temperature, the concrete reverts into linear contraction.

Thus, a partially saturated concrete specimen may demonstrate one of three different types of response depending on its microstructure and internal relative humidity (Xia et al. 2017). Type 1 is the behavior described above that involves a contraction followed by significant expansion which is in turn followed by contraction. Type 2 is similar to Type 1 but with a relatively minor expansion phase (depending on the moisture content) (Xia et al.

2017). Alternatively, Type 3 involves continuous linear contraction with decreasing temperature i.e., when the concrete is dry (Xia et al. 2017).

5.2.2 Proposed model

An empirical hysteretic model was formulated in this work to take into account the temperature dependence of ECTE as shown in Figure 5.5. This model was developed by identifying several critical points (labelled A to M in Figure 5.5) and adhering to a set of defined rules relating to the segment slopes which represent the values of the ECTE in different temperature regimes (Numbered 1 to 6 in Figure 5.5). Note that most of the critical points are associated with strain reversals under monotonic temperature changes. It should also be noted that the proposed model was assumed to be linear between milestone points. The assumption of linearity was made for the sake of simplicity with no loss of generality of the approach and is mostly consistent with the empirical evidence presented above.

Point A represents the start of the cooling cycle and thus has a reference strain $\varepsilon = 0$ and a temperature equal to the ambient temperature (Typically 20℃). Upon cooling, the strain in concrete is expected to drop to a negative value at Point B (between -5 and -10℃ , with the slope of segment AB (slope 1) being equal to the thermal expansion coefficient of dry concrete (typically between 8 to 10×10^{-6}/℃). At temperatures below that of Point B, concrete expands until point C; (the temperature associated with this point ranges from -50 to -70℃). The slope of segment BC (slope 2) was approximated based on published experimental evidence from the literature (around -13×10^{-6}/℃). Once all the pore water has solidified, the concrete reverts to contracting as the temperature decreases down from Point C to D. The slope of Segment CD (slope 3) is equal to the slope of segment AB (slope 1) in accordance with published experimental evidence (Planas et al. 1984).

Upon temperature reversal, the concrete expands from point D to Point E, which corresponds to a temperature in the range of -40 to -20℃. The slope of segment DE (Slope 4) is equal to the slope of segment CD (Slope 3). With temperature increase beyond E, the concrete contracts up to point F which occurs around -5℃, the temperature at solid ice formation. The slope of Segment EF (Slope 5) is equal to the slope of segment BC

(Slope 2). Finally, as the temperature increases beyond point F, the concrete expands to point G with the slope of segment FG (Slope 6) being equal to that of segment AB (Slope 1) (Planas et al. 1984).

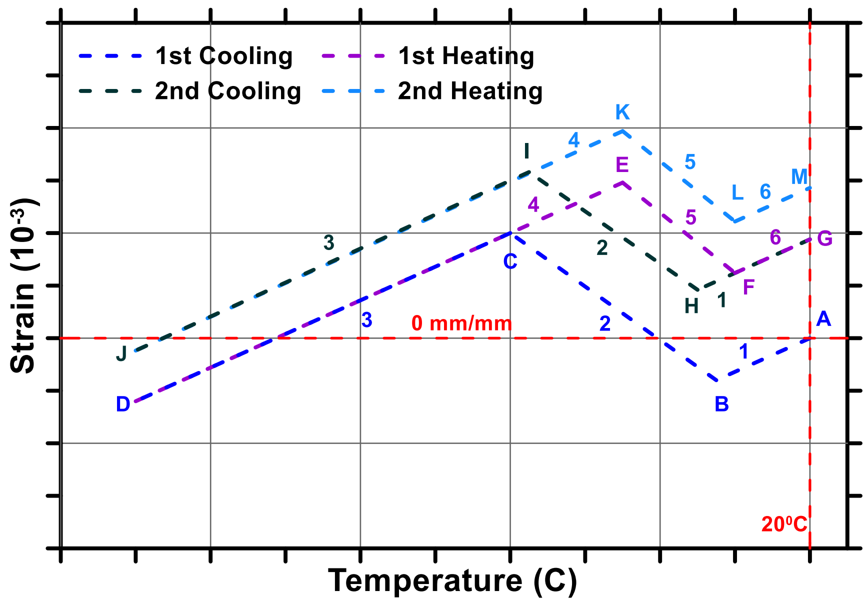

Figure 5.5: Proposed generic model for temperature versus thermal strain in concrete.

The 2nd heating and cooling cycle follows the same trend as the first cycle. It should be noted that the starting point at ambient temperature is now translated in the axis of strain (length change) on account of the residual expansion that has been caused by the accumulation of damage. The rules of the first cycle apply to the second cooling-heating cycle, but also to any additional cooling-heating cycles that follow. Furthermore, with each additional cycle, the amount of additional residual strain at room temperature decreases until eventually a point is reached where no additional strain buildup is observed as per (Rostasy et al. 1979).

Once the major points for the full cycles are identified, the next step is to determine the behaviour of concrete if the cooling cycles do not reach the lowest temperature (i.e., if the temperature doesn't reach Point D and reversal starts at point H as shown in Figure 5.6). This was achieved by using an algorithm that determines the different critical points based on the minimum temperature reached during a cooling cycle. The procedure followed is highlighted in Figure 5.6. The figure shows one full cooling-heating cycle and one shortened cycle in which the minimum temperature (Point H) is still higher than the temperature at Point C. Note that the shortened cycle maintains the same shape and slopes of the full cycle with the position of critical points dependent on the temperature value at point H. The detailed steps to determine the critical points of the shortened cycle are provided in Appendix A.

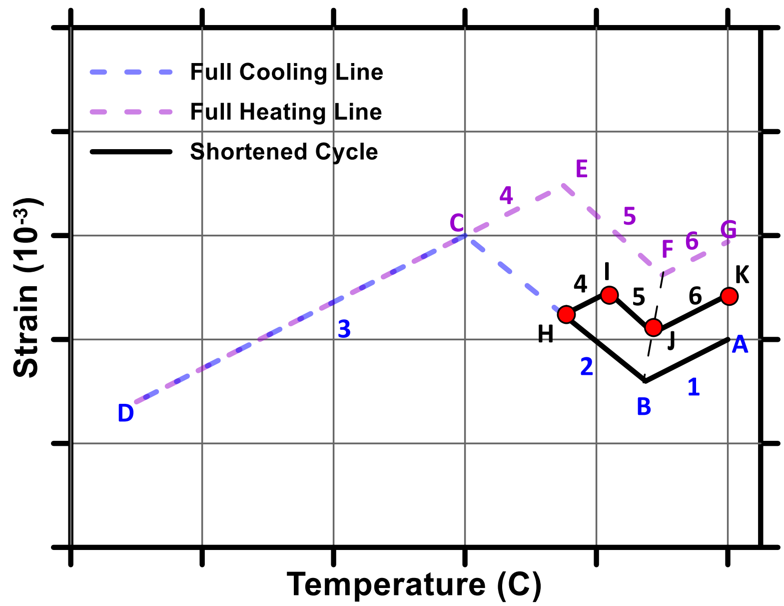

Figure 5.6: Estimation of temperature versus thermal strain relationship for cycles reaching smaller temperatures.

5.3 Materials and methods

With the relationship between thermal strain and temperature known, the next step in the investigation was to conduct a validation study to ensure that the proposed hysteretic model for the ECTE reproduces the observed response of actual case studies. After validation, the model was used to study the structural implications of the expansive process of concrete during cooling of a saturated structure: to this end, three cold wave events were selected to be used as boundary conditions in the thermal finite element simulations to determine the thermal load. The resulting load was applied for stress analysis on a concrete box bridge girder which was selected as a case study in the present work.

5.3.1 Climate data for cold events

For the case study investigation, three cold wave events were chosen to represent different intensities based on the minimum ambient temperature observed during the cold wave. The low intensity event occurred in January of 2007 in Toronto, Ontario and had a minimum ambient temperature of -21 ℃. The medium intensity event occurred in Old Crow, Yukon in February of 2005. A minimum ambient temperature of -31.5 ℃ was observed.

Furthermore, the high intensity event occurred in January of 2005 in Old Crow, Yukon with a minimum recorded ambient temperature of -49 ℃. The climate data (i.e., ambient temperature, dew point temperature, windspeed, cloud cover, and solar radiation) for all three periods was collected from the Canadian Weather Energy and Engineering Datasets (CWEEDS 2020); relevant ambient temperature and windspeed time histories for all events are depicted in Figure 5.7.

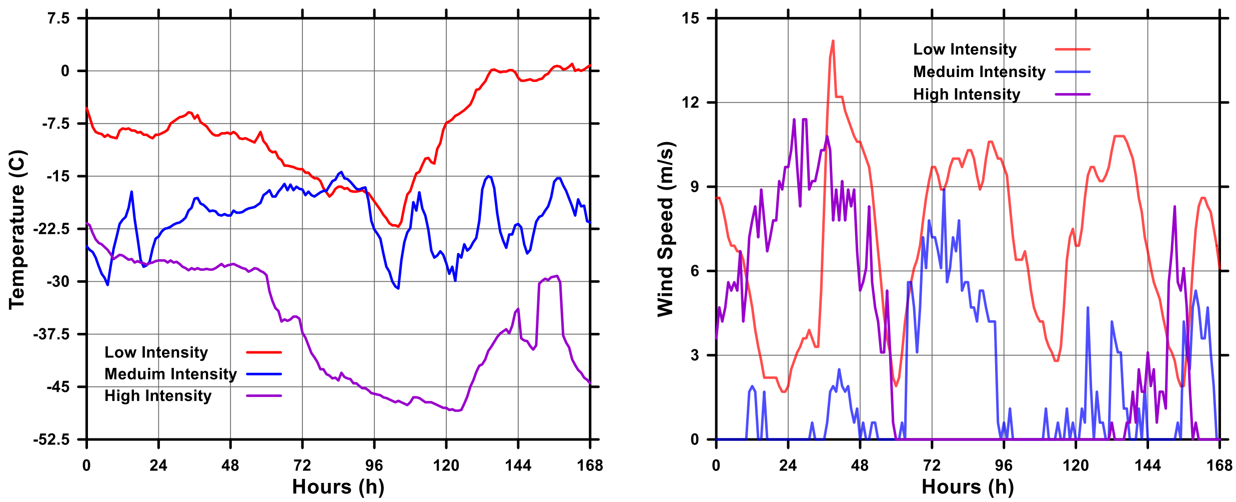

Figure 5.7: Temperature and wind speed data for all cold wave events. Data from (CWEEDS 2020).

5.3.2 Bridge cross section and reinforcement

A $24\ m$ long box girder bridge was selected from (Ferdjani 1987) to evaluate the effect of the different cold waves on the thermal and structural responses. The bottom and top flanges of the bridge had a constant thickness of $200\ mm$ while the webs were $250\ mm$ thick. The girder was $1.6\ m$ in depth. The bridge was oriented in the South/North direction. Moreover, the concrete was overlain with an $110\ mm$ thick layer of asphalt. The bridge cross section is shown in Figure 5.8. The bridge was reinforced with three layers of prestressing tendons in each web. The strands had an area of $1018\ mm^2$ and were stressed to $600\ MPa$. Additionally, the bridge was reinforced with $10\ mm$ reinforcement and stirrups. The reinforcement details were obtained from (Ferdjani 1987) and are shown in Appendix B.

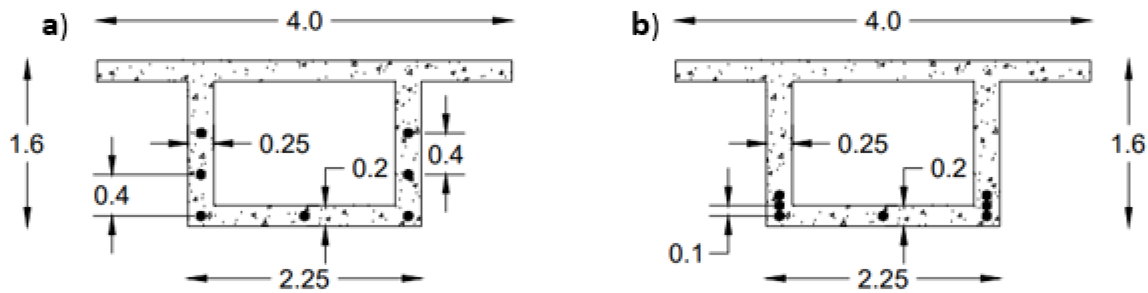

Figure 5.8: Bridge cross section at a) support and b) Midspan. All dimensions in meters.

5.4 Thermal simulation

The thermal model simulates the interaction between the bridge surface and the surrounding environment to predict the temperature distribution within. This interaction was governed by three physical processes which are, 1) the shortwave radiation, 2) the longwave radiation, and 3) the convective heat transfer. A full transient thermal model was developed (using a physico-mechanical modeling framework) to predict the temperature distribution along the depth of the bridge cross section using the ANSYS finite element platform (ANSYS 2019). The model had been verified and then validated against experimental results from a bridge located in Jiangsu, China as described in (Saad et al. 2022) and Chapter II of this thesis. The three cold wave events were then applied as boundary conditions to determine the temperature distribution within the cross section.

5.4.1 Model properties

The initial temperature of the bridge was assumed to be uniform and equal to the initial ambient temperature. The ends of the cross section were assumed to be perfectly insulated and the temperature of the air inside the core of the cross section was taken as 1.5℃ higher than the ambient temperature in accordance with (Elbadry et al. 1983). The element used for modelling both the asphalt and the concrete was a 3-D 20-node prism-shaped, thermal element (Solid90 (ANSYS 2019)) and the total number of elements used for the bridge cross section and the asphalt layer was 357120 and 76800 respectively. The thermal properties used for the concrete and asphalt were taken from (Gu et al. 2014) and are shown in Table 5.1.

Table 5.1: Material properties used in the model. Data from (Gu et al 2014).

Material	Density (kg/m^3)	Heat Capacity ($\frac{J}{kg°C}$)	Conductivity ($\frac{W}{m°C}$)	Emissivity	Absorptivity
Concrete	2500	1010	1.17	0.9	0.65
Asphalt	2100	886	0.98	0.9	0.9

5.4.2 Thermal results

Figure 5.9 depicts the negative temperature differentials obtained along the web of the cross section for the three thermal events. The differentials shown represent the largest difference between the exterior surface and the interior of the cross section. The figure also shows the reference negative differential recommended by AAHSTO based on guidelines for Alaska since it is the American region closest to Old Crow, Canada where medium and high intensity events had occurred. The differentials obtained from the simulations and the one recommended by AASHTO differ in magnitude both near the top and bottom of the cross section. It was observed that AASHTO guidance significantly underestimates the differential that occurs near the bottom of the cross section for all events. Furthermore, the differential that occurred during the low intensity event at the bottom of the cross section (-2.5℃) is lower than the differential observed during the medium and high intensity events ($-5\ to - 6$℃ respectively). On the other hand, the AASHTO guidance covered the low intensity event differential at the top but still underestimated the medium and high intensity event differentials by about 2 and 4℃ respectively.

Figure 5.10 shows the temperature time history at three different points across the web for each of the events. These points represent the top, middle, and bottom of the web. For the low intensity event, it was found that the temperature variation follows a sinusoidal-like pattern with uniform cooling followed by uniform heating. During the medium intensity event, temperature varied significantly with time. However, the overall temperature trend was to increase (heating) from the start time to about $t = 100\ hrs$ which was then followed by cooling until time $t = 120\ hrs$. From that point on, a heating trend could be observed. On the other hand, the trend for the high intensity event was cooling until time $t = 120\ hrs$ which then reverted to heating. Furthermore, the trend can be described as composed of linear segments with the exception occurring at around time $t = 140$ hours where a significant jump in temperature occurred at all points of the cross section. Note that the points at which the behaviour changed from heating to cooling and vice versa are of particular interest since the temperature at these points defined the limits of the hysteretic loops in the generic model for thermal strain proposed in Section 5.2.2.

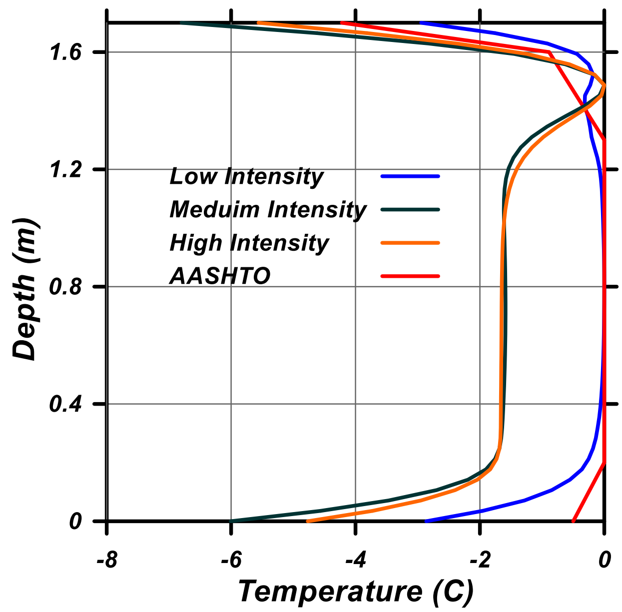

Figure 5.9: Maximum negative gradients for each cold event and the AAASHTO recommended gradient.

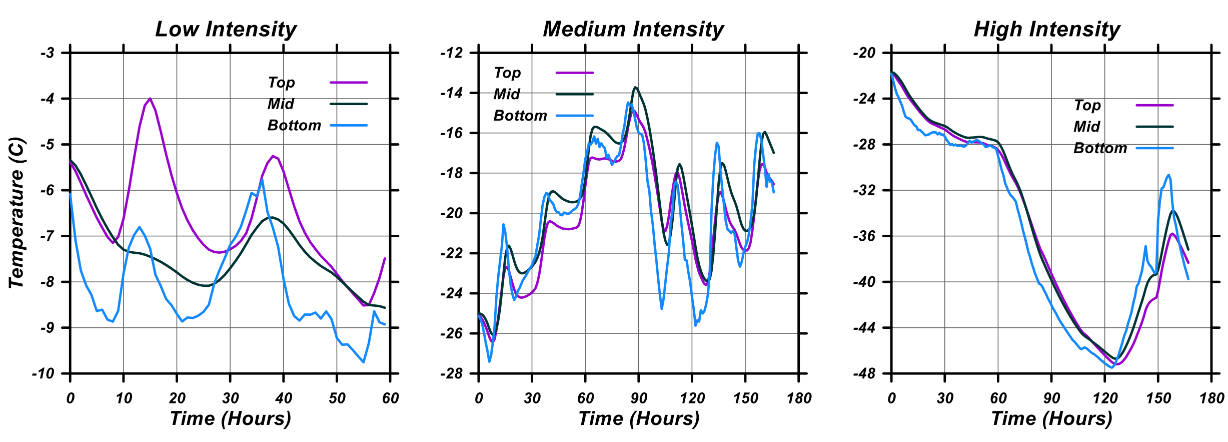

Figure 5.10: Temperature Time history for different points along the web of the cross section.

5.5 Structural simulation

5.5.1 Structural modelling

The structural model was also developed in ANSYS using the Menetrey-Willam (Menetrey 1994) damage plasticity material model for concrete, and a linear elastic model for reinforcement and prestressing steel. The tensile strength of concrete was taken as $3\ MPa$ while the uniaxial and biaxial compressive strengths were taken as 30 and $36\ MPa$ respectively. The elastic modulus was equal to $30\ GPa$. The prestressing steel tendons were modelled using beam elements with the prestressing force applied as an initial stress. The theoretical thermal expansion coefficient of concrete was taken as $1 \times 10^{-5}/°\mathrm{C}$ for the simulations that are used as benchmark reference. On the other hand, for the simulations where the effect of temperature on thermal strain was incorporated, the thermal strain versus temperature relationship for each cold event was input into the model. All other material properties were considered at a reference temperature of 20°C (i.e., the effect of temperature on these properties was not considered). The temperature distribution within the bridge deck, obtained from the thermal model, is applied as a thermal load in the form of a boundary condition. In addition to the applied prestressing and thermal load, the self-weight of the bridge was also considered in the model. Furthermore, the bridge deck was modelled as a simply supported member. The asphalt layer was only considered as a self-weight in the structural model.

5.5.2 Model verification

Before running the simulations, the approach used to define a temperature dependent thermal expansion coefficient in the model was verified. It was deemed essential to verify this aspect of the structural model, since the introduction of a temperature and history dependent thermal expansion coefficient is a novel concept in the field. One of the verification examples used is outlined in the following.

In this example, a $5\ m$ rectangular beam component with a width of $1\ m$ and a depth of $0.5\ m$ was considered. The end supports of the cross section were assumed fully fixed. A time varying temperature load, shown in Figure 5.11, was applied uniformly across the cross section of the component. The initial temperature of the cross section was assumed uniform throughout the beam and was taken equal to the initial value of the time-varying temperature load. Figure 5.11 also highlights the different stages of heating and cooling that the beam undergoes, and these stages are labelled from 1 to 7. These labels correspond to the time intervals shown in the lower axis of the figure and are used to relate the applied load and the strain versus temperature relation to the results obtained.

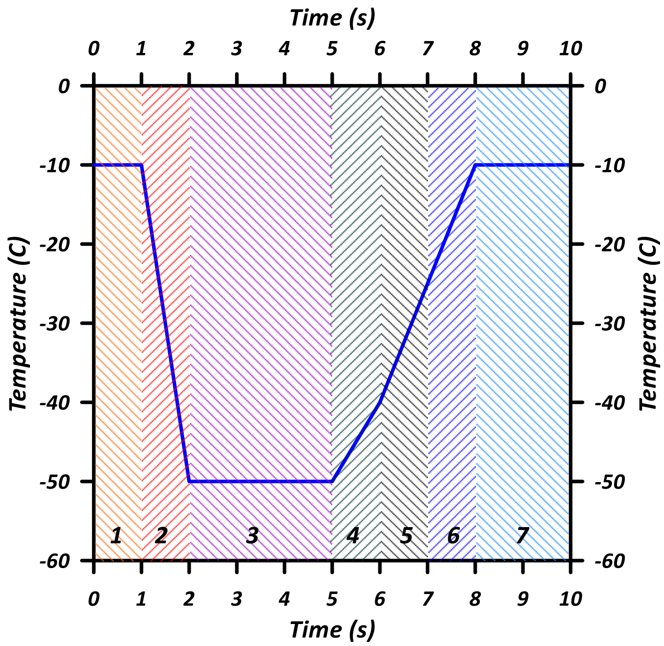

Figure 5.11: Temperature-Time history of the applied temperature load.

From Figure 5.11, it may be observed that the beam cools down to a temperature of -50℃, before warming back to a temperature of -10℃. Therefore, the thermal strain versus temperature relationship may be determined based on the model proposed in Section 5.2.2 with a minimum temperature of -50℃ (the resulting strain relationship is illustrated in Figure 5.12a). The relationship is then used as input in the finite element model to determine the mechanical strain at the centroid of the beam (i.e., at the intersection of the central longitudinal axis with the cross-sectional axis of symmetry). Since the beam is fully restrained, the mechanical strain at each temperature level is equal to the thermal strain at that temperature (but opposite in sign to maintain geometric compatibility).

During Stages 1 and 2 (both on the cooling part of the strain versus temperature relation that is shown in Figure 5.12a), the mechanical strain started as constant and then decreased down to $-373\ \mu m/m$ in compression at the end of Stage 2 (Figure 5.12b). At Stage 3, the temperature was constant which means that the mechanical strain also remained constant. During Stages 4 and 5, the beam experienced a reversal in temperature from $-50℃$ to $-25℃$ which means that the concrete still tends to expand (denoted by the heating branch of Figure 5.12a) and therefore it was subjected to additional compression (Figure 5.12b). At Stage 6, the temperature increased from $-25℃$ to $-10℃$ which caused concrete to contract (Figure 5.12a) and therefore resulted in tensile strains as shown in Figure 5.12b.

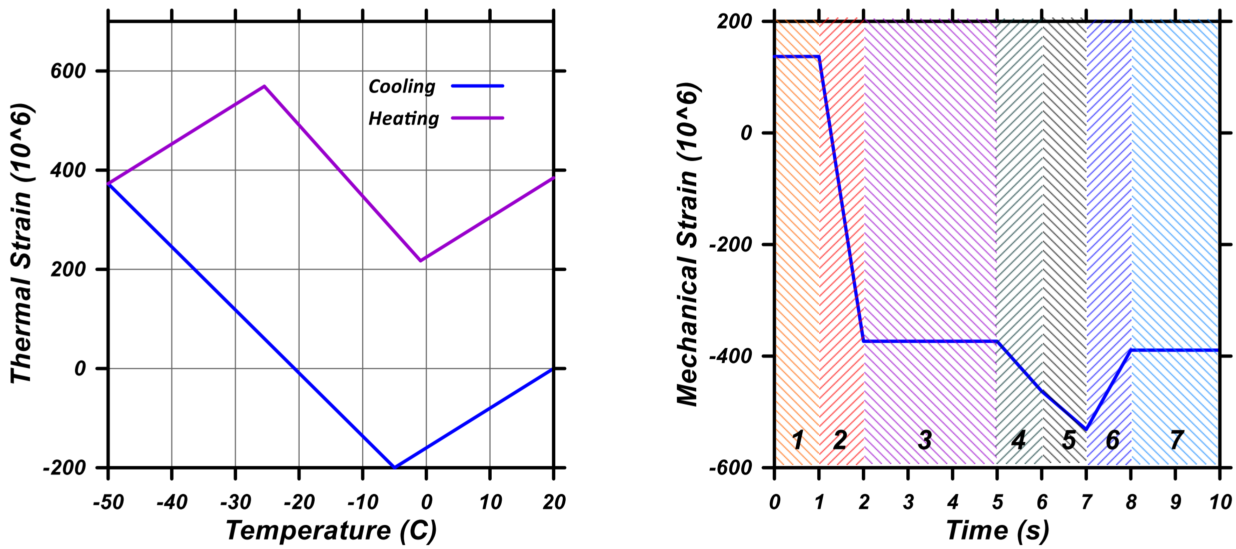

Figure 5.12: a) Thermal strain versus temperature relationship, b) Resulting mechanical strain at all time intervals.

Based on the results and discussion above, as well as additional verification tests, it was concluded that the model successfully reproduces the trends of the thermal strain versus temperature relationship.

5.5.3 Model validation

The model was validated against measurements from a two-span prestressed concrete box bridge located in Pennsylvania. The bridge was instrumented with strain gauges and monitored for a period of two years. Temperature records for the bridge location indicated that the ambient temperature in the vicinity of the bridge dropped down to around $-24℃$ in the period between January 28 and February 1 of 2019. This bridge was considered a good example for validation as it satisfies the conditions of having been instrumented with strain gauges during operation and having been subjected to cold temperatures. Identifying such an example was a challenge as the literature lacks experiments on bridges which satisfy both these conditions.

This bridge consists of eight pretensioned adjacent and parallel concrete box beams. Each span is 25.2 meters long. There is no connection between the two spans. The beams are reinforced with 54 Grade 250, 3/8-in diameter, seven-wire strands as well as ASTM A615 Grade 40 steel stirrups. The full bridge cross section and reinforcement details are provided in (Ghahremani et al. 2022).

The thermal structural model, built in ANSYS finite element platform, was used to simulate the behavior of a single span of the bridge. The model included prestressing tendons and non-prestressed reinforcement. Material properties were based on those presented in (Ghahremani et al. 2022). The model loads included thermal load, dead loads, and prestressing loads. Climate conditions for the bridge location were obtained from (Iowa state University 2023) with the ambient temperature and windspeed values for the period of interest (January 28-February 1, 2019) shown in Figure 5.13.

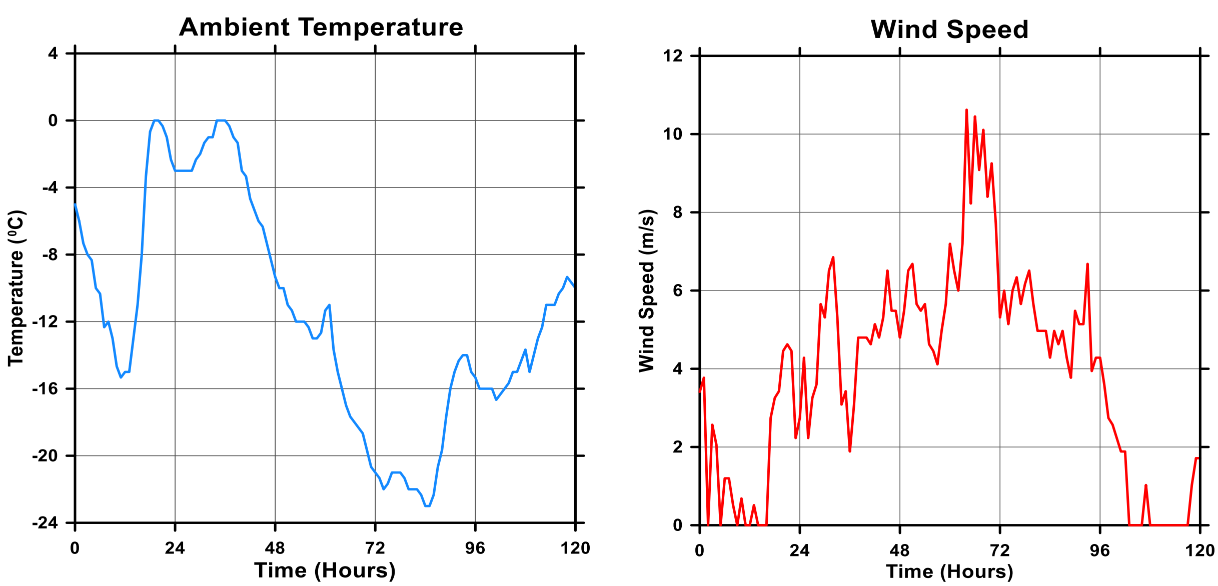

Figure 5.13: Ambient temperature and windspeed data for the bridge location From January 28-February 1, 2019.

Once the thermal response and minimum temperature within the bridge were simulated, the proposed model for determining the relationship between temperature and the effective coefficient of thermal expansion of concrete was applied. The resulting relationship is shown in Figure 5.14. The thermal results were then applied as a thermal load in the finite element structural model (Figure 5.15) which incorporates this relationship. The strain value at the location of the strain gauges was then obtained and compared against the measured strain. To account for the difference in initial conditions between the model and the bridge, the calculated change in strain values was compared with their measured counterparts. Figure 5.16 shows a satisfactory correlation between the predicted and measured results for both gauge S02 and gauge S09, (where gauges S02 and S09 are gauges placed at the bottom midpoint of each of the external edge beams of the span). Note that for gauge S09, both the simulated and observed change in strain are negligible. Therefore, it was concluded that the developed model performs well in replicating the interaction between the climate and the bridge deck while incorporating the effect of subfreezing temperature on the ECTE. However, it should be noted that there is lack of measured data in the literature that would enable further validation. Future work should aim to fill this void with data obtained either from field measurements or laboratory experiments.

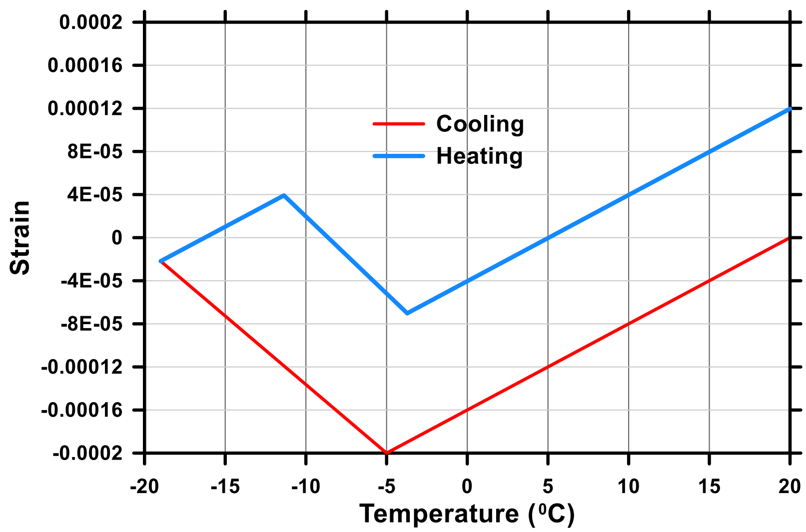

Figure 5.14: The relationship between temperature and thermal strain used in the structural analysis.

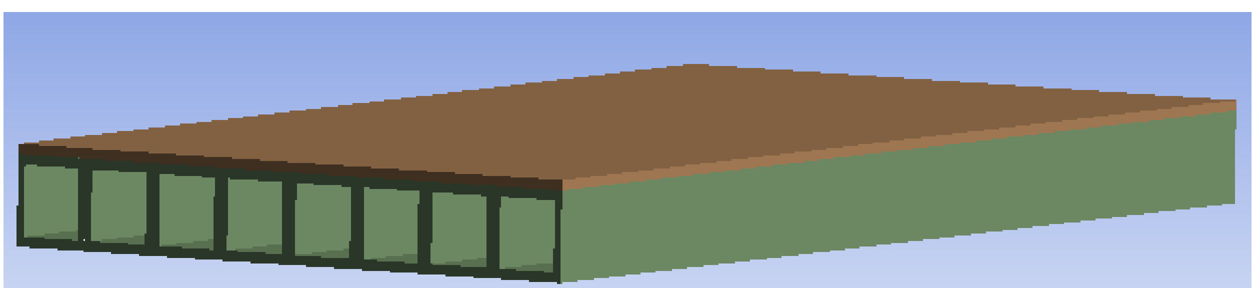

Figure 5.15: ANSYS Model.

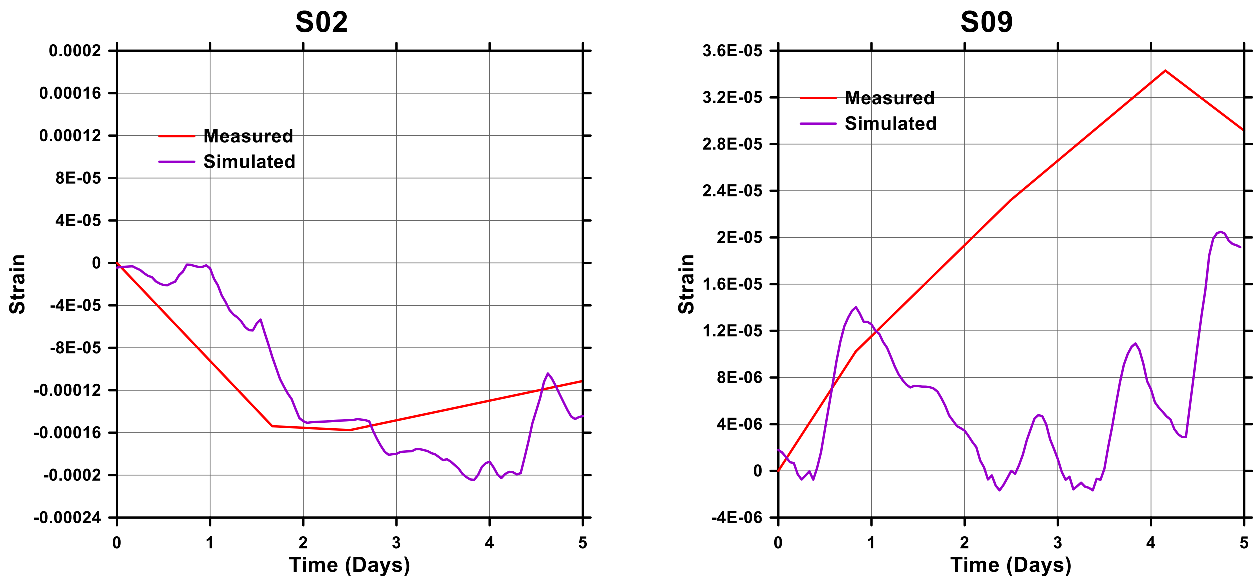

Figure 5.16: Measured and simulated change in strains for gauges S02 and S09.

5.6 Structural results for the bridge

As mentioned earlier, the temperature distribution within the cross section obtained from the thermal model was applied as a boundary condition in the structural model of the bridge. Furthermore, each of the cold waves had a different temperature time history which would result in a different thermal strain versus temperature time history, depending on the minimum temperature that the concrete reached. Figure 5.17 shows the resulting hysteretic behavior for each of these events. Note that a maximum of two heating cooling cycles were considered.

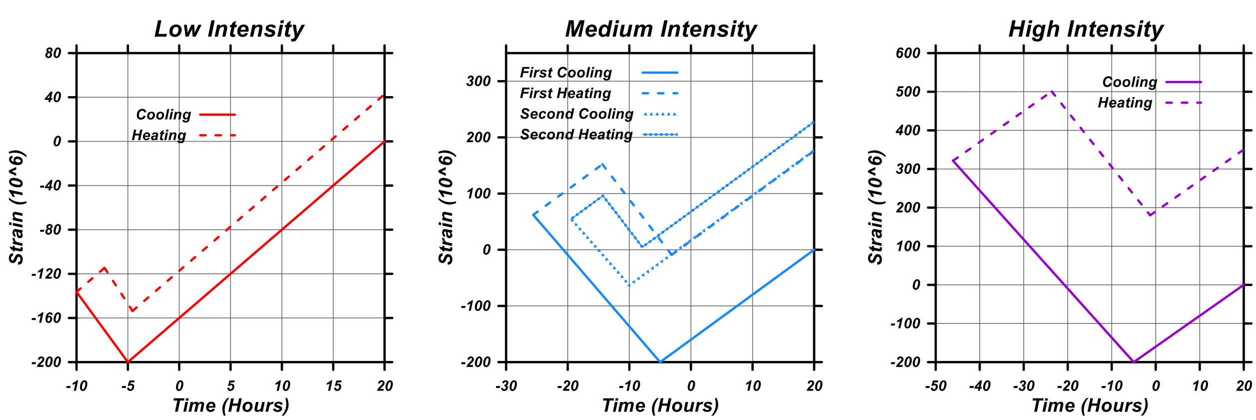

Figure 5.17: Thermal strain versus temperature hysteretic response for each of the cold events.

Strain values were then obtained from simulations of the various events. Figure 5.18 plots the maximum compressive longitudinal strains observed from all three events. The left-hand side figures represent the reference simulations which have a constant value of ECTE, while the right-hand side figures show the strain obtained from the simulations with a temperature dependent ECTE. The results indicated that the longitudinal strains are similar in magnitude between simulations with a variable and constant ECTE for the low and medium intensity events. On the other hand, the compressive longitudinal strains observed from the simulations with a variable ECTE ($-283\ \mu m/m$) were significantly larger than those observed from simulations with a constant ECTE ($-15\ \mu m/m$). This represents a significant amount of compressive strain which if unaccounted for may lead to delamination of the cover in concrete.

Furthermore, Figure 5.19 shows the maximum transverse strains (i.e., along the vertical axis of the cross section) observed in both simulations for all three cold wave events. The vertical strains observed from the two simulations (constant and varying ECTE) in both low and medium intensity events were very close in magnitude, similar to the case of the compressive longitudinal strains. On the other hand, significant tensile strain was observed for the simulation with a temperature dependent ECTE for a high intensity event. This tensile strain reached about $130\ \mu m/m$ which exceeds the cracking strain of concrete ($= 3MPa/30GPa$). On the other hand, the tensile strain observed in the simulation with a constant ECTE in a high intensity event is negligible. These findings highlight the issue that neglecting the effect of sub-freezing temperature on the coefficient of thermal expansion may lead to development of tensile strains in an unrestrained direction which in turn may cause cracking and cover delamination.

Moreover, the compressive strains in the lateral direction were significantly larger in simulations with a temperature dependent, variable ECTE when compared with simulations with a constant ECTE during a high intensity cold wave (Figure 5.20). However, the lateral strains are almost identical when considering medium and low intensity events. Furthermore, it can be observed from Figure 5.21, which shows the maximum transverse tensile strains on the side wall of the box girder, that the tensile strains simulated during a high intensity event varied significantly between the simulations with a constant ECTE and the simulation with a variable ECTE. The simulation with a temperature dependent ECTE resulted in a tensile strain of $210\ \mu m/m$ (well beyond the cracking limit) as opposed to the negligible strain observed in the simulation with a constant ECTE. On the other hand, the tensile transverse strains observed for both simulations in the low and intensity events were comparable and negligible.

When looking at the overall trend in the results, it becomes clear that using the temperature dependent ECTE in simulations for high intensity cold wave events has a large impact on the structural performance. Significant increases in both tensile and compressive strains in various directions are observed. This is expected due to the stark difference in the assumed relationship between thermal strain and temperature of the two simulations. On the other hand, simulations with constant and variable ECTE that were performed for low intensity cold wave events resulted in minimal difference. This is because the minimum temperature that the concrete reached was about $-10℃$ which was not low enough to cause a significant change in the relationship between thermal strain and temperature between the two simulations. Therefore, it is likely that in low intensity events, as defined herein, the effect of subfreezing temperature on the ECTE will have limited impact on structural behavior. Based on these observations, one would expect that the two simulations for medium intensity events show an intermediate difference between the two. However, the presented results showed a negligible difference between them. This is explained by the fact that the concrete temperature during the medium intensity cold wave event ranged from $-16℃$ to $-26℃$. The $10℃$ change in concrete temperature was not large enough to cause a noticeable change in results between the two simulations. This finding highlights the fact that the effect of cold waves on structural performance is not only a function of the minimum temperature reached and the thermal strain-temperature relationship only, but it also depends on the temperature development and the rate of temperature change in the concrete i.e., a medium intensity event with a similar minimum temperature may cause more severe effects depending on the history of ambient temperature changes.

Another noticeable effect that was observed in the simulations for the high intensity cold wave event is the increase in the stirrup load in the simulation with a temperature dependent ECTE in comparison with the simulation with a constant ECTE. The tensile load in the stirrups increased by about $5000\ N$ per stirrup, which represents an increase of about $65\ MPa$ in terms of stress. This represents about 25% of the yield capacity of the stirrups and must not be underestimated in the design process. Furthermore, about an 8% increase in the axial force in the tendons is observed in the simulation with temperature dependent ECTE.

5.7 Conclusions

Using three-dimensional finite element thermal and structural models, this study investigated the impact of incorporating the temperature dependence of ECTE of concrete on the development of strains in a prestressed concrete box girder. The study also investigated the suitability of the AASHTO recommended thermal guidance with a constant ECTE. Initially, a model that defines the relationship between thermal strain and temperature is proposed based on experimental data from the literature. Three historical cold wave events of varying levels of intensity, that were selected based on the minimum attained ambient temperature, were selected from two different locations across Canada. The minimum temperatures obtained during the events were $-21℃, -32℃,$ and $-50℃$ for the low, medium, and high intensity events, respectively. The thermal model was used to obtain temperature distributions within the box girder cross section due to these cold events. The simulated temperature distributions were then applied as boundary conditions in structural models in order to determine their effect on the structural response. These structural models incorporated the calculated thermal strain and temperature history, which were derived based on the minimum bridge temperature estimated for each event. The following conclusions may be drawn from this investigation as follows:

- The temperature dependence of ECTE can be implemented via the thermal strain approach proposed in this research. Furthermore, the modelling framework presented was able to reproduce and quantify this effect.
- The temperature distributions obtained from the thermal modelling of the cold wave events, indicate that the AASHTO recommended gradient does not accurately account for the magnitude of the negative gradients near the bottom of the cross section for any of the events. It was concluded that the AASHTO recommendations failed to reproduce the top temperature differentials for both medium and high intensity events.
- The effect of temperature dependence of ECTE on resulting strains is significant for cold events of high intensity when compared with simulations that use a constant ECTE. On the other hand, minimal effect is observed in simulations for low intensity cold wave events. Medium intensity events are expected to yield

intermediate effects. However, the impact of medium intensity events is highly influenced by the temperature range and time history evolution as was the case here.

- Furthermore, the structural results for the high intensity event show a significant increase in tensile stress in both transverse and vertical direction which can cause concrete cracking. In addition, a significant increase in compressive strains as well as reinforcement stresses was also observed.
- The AASHTO prescribed gradients and the assumption of a constant ECTE might be adequate for more southern cold regions (such as Toronto) with low intensity cold events, however considerable differences in predicted and actual structural performance may be expected for more Northern Locations.
- Instrumentation of bridges to measure thermal and structural performance is of paramount importance to further validate the current model and to develop robust models.

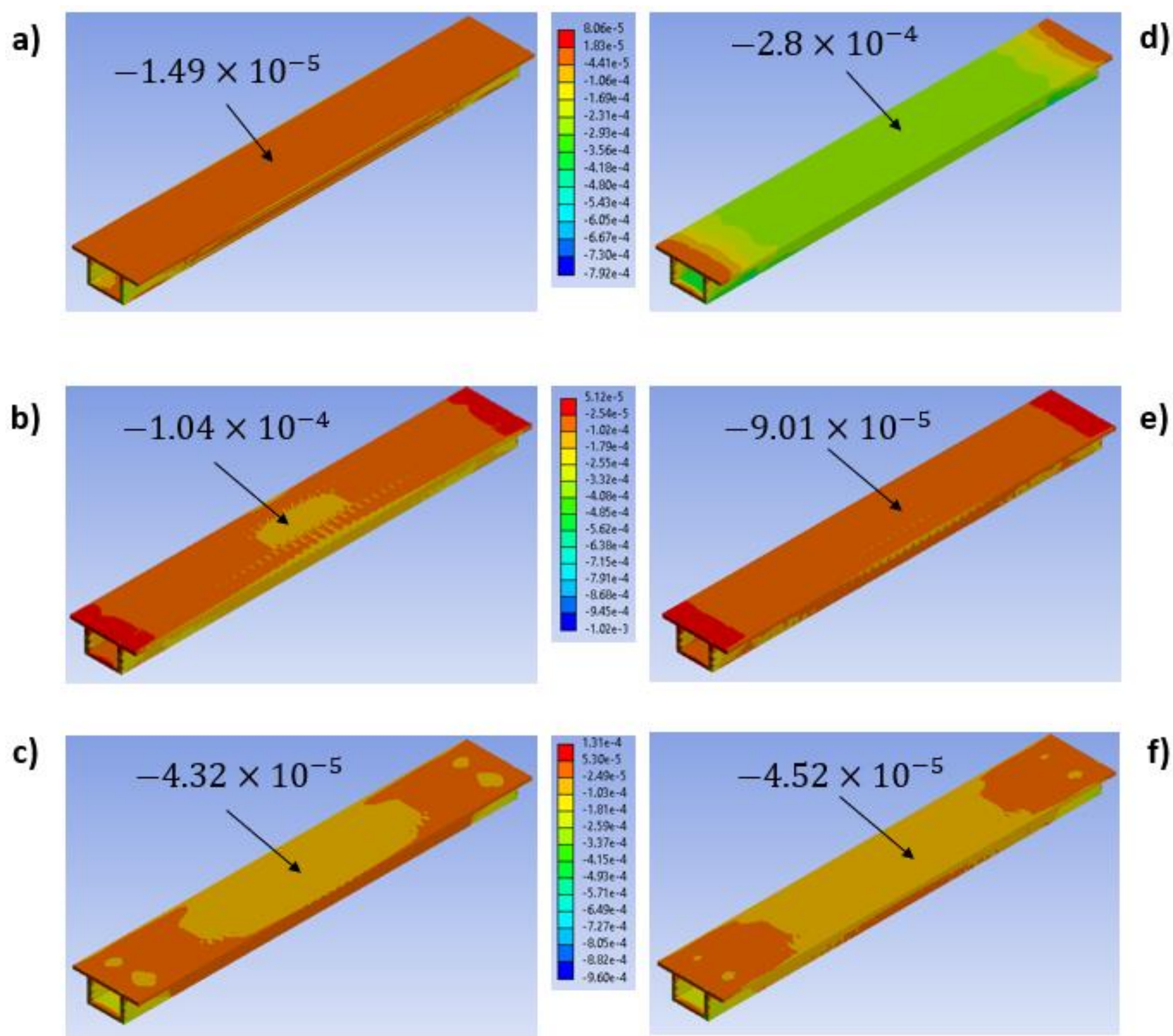

Figure 5.18: Maximum longitudinal compressive strain in simulation with constant ECTE [a) High intensity event, b) medium intensity event, and c) low intensity event] and in simulation with temperature dependent ECTE [d) High intensity event, e) medium intensity event, and f) low intensity event].

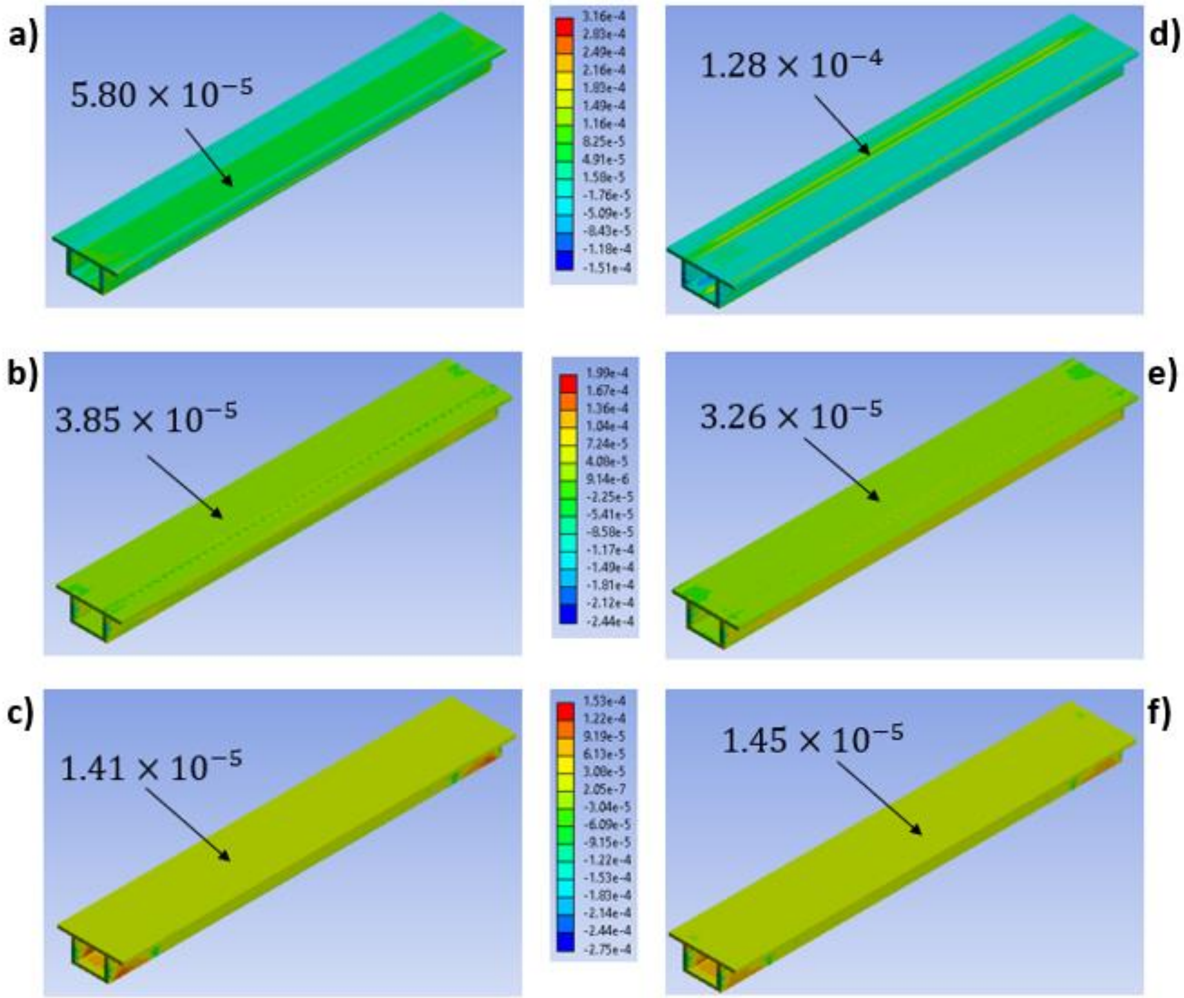

Figure 5.19: Maximum vertical tensile strain in simulation with constant ECTE [a) High intensity event, b) medium intensity event, and c) low intensity event] and in simulation with temperature dependent ECTE [d) High intensity event, e) medium intensity event, and f) low intensity event].

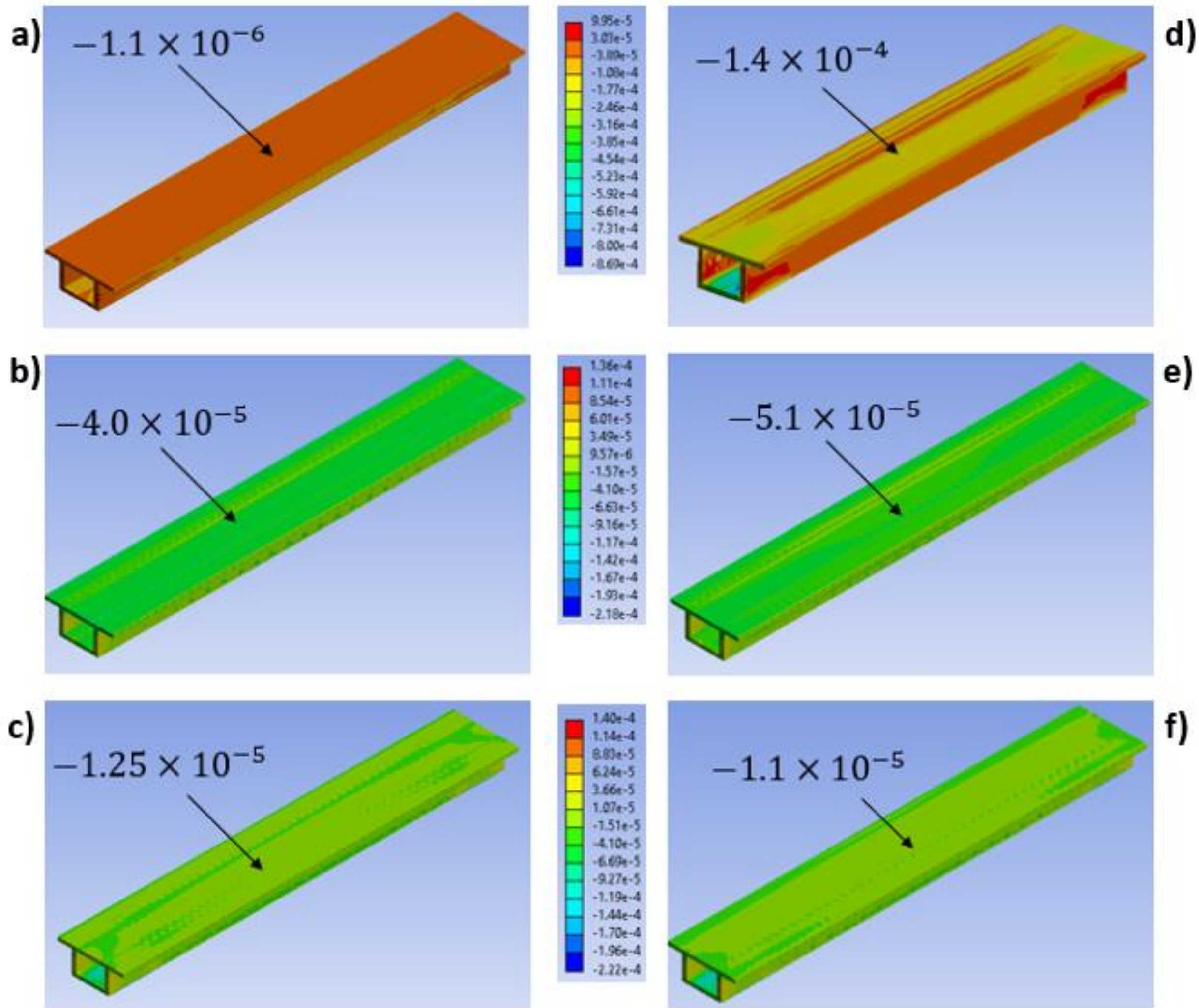

Figure 5.20: Maximum lateral compressive strain in simulation with constant ECTE [a) High intensity event, b) medium intensity event, and c) low intensity event] and in simulation with temperature dependent ECTE [d) High intensity event, e) medium intensity event, and f) low intensity event].

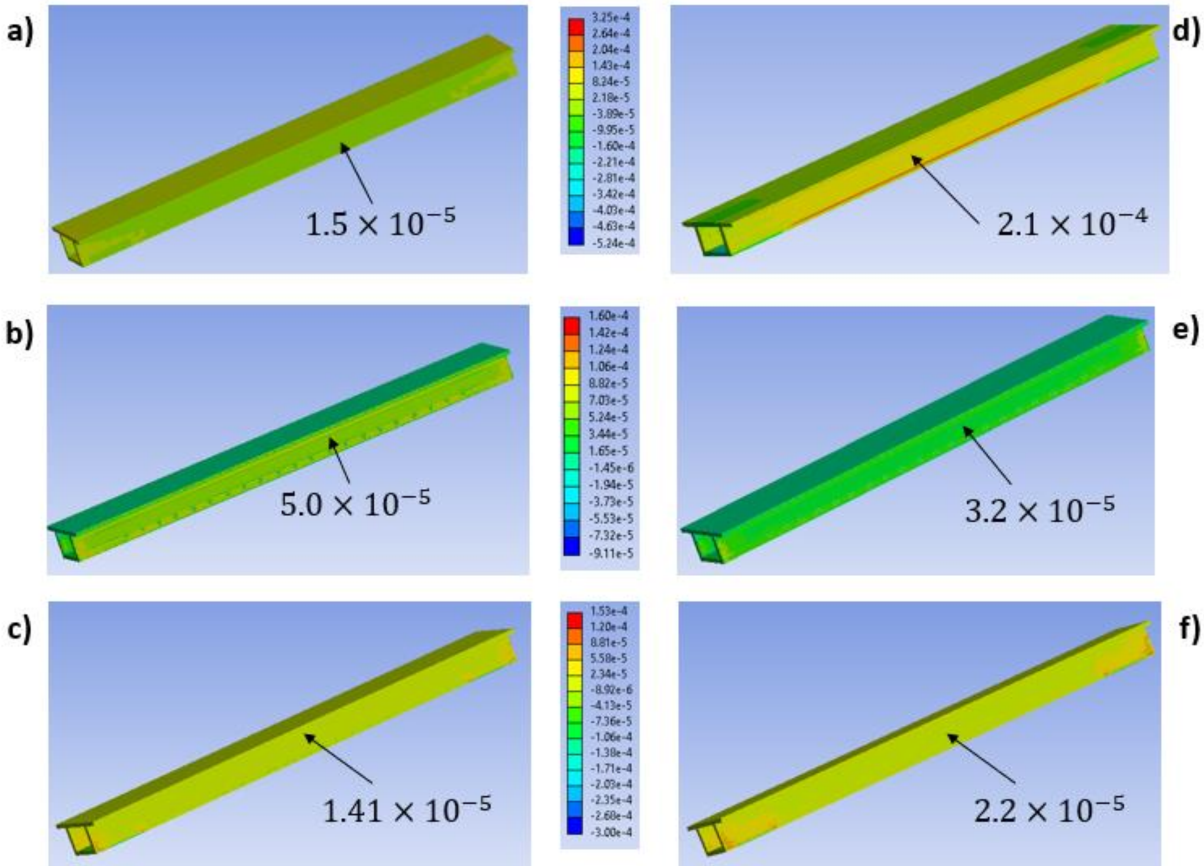

Figure 5.21: Maximum lateral tensile strain in simulation with constant ECTE [a) High intensity event, b) medium intensity event, and c) low intensity event] and in simulation with temperature dependent ECTE [d) High intensity event, e) medium intensity event, and f) low intensity event].

5.8 Appendices

5.8.1 Appendix A

The steps below highlight the process used to determine the critical points in the thermal strain versus temperature relationship for a shortened cycle, in which the ice doesn't fully freeze.

1. **Step 1**: Determine coordinates of Point H. This is easily achieved since Point H belongs to Segment BC and the X-coordinate of point B is known (i.e., minimum temperature reached).
2. **Step 2**: Determine the coordinates of Point K. The X-coordinate of Point K is equal to the X-coordinate of Point A. The Y-coordinate can be determined using linear interpolation as per Eq. (5.2).

$$y_K = y_C + \frac{(x_H - x_C)(y_B - y_C)}{x_B - x_C} \tag{5.2}$$

3. **Step 3**: Determine the X-coordinates of Point J so that:

$$\frac{Projection(BH) on\ horizontal}{Projection(BC) on\ horizontal} = \frac{Projection(BJ) on\ horizontal}{Projection(BF) on\ horizontal} \rightarrow x_J = x_B + \frac{(x_H - x_B)(x_F - x_B)}{x_B - x_C} \tag{5.3}$$

4. **Step 4**: Determine the Y-coordinates of Point J. This can be done by using the slope of segment JK (equal to slope 6) and the X-coordinate of Point J.
5. **Step 5**: Determine the coordinates of Point I. The coordinates can be found as the intersection of segment HI (slope HI equal to slope 4) and segment IJ (slope IJ equal to slope 5)

5.8.2 Appendix B

Figures 5.22-5.25 show the prestressing tendons and non prestressed reinforcement in the webs, top slab, bottom slab and the cross section. Note that the color blue represents the outline of the structure.

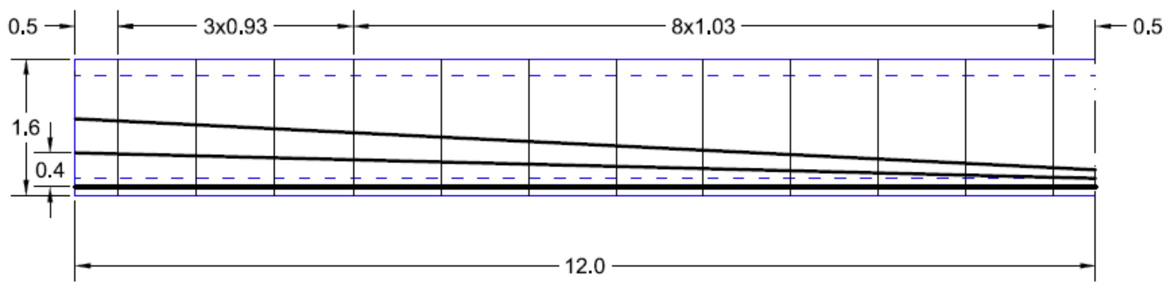

Figure 5.22: Web reinforcement. Lateral and transvers reinforcement in the slabs not shown.

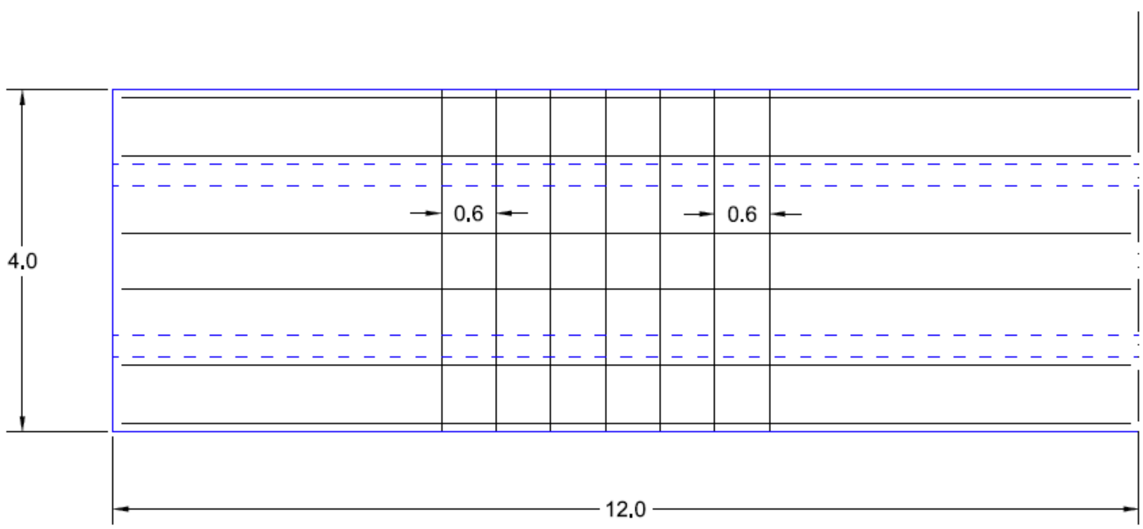

Figure 5.23: Top slab non prestressed reinforcement.

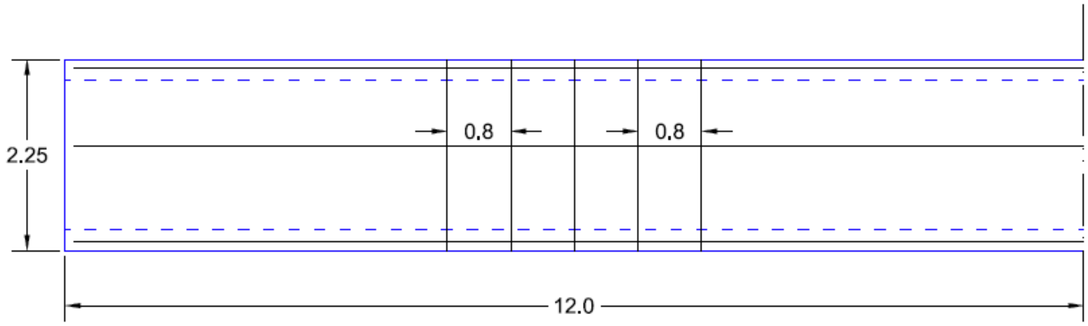

Figure 5.24: Bottom slab non prestressed reinforcement.

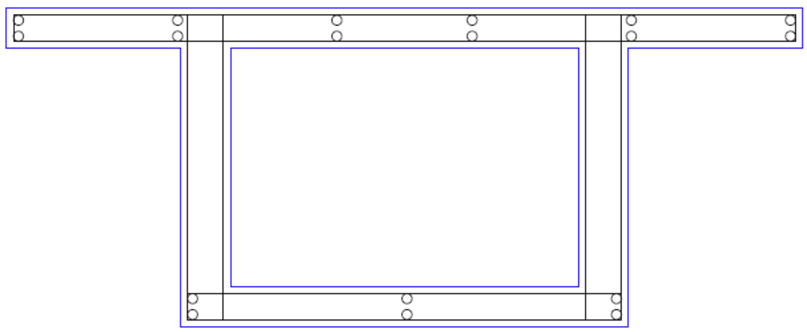

Figure 5.25: Cross section non prestressed reinforcement.

Chapter **VI**

The Effect of Climate Change on Thermal Loads in Concrete Box Girders

<u>Note:</u> The content of this chapter is presented as submitted for publication in the Journal of Bridge Engineering. The format (headings, caption numbering, and citations) has been edited to match the thesis format.

6.1 Introduction

Bridges are essential components of our transportation infrastructure, providing safe and efficient passage for vehicles, pedestrians, and cargo, over rivers, valleys, and other obstacles. However, bridges are subject to a wide range of environmental stressors that can cause damage and shorten their lifespan. One of the most significant stressors are the temperature changes that occur continuously and may cause significant thermal effects (e.g., restrained expansion, or cracking) on bridge decks.

The temperature distribution within a structure may be decomposed into several parts, including a uniform temperature across the entire section, linear vertical and horizontal temperature gradients, and a non-linear gradient. The uniform temperature component is mainly due to long-term changes in the ambient conditions (e.g., the average temperature shift occurring during seasonal changes), whereas the gradients arise over shorter periods of time (Larsson 2012). The uniform temperature component can cause bridge decks to expand and contract, leading to cracks and other forms of damage. On the other hand, thermal gradients across the bridge deck may lead to differential expansion and contraction that can cause warping, twisting, and other forms of deformation (Larsson 2012).

The thermal effects on bridge decks are influenced by several factors, including the material properties of the bridge deck, the local climate, and the intensity and frequency of temperature fluctuations. To mitigate thermal effects on bridge decks, many bridge design codes, such as the AASHTO LRFD Bridge Design Specifications

(AASHTO 2012) and the Canadian Highway Bridge Design Code (CSA 2014), include guidelines for addressing thermal loads (Figure 6.1). Nonetheless, when dealing with thermal impacts, a prominent challenge within the realm of bridge engineering arises when aiming for extended design lifespans – namely, the anticipated alterations in climate conditions expected over the course of the next century. Bridge codes traditionally rely on the extrapolation of historical climate data for predicting future environmental loads. These data are subsequently subjected to rigorous statistical analysis to establish design values for a range of prospective environmental variables, including wind speeds, temperatures, precipitation, rainfall intensity, and snow-related impacts. The probability of occurrence of these design events is typically $1/n$, where n is the return period. However, due to climate change, the return period for these design events is decreasing, resulting in a higher frequency of exposure to events that were once considered extreme (Meehl et al. 2000). Consequently, bridge structures can encounter extreme events that exceed the structural criteria prescribed by the design codes throughout their operational lifespan.

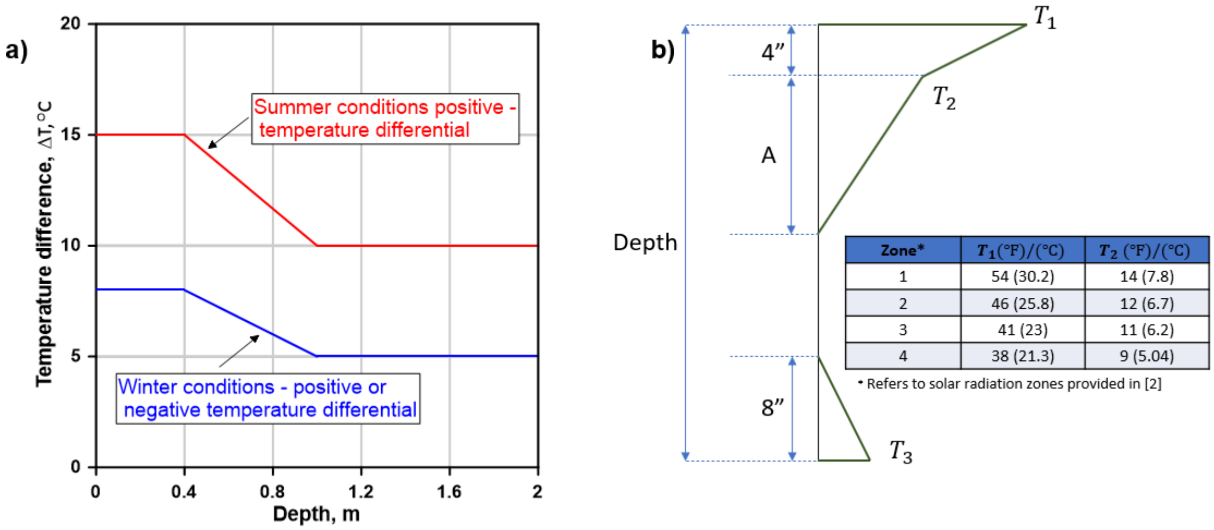

Figure 6.1: a) CHBDC prescribed differential between the top and bottom of the bridge cross section. Modified from (CSA 2014). b) AASHTO prescribed temperature differential in a concrete cross section (dimensions in inches). Modified from (AASHTO 2012).

Hence, it is imperative that bridge codes around the world undergo revisions to align with the forthcoming climate-induced demands. However, this endeavor will necessitate substantial dedication and close collaboration between engineers and climate scientists. To project thermal loads for future climatic conditions, several hurdles must be surmounted, including: the lack of familiarity among bridge engineers with climate change scenarios and their assessment, the absence of future climate data with the necessary spatial and temporal resolution for such assessment, the sheer multitude of Global Climate Models (GCMs) and emission scenarios to consider, and the unavailability of many of the required climate variables for such an evaluation. Currently, the peer-reviewed literature lacks information on methods for predicting thermal loads on bridges in the context of future climatic conditions and the potential ramifications for bridge structures.

The objective of this chapter is threefold: 1) to provide guidance to engineers on climate modelling procedures (their limitations, their implications, and their application), 2) to quantify the interaction between climate variables and thermal differentials in bridges, and 3) to determine the effect of climate change on thermal differentials in bridges. The first objective is achieved by employing a methodology by which future climate projections from several climate models and different emission scenarios are downscaled using a weather generator. The projections are downscaled on both a temporal and spatial scale so that they can be used in assessments such as thermal modelling in bridges. This methodology is applicable not only to bridge engineering but also to other engineering disciplines for such situations requiring the forecasting of future hourly climate data at the spatial scale essential for comprehensive assessment. The second objective is achieved through the development of a finite element 3D thermal model of the bridge structure. The final objective is accomplished by using the generated climate data as a boundary condition in the thermal finite element model to determine the potential effect of climate change for different emission scenarios on the thermal gradients that could potentially develop in the bridge. To illustrate the conceptual framework, we examine two distinct emission scenarios while focusing on an idealized concrete box girder bridge situated in two markedly disparate Canadian locations: Toronto, Ontario, and Whitehorse, Yukon. The methodology developed as part of this research is summarized in Figure 6.2 and detailed in the sections below.

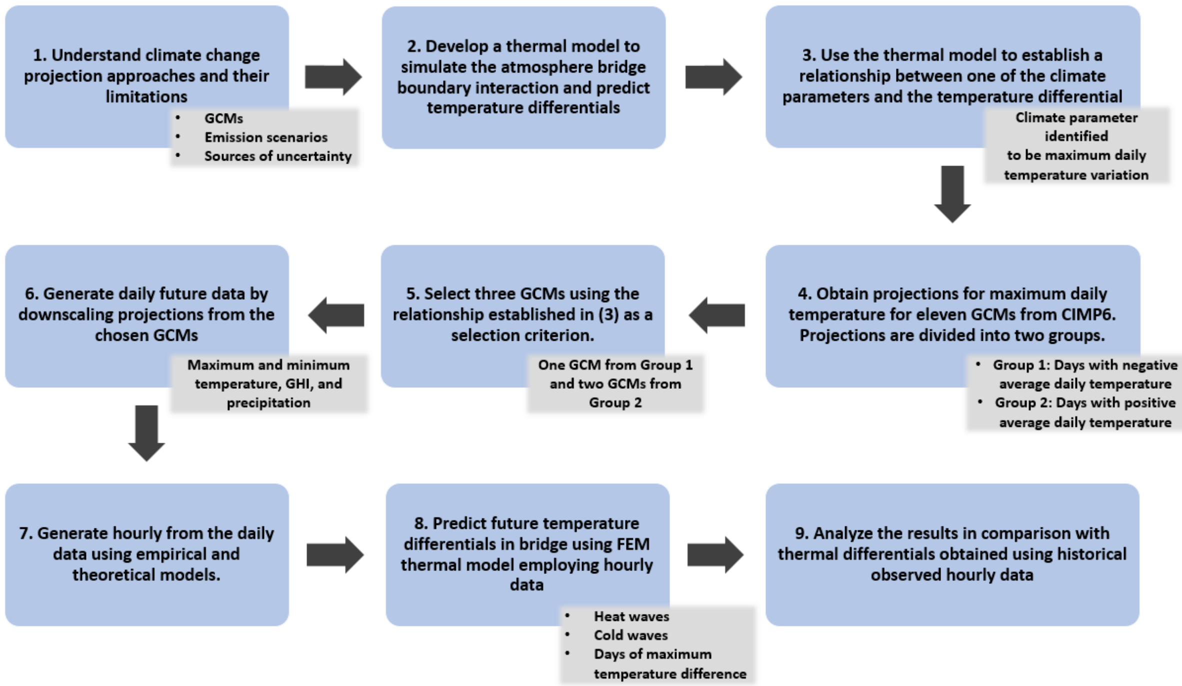

Figure 6.2: Flow chart summarizing the methodology followed.

6.2 Climate change projections: An overview

Global Climate Models (GCMs) are used to perform climate projections. These models are designed to simulate the physical processes that determine the global climate, using mathematical formulae to represent atmospheric and oceanic processes. GCMs consider past and present empirical evidence and attempt to project future conditions (Wayne 2014). GCMs encompass the modeling of various physical processes, including but not limited to convection, solar radiation, infrared radiation, cloud formation, and transpiration.

While Global Climate Models (GCMs) are powerful tools for predicting future climate, they also have some limitations in terms of their spatial resolution, parameterization, complexity, boundary conditions, confidence in assessing future emissions, and natural variability (Bader et al. 2008; Lupo et al. 2013; Hartmann et al. 2015). The resolution limitation refers to the inability of climate models to capture small scale features at a local level (i.e., the topography or weather at a specific location) which limits the model's ability to predict local climate and extreme events. Furthermore, it is necessary in the GCMs to rely on the parameterization (i.e., simplification) of complex processes and phenomena which can increase the uncertainty of any projections made. These phenomena include cloud formation physics, ocean mixing, as well as other land surface processes. Another issue for GCMs is that they require significant computational resources due to their high complexity. Access to such computational power may not always be available. Furthermore, to make future projections, GCMs must make assumptions about future greenhouse gas emissions. The uncertainties in these assumptions will in turn lead to uncertainties in the model predictions. Moreover, the boundary conditions of GCMs can significantly influence their results. These include sea surface temperature, ice conditions, and Ocean Inflow/Outflow. Finally, GCMs do not consider the natural variability of earth's climate system (phenomena such as El Niño/La Niña, the North Atlantic Oscillation, and the Pacific Decadal Oscillation) or are unable to separate these effects from the effect of climate change. GCMs perform best in simulating global mean surface temperature, large-scale atmospheric circulations (such as the position and strength of the jet stream), precipitation, as well as ocean circulation.

With all the limitations and uncertainties associated with GCMs, a need for guidance and standardized climate simulations emerged. For this reason, the Coupled Model Intercomparison Project (CIMP) was founded. This is a collaborative effort within the global climate modeling community to improve understanding of the Earth's climate system and to provide a basis for assessing the potential impacts of climate change (Wayne 2014). CMIP5 and CMIP6 are both phases of the Coupled Model Intercomparison Project. CMIP5, which ran from 2008 to 2014, was a major international climate modeling effort involving 20 modeling groups from around the world (Meehl and Bony 2011). The models were used to produce simulations for different climate change scenarios, including historical, current, and future conditions, with a focus on the period from 2006 to 2100. The results from these simulations played a crucial role in shaping the findings of the IPCC Fifth Assessment Report, released between 2013 and 2014 (Meehl and Bony 2011). CMIP6, which began in 2016 and is still ongoing, involves an expanded range of modeling groups and includes more comprehensive simulations than CMIP5. Furthermore, CMIP6 includes higher spatial and temporal resolutions, improved representation of physical processes such as clouds, aerosols, and biogeochemical cycles, and additional components such as ice sheets and ocean ecosystems. The output from CMIP6 simulations formed the basis of the IPCC Sixth Assessment Report (O'Neill et al. 2016).

To perform the simulations discussed above (CMIP5 and CMIP6), emission scenarios had to be developed to predict the amounts of expected future emissions. These scenarios are known as RCP (Representative Concentration Pathways, (CMIP5)) and SSP (Shared Socioeconomic Pathways, (CMIP6)) respectively (Eyring et al.

2016). RCPs focus on greenhouse gas emissions and resulting radiative forcing, while SSPs consider a broader set of social, economic, and technological factors that can influence greenhouse gas emissions and the global climate. While RCPs and SSPs are different, they are both useful for exploring possible future scenarios and assessing the potential impacts of climate change.

There are a total of four RCPs and five SSPs. The four RCPs are known as RCP 2.6, RCP 4.5, RCP 6, and RCP 8.5. The number in the RCP identification code represents the projected level of radiative forcing by the end of the year 2100 where the term *radiative forcing* is the measure of how much extra energy, resulting from human activity, the earth will retain in comparison with pre-industrial times (Wayne 2014). RCP 2.6 is representative of the best-case scenario which leads to a low concentration of greenhouse gas emissions. RCPs 4.5 and 6 are stabilization scenarios in which the levels of radiative forcing are stabilized by the year 2100. Furthermore, RCP 8.5 is characterized by increasing greenhouse gas emissions over time as radiative forcing levels reach $8.5\ W/m^2$ by 2100 and continue rising (Wayne 2014). The Shared Socioeconomic Pathways (SSPs) encompass five distinct scenarios that offer a comprehensive view of potential future societal trajectories. SSP 1 embodies a sustainable future characterized by low inequality and controlled population growth. SSP 2 outlines a moderate scenario with intermediate levels of inequality and population growth. In contrast, SSP 3 portrays a scenario marked by regional rivalry, heightened conflict, nationalism, and high levels of population growth and inequality. SSP 4 is characterized by robust economic growth but limited progress in sustainability and climate mitigation. Finally, SSP 5 represents the most concerning scenario, marked by high economic growth and substantial fossil fuel consumption, resulting in the highest levels of emissions. The resulting greenhouse gas emissions and concentrations were then quantified by studying their implications on energy balance systems and land use changes (O'Neill et al. 2016; Eyring et al. 2016; Bauer et al. 2017; Popp et al. 2017). These scenarios (SSPS and RCPs) can then be used by climate modelers in the respective GCM's to project trends for different climate parameters. Note that within each SSP, there are different scenarios which represent different radiative levels. For example, SSP5-8.5 refers to SSP 5 with a radiative forcing of $8.5\ W/m^2$. Figure 6.3 shows the historical and projected annual levels of CO_2 emissions between the years 1950 – 2100 for the four RCPs and certain SSPs.

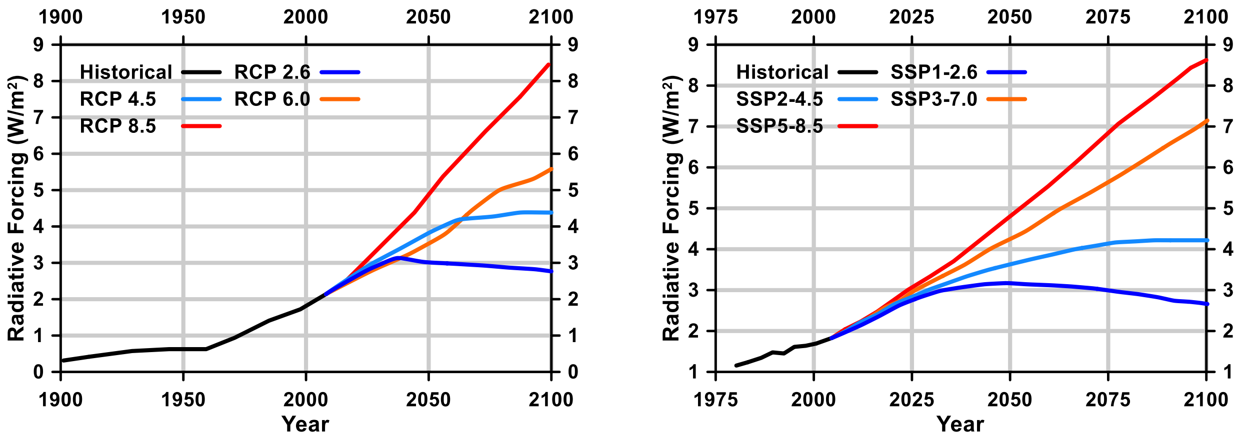

Figure 6.3: Emission levels for different RCPs and SSPs (taken from (Meehl et al. 2000; Wayne 2014)).

6.3 Thermal model with bridge-atmosphere boundary

To predict the impact of climate change on thermal loads, it is essential to thoroughly investigate the interaction between the various climate parameters and the bridge boundaries. This investigation helps identify the various climate parameters that influence the thermal variations in bridges. An investigation of this kind is essential for any study that intends to use future climate projections for any application since it allows researchers to better understand the uncertainties associated with the research. It is important to emphasize that in this study, the interaction between the climate and the bridge surfaces, which governs the temperature distribution within the bridge, is referred to as the 'atmosphere-bridge boundary' interaction, and it has been extensively examined by the author before (Saad et al. 2022; Chapters II and III).

In brief, the atmosphere-bridge boundary interaction is governed by three primary processes, which can be categorized as follows: 1) convection heat transfer occurring between the bridge surfaces and the surrounding air, 2) the exchange of shortwave (solar) radiation between the bridge and its immediate environment, and 3) the exchange of longwave radiation between the bridge surfaces and any other adjacent surfaces within the bridge vicinity. Convective heat transfer is a function of windspeed and the ambient air temperature in the vicinity of the bridge. On the other hand, the shortwave radiation exchange is a function of the incoming solar radiation and its components (the direct radiation, the diffuse radiation, and the reflected radiation). The shortwave radiation exchange is also dependent on the geographic location of the bridge and its geometry. The longwave radiation exchange can be estimated based on the dew point temperature, the ambient temperature, and the cloud cover.

The atmospheric bridge boundary interaction was used to develop a 3D thermal finite element model using the ANSYS finite element platform (ANSYS 2019). The model employs the aforementioned climate variables (including dew point temperature, ambient temperature, cloud cover, solar radiation, and windspeed) as boundary conditions to simulate the interaction between the atmosphere and the bridge boundary. The output of this analysis is the temperature distribution within the bridge deck. That, in turn, may be used to determine the thermal gradient developed in the bridge cross section at any point in time. A comprehensive discussion and validation of the Finite Element Model can be found in (Saad et al. 2022). It is used here in conjugation with observed historical climate data and GCM generated future climate projections, in order to predict the impact of climate change on thermal loads in bridges.

6.4 GCM selection criteria

Even though the Coupled Model Intercomparison Project has standardized the guidance for global climate models, there are still several global climate models, each yielding different predictions for different time periods across the world. Hence, undertaking a comprehensive study encompassing all available climate models presents a considerable challenge due to the substantial time and resources it demands. One way in which the resource allocation can be reduced is by selecting a few representative GCMs rather than using all the available ones. Therefore, it became necessary to establish a criterion for selecting and eliminating models. In this study, the chosen approach involves concentrating on a specific climate variable and comparing the projections provided by different climate models for that variable. The selection of Global Climate Models (GCMs) is then contingent on how the selected variable influences thermal differentials within the bridge. However, lingering questions remain regarding which climate variable should serve as the foundation for this selection process.

Given the constraints in forecasting future climate conditions and the influential factors shaping temperature variations in a bridge deck, it is reasonable to assert that the primary climate variable with a reasonably predictable nature and substantial impact on bridge temperature is the ambient temperature. In contrast, the other two pivotal factors in bridge boundary interactions—solar radiation and windspeed—carry a notable level of uncertainty in future projections, making them less reliable for this purpose. Consequently, temperature projections were employed as the foundational criterion for selecting Global Climate Models (GCMs).

To determine a relationship between ambient temperature and the resulting temperature differential in the bridge deck, twelve thermal finite element simulations on a 10 m long concrete box girder were performed (Figure 6.4 shows the box girder cross section). Each simulation considered a time span of seven consecutive days of historical climate data for Old Crow, Yukon in Canada. The simulations were chosen to represent a wide range of temperatures and to also ensure a wide variety of maximum daily temperature differences. Moreover, the twelve simulations were split into two groups of six, each based on the average daily temperature of the days within each simulation. The average daily temperature for all days in the first group (Group 1) was negative while the average daily temperature for all days in the second group (Group 2) was positive. The simulations were used to extract the maximum positive temperature differential that occurred in the deck during each day (a total of 84 days). Additional details on the thermal model and thermal simulations are provided in Appendix A and Appendix B respectively.

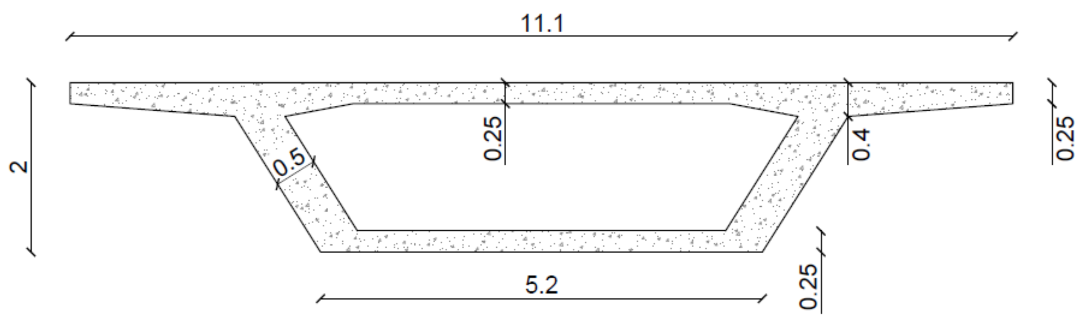

Figure 6.4: Box girder cross section. All dimensions are in m.

After scrutinizing the results, a robust linear relationship emerged between the peak temperature differential in the bridge and the maximum daily ambient temperature difference (difference between the maximum and minimum near surface temperature recorded during the day). These findings have been graphically represented in Figure 6.5. It's essential to note that the analysis excluded the first day of each simulation to accommodate initial conditions. Consequently, the inference drawn was that the anticipated maximum daily temperature difference serves as a viable criterion for selecting global climate models for the scrutiny of thermal loads in future scenarios. Moreover, an interesting observation is the variation in the slope of the resulting linear relationship between Groups 1 and 2.

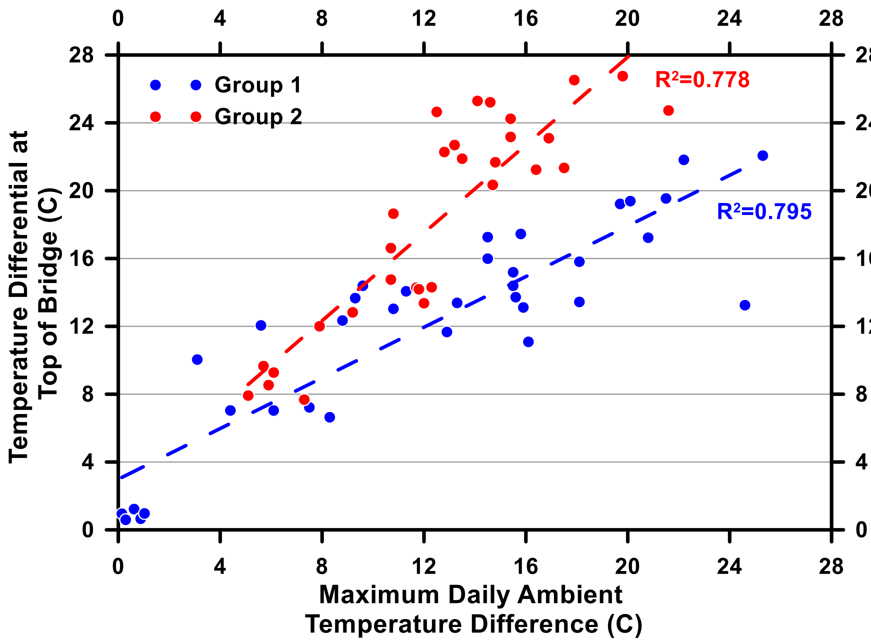

Figure 6.5: Maximum temperature differential at the top of the bridge against the maximum daily ambient temperature difference.

6.5 GCM selection: A demonstration of methodology

Next, GCMs were selected for two different geographic locations (Toronto (43.65 N, 79.4 W) and Whitehorse (60.7 N, 135.1 W)). The minimum and maximum daily projected temperature data up to the year 2100 were analyzed for eleven different CMIP6 GCMs. The scenarios considered were SSP2-4.5 and SSP5-8.5 for all models since SSP2-4.5 is the most likely scenario to occur whereas SSP5-8.5 is the worst-case scenario. In the following example, the approach used will be demonstrated for SSP5-8.5 for Toronto. Note that all the models that give daily projections for the location (Toronto, Ontario) and time period (1976-2100) were considered. The eleven models used are shown in Table 6.1.

The global maximum and minimum daily temperature projections from these models were obtained from (Climate Data Store 2021). The maximum temperature difference for each day between 2020 – 2100 is then determined. The next step was to determine the maximum daily temperature difference that occurred within each year. However, rather than calculating a single value for each year, the year was divided into two segments: the first part comprises days with a negative average temperature, while the second part includes days with a positive average temperature. This division acknowledges the potential variance in bridge response based on whether the average temperature is positive or negative, as illustrated in Group 1 and Group 2 above (Figure 6.5) for the case of Old Crow. Thus, two values for each year were obtained such that:

- $\Delta T_{Max,\,1}$ is the maximum daily temperature difference that occurred over the part of the year with a negative average ambient temperature.
- $\Delta T_{Max,\,2}$ is the maximum daily temperature difference that occurred over the part of the year with a positive average ambient temperature.

Afterwards, the maximum value of $\Delta T_{Max,\,1}$ and $\Delta T_{Max,\,2}$ was found over every ten-year period i.e., $2020-2030$, $2030-2040$, $2040-2050$ and so forth. The results for the different models and the two groups are shown in Figures 6.6 and 6.7.

Table 6.1: Selected Models for Toronto for SSP8.5.

Global Climate Models (GCMs)			
NorESM2-MM	BCC-CSM2-MR	CESM2	ACCESS-CM2
CanESM5	INM-CM5-0	CESM2-WACCM	NorESM2-LM
CMCC-ESM2	EC-Earth3-CC	AWI-CM-1-MP	

The results of Figures 6.6 and 6.7 were then analyzed in order to select models that predict the largest increase in maximum daily temperature difference. The objective was to select a total of three models with one being selected from Group 1 and two from Group 2 since the maximum daily temperature differences were larger in Group 2. The BCC-CSM2-MR, EC-EARTH3-CC, and the CESM2 models showed the highest value of future maximum daily temperature difference (28.3℃, 26.5℃, and 27.5℃ respectively) for Group 1 (Figure 6.6). The BCC-CSM2-MR model also projected high values of maximum daily temperature difference in Group 2. Thus, the **BCC-CSM2-MR** model was chosen as one of the three models. Similarly, the **NorESM2-LM** model and the **EC-Earth3-CC** model were chosen from the analysis of Figure 6.7. These two models were selected since they represented the second and third-largest maximum daily temperature differences throughout the century (the

BCC-CSM2-MR model having previously been chosen). Furthermore, the number of events that exceeded the maximum historic temperature difference (22℃ and 24℃ for Group 1 and Group 2) was considered (Figure 6.8). The results showed that the chosen models have the highest frequency of events exceeding the historical maxima. The models chosen for the remaining emission scenarios and locations are presented in the results section.

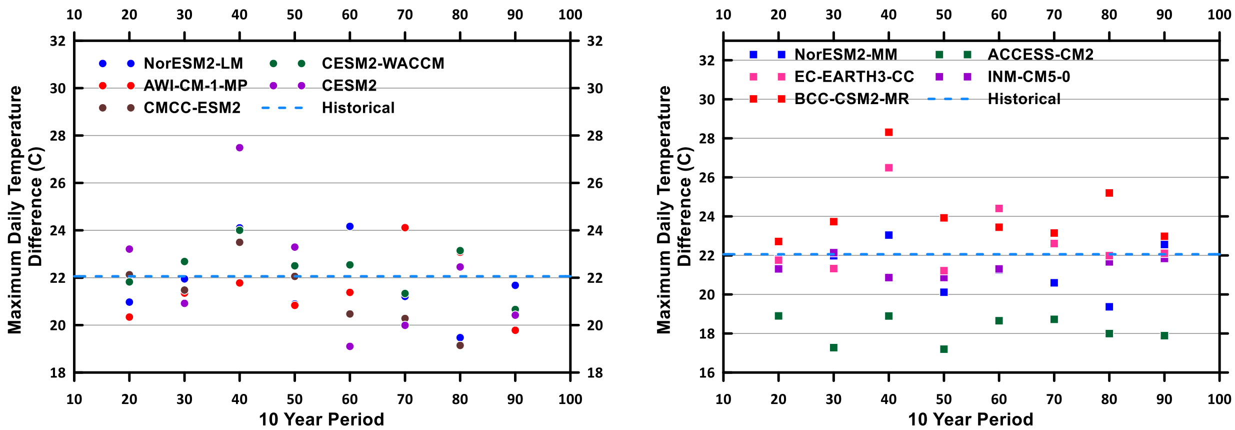

Figure 6.6: Projected maximum daily temperature difference in Toronto for Group 1 for all Models for SSP5-8.5.

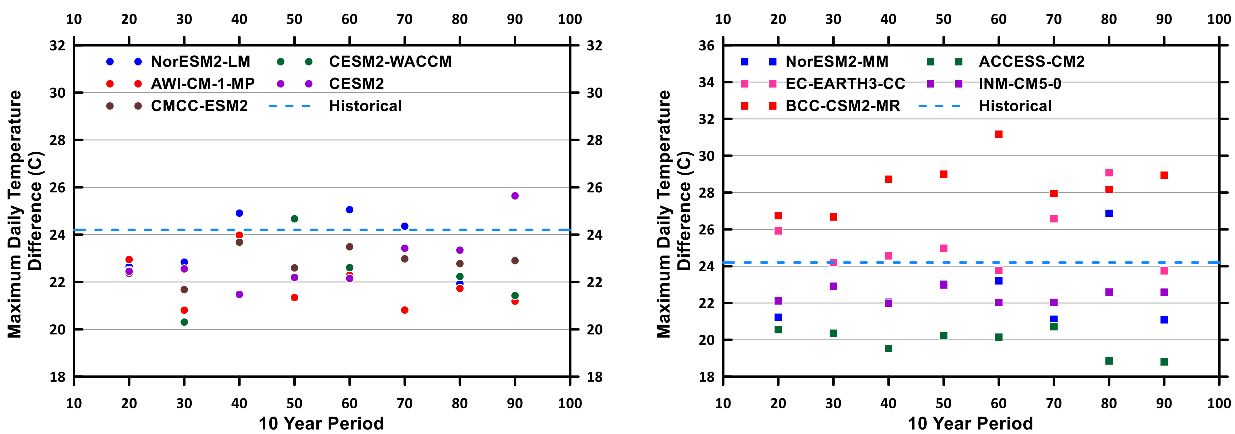

Figure 6.7: Projected maximum daily temperature difference in Toronto for Group 2 for all Models for SSP5-8.5.

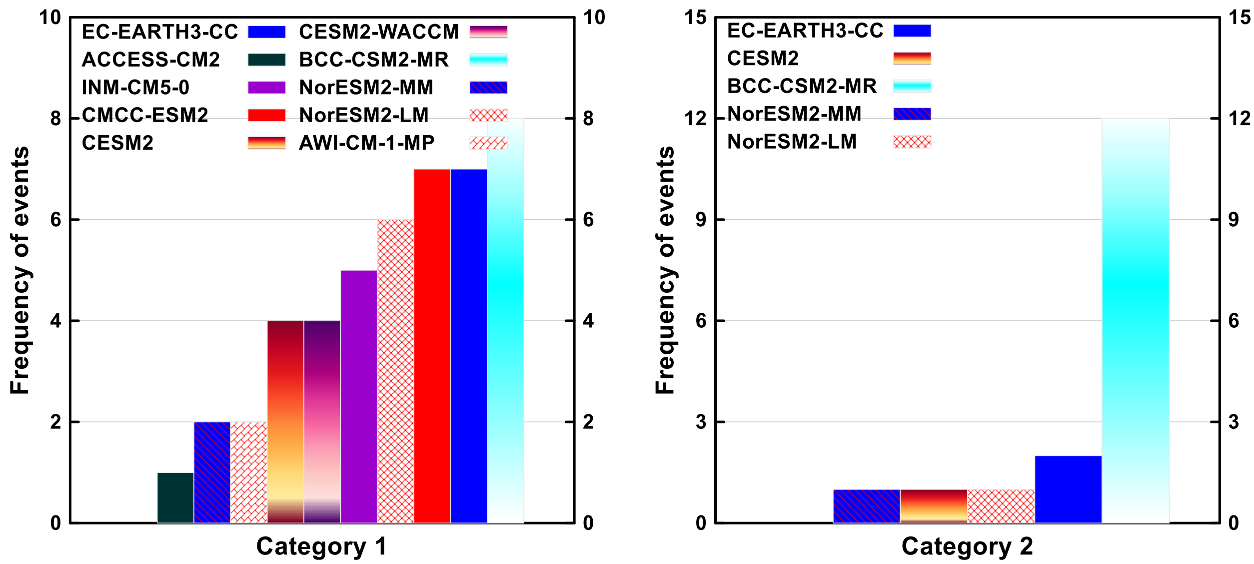

Figure 6.8: Number of events exceeding the maximum historic temperature difference for Group 1 and Group 2.

6.6 Downscaling using a climate generator

Having selected the global models to be used for future simulations, the next step in this study was to obtain future projected data for the required spatial and temporal scale which will then be used to perform the thermal finite element simulations. The projections from these models cannot be used directly and must first undergo a process known as downscaling. A brief overview of the process of downscaling and its purpose is provided in the following section, along with a demonstration of the approach followed for downscaling in this study.

Generally, global climate models provide predictions on a large scale with a resolution of about $100\ km$ or more. This means that the Earth's surface is divided into grid cells that are $100\ km$ by $100\ km$ along each side. In each grid cell, climate variables such as temperature and rainfall, and even the topography, have a single average value. This means global climate models do not incorporate the regional detail of climate change at local scales. The models cannot distinguish between valleys, coastlines, and mountains within a single grid cell. Moreover, it is currently not possible to use a finer grid, as that would require more computer resources than are presently available. For this level of detail, local climate projections are obtained from global climate models using a process known as downscaling. Downscaling can be defined as any procedure which is used to infer high resolution information from low resolution variables. Two types of downscaling can be used: Statistical and Dynamic downscaling (Wilby and Wigley 1997).

Dynamic downscaling involves using the output from the GCM to drive a regional, numerical model in higher spatial resolution, which can simulate local conditions in greater detail. Statistical downscaling involves establishing a statistical relationship between the output of GCMs and local or regional climate variables. These relationships are often based on historical climate and weather data and can be applied to the GCM output to produce downscaled climate projections for specific locations or regions (Wilby and Wigley 1997).

Downscaling climate projections for use in civil engineering applications is not a straightforward process, particularly in the case of dynamic downscaling, due to its increased complexity and computational intensity (ASCE 2015). Therefore, this study will be using a statistical downscaling technique to predict future climate data at a local scale. One effective and simple method for statistical downscaling is the use of a stochastic weather generator which produces synthetic time series of weather data of unlimited length for a location, based on the statistical characteristics of the weather observed at that location. The future changes projected by global climate models can be incorporated into the software to predict the future climate at the local level. The use of weather generators for downscaling has been previously discussed and studied in (Wilby and Wigley 1997; King et al. 2009; Munawar et al. 2022).

The weather generator used in this study was LARS-WG (Semenov and Barrow 2002), which can forecast daily values of maximum and minimum temperature, precipitation (mm), and solar radiation ($MJm^{-2}day^{-1}$) for any location. The climate variables required by the LARS-WG program as input are the same as those that the algorithm forecasts for the future (daily maximum and minimum temperature, total daily precipitation (mm), and total daily solar radiation ($MJm^{-2}day^{-1}$)). In this study, the observed historic daily maximum temperature, minimum temperature, and solar radiation (Global horizontal irradiance) for a location, were obtained from the Canadian weather energy and engineering data sets (Environment and Climate Change Canada 2019a). Daily precipitation data for Toronto was obtained from the digital archive of Canadian Climatological Data (Environment and Climate Change Canada 2019b).

The compiled observed data for the location from 1976-2005 is then input into LARS-WG to generate synthetic weather data. The generated synthetic data is calibrated to have the same statistical characteristics as the observed data. The next step is to input the values of future climate change projections that will allow LARS-

WG to generate synthetic future data. Certain GCMs and emission scenarios are built in as default into LARS-WG. Nineteen different GCMs from CMIP5 are available for emission scenarios RCP4.5 and RCP8.5. However, GCMs from CMIP6 are not built into LARS-WG. However, LARS-WG does provide the flexibility to insert climate change projections manually by allowing the user to provide information which LARS-WG then uses to perturb the weather generator parameter files. The necessary information includes the following: relative changes in monthly mean rainfall, relative changes in the duration of wet spells, relative changes in the duration of dry spells, absolute changes in monthly mean minimum temperature, absolute changes in monthly mean maximum temperature, relative changes in daily temperature variability, and relative changes in mean monthly radiation. In this study, the scenarios were inserted manually since models from CMIP6 are being used. The changes required were calculated based on the difference between the projected global future data and the projected historical data from the GCM. The calculated changes for Toronto (SSP5-8.5) are presented and discussed in the section below.

6.7 Future climate data generation

Future data (maximum temperature, minimum temperature, radiation, and precipitation) for the three chosen models was generated using the Lars-WG weather simulator for each location (Toronto and Whitehorse) and emission scenario (SSP2-4.5 AND SSP5-8.5). The simulator uses historical observed data as a starting point and generates future data using projected changes calculated from each climate model (BCC-CSM2-MR, NorESM2-LM, EC-Earth3-CC). A sample of the projected future changes from January to April for each of the models used for Toronto (SSP5-8.5), are shown in Table 6.2. The projected monthly changes shown are an average of the projected monthly changes between the years 2040-2100. The data for the complete year are provided in Appendix C.

Figure 6.9 shows the distribution of the future climate parameters predicted by LARS-WG for Toronto for SSP5-8.5. Note that the precipitation values are omitted from the figure as they are not relevant for the current analysis. The figure shows that the difference in global horizontal irradiance values amongst models and between the models and historic observed distribution is negligible. The BCC-CSM2-MR and NorESM2-LM model predict a significant increase in both the minimum and maximum temperature when compared with the historic values. On the other hand, the EC-Earth3-CC model predicts maximum and minimum temperature values similar to historic values.

Table 6.2: Projected changes for each climate model as input into the weather generator.

Month	Model	ΔR monthly mean rainfall	ΔR durati -on of wet spell	ΔR durati- on of dry spell	ΔA monthly mean min temp.	ΔA monthly mean max temp	ΔR daily temp. variability	ΔR mean monthly radiation
Janu	BCC-CSM2-MR	1.32	0.31	2.57	4.45	2.01	1.16	0.94
	NorESM2-LM	1.08	0.88	1.05	4.69	-2.21	0.81	0.97
	EC-Earth3-CC	1.527	0.52	2.34	5.13	6.98	0.92	1
Feb	BCC-CSM2-MR	1.35	0.28	2.4	6.6	1.94	1.12	0.91
	NorESM2-LM	1.1	0.96	1.14	6.12	3.66	0.99	0.95
	EC-Earth3-CC	1.82	0.481	1.75	5.33	6.93	1.01	1
March	BCC-CSM2-MR	1.37	0.26	2.1	6.21	2.35	0.98	0.9
	NorESM2-LM	1.3	1.01	0.88	3.14	6.29	0.99	0.97
	EC-Earth3-CC	2.038	0.52	1.74	4.91	5.93	0.87	1
April	BCC-CSM2-MR	1.06	0.25	1.8	4.69	3.85	1.05	1.02
	NorESM2-LM	1.17	0.87	1.23	2.86	7.69	0.98	1.01
	EC-Earth3-CC	1.46	0.6	1.71	4.26	4.75	0.95	0.99

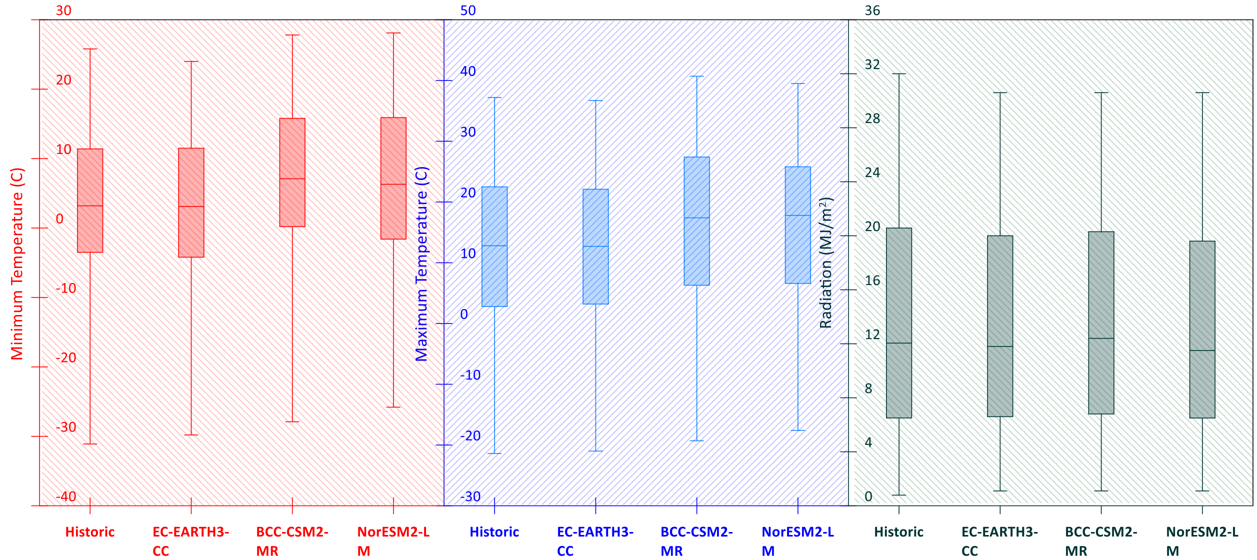

Figure 6.9: Box and whisker plot showing the distribution of maximum temperature, minimum temperature, and radiation generated from LARS-WG for three climate models and compared against historic observed values.

6.7.1 Temperature cycle

Once daily future climate data at a local level was generated by Lars-WG, the next step was to determine a distribution of hourly data for all parameters needed. Hourly temperature distribution can be predicted through an empirical mathematical model, which relies on knowledge of the maximum and minimum daily temperatures (T_x and T_n respectively). In this study, we utilized the sinusoidal model presented in Eq. (6.1) (Wann et al. 1985).

$$T(t) = \begin{cases} \frac{1}{2}(T_x + T_n) - \frac{1}{2}(T_x - T_n)\cos\left[\frac{\pi(t-t_r-\beta)}{\frac{l}{2}+\alpha-\beta}\right] & t_n \le t \le t_x \\ \frac{1}{2}(T_x + T_n') + \frac{1}{2}(T_x - T_n')\cos\frac{\pi[t-\frac{1}{2}(t_r+t_s)-\alpha]}{24-\left(\frac{l}{2}\right)-\alpha+\beta} & t_x \le t \le t_n' \end{cases} \quad (6.1)$$

where, t_s and t_r are the sunset and sunrise time respectively (Wann et al. 1985). t_x is the time of maximum temperature which can be expressed as per Eq. (6.2):

$$t_x = \frac{1}{2}(t_r + t_s) + \alpha$$

(6.2)

where, α is the time difference between t_x and the temperature at midday. Similarly, the time of minimum temperature t_n can be calculated as per Eq. (6.3):

$$t_n = t_r + \beta$$

(6.3)

where, β is the time difference between t_n and the time at sunrise. Furthermore, Eq. (6.4) must be satisfied to guarantee that the minimum temperature will occur before the time of maximum temperature and that maximum temperature will occur before sunset.

$$\frac{1}{2}(t_r - t_s) + \beta < \alpha < \frac{1}{2}(t_s - t_r)$$

(6.4)

Daylength l in Eq. (6.1) was calculated as $t_s - t_r$ and $t_n{}'$ is the time of minimum temperature for the day after the day for which the temperature cycle is being modelled. The sunrise and sunset days for Toronto were determined from (Thorsen 2023) while the times of maximum and minimum temperature were obtained from (Weather Stats 2023).

This model was then verified by comparing the simulated temperatures to the observed temperatures recorded over Toronto for two time periods selected at random (July 5-7, 1987, and October 16-18, 1996). The results indicate close proximity between the simulated and observed temperatures as shown in Figure 6.10.

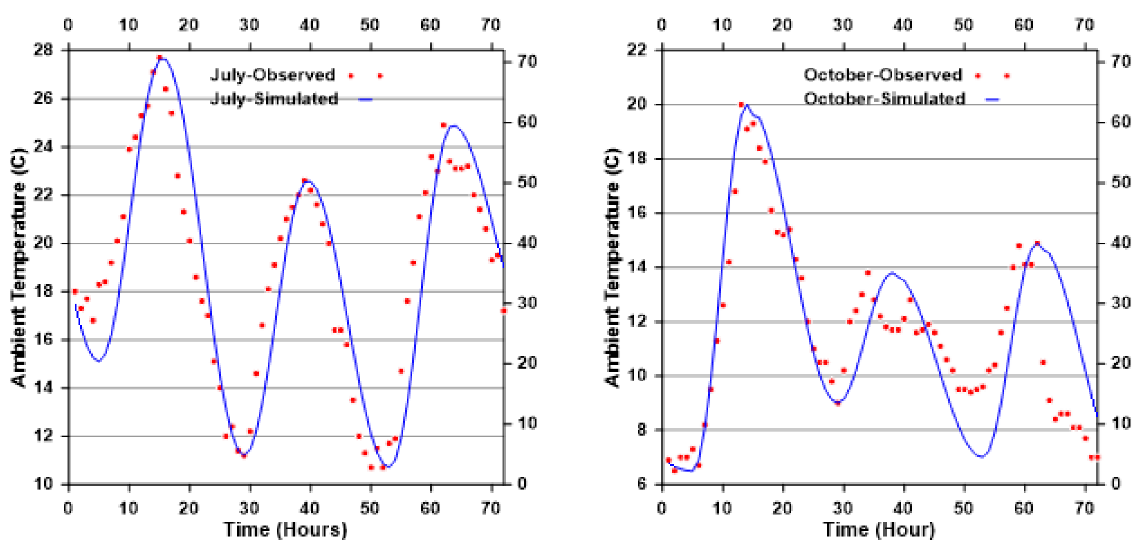

Figure 6.10: Observed temperatures versus simulated temperatures in Toronto for July 5-7, 1987, and October 16-18, 1996.

6.7.2 Dew point temperature

After simulating the hourly ambient temperature, the next step was to simulate the hourly dew point temperature. The LARS-WG generator doesn't provide any information on the dew point temperature and thus it becomes necessary to estimate the dew point temperature from the available ambient temperature data. This was achieved through the use of an empirical model developed in (Kimball et al. 1997) which uses daily air temperature data, the daily potential evaporation ($l_{EP,day}$), and annual precipitation ($l_{P,ann}$) to predict the dew point temperature ($T_{d,est}$). The model can be expressed as shown in Eq. (6.5):

$$T_{d,est} = T_n(-0.127 + 1.121(1.003 - 1.44EF + 12.312EF^2 - 32.76EF^3) + 0.0006(T_x - T_n)] \quad (6.5)$$

where, $EF = l_{EP,day}/l_{P,ann}$. The value of $l_{P,ann}$ can be calculated using the daily precipitation data which is available as an output from LARS-WG. The daily potential evaporation can be estimated as per Eq. (6.6),

$$l_{EP,day} = 0.0023 \times R_a(T_s + 17.8) \times T_R^{0.5} \quad (6.6)$$

where, R_a is the extraterrestrial solar radiation (mm/day), T_c is the average of the maximum and minimum daily temperature ($(T_s = 0.5(T_x + T_n))$), and T_R is the difference between the maximum and minimum daily temperature ($T_R = T_x - T_n$) (Torres et al. 2011). The calculation procedure for R_a is shown in Appendix D.

To verify this estimation model, the simulated daily dew point temperature for Toronto over a 100-day period (from Jan 1- April 10, 1976), was compared against the observed dew point temperature at that location. The results (shown in Figure 6.11) show close proximity and it was concluded that this model can be used for the purpose of this study.

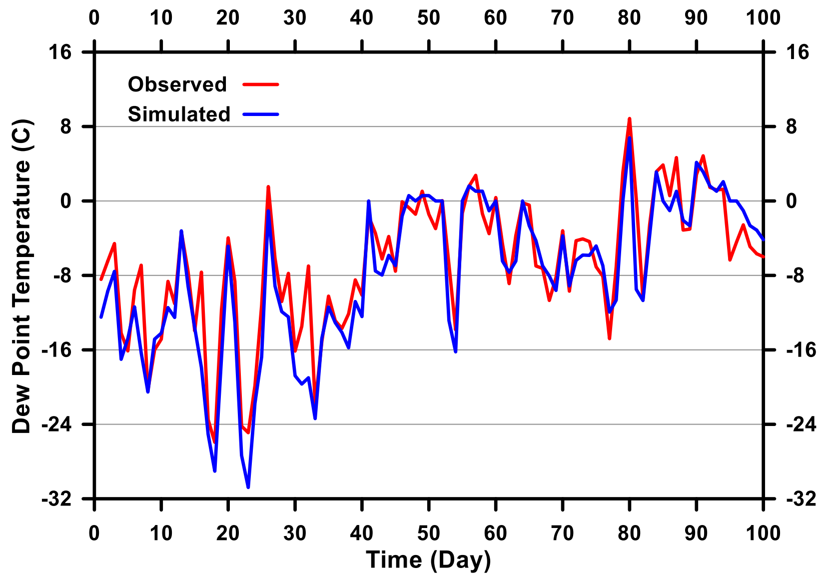

Figure 6.11: Simulated and observed daily dew point temperature for Toronto (from Jan 1- April 10, 1976).

The next step was to estimate the hourly dew point temperature from the estimated daily dew point temperature. The value of the daily relative humidity must be obtained for this estimation. This can be achieved using the daily ambient and dew point temperature values based on the relations shown in Eq. (6.7).

$$T_{dew} = \frac{237.7 \ln[\frac{e_a(T)}{0.6108}]}{17.27 - \ln[\frac{e_a(T)}{0.6108}]} \quad and\ e_a(T) = e_s(T) \times RH \tag{6.7}$$

where, $e_a(T)$, $e_s(T)$, and RH are the actual vapor pressure, the saturation vapor pressure, and the relative humidity respectively (Upreti and Ojha 2017). The next step was to determine the historic (averaged over a 30-year period from 1976-2005) relative humidity at the hour of interest as a fraction of the average relative humidity of that day. Once the hourly relative humidity and the hourly ambient temperature are known, the hourly dew point temperature can then be calculated based on Eq. (6.7). In order to verify this approach, the hourly dew point temperature over Toronto is estimated for the day of January 10, 1976. The results (shown in Figure 6.12) show a reasonable approximation between estimated and observed data.

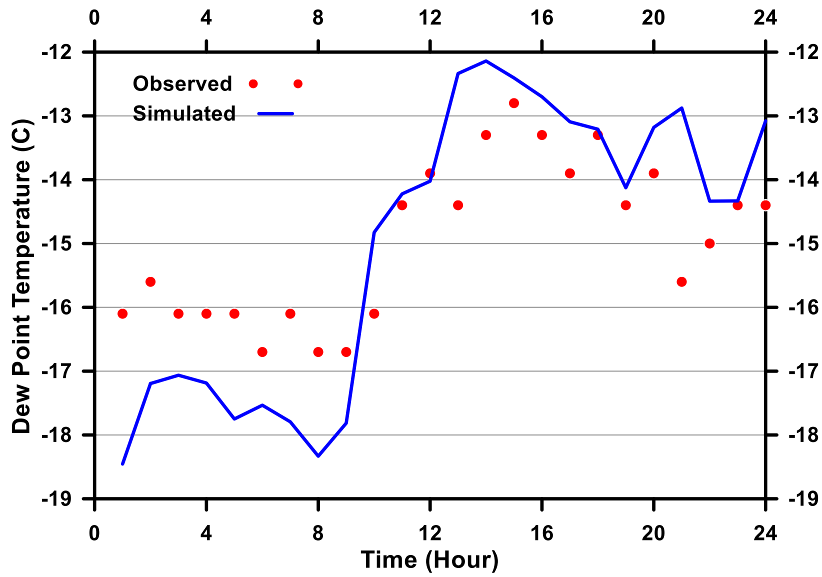

Figure 6.12: Comparison between observed and simulated hourly dew point temperature data for January 10, 1976.

6.7.3 Solar radiation

The total daily solar radiation value obtained from the weather generator represents the global horizontal irradiance (GHI) which refers to the total amount of shortwave radiation received by a horizontal surface. To determine the hourly global horizontal irradiance, the daily value may be fitted into an hourly cycle based on the historic hourly global horizontal irradiance data as was done with the relative humidity in the section above.

Once the hourly GHI data was known, the incoming shortwave radiation on the top and bottom surface were calculated (the incoming radiation at the top is equal to the GHI, while the incoming radiation on the bottom surface can be determined directly from the GHI as in (Saad et al. 2022 and Chapter II)). On the other hand, calculating the incoming radiation on the side surfaces would require more detail on how the GHI is broken down into its two main components which are the direct normal irradiance (DNI) and the diffuse horizontal irradiance (DHI). Therefore, an estimation of the DNI was used.

The DNI may be estimated through the determination of the hourly extraterrestrial irradiance I_0 at the location of interest. This value can be calculated mathematically and is also available from Climate databases. The extraterrestrial irradiance doesn't change for different years i.e., for a particular hour of a particular day, the extraterrestrial irradiance is the same for all years. Furthermore, extraterrestrial irradiance doesn't change when considering the effects of climate change. Once the hourly extraterrestrial irradiance is determined, the next step is to determine the portion of the solar constant that passes through the atmosphere directly without being scattered or reflected (i.e., DNI) using Eq. (6.8).

$$DNI = a(I_o) \tag{6.8}$$

Parameter a is the atmospheric attenuation factor. For the purpose of this study a will be calculated based on its historic value for every hour throughout the year over the 30-year period from 1976 to 2005. Once the DNI value is determined, the DHI value can be calculated from Eq. (6.9) since the GHI value is known. At this point, the incoming radiation at an inclined surface of the bridge can be calculated as described in (Saad et al. 2022 and Chapter II).

$$DHI = GHI - DNI \cos\theta \tag{6.9}$$

Where θ is the angle between the sun rays and a horizontal angle.

To verify this approach, two case studies were investigated. In both cases, the incoming radiation on a vertical side wall of a bridge was estimated once using the observed DNI and DHI and once using the estimated values. Both case studies investigate the same day in Toronto (September 9) but for different years (1990 and 1998). Those particular years were chosen because they represent the two extreme cases when it comes to cloud cover (a variable that is directly linked to atmospheric attenuation). For 1990, the cloud cover was low which means that the observed atmospheric attenuation was higher than the one used in the estimation. On the other hand, the cloud cover value was high for the 1998 case which indicates that the atmospheric attenuation was lower than the one used in the estimation. Figure 6.13 shows the obtained results for both studies. Even though the simulation was compared against the two extreme scenarios, the incoming radiation was estimated within a margin of 20%. This approximation is reasonable for the purposes of this study since this is only an estimation of the radiation on an inclined surface of a bridge when the radiation on horizontal surfaces is known.

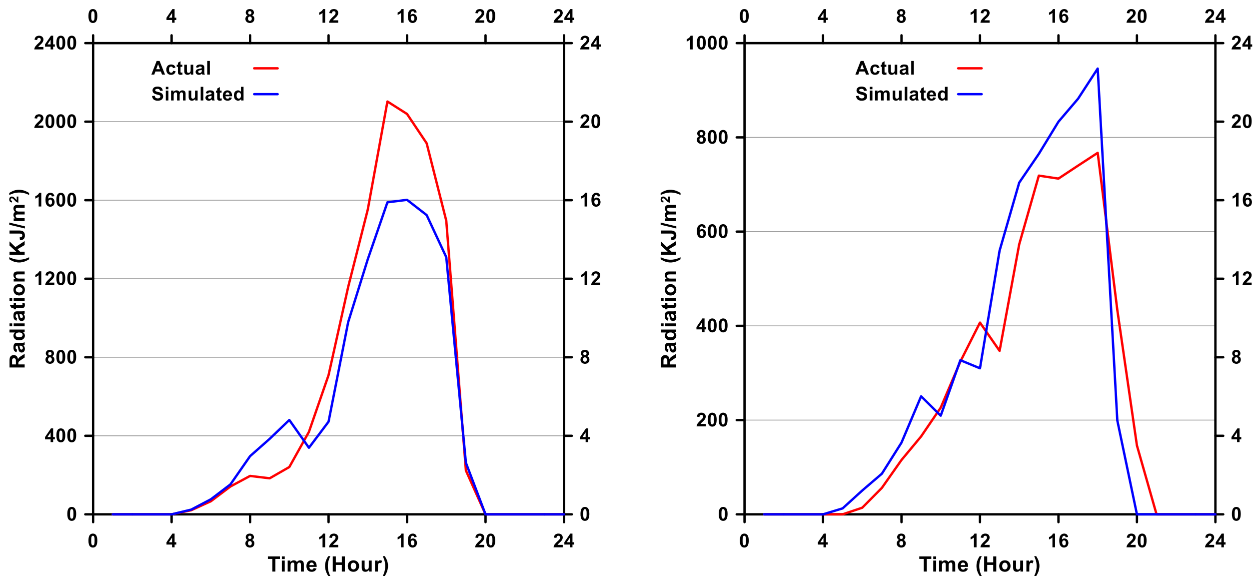

Figure 6.13: Actual and simulated results for the incoming solar radiation on a sidewall of a bridge.

6.7.4 Wind speed

Projections of wind speed carry the highest level of uncertainty and GCMS only provide estimates for monthly (not daily) wind speed values. Moreover, the weather generator used in this study provides no indication of the future wind speed. In addition to that, there has been limited to no success in past attempts to empirically model wind speed as a function of other climate factors (Pryor and Barthelmie 2010). Finally, the hourly windspeed does not follow a particular cycle or pattern as was the case with temperature. Based on the preceding, it was concluded that there will be no confidence in any prediction made for the hourly wind speed. Thus, a simplifying assumption was made, that the hourly wind speed would be equal to the average hourly wind speed over the 30-year period from 1976-2005. However, in order to account for the fact that the majority of climate scientists agree on a 10% decrease in global speed, the hourly wind speed value for future projections was reduced by ten percent (Pryor and Barthelmie 2010).

An investigation was performed to ensure that the assumptions related to windspeed do not significantly affect any of the thermal simulations carried out as part of this research. The investigations involved running four different simulations on the same bridge cross section. The simulations used observed historical climate data in Toronto for different seven-day time periods. The time periods were selected from (Environment and Climate Change Canada 2019) such that the maximum daily temperature difference was significant. Several simulations were carried out by amplifying and attenuating the wind speed by multipliers of $0.4, 0.7, 1.3$, and 1.6. Other climate variables were kept constant. Figure 6.14 displays the maximum positive differentials obtained for each simulation, plotted against the windspeed scaling factor. The results indicate that the relationship between the windspeed and the maximum gradient is almost linear. However, changing the windspeed scaling factor from 0.4 to 1.6 resulted in a maximum decrease in differential by about 5.2℃ (17%). Therefore, it is reasonable to state that the assumption made for using the average wind speed reduced by only 10% will not significantly impact the result of the simulations.

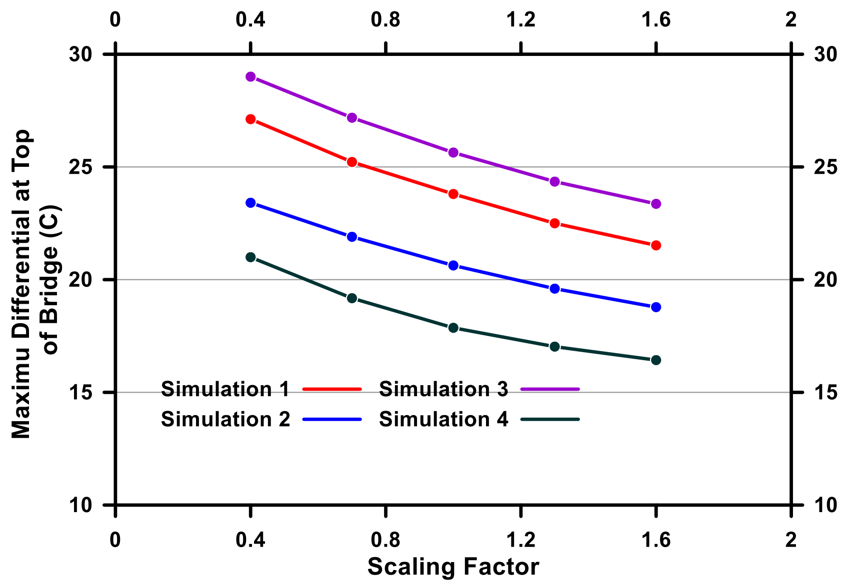

Figure 6.14: Maximum temperature differential for different windspeed scaling factors.

6.8 Future climate projections and their implications

The methodology described in the preceding was applied to the two locations under consideration, namely, Toronto, Ontario (43.65 N, 79.4 W) and Whitehorse, Yukon (60.7 N, 135.1 W). These locations were selected for specific reasons. Toronto, being a major international city and one of the most densely populated regions in North America, represents an urban center of significant interest. Conversely, Whitehorse, though relatively small, was chosen due to its location in Northern Canada, an area expected to experience amplified warming as a result of the Arctic warming effect. The artic warming effect refers to the positive feedback cycle that will occur near the arctic circle since the melting of ice at the arctic due to climate change will lead to less solar reflected radiation which in turn will amplify the warming further (Hartmann 2015). The sections below describe the processes followed to determine the temperature differentials in projected future scenarios for $SSP5 - 8.5$ for Toronto. The remaining results of other scenarios (Toronto-$SSP2 - 4.5$, Whitehorse-$SSP5 - 8.5, SSP2 - 4.5$) are also discussed.

6.8.1 Maximum thermal load: Historical climate

The first step in the analysis was to determine the maximum temperature differentials that occurred across the box girder cross section during the historical time period. Therefore, nine simulations were conducted using historical data for Toronto. Three simulations were chosen to represent the maximum daily difference that occurred from the years 1976-2005. In addition, three simulations were performed to represent heat wave conditions and three simulations were chosen to represent cold wave conditions. For the purpose of this study, a cold wave is defined as a three-day period in which the minimum temperature is lower than the 2nd percentile temperature value for the time period under consideration. Similarly, a heat wave is defined as a three-day period in which the maximum temperature exceeds the 98th percentile temperature for the time period under consideration. The temperature distribution along the web of the cross section at the instance of maximum positive differential and the maximum negative differential at the top of cross section was extracted from each simulation.

6.8.2 Maximum thermal load: Future climate

As discussed, future hourly data was forecast using a combination of the Lars-WG weather simulator and empirical models. Following this, a total of nine simulations were performed using the generated future data, with nine simulations dedicated to each climate model. The selection of simulation dates mirrors the approach employed for historical data, with three simulations allocated to represent maximum daily temperature differences, three for simulating heatwaves, and three to depict cold waves. Sample plots for both observed historical and simulated future cold waves and heat waves are shown in Appendix E.

The temperature distributions along the web of the cross section at the instances of maximum positive differential and the maximum negative differential at the top of cross section were then compared against those obtained from the historical climate data simulations. The results for the BCC-CSM2-MR model for $SSP5 - 8.5$ for Toronto are shown in Figure 6.15, particularly the instances of maximum positive differential at the top of the cross section. The results showed that for the maximum daily temperature difference, the top differential for the projected climate was significantly larger than the top differential resulting from the historical climate (Figure 6.15a). The maximum top differential from one simulation of future climate was 36℃ while the maximum top differential from one simulation of historical climate was 24℃. Furthermore, the average top differential of the three future climate simulations was 29℃ whereas the average top differential for the three historical climate simulations was 23℃. Similar observations can be made from the results for the heat wave simulations (Figure 6.15b). The maximum top differential for the future heatwaves was 36℃, which is larger than the equivalent top differential for the historical heatwaves (31℃). The cold wave results indicated similar patterns where the maximum and average top differentials for future cold waves were 23℃ and 19℃ respectively as opposed to 17℃ and 16℃ respectively for historical cold waves (Figure 6.15c).

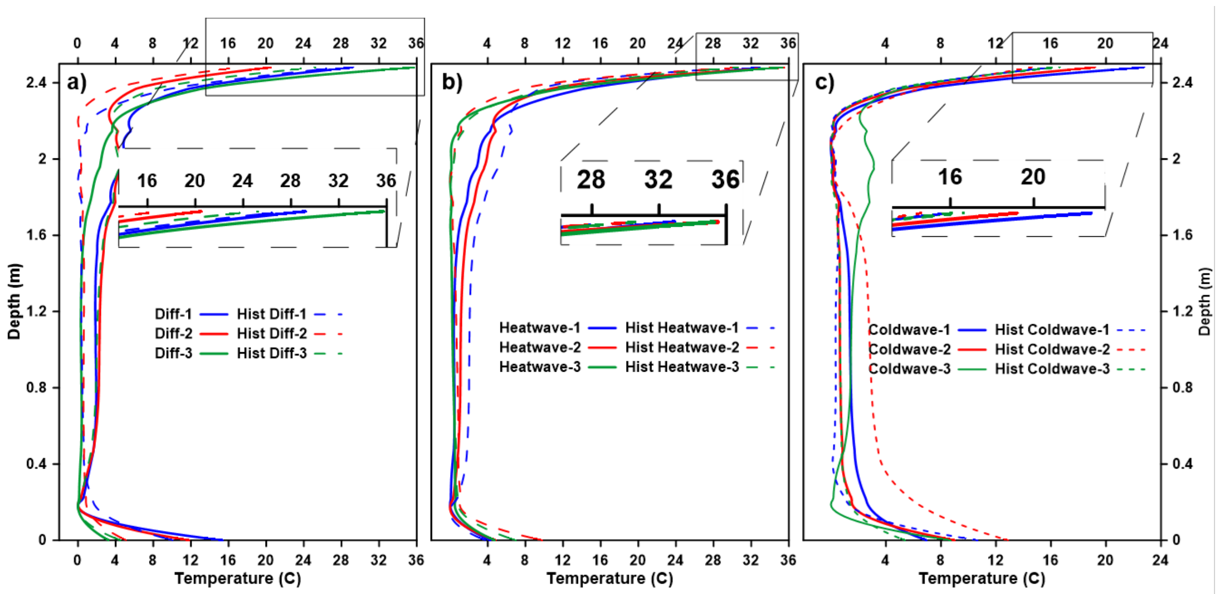

Figure 6.15: Comparison between temperature distributions within the web between historical and future model simulations from BCC-CSM2-MR for a) maximum daily temperature difference, b) heatwaves, and c) cold waves (from left to right).

Having considered the results from one model on the positive thermal differential, the effect of the climate change models for emissions scenario SSP2-4.5 and SSP5-8.5 for both locations on both the positive and negative differentials is presented next. The average top thermal differential obtained from the historical daily differences, heatwaves, and cold waves, are compared with the respective values from the global climate models for both Toronto and Whitehorse. For Toronto, Figure 6.16 shows that the positive differentials observed for emission scenario SSP2-4.5 are similar to those observed for the historical climate in the case of cold waves as well as during days of maximum daily ambient temperature differences. Future heatwaves result in a larger positive top differential (average of 33℃) than historic heat waves (30.5℃). Future models also exhibit a general uptrend in negative top differentials during heatwaves, cold waves, and days with maximum temperature differences, reflecting increases of 2°C, 3°C, and 1°C, respectively). Note that for the purpose of this study, the negative differentials are compared in terms of their absolute values i.e., a 2℃ absolute increase indicates that the temperature is more negative. Furthermore, it was observed for SSP5-8.5, that most cases exhibit a significant increase in the positive temperature differential. The average increase predicted for SSP5-8.5 is larger than the one predicted for SSP2-4.5 in all cases (increases of 3℃, 2.5℃, and 4℃ for periods of maximum daily differences, cold waves, and heatwaves respectively). Future models for SSP5-8.5 also show a significant increase in the negative temperature differentials, with an average increase of 2.5℃ for all three cases investigated. Furthermore, it is noted that CHBDC guidelines prescribe a top differential of 15℃ which means that a 4℃ increase in top differential due to heatwaves for SSP5-8.5 represents an increase by 26%. Moreover, the above-mentioned increases represent an increase in the average values; thus, the increase would be significantly larger if maximum values were to be considered (maximum values for heat waves and cold waves are highlighted in Figure 6.16).

The results for Whitehorse (Figure 6.17) do not indicate an increase in positive temperature differential during both heat waves and periods with maximum daily difference for SSP2-4.5. On the other hand, a significant increase of about 6℃ in positive temperature differential is observed during cold waves. In addition, the models predict an average increase by 2°C and 9°C in the negative temperature differentials during periods of maximum ambient temperature difference and cold waves, respectively, as opposed to the decrease observed during heat waves. SSP5-8.5 results for positive thermal differentials show a similar trend to those of SSP2-4.5 since no average increase is observed for heat waves and the daily maximum difference while a significant average increase of 5℃ is observed for cold waves. The main impact of climate change is observed in SSP5-8.5 predictions for the negative thermal gradients in which the models predict an average increase of 5℃ and 8℃ for maximum daily difference and cold waves, respectively.

In summary, the effects of climate change on the thermal load vary depending on the location and the emission scenario considered. It was observed that for Toronto, a location with a humid continental climate, an increase in the positive thermal differential will occur during heat waves projected using SSP2-4.5. A significant increase in the positive temperature differential is also predicted using SSP5-8.5 for all extreme cases. Predictions for the negative temperature differential using both SSP2-4.5 and SSP5-8.5 show a similar overall increase. The results obtained for Whitehorse, a region characterized by a subarctic climate, suggest that climate change will have no discernible impact on positive temperature gradients during both heatwaves and periods of maximum daily difference, irrespective of the climate change scenarios. However, in the case of cold waves, the positive temperature differential is projected to increase for both emission scenarios. Additionally, the negative temperature differential in Whitehorse is anticipated to experience a significant increase during cold waves and periods of maximum daily difference for both emission scenarios.

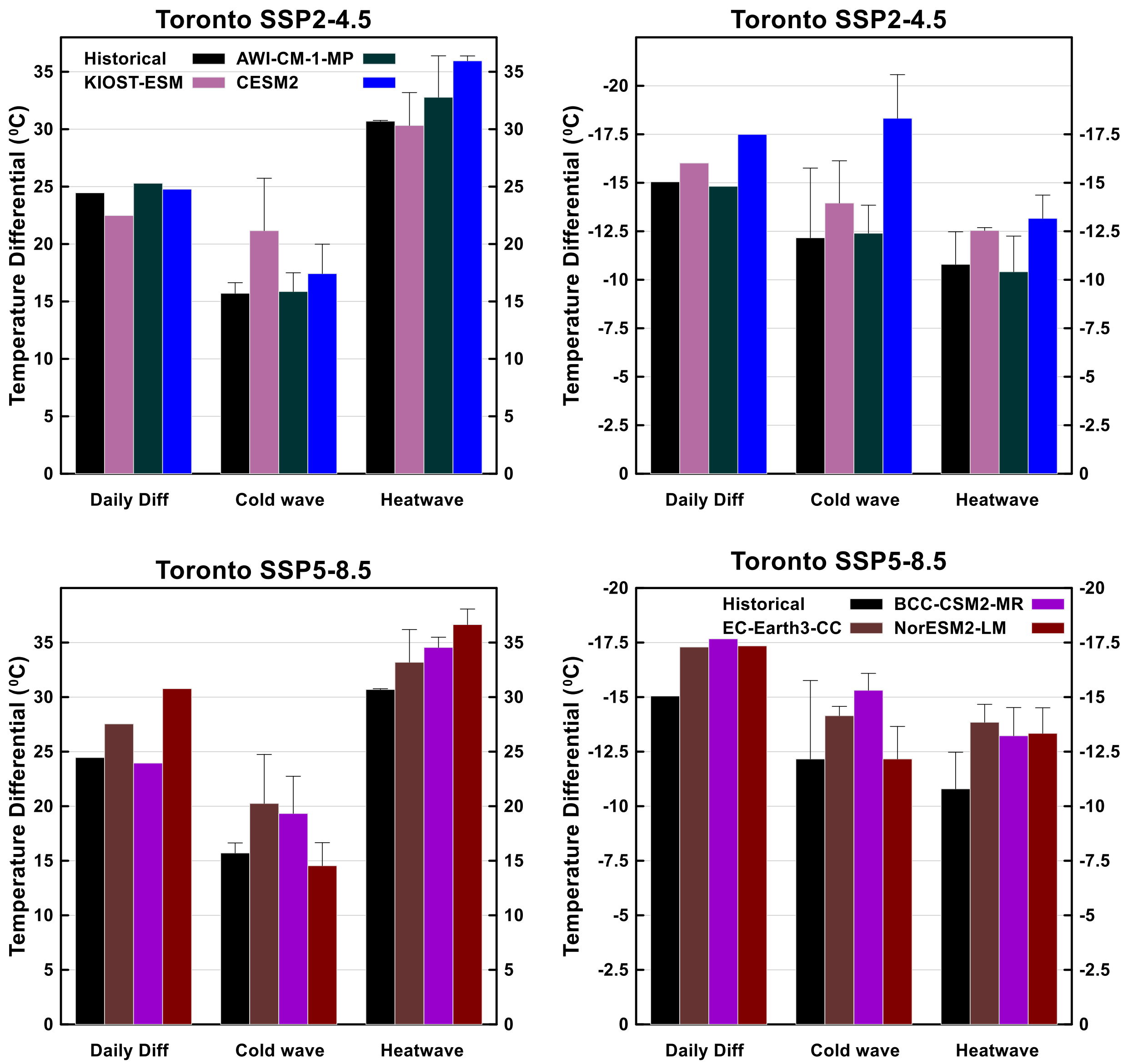

Figure 6.16: Effect of climate change on the positive and negative top temperature differentials in Toronto for SSP8.5 and SSP4.5 for three different climate models.

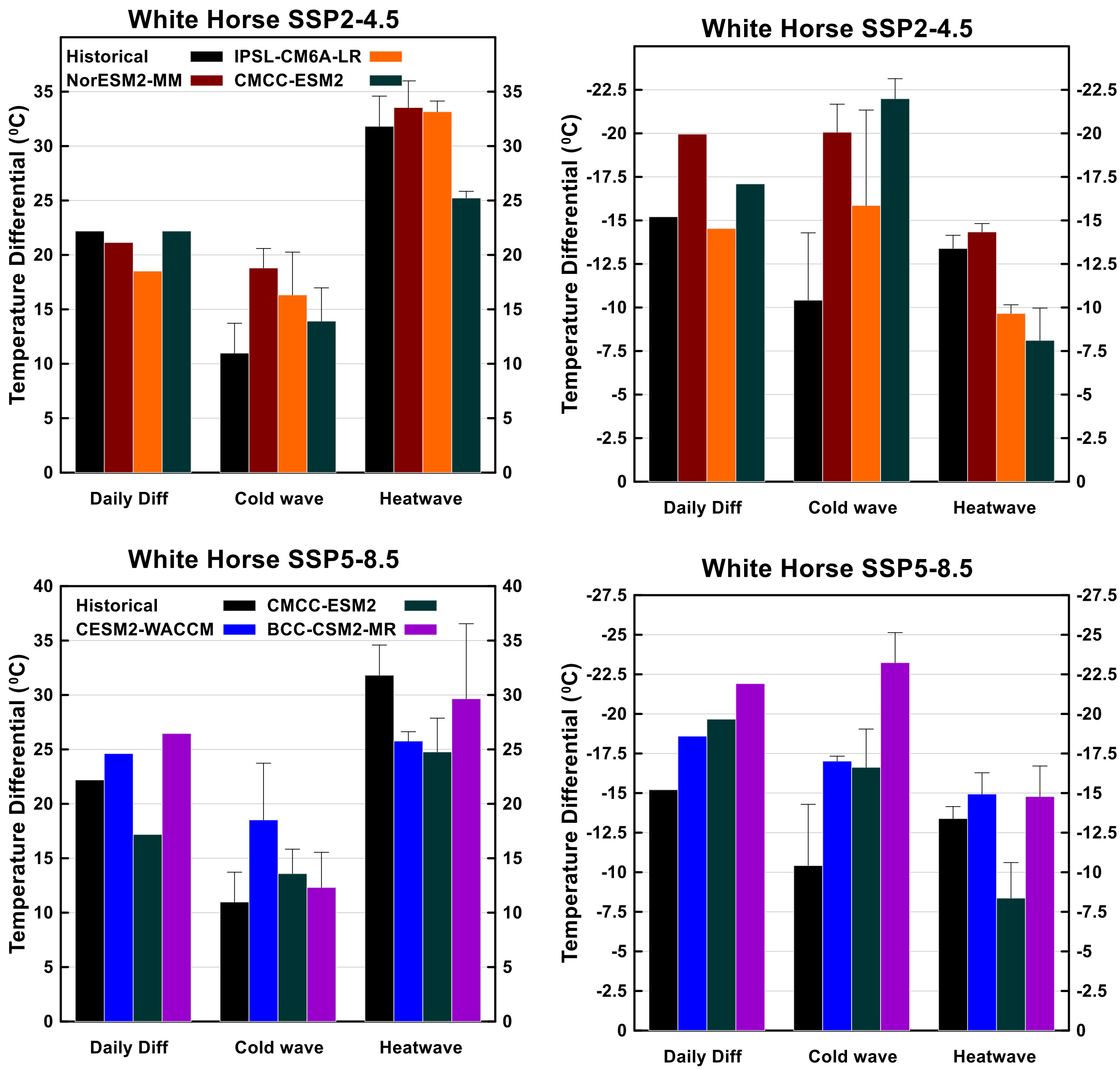

Figure 6.17: Effect of climate change on the positive and negative top temperature differentials in White Horse for SSP8.5 and SSP4.5 for three different climate models.

6.9 Conclusions

In this study, an investigation on the effect of climate change on the thermal load in concrete bridges was conducted. Initially, the relationship between the maximum daily ambient air temperature difference and the resulting temperature differential in a bridge deck was investigated using a thermal finite element model. The established relationship was then used as a criterion for the selection of global climate models. Three Global climate models were selected for each emission scenario and each location, based on their future projected maximum daily temperature (two emission scenarios and two locations were considered). Next, the projections from these models were used as input in a weather generator which performs statistical downscaling to obtain daily values of climate variables at the locations of interest. Subsequently, the daily values were used to obtain hourly values using empirical models. Thermal simulations were conducted for future scenarios using the hourly climate variables as boundary conditions. Three scenarios were considered: heatwaves, cold waves, and periods of maximum daily temperature variations. Based on the results of the investigation, the following conclusions can be made:

- The thermal differential at the top of the cross section is closely related to the maximum daily temperature difference. As the difference increases, the thermal differentials also increase.
- Future projections vary significantly between different global climate models.
- Future projections from global climate models can be used in conjugation with weather generators and empirical models to produce hourly downscaled projections with a reasonable accuracy.
- The effect of climate change on the thermal differential is highly dependent on the emission scenario and geographic location. For example, a significant increase in the positive temperature differential is predicted using SSP5-8.5 for the three cases in Toronto whereas predictions made for SSP2-4.5 show increases only in the case of heat waves. On the other hand, it was found that for both SSP2-4.5 and SSP5-8.5 heat waves have limited effect on the top positive differential in White Horse. Only future cold waves were found to cause increased positive thermal differentials in White horse since they are attenuated compared to the historical ones.
- It was determined that climate change can cause an increase of about 5℃ in the absolute maximum positive thermal differential in bridges located in Toronto. On the other hand, climate change can lead to a 6℃ increase in positive thermal differentials in bridges located in Whitehorse.
- Climate change also has a significant effect on the maximum negative thermal differential in both locations. Negative differentials in bridges increased by a maximum of about 4℃ and 8℃ in Toronto and Whitehorse respectively.

- This study provided a methodology and demonstration of the approach required to quantify the effect of climate change on thermal load in bridges. Future research should focus on quantifying this effect at additional locations, to incorporate these effects into bridge Codes.
- The methodology proposed as part of this research for generating future hourly climate data, aimed at estimating thermal loads, holds significant value not only for bridge engineers but also for professionals in various scientific and engineering disciplines impacted by climate considerations.
- Future studies should also focus on understanding the relationship between the prevailing climate type at a location of it and the effect of climate change on the thermal load at that particular location.

6.10 Appendices

6.10.1 Appendix A: Thermal model

The thermal model will require input in the form of hourly values for each of the following climate parameters: Windspeed, air temperature, dew point temperature, cloud cover, Direct Normal Irradiance, Diffuse Irradiance, and Global Horizontal Irradiance. A timestep of 30 minutes was used in the model. The girder with the cross section shown in Figure 6.3 has a span of $10\ m$ and was modelled with perfectly insulated ends. The model includes a $100\ mm$ thick asphalt layer topping the deck, with separate thermal properties. The thermal properties of the asphalt and concrete were taken from (Gu et la. 2014). Both the concrete and asphalt were modelled using a 3-D, twenty node prism- shaped thermal element (Solid90) (ANSYS 2019). The initial temperature of the bridge was assumed to be uniform within the cross section and equal to the ambient temperature at the start of the simulation. The model can predict the temperature distribution through the depth of the cross section. Figure 6.18 shows the typical output of the model.

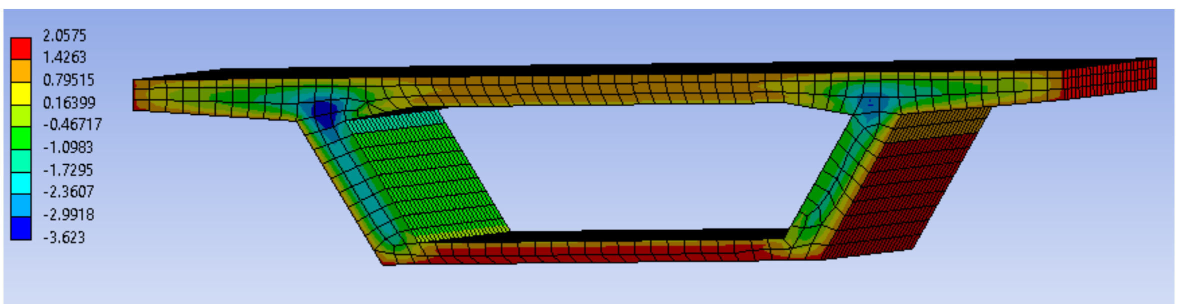

Figure 6.18: Typical model output.

6.10.2 Appendix B: Thermal simulations

As stated above, a total of 12 thermal simulations were performed with each simulation comprising seven consecutive days using hourly climate data from Old Crow, Canada. The simulations were divided into two groups in which Group 2 represents days with a negative average daily temperature while Group 2 is composed of days with a positive average daily temperature. The dates for the six simulations in both groups are shown in Table 6.3. Figure 6.19 shows the ambient air temperature time history for simulation 1 from both groups.

Table 6.3: Simulation Dates.

Group	Sim No.1	Sim No.2	Sim No.3	Sim No.4	Sim No.5	Sim No.6
Group 1	10/04/2013-17/04/2013	10/03/2009-16/03/2009	31/03/2007-06/04/2007	27/03/2005-02/03/2005	19/01/2005-25/01/2005	02/04/2003-08/04/2003
Group 2	02/08/2017-06/08/2017	14/05/2009-20/05/2009	04/07/2007-10/07/2007	21/07/2006-27/07/2006	22/07/2005-28/07/2005	14/06/2005-20/06/2005

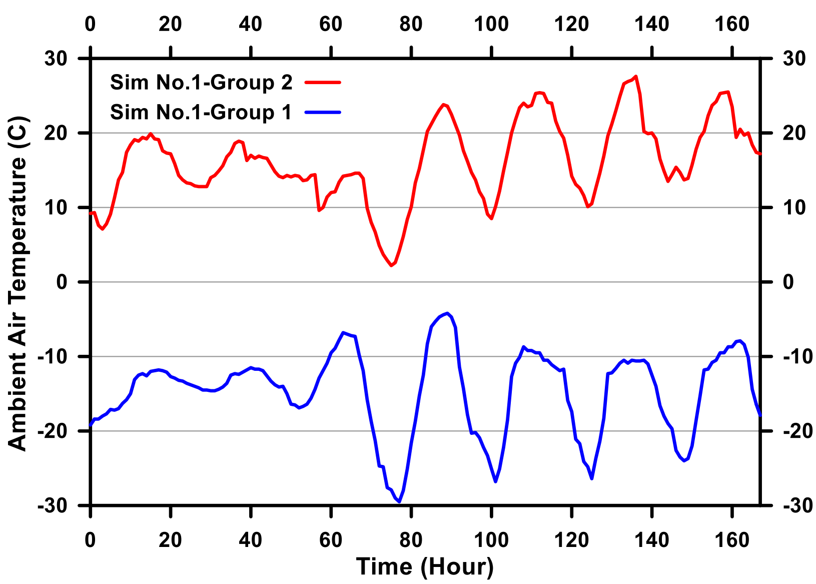

Figure 6.19: Ambient Air temperature for the seven days of Simulation No.1 (Group 1 and Group 2).

6.10.3 Appendix C: Projected changes for the entire year

Table 6.4 is an extension of Table 6.2 and provides the projected changes for each climate model for the entire year (as input into the weather generator).

Table 6.4: Projected changes for each climate model as input into the weather generator for the entire year.

	ΔR monthly mean rainfall	ΔR duration of wet spell	ΔR duration of dry spell	ΔA monthly mean min temperature	ΔA monthly mean max temperatur
-MR	0.75	0.32	2.3	4.13	5.91
LM	1.11	1.14	1.03	3.93	6.81
-CC	0.62	0.58	5.8	5.61	5.71
-MR	0.8	0.34	2.65	4.18	4.98
LM	0.75	0.84	1.19	4.04	1.7
-CC	0.4	0.45	10.5	6.41	6.71
-MR	1.16	0.46	2.62	4.88	4.83
LM	1.05	0.98	0.91	5.42	4.08
-CC	0.53	0.55	8.72	7.26	7.6
-MR	0.86	0.4	4.17	5.43	6.65
LM	1.15	1.04	0.83	5.56	3.28
-CC	0.274	0.64	5.92	7.89	8.77
-MR	0.76	0.47	3.32	4.19	6.78
LM	1.17	1.11	1.02	4.7	4.06
-CC	0.516	0.5	2.16	8.13	8.51
-MR	0.8	0.37	2.67	3.8	6.4
LM	1.17	0.91	1.01	3.31	2.53
-CC	1.105	0.72	2.45	6.51	6.78
-MR	1.06	0.36	2.07	5.67	4.65
LM	1.33	0.94	0.96	3.1	7.74
-CC	1.88	0.67	1.78	6.31	7
-MR	1.2	0.29	2.53	5.81	2.59
LM	1.29	0.86	1.13	2.8	1.67
-CC	2	0.59	2.11	4.9	6.9

6.10.4 Appendix D: Calculation of $\boldsymbol{R_a}$

The extraterrestrial irradiance R_a can be calculated from the equation below:

$$R_a = \frac{1}{\gamma} \cdot (37.6 \times d_r(w_s \sin \emptyset_t \sin \delta + \cos \emptyset_t \sin w_s)) \quad (6.10)$$

- $w_s = \cos(\tan \emptyset_t \tan \delta)$
- $d_r = 1 + 0.033 \times \cos\left(\frac{2\pi J}{365}\right)$ where $J\ is\ the\ Julian\ Day$
- $\delta = 0.4093 \times \sin(\frac{2\pi(284+J)}{365})$
- $\emptyset_t\ is\ the\ latitude\ angle\ (rad)$
- $\delta\ is\ the\ declination\ of\ the\ sun\ (rad)$
- $w_s\ is\ the\ sunset\ hour\ angle\ (rad)$
- $\gamma\ is\ the\ latent\ heat\ of\ vaporization, \gamma = 2.54$, Divide by 0.04167 to convert from $\frac{MJ}{m^2}$ to mm/day

6.10.5 Appendix E: Sample Data

Figure 6.20 shows the temperature time history for both observed historical and model (BCC-CSM2-MR) simulated heat waves and cold waves.

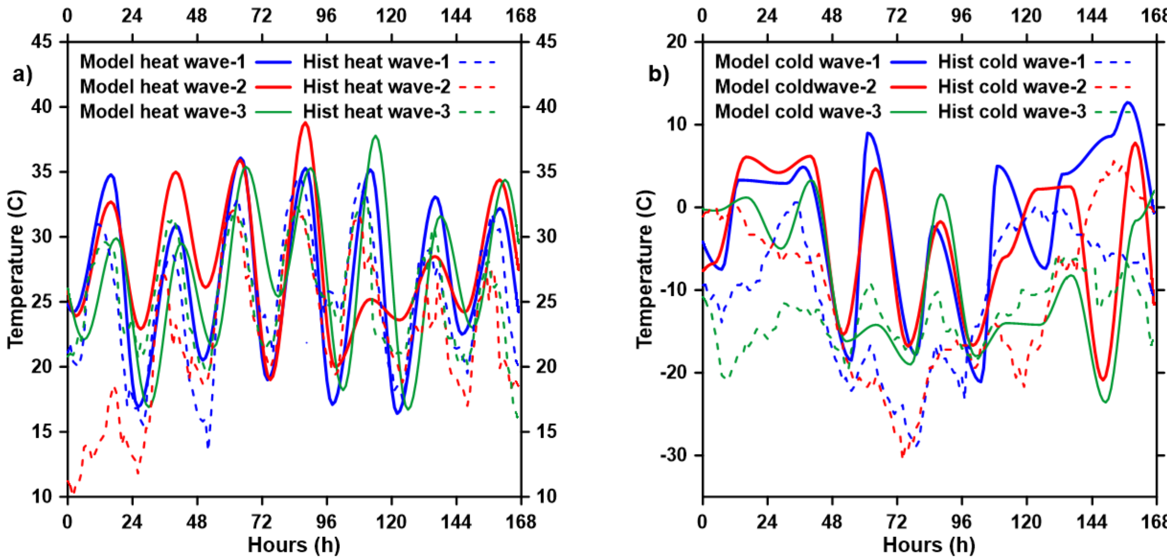

Figure 6.20: Temperature time history for both observed historical and model (BCC-CSM2-MR) simulated a) heat waves and b) cold waves.

Chapter **VII**

Summary, Conclusions and Recommendations for Future Research

7.1 Summary and conclusions

Various aspects of the effect of climate and climate change on the thermal behavior of concrete bridges were investigated in this thesis. A numerical finite element thermal model that simulates the atmosphere bridge boundary interaction was developed based on the physical processes that influence the heat exchange. The physical processes modelled were the shortwave radiation exchange, the longwave radiation exchange, and the convection heat exchange. The model calculates the temperature distribution within the bridge deck. A structural finite element model, incorporating the outcomes of the thermal model as boundary conditions, was developed to predict the structural response. The structural model accounts for the non-linearity of the concrete and can simulate both prestressed and non-prestressed reinforcement.

Initially, the model was used to investigate the relevance of guidelines in current bridge Codes in estimating the negative thermal gradients that occur in a concrete box girder during cold wave events. Four different cold events were considered for the analysis. Climate data for the four events were used as input in the thermal model of a concrete box girder. The maximum negative temperature gradients were then obtained and compared against Code prescribed gradients. Furthermore, the structural model was then used to study the structural response to the simulated gradients The findings of the investigation indicated that the magnitude of the AASHTO prescribed negative gradient was significantly lower than the magnitude of the simulated thermal gradient, particularly at the bottom of the cross section. It was also determined that this difference in thermal load has severe structural implications for the bridges. Upon comparing the cold wave simulation results with those of a structural simulation incorporating the AASHTO gradient as a load, a notable increase by approximately 3 MPa in concrete tensile stresses was observed for all events. This increment is substantial, surpassing the cracking stress of concrete. The results of this study lead to the conclusion that there are deficiencies in the existing code concerning the accurate representation of thermal gradients and structural performance. It may also be concluded that relying on the Code estimations may lead to potential miscalculations of tensile stresses, ultimately resulting in reduced performance. It is also concluded that before studying the effect of climate change on thermal load, it is essential to first address the deficiencies in current guidance, particularly during cold wave events.

Another study was then conducted with the aim of helping improve current guidelines on thermal load and enabling these guidelines to be more location specific. The objective of this study was to establish a relationship between the most significant climate parameter and the resulting thermal gradient in bridges over a large spatial scale. This capability would empower engineers and authorities to estimate the thermal loads on bridge decks exclusively based on climate data. The objective is achieved by performing 140 thermal simulations in which a concrete box girder is subjected to climate conditions from 20 cities across Canada (7 simulations from each city). The thermal differentials obtained from the simulations were subsequently examined, leading to the identification of a discernible correlation. This correlation establishes a relationship between the maximum thermal differential observed at the uppermost part of the cross section and the seven-day average direct normal irradiance (DNI) value. Notably, the thermal differential at the top increases proportionally with the rise in DNI. Four categories, relating the DNI to the top differential were proposed. It was also noted that the CHBDC Code limits are exceeded when the seven-day DNI value exceeds $1200\ KJ/m^2$. Based on this observation, a map is presented highlighting the Canadian provinces in which code limits are likely to be exceeded. The map shows that code limits are exceeded in Central and Western provinces as well as some of the Northern territories. Hence, this study not only underscores additional deficiencies in the current guidance regarding thermal loads but also introduces a model that can serve as a foundation for enhancing this guidance. The results and analyses of this study lead to the following general conclusions.

1. The current guidance should be made more location specific.
2. Climate classification can play an important role in understanding thermal regime in bridges.

3. On a larger spatial scale, the DNI appears to correlate well with the development of thermal differential that occurs at the top of the bridge deck cross section.
4. For Canada, bridges in Central and Western provinces as well as some of the Northern territories can be prone to exceed the code limits.

A study on the effect of subfreezing temperature on the ECTE of concrete was another aspect of the investigation on current bridge design procedures. In this study, an experimental investigation was conducted in which thermal strain was measured in concrete specimens from different mixes subjected to freeze thaw cycles down to a temperature of $-40°C$. The findings confirm the existence of a critical degree of saturation (80%) below which temperature has no effect on the effective CTE of concrete. For higher degrees of saturation, three different behaviors were observed. Some samples showed significant hysteretic expansion and therefore a large reduction in the effective coefficient of thermal expansion during cooling. Others demonstrated an effective thermal expansion coefficient equal to that of dry samples and displayed negligible residual strain. The third behavior was an intermediate behavior with moderate hysteretic expansion and residual strain. Furthermore, the aggregate size also influences the relationship. A numerical investigation was then conducted in which the structural model was modified to incorporate a temperature dependent ECTE (based on the experimental results) and was used to study freezing/ thawing on a concrete beam. It was concluded that the relationship between temperature and thermal strain is a function of the w/c ratio; Larger w/c ratios were found to cause greater expansion and residual strain in concrete when subjected to freezing temperatures. It was found that the aggregate size also influences this behavior. Furthermore, the results of the numerical investigation led to the conclusion that the effect of sub-freezing temperature on the ECTE of concrete can lead to significant variation in the magnitude of compressive strains in addition to affecting the location of tensile strains within the cross section.

The structural model was then used in a full-scale investigation that incorporates both the effect of cold wave intensity and the effect of temperature on the effective CTE of concrete. Climate data from three cold wave events of varying intensity were applied as boundary condition on a prestressed concrete box girder. The results and analyses of this study lead to the following general conclusions.

1. For a low cold intensity cold wave event, incorporating the effect of sub-freezing temperature on the effective thermal expansion coefficient of concrete has minimal effect on structural performance.
2. Significant differences are observed between simulations with a constant ECTE and simulations with a time dependent ECTE for the high intensity event. Simulations with a temperature dependent ECTE resulted in a significant increase in tensile strains in both transverse and vertical directions.
3. The previous findings, that the AASHTO (2014) guidelines for thermal load fail to capture the negative gradients that occur during cold wave events, are further reinforced by the results from the thermal finite element model.

Finally, the effect of climate change on thermal load was investigated. To perform thermal simulations that take climate change into account, the generation of future climate data was required. A criterion for the selection of GCMs to be used in the data generation was established based on the maximum daily temperature difference that these models predict. A methodology for downscaling the projected global climate data to the required spatial scale using a weather generator was presented. Furthermore, a combination of empirical and theoretical models was used to produce hourly data from the generated daily data. This approach was used to generate future data for two locations (Toronto and Whitehorse) and determine future thermal differentials that will occur during future heatwaves, cold waves, and days of maximum daily temperature difference. The obtained differentials were compared with historic thermal differentials. It was concluded that climate change will generally lead to a significant increase in thermal loads on bridge decks. A significant increase in both the positive and the negative temperature differentials was predicted using SSP5-8.5 for the three cases in Toronto. Similarly, the positive and negative differentials predicted in Whitehorse also increased significantly due to climate change. A maximum increase of about $6℃$ and $8℃$ was estimated for positive and negative differentials respectively. It was also concluded that the effect of climate change on thermal load is highly dependent on the emission scenario and geographic location (i.e., location climate).

7.2 Recommendations for future work

The following are recommendations for future work which can enhance the research presented in this dissertation.

- The work presented in this dissertation focused mainly on box girder cross sections. Additional research is needed to investigate the applicability of current thermal load guidelines on different cross-sectional shapes and dimensions. These cross sections may include but are not limited to I girders, T girders, and hollow core decks.
- The methodology presented in Chapter III could be extended beyond the boundaries of Canada. This will determine whether the established relationship between direct normal irradiance and temperature differentials holds in other climate types that do not occur in Canada. If that is the case, it would be possible to derive maps that show seven-day average values of DNI for the entire world and to link these to resulting thermal differentials. Alternatively, this kind of investigation could also lead to the discovery of additional relationships between climate parameters and thermal gradients in climate types present outside of Canada.
- The methodology presented in Chapter VI was used to quantify the effect of climate change on bridges in two Canadian locations for demonstration purposes. Additional research, using this methodology, is required to study more locations across Canada to form a comprehensive understanding of the effects of climate change on thermal loads.
- This study focused on evaluating thermal effects in terms of the thermal gradients that arise in bridges. However, uniform temperature loads also form a significant component of the thermal load and can be investigated in a similar manner.
- Sub-freezing temperature impacts both the thermal and structural material properties, not only the expansion coefficient of concrete. The effect of sub-freezing temperature on structural properties (elastic modulus, compressive strength, and tensile strength) and thermal properties (Conductivity, specific heat capacity) should also be considered for incorporation into the thermal and structural models.
- The investigation of the effect of climate change on thermal effects highlighted significant differences between temperature differentials calculated for future and historic conditions. The structural implications of these difference need to be quantified and evaluated.

- Instrumentation of bridges to measure thermal and structural performance is needed to further validate the current model and develop more robust models. In particular, bridge instrumentation is required in cold regions to monitor bridge behavior during cold wave events. The literature is lacking in this area as most instrumented bridges have been in locations where cold waves are not a frequent occurrence.
- Future research should focus on developing a fundamental relationship between capillary porosity distribution, relative humidity, and the hysteretic strain - temperature relationship, as well as the exploring better the connection between the residual ultimate expansion resulting from freeze - thaw cycles and the w/c ratio and aggregate distribution.

Abbreviations and Notations

8.1 Abbreviations

The following abbreviations have been used throughout the text:

DNI is the direct normal irradiance.

GHI is the global horizontal irradiance.

CDS is the critical degree of saturation.

CHBDC is the Canadian highway bridge design code.

AASHTO is the American Association of State Highway and Transportation Officials

CTE is the coefficient of thermal expansion.

ECTE is the effective coefficient of thermal expansion.

CMIP6 is the Coupled Model Intercomparison Project Phase 6.

CMIP5 is the Coupled Model Intercomparison Project Phase 5.

RCP is representative concentration pathway.

SSP is the shared socioeconomic pathway.

GCM is the Global Climate Model.

CWEEDS is the Canadian Weather Energy and Environmental Datasets.

CPCI is the Canadian Precast/Prestressed Concrete Institute.

CSA is the Canadian Standards Association.

IPCC is the Intergovernmental Panel on Climate Change.

ACSE is the American Society of Civil Engineers.

8.2 Notations

The following notation has been used throughout the text:

q_b is the direct (beam) radiation.

q_d is the diffuse radiation.

q_g is the reflected radiation.

q_r is the net flux of longwave radiation.

σ is the Stefan Boltzmann constant.

ε is the emissivity of the concrete surface.

E_c is the emitted longwave radiation from the bridge surface.

E_{sur} is the emitted longwave radiation from all other surrounding surfaces.

T_c is the concrete surface temperature.

T_{sur} is the temperature of the surrounding environment.

q_c is the convective heat flux.

h_c is the convective heat transfer coefficient of the concrete surface.

T_a is the air temperature.

w is the wind speed.

ρ is the density.

c is the specific heat capacity.

$\frac{\partial T}{\partial t}$ is the change in temperature over time.

k is the thermal conductivity.

$\frac{\partial^2 T}{\partial x^2}, \frac{\partial^2 T}{\partial y^2}, \frac{\partial^2 T}{\partial z^2}$ are the second spatial derivatives of the temperature in the x, y, and z directions respectively.

T_{inf} is the fluid temperature far away from the surface.

I_B is the direct (beam) radiation.

I_D is the diffuse radiation.

I_R is the reflected radiation.

I_G is the total solar radiation arriving on a bridge surface.

$I_{B,n}$ is the direct normal irradiance.

θ is the angle of incidence.

$I_{D,h}$ is the diffuse radiation on a horizontal surface (referred to as horizontal diffuse irradiance in solar datasets).

β is the slope angle which forms between the horizontal and the plane of the surface.

I_H is the global horizontal irradiance.

ρ_R is the reflection factor of the ground surface.

T_{sky} is the sky temperature.

q_{in} is the heat transfer at an internal bridge surface.

$q_{c,in}$ is the internal convective heat transfer.

$q_{r,in}$ is the internal radiative heat transfer.

$T_{s,in}$ is the internal bridge surface temperature.

$T_{a,in}$ is the internal air temperature.

h_r is the heat radiation coefficient.

$\partial T/\partial x, \partial T/\partial y, \partial T/\partial z$ are the temperature fluxes in the x, y, and z directions.

n_x, n_y, n_z are the direction cosines of the unit outward vector normal to the boundary surface.

q is the rate of heat transferred from the environment to the concrete surface per unit area.

N is the number of years in the averaging period.

x_o is a variable in the present-day period.

$(x_0)_h$ is the variable x_0 averaged hourly over the baseline period.

q_{sky} is the incident long wave heat radiation recorded by a pyrgeometer.

ε_{sky} is the emissivity of the sky.

ε_{at} is the integrated effective emissivity of the atmosphere and canopy.

T_{dew} is the dew point temperature.

C_{cloud} is the cloud cover.

e_a is the surface vapor pressure.

k_{meas} is the measured extra-terrestrial irradiance.

k_{theo} is the theoretical extra-terrestrial irradiance.

θ_s is the solar zenith angle.

T_{eq} is the equivalent temperature.

ΔL is the linear change in length of a solid material.

α_l is the material linear coefficient of thermal expansion.

T_f is the final temperature.

T_0 is the initial temperature.

ΔT is the change in temperature.

L_0 is the initial length at temperature T_0.

V_0 is the volume of unrestrained material.

ΔV is the change in volume.

α_V is the volumetric expansion coefficient.

w/c is the water to cement ratio.

X is the degree of saturation.

$S_{0.61}80(2)$ represents the second specimen from mix $S_{0.61}$ (with a $\frac{w}{c}$ratio of 0.61) tested at $X = 80\%$.

ε_1 is the thermal strains at the start of the cooling stage.

ε_2 is the thermal strains at the end of the cooling stage.

T_1 is the temperature at the start of the cooling stage.

T_2 is the temperature at the end of the cooling stage.

r_0 is the hydraulic mean radius.

$r_{0,A}$ is the hydraulic mean radius for Mix A.

x_B is the X-coordinate of point B.

y_B is the Y-coordinate of point B.

T_x is the maximum daily temperature.

T_n is the minimum daily temperature.

t_s is the sunset time.

t_r is the sunrise time.

t_x is the time of maximum temperature.

t_n is the time of minimum temperature.

α is the time difference between t_x and the temperature at midday.

β is the time difference between t_n and the time at sunrise.

t_n' is the time of minimum temperature for the day after the day for which the temperature cycle is being modelled.

l is the daylength.

$l_{EP,day}$ is the daily potential evaporation.

$l_{P,ann}$ is the annual precipitation.

$T_{d,est}$ is the estimated dew point temperature.

R_a is the extraterrestrial solar radiation.

T_s is the average of the maximum and minimum daily temperature.

T_R is the difference between the maximum and minimum daily temperature.

$e_a(T)$ is the actual vapor pressure.

$e_s(T)$ is the saturation vapor pressure.

RH is the relative humidity.

T_{dew} is the estimated hourly dew point temperature.

I_0 is the hourly extraterrestrial irradiance.

a is the atmospheric attenuation factor.

$\emptyset_t$ is the latitude angle.

δ is the declination of the sun.

w_s is the sunset hour angle.

γ is the latent heat of vaporization.

References

AASHTO (American Association of State Highway and Transportation Officials). 2012. *AASHTO LRFD bridge design specifications. 6TH Ed, Washington, D.C*

Abi Shdid, C. and El-Masri, O. 2019. “Effect of transient thermal gradient on stresses in composite bridges”. In *ISEC 2019-10th International Structural Engineering and Construction Conference*, ISEC Press, North Dakota, USA, 848-853

Andrade, C., Bettencourt-Ribeiro, A., Buenfeld, N. R., Carcasses, M., Carino, N. J., Ehrenberg, F., ... and Whiting, D. 1999. “Preconditioning of concrete test specimens for the measurement of gas permeability and capillary absorption of water”. *Materials and Structures*, *32*(217), 174-176.

ANSYS. 2019. Ansys® academic research mechanical; release 19.1. Canonsburg, PA: Ansys.

ASCE (American Society of Civil Engineers). 2015. *Adapting infrastructure and civil engineering practice to a changing climate*. Reston, VA: ASCE.

Aydin, F. 2018. “Experimental investigation of thermal expansion and concrete strength effects on FRP bars behavior embedded in concrete.” *Construction and Building Materials*, *163*, 1-8.

Bader, D., Covey, C., Gutowski, W., Held, I., Kunkel, K., Miller, R., ... and Zhang, M. 2008. “Climate models: an assessment of strengths and limitations.” *US Department of Energy Publications*, 8.

Barr, P., Halling, M., and Rojas, E. 2014. “Bridge response due to temperature variations.” *Final Report*. CAIT-UTC-034, Center for Advanced Infrastructure and Transportation, Utah State University, Logan, Ut.

Bauer, N., Calvin, K., Emmerling, J., Fricko, O., Fujimori, S., Hilaire, J., ... and van Vuuren, D. P. 2017. "Shared socio-economic pathways of the energy sector–quantifying the narratives." *Global Environmental Change*, *42*, 316-330.

Belcher, S., Hacker, J., and Powell, D. 2005. "Constructing design weather data for future climates." *Building Services Engineering Research and Technology,* 26(1), 49–61.

Bidsandtenders. 2023. "Ontario: Bids and Tenders." Accessed February 1, 2022. Available from https://tinyurl.com/2p85wxnj

Note: The plans are available in the tender drawings files, pages 8, 9 and 12

Bidsandtenders. 2023. "Ontario: Bids and Tenders." Accessed February 1, 2022. Available from https://tinyurl.com/4mpma64a

Note: The plans are available in the drawings files, pages 4 and 9

Black, W., Moss, D., and Emerson, M. 1976. "Bridge temperatures derived from measurement of movement." *Report No. TRRL Report SR 748*, Transport Research Laboratory, Crowthorne, England

Browne, R.D., and Bamforth, P.B. 1981. "The use of concrete for cryogenic storage: A summary of research, past and present." *First International Conference on Cryogenic Concrete*

Copernicus Climate Change Service. 2021. "CMIP6 climate projections." *Climate Data Store (CDS).* Accessed February 20, 2023. 10.24381/cds.c866074c

Cran, J.A. 1963. "An investigation of the low temperature properties of concrete and reinforced concrete slabs." Master's thesis, Department of Civil Engineering, University of Manitoba.

CSA (Canadian Standard Association). 2014.Canadian highway bridge design code. CSA Group: S6-14. Rexdale, ON, Canada: CSA.

Dahmani, L., Khennane, A., and Kaci, S. 2007. "Behavior of the reinforced concrete at cryogenic temperatures.” *Cryogenics, 47,* 517-525.

Downie, B. 2005. “Effect of moisture and temperature on the mechanical properties of concrete.” Master’s thesis, College of Engineering and Mineral Resources, West Virginia University.

Duffie, J. and Beckman, W. 2006. *Solar Engineering of Thermal Processes*. Wiley, Hoboken, New Jersey, 3 edition.

Elbadry, M.M. and Ghali, A., 1983. “Temperature variations in concrete bridges.” *Journal of Structural Engineering*, *109*(10), 2355-2374.

Environment and Climate Change Canada. 2019. “Historical Data.” Accessed February 20, 2023 Available from https://climate.weather.gc.ca/historical_data/search_historic_data_e.html

Environment and Climate Change Canada. 2019.“Canadian weather energy and engineering data sets (CWEEDS).” *Engineering Climate Datasets*. Accessed February 20, 2023. Available from https://climate.weather.gc.ca/prodsservs/engineeringe.html

Esmaeeli, H. S., Farnam, Y., Bentz, D. P., Zavattieri, P. D., & Weiss, W. J. (2017). Numerical simulation of the freeze–thaw behavior of mortar containing deicing salt solution. *Materials and Structures*, *50*, 1-20.

Eyring, V., Bony, S., Meehl, G. A., Senior, C. A., Stevens, B., Stouffer, R. J., and Taylor, K. E. 2016. “Overview of the Coupled Model Intercomparison Project Phase 6 (CMIP6) experimental design and organization.” *Geoscientific Model Development*, *9*(5), 1937-1958.

Fagerlund, G. 1977. “The critical degree of saturation method of assessing the freeze/thaw resistance of concrete. *Materials and Structures*, *10*, 217-229.

Fagerlund, G. 1977. “The international cooperative test of the critical degree of saturation method of assessing the freeze/thaw resistance of concrete.” *Materials and Structures*, *10*, 231-253.

Fagerlund, G. 1973. "*Significance of critical degrees of saturation at freezing of porous and brittle materials*." *Rep. No.* 34, Div. of Building Technology, Lund Institute of Technology, Lund, Sweden (in Swedish).

Ferdjani, O., 1987. "Behaviour of a one cell prestressed concrete box girder bridge: analytical study." Master's thesis, Department of Civil Engineering and Applied Mechanics, McGill University

FIB (The International Federation of Structural Concrete).1985. *Thermal Effects in the Design of Concrete Structures. Bulletin 167, Rotterdam , Netherlands*

FIP (Federation Internationale de la Precontrainte). 1982. "Cryogenic Behaviour of Materials for Prestressed Concrete." *State of the Art Report*, 84

Fu, T. C., Yeih, W., Chang, J. J., and Huang, R. 2014. "The influence of aggregate size and binder material on the properties of pervious concrete." *Advances in Materials Science and Engineering*, 2014:963971. *https://doi.org/10.1155/2014/963971*

Ghahremani, B., Enshaeian, A. and Rizzo, P., 2022. "Bridge Health Monitoring Using Strain Data and High-Fidelity Finite Element Analysis." *Sensors*, *22*(14), 5172.

Ghantous, R. M., & Weiss, W. J. 2019. "Does the water to cement ratio of concrete impact the value of its critical degree of saturation?" In *10th International Conference on Fracture Mechanics of Concrete and Concrete Structures,* Bayonne (France).

Ghantous, R. M., Madland, H., Kwong, J., & Weiss, J. 2019. "Examining the influence of the degree of saturation on length change and freeze-thaw damage." *Advances in Civil Engineering Materials*, *8*(1), 365-374.

Ghimire S. 2014. "Restraint Moments Due to Thermal Gradients in Continuous Prestressed Concrete Girder Bridges." Master's thesis, The Department of Civil and Environmental Engineering, Louisiana State University.

Gu, B., Chen, Z., and Chen, X. 2014. “Temperature gradients in concrete box girder bridge under effect of cold wave.” *Journal of Central South University*, 21(3), 1227–1241.

Hagedorn, R., Martí-Vargas, J., Dang, C., Hale, W., and Floyd, R. (2019). “Temperature gradients in bridge concrete I-girders under heat wave.” *Journal of Bridge Engineering*, 24(8).

Hall, R., Krueger, R., Nicholson, N., Bercuson, D., and Morton, W. 2022. “Canada.” *Encyclopedia Britannica*, <https://www.britannica.com/place/Canada.> (Nov. 8, 2022).

Hartmann, D. L. 2015. *Global physical climatology (Vol. 103).* Newnes.

Hedegaard, B. D., French, C. E., and Shield, C. K. 2013. “Investigation of thermal gradient effects in the I-35W St. Anthony Falls Bridge.” *Journal of Bridge Engineering*, *18*(9), 890-900.

Hossain, T., Segura, S. and Okeil, A.M. 2020. “Structural effects of temperature gradient on a continuous prestressed concrete girder bridge: analysis and field measurements.” *Structure and Infrastructure Engineering*, *16*(11), 1539-1550.

Incropera, F., Dewitt, D., Bergman, T., and Lavine, A. 2007. *Fundamentals of Momentum, Heat and Mass Transfer*. Wiley, United States of America, 6 edition.

Iowa State University 2023. “ASOS Network”. Accessed January 10,2023. Available from https://mesonet.agron.iastate.edu/ASOS/

IPCC (Intergovernmental Panel on Climate Change). 2014. *Synthesis Report Summary for Policymakers Summary for Policymakers.*

Kanagaraj, S., and Pattanayak, S. 2003. “Measurement of the thermal expansion of metal and FRPs.” *Cryogenics*, *43*(7), pp.399-424.

Kimball, J. S., Running, S. W., and Nemani, R. 1997. “An improved method for estimating surface humidity from daily minimum temperature.” *Agricultural and forest meteorology*, *85*(1-2), 87-98.

King, L., Solaiman, T., and Simonovic, S. P. 2009. “Assessment of climate vulnerability in the Upper Thames River basin.” Water Resources Research Report No. 064, Facility for Intelligent Decision Support, Dept. of Civil and Environmental Engineering, London, Ontario, Canada.

Larsson, O. 2012. “Climate related thermal actions for reliable design of concrete structures.” Ph.D. thesis, Division of Structural Engineering, Lund Univ.

Lee, H.R., Ahn, N.S. and Yang, S.C., 2003. “Experimental Measurement of Concrete Thermal Expansion according to Aggregate Types.” *Journal of the Eastern Asia Society for Transportation Studies*, pp.145-150.

Lee, J. 2012. “Behavior of precast prestressed concrete bridge girders involving thermal effects and initial imperfections during construction.” *Engineering Structures*, 42, 1–8.

Lee, J. 2012. “Investigation of Extreme Environmental Conditions and Design Thermal Gradients during Construction for Prestressed Concrete Bridge Girders.” *Journal of Bridge Engineering*, 17(3), 547-566

Lee, J., and Kalkan, I. 2012. “Analysis of Thermal Environmental Effects on Precast, Prestressed Concrete Bridge Girders: Temperature Differentials and Thermal Deformations.” *Advances in Structural Engineering*, 15(3), 447–459.

Li, W., Pour-Ghaz, M., Castro, J., and Weiss, J. 2012. “Water absorption and critical degree of saturation relating to freeze-thaw damage in concrete pavement joints.” *Journal of Materials in Civil Engineering*, *24*(3), 299-307.

Li, W., Pour-Ghaz, M., Castro, J., and Weiss, J. 2012. “Water absorption and critical degree of saturation relating to freeze-thaw damage in concrete pavement joints.” *Journal of Materials in Civil Engineering*, *24*(3), 299-307.

Litvan, G. G. 1976. “Frost action in cement in the presence of de-icers.” *Cement and Concrete Research*, *6*(3), 351-356.

Litvan, G. G. 1976. “Frost action in cement in the presence of de-icers.” *Cement and Concrete Research*, *6*(3), 351-356.

Liu, L., Qin, G., Qin, S., & Tao, G. 2020. “Simulation of the volumetric deformation and changes in the pore structure of unsaturated cement-based materials subjected to freezing/thawing.” *Construction and Building Materials*, *230*, 116964.

Lu, Y., Li, D., Wang, K., and Jia, S. 2021. “Study on solar radiation and the extreme thermal effect on concrete box girder bridges.” *Applied Sciences*, 11(14).

Lupo, A., Kininmonth, W., Armstrong, J. S., and Green, K. 2013. “Global climate models and their limitations.” *Climate change reconsidered II: Physical science*, *9*-148.

Ma, W., Yang, C., Chu, C., Li, T., Tan, J., and Kan, H. 2013. “The impact of the 2008 cold spell on mortality in Shanghai, China.” *Int J Biometeorol, 57(1),* 179-184

Meehl, G. A., and Bony, S. 2011. “Introduction to CMIP5.” *Clivar Exchanges*, *16*(56), 4-5.

Meehl, G. A., Zwiers, F., Evans, J., Knutson, T., Mearns, L., and Whetton, P. 2000. “Trends in extreme weather and climate events: issues related to modeling extremes in projections of future climate change.” *Bulletin of the American Meteorological Society*, *81*(3), 427-436.

Menetrey, P. 1994. “Numerical Analysis of Punching Failure in Reinforced Concrete Structures.” Ph.D. thesis, Department of Civil Engineering, Ecole Polytechnique Federale de Lausanne

Miura, T. 1989. “The properties of concrete at very low temperatures.” *Materials and Structures*, *22*(4), 243-254.

Morton, W. L., Hall, R. D., Nicholson, N. L., Krueger, R. R. and, Bercuson, D. J. (N.D.). “Canada.” *Encyclopedia Britannica.* Accessed February 20, 2023.

https://www.britannica.com/place/Canada

Munawar, S., Rahman, G., Moazzam, M. F. U., Miandad, M., Ullah, K., Al-Ansari, N., and Linh, N. T. T. 2022. “Future climate projections using SDSM and LARS-WG downscaling methods for CMIP5 GCMs over the transboundary Jhelum River Basin of the Himalayas Region.” *Atmosphere*, *13*(6), 898.

Nevander, L. and Elmarsson, B. 2006. *Moisture Handbook: Practice and Theory*. Swedish Construction Service, Stockholm, Sweden, 3 edition.

NOAA (National Oceanic and Atmospheric Adminstration). 2023. “National Weather Service.” Accessed February 1, 2022. Available from https://www.weather.gov/.

Novikova, S. I. 1984. “Anisotropy of thermal expansion of solids.” *Measurement Techniques*, *27*(10), 933-938.

Obla, K., Kim, H., and Lobo, C. 2016. “Criteria for freeze-thaw resistant concrete mixtures.” *Advances in Civil Engineering Materials*, *5*(2), 119-141.

Oliver, J. 2005. *Encyclopedia of world climatology*. Springer, Dordrecht, The Netherlands, 2 edition.

O'Neill, B. C., Tebaldi, C., Van Vuuren, D. P., Eyring, V., Friedlingstein, P., Hurtt, G., ... and Sanderson, B. M. 2016. “The scenario model intercomparison project (ScenarioMIP) for CMIP6.” *Geoscientific Model Development*, *9*(9), 3461-3482

Pantazopoulou, S. J., and Mills, R. H. 1995. “Microstructural aspects of the mechanical response of plain concrete.” ACI *Materials J.*, *92*(6), 605-616.

Parrott, L. J. 1994. “Moisture conditioning and transport properties of concrete test specimens.” *Materials and Structures*, *27*, 460-468.

Peterson, A. 2016. “Köppen climate types of Canada.” *Wikimedia Commons*, Accessed November 8, 2022. Available from https://tinyurl.com/mryvppdk.

Pisani, M.A. 2004. “Non-linear strain distributions due to temperature effects in compact cross-sections.” *Engineering Structures*, 26 (10), 1349-1363.

Planas, J., Corres, H., Elices, M., and Chueca, R. 1984. “Thermal deformation of loaded concrete during thermal cycles from 20° C to– 165° C.” *Cement and Concrete Research*, *14*(5), 639-644.

Popp, A., Calvin, K., Fujimori, S., Havlik, P., Humpenöder, F., Stehfest, E., ... and van Vuuren, D. P. 2017. “Land-use futures in the shared socio-economic pathways.” *Global Environmental Change*, *42*, 331-345.

Powell-Palm, M.J., Rubinsky, B. and Sun, W., 2020. “Freezing water at constant volume and under confinement.” *Communications Physics*, *3*(1), 39-47

Powers, T. C., and Helmuth, R. A. 1953. “Theory of volume changes in hardened portland-cement paste during freezing.” *Materials and Construction*, 32, 285-297(Vol. 32).

Pryor, S. C., and Barthelmie, R. J. 2010. “Climate change impacts on wind energy: A review.” *Renewable and sustainable energy reviews*, *14*(1), 430-437.

Roeder, C. 2002. “Thermal movement design procedure for steel and concrete bridges.” *Final Report. NCHRP 20-07/106*, Department of Civil Engineering, University of Washington, Seattle, WA.

Rostasy, F. S., Schneider, U., and Wiedemann, G. 1979. “Behaviour of mortar and concrete at extremely low temperatures.” *Cement and Concrete Research*, *9*(3), 365-376.

Saad, S., Bashir, R., and Pantazopoulou, S. 2022. “The effect of cold waves on the structural performance of concrete box girders.” *Structural Engineering International*, 32(4), 596–604.

Saad, S., Nasir, A., Bashir, R., and Pantazopoulou, S. J. 2023. "Numerical Study on the Effect of Climate Parameters on the Extreme Thermal Gradients in Concrete Box Girders." *Journal of Bridge Engineering*, *28*(10), 04023069.

Safiuddin, M., and Hearn, N. 2005. "Comparison of ASTM saturation techniques for measuring the permeable porosity of concrete." *Cement and Concrete Research*, *35*(5), 1008-1013.

Scherer, G.W. and Valenza, J.J. 2005. "Mechanisms of frost damage." *Materials Science of Concrete*, 7 (60), 209-246.

Semenov, M. A., Barrow, E. M., and Lars-Wg, A. 2002. "A stochastic weather generator for use in climate impact studies." *User Manual.* Hertfordshire, UK 0–27

Siddiqui, M. S., and Fowler, D. W. 2015. "Effect of internal water pressure on the measured coefficient of thermal expansion of concrete." *Journal of materials in civil engineering*, *27*(4), 04014151.

Siddiqui, M. S., and Fowler, D. W. 2017. "Experimental investigation to improve the thermomechanical response of concrete samples subjected to coefficient of thermal expansion testing." *Journal of Materials in Civil Engineering*, *29*(9), 04017144.

Solcast, 2019. "Global solar irradiance data and PV system power output data." Accessed February 1, 2022, Available from https://solcast.com/

Song, X., Melhem, H., Li, J., Xu, Q., and Cheng, L. 2016. "Effects of Solar Temperature Gradient on Long-Span Concrete Box Girder during Cantilever Construction." *Journal of Bridge Engineering*, 21(3).

Tan, H., Qian, D., Xu, Y., Yuan, M. and Zhao, H. 2023. "Analysis of vertical temperature gradients and their effects on hybrid girder cable-stayed bridges." *Sustainability*, *15*(2), 1053.

Thevenard, D. and Haddad, K. 2005. "Ground reflectivity in the context of building energy simulation." *Energy and Buildings*, 38(8), 972–980.

Thorsen, S. (2023). “Toronto, Ontario, Canada - sunrise, sunset, and daylength, December 2023.” *Time and Date*. Accessed February 20, 2023 https://www.timeanddate.com/sun/canada/toronto?month=12.+Up

Torres, A. F., Walker, W. R., and McKee, M. 2011. “Forecasting daily potential evapotranspiration using machine learning and limited climatic data.” *Agricultural Water Management*, *98*(4), 553-562.

Upreti, H., and Ojha, C. S. P. 2017. “Estimation of relative humidity and dew point temperature using limited meteorological data.” *Journal of Irrigation and Drainage Engineering*, *143*(9), 05017005.

Van de Veen, V. 1987. “Properties of concrete at very low temperatures: A survey of the literature.” *Report Stevin Laboratory, Concrete Structures 25-87-2*

Vuorinen, J., 1970. “On Use of Dilation Factor and Degree of Saturation in Testing Concrete for Frost Resistance,” *Materials Science*, *14(1)*, 37-64.

Wann, M., Yen, D., and Gold, H. J. 1985. “Evaluation and calibration of three models for daily cycle of air temperature”. *Agricultural and forest meteorology*, *34*(2-3), 121-128.

Wayne, G. P. 2014. Representative concentration pathways. *Skeptical science*, *24*. Accessed February 20, 2023. Available from http://www.skepticalscience.com/docs/RCP_Guide.pdfGuide.pdf

Weather stats *(2023). “*Temperature - hourly data for Toronto.” *Canada Weather Stats.* Accessed February 20, 2023 Available from https://toronto.weatherstats.ca/charts/temperature-hourly.html

Wilby, R. L., and Wigley, T. M. 1997. “Downscaling general circulation model output: a review of methods and limitations.” *Progress in physical geography*, *21*(4), 530-548.

Wolfram Research, 2013. “Heat transfer”. Accessed February 1, 2022. Available from https://tinyurl.com/yckvewvd

Xia, J., Xi, Y., and Jin, W. L. 2017. “Temperature-dependent coefficient of thermal expansion of concrete in freezing process.” *Journal of Engineering Mechanics*, *143*(8), 04017043.

Xia, Q., Zhou, L., and Zhang, J., 2018. “Thermal performance analysis of a long-span suspension bridge with long-term monitoring data.” *J. Civ. Struct. Heal. Monit. 8(4)*, 543–553

Xie, H., Yao, Z., Zhang, Y., Yanjun, X., Xu, X., Liu, T., Lin, H., Lao, X., Rutherford, S., Chu, C., Huang, C., Baum, S., and Ma, W. 2012. “Short-Term Effects of the 2008 Cold Spell on Mortality in Three Subtropical Cities in Guangdong Province, China.” *Environmental health perspectives, 121 (10)*

Xie, J., and Yan, J.B. 2018. “Experimental studies and analysis on compressive strength of normal-weight concrete at low temperatures.” *Structural Concrete, 19,* 1235– 1244.

Xie, J., Li, X. and Wu, H. (2014). “Experimental study on the axial-compression performance of concrete at cryogenic temperatures.” *Construction and Building Materials. 72,* 380–388.

Yamane,S., Kasami,H., and Okuno, T. 1978. “Properties of concrete at very low temperatures.” In *Douglas McHenry international symposium on concrete and concrete structures, American Concrete Institute Special publication 55*, 207-222

Yamina, K. 2018. “Mechanical Behavior of Hydraulic Concrete to Extreme Service Temperatures: The Influence of the Particle Size.” In *Materials for Sustainable Infrastructure: Proceedings of the 1st GeoMEast International Congress and Exhibition,* 294-305

Zhengwu, J., Cong, Z., Zilong, D., Xinping, Z., and Wenting, L. 2019. “Thermal strain of cement-based materials under cryogenic temperatures and its freeze-thaw cycles using fibre Bragg grating sensor”. *Cryogenics*, *100*, 1-10.

Zhou, G.D., Yi, T.H., Chen, B. and Zhang, H. 2015. “Analysis of three-dimensional thermal gradients for arch bridge girders using long-term monitoring data.” *Smart Structures and Systems*, *15*, 469-488.